SMIP19

SMIP19 SEMINAR ON
UTILIZATION OF STRONG-MOTION DATA

Los Angeles, California
October 18, 2019

PROCEEDINGS

Sponsored by

California Strong Motion Instrumentation Program
California Geological Survey
California Department of Conservation

Co-Sponsors

California Seismic Safety Commission
California Governor's Office of Emergency Services
Office of Statewide Health Planning and Development
California Department of Transportation

California
**Department of
Conservation**
California Geological Survey

The California Strong Motion Instrumentation Program (CSMIP), a program within the California Geological Survey (CGS) of the California Department of Conservation, records the strong shaking of the ground and structures during earthquakes for analysis and utilization by the engineering and seismology communities, through a statewide network of strong motion instruments (www.conservation.ca.gov/CGS/smip). CSMIP is advised by the Strong Motion Instrumentation Advisory Committee (SMIAC), a committee of the California Seismic Safety Commission. Major program funding is provided by an assessment on construction costs for building permits issued by cities and counties in California, with additional funding from the California Governor's Office of Emergency Services (Cal OES), the Office of Statewide Health Planning and Development (OSHPD) and the California Department of Transportation (Caltrans)

In July 2001, the California Governor's Office of Emergency Services (Cal OES) began funding for the California Integrated Seismic Network (CISN), a newly formed consortium of institutions engaged in statewide earthquake monitoring that grew out of TriNet, funded by FEMA, and including CGS, USGS, Caltech and UC Berkeley. The goals are to record and rapidly communicate ground shaking information in California, and to analyze the data for the improvement of seismic codes and standards (www.cisn.org). CISN produces ShakeMaps of ground shaking, based on shaking recorded by stations in the network, within minutes following an earthquake. The ShakeMap identifies areas of greatest ground shaking for use by OES and other emergency response agencies in the event of a damaging earthquake.

The Center for Engineering Strong Motion Data (CESMD) is operated by the CSMIP in cooperation with the National Strong-Motion Project (NSMP), a part of the Advanced National Seismic System (ANSS) of the U.S. Geological Survey (USGS). The CESMD builds on and incorporates the CISN Engineering Data Center and will continue to serve the California region while expanding to serve other ANSS regions. The Data Center provides strong-motion data rapidly after a significant earthquake in the United States. Users also have direct access to data from previous earthquakes and detailed information about the instrumented structures and sites. The CESMD also provides access to the U.S. and international strong ground motion records through its Virtual Data Center (VDC). The Data Center is co-hosted by CGS and USGS at www.strongmotioncenter.org

DISCLAIMER

Neither the sponsoring nor supporting agencies assume responsibility for the accuracy of the information presented in this report or for the opinions expressed herein. The material presented in this publication should not be used or relied upon for any specific application without competent examination and verification of its accuracy, suitability, and applicability by qualified professionals. Users of information from this publication assume all liability arising from such use.

SMIP19

SMIP19 SEMINAR ON
UTILIZATION OF STRONG-MOTION DATA

Los Angeles, California
October 18, 2019

<u>PROCEEDINGS</u>

Edited by

Daniel Swensen

Sponsored by

California Strong Motion Instrumentation Program
California Geological Survey
California Department of Conservation

Co-Sponsors

California Seismic Safety Commission
California Governor's Emergency Services
Office of Statewide Health Planning and Development
California Department of Transportation

PREFACE

The California Strong Motion Instrumentation Program (CSMIP) in the California Geological Survey of the California Department of Conservation established a Data Interpretation Project in 1989. Each year CSMIP funds several data interpretation contracts for the analysis and utilization of strong-motion data. The primary objectives of the Data Interpretation Project are to further the understanding of strong ground shaking and the response of structures, and to increase the utilization of strong-motion data in improving post-earthquake response, seismic code provisions and design practices.

As part of the Data Interpretation Project, CSMIP holds annual seminars to transfer recent research findings on strong-motion data to practicing seismic design professionals, earth scientists and post-earthquake response personnel. The purpose of the annual seminar is to provide information that will be useful immediately in seismic design practice and post-earthquake response, and in the longer term, useful in the improvement of seismic design codes and practices. Due to State budget constraints, CSMIP did not hold an annual seminar in 2010 or 2011. The SMIP19 Seminar is the twenty-eighth in this series of annual seminars.

The SMIP19 Seminar is divided into two sessions in the morning and two sessions in the afternoon. There are eight presentations on the results from CSMIP-funded projects and one invited presentation. The sessions in the morning include five presentations. The first session will focus on lifeline structures. Professor Elgamal of UC San Diego will present on the seismic response of the Eureka Channel Bridge. He will be followed by a presentation from Professor Zareian of UC Irvine on Caltrans bridge modeling. The second session will focus on ground motion issues. Professor Stewart of UCLA will present on the topic of site response and its predictability. Professor Taciroglu, also of UCLA, will then present on earthquake input excitations for buildings. The final presentation of the second session will be an invited presentation from Professor Stewart of UCLA and Janis Hernandez of CGS on the recent Ridgecrest Earthquake sequence.

The two sessions in the afternoon include four presentations on building response topics. In the third session, Professor Hutchinson of UC San Diego will present on the seismic response of nonstructural components in buildings. She will be followed by a presentation from Professor Loh, also of UC San Diego, on building response analysis and damage detection. The last session will include presentations on column base flexibility in buildings by Professor Kanvinde of UC Davis, and FEMA P58 and the potential for automated loss estimation by Professor Moehle of UC Berkeley. Individual papers and the proceedings are available for download by the SMIP19 participants at the provided link, and will be available at the CSMIP website in the future.

Daniel Swensen
CSMIP Data Interpretation Project Manager

Appreciation to Members of the
Strong Motion Instrumentation Advisory Committee

Main Committee
Farzad Naeim, Chair, Farzad Naeim, Inc.
Norman Abrahamson, Pacific Gas & Electric Company
Bruce Clark, Leighton & Associates
Martin Eskijian, California State Lands Commission (retired)
David Gutierrez, GEI Consultants
Wilfred Iwan, California Institute of Technology
Mark Mahan, Caltrans
Marshall Lew, Wood
Bret Lizundia, Rutherford + Chekene
Chris Tokas, Office of Statewide Health Planning and Development
Robert Anderson (ex-officio), Seismic Safety Commission

Ground Response Subcommittee
Marshall Lew, Chair, Wood
Zia Zafir, Kleinfelder
Geoffrey Martin, Univ. of Southern California

Buildings Subcommittee
Bret Lizundia, Chair, Rutherford + Chekene
Lucie Fougner, Degenkolb Engineers
Ifa Kashefi, City of Los Angeles (retired)
Michelle Yu, City of San Francisco
Eduardo Miranda, Stanford University
Roy Lobo, Office of Statewide Health Planning and Development
Chia-Ming Uang, UC San Diego

Lifelines Subcommittee
Martin Eskijian, Chair, California State Lands Commission (retired)
David Gutierrez, GEI Consultants
Mark Mahan, Caltrans
Faiz Makdisi, SAGE Engineers

Data Utilization Subcommittee
Wilfred Iwan, Chair, California Institute of Technology
Representatives from each Subcommittee

EUREKA CHANNEL BRIDGE: SEISMIC RESPONSE AND SYSTEM IDENTIFICATION

Ahmed Elgamal[1], Ning Wang[2], and John Li[1]

[1] University of California, San Diego, Dept. of Structural Engineering, La Jolla, CA 92093-0085
[2] Institute of Geophysics, China Earthquake Administration, Beijing, 100081, China

Abstract

A unique opportunity for gaining insights is facilitated by availability of the CSMIP Eureka Channel Bridge seismic records. Of special interest is the recorded response of a bridge pier at the deck, pile cap and within the underlying pile foundation. In this study, recorded response from the strongest to date 2010 Ferndale earthquake (PGA of about 0.25g), along with other available low-amplitude events are employed to evaluate the pile foundation, and overall bridge seismic response. Finite Element modeling is employed along with the optimization framework SNOPT, to derive salient characteristics of the overall bridge system response.

Introduction

A large set of earthquake records from the highly instrumented Eureka Channel bridge-ground system (Figure 1) has been compiled and made available by the California Geological Survey (http://www.strongmotioncenter.org). During a large number of seismic events, more than 20 data channels have been documenting the seismic response of the deck, foundation, abutments, and adjacent ground surface. Of special interest is the response of a pier instrumented at the deck, pile cap, and below ground in the foundation.

Bridge Configuration and Instrumentation

The Eureka Channel bridge configuration is shown in Figure 2. In this Figure, dense instrumentation is seen along the deck, at the abutments, and on the nearby ground surface. In addition, a Pier (E7) is instrumented at the pile cap and within the underlying pile foundation. It may be noted (Figure 2) that the bridge includes a substantial horizontal curve, which results in significant coupling in its longitudinal (LONG) and transverse (TRAN) response.

Significant variability in the ground stratification and soil properties may be observed (Figures 2). The soil profile (Figure 2) reveals that the site is mantled by very soft silty clay underlain by medium clay and compact gray sand. Stiff clay was encountered at the elevation of about -12 m and continues to the maximum explored depth. Soil layers vary in thickness and are not continuous horizontally (Caltrans 2002).

Earthquake Motions

Records from a large number of earthquakes (Table 1) during the period of June 2007 through March 2014 are currently available with Magnitudes in the range of 4.5 M_L (local magnitude) to 6.8 M_w (moment magnitude). To date, the highest levels of recorded acceleration are due to the 2010 $M_w = 6.5$ Ferndale Earthquake approximately 35 km away from Ferndale, CA in a deformation zone of the southernmost Gorda Plate (http://earthquake.usgs.gov, Storesund et al. 2010). During this event, the recorded Transverse peak acceleration was 0.25 g at the ground surface near the bridge, and 0.51 g at the bridge deck.

(a)

(b)

Figure 1. Bridge Configuration: (a) Samoa Channel Bridge, Eureka Geotechnical Array, Middle Channel Bridge and Eureka Channel Bridge (Map Data @ 2015 Google), and (b) Close-up of the Eureka Channel Bridge (http://www.strongmotioncenter.org)
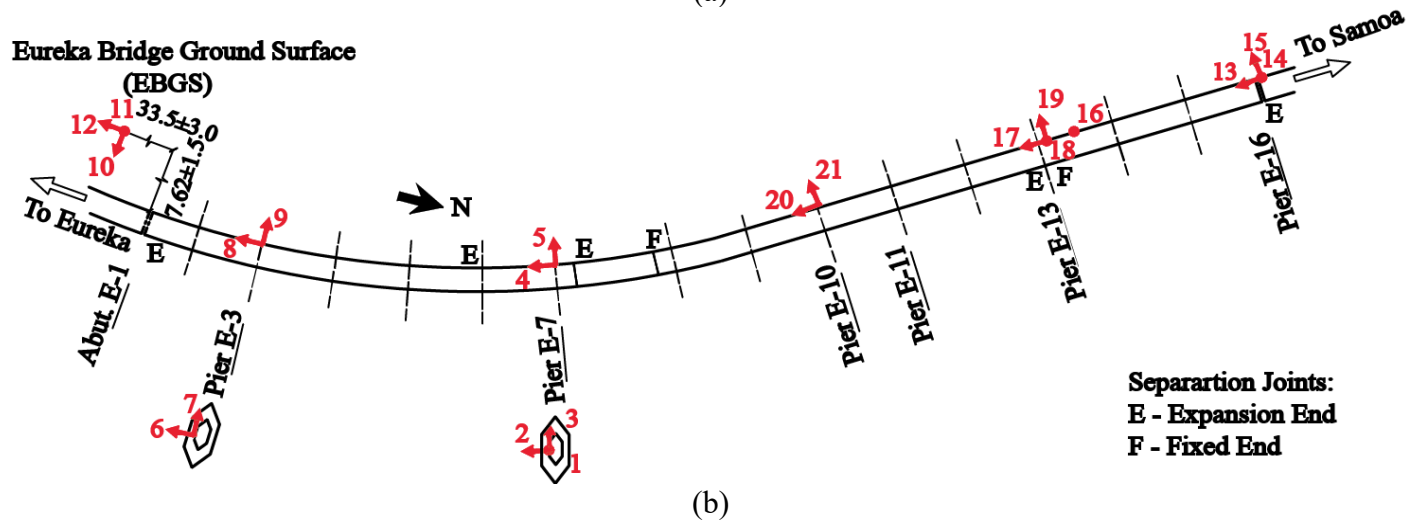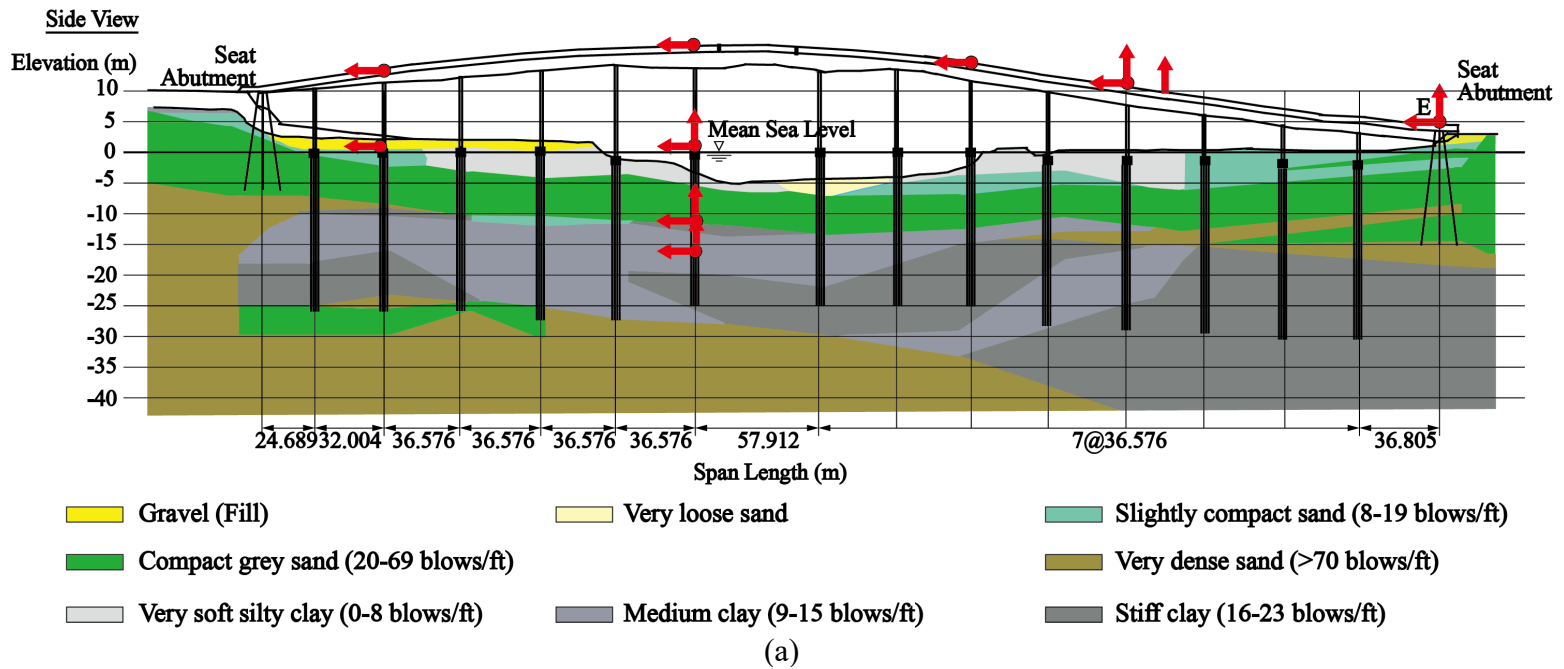
Side View

Elevation (m)

Seat Abutment

Mean Sea Level

Seat Abutment

Span Length (m)

24.689 32.004 36.576 36.576 36.576 36.576 57.912 7@36.576 36.805

	Gravel (Fill)		Very loose sand		Slightly compact sand (8-19 blows/ft)
	Compact grey sand (20-69 blows/ft)				Very dense sand (>70 blows/ft)
	Very soft silty clay (0-8 blows/ft)		Medium clay (9-15 blows/ft)		Stiff clay (16-23 blows/ft)

(a)

Eureka Bridge Ground Surface (EBGS)

33.5±3.0

7.62±1.5

To Eureka

N

To Samoa

Abut. E-1

Pier E-3

Pier E-7

Pier E-10

Pier E-11

Pier E-13

Pier E-16

Separartion Joints:
E - Expansion End
F - Fixed End

(b)

Figure 2. Layout of Instrumentation at the Eureka Channel Bridge: (a) Bridge-ground side view (Caltrans 2002), and (b) Plan view
(http://www.strongmotioncenter.org)

Table 1 Recorded earthquakes at the bridge site (arranged by order of peak acceleration)

Earthquake	Epicentral Distance (km)	E-7 Pile -16.46 m		Bridge	
		TRAN	LONG	TRAN	LONG
Ferndale 2010[*] (M_w=6.5)	54.5	0.130	0.158	0.510	0.955[**] 0.540[***]
Ferndale 2014 (M_w=6.8)	82.7	0.020	0.014	0.072	0.048
Trinidad 2008 (M_w=4.6)	41.7	0.009	0.013	0.060	0.047
Humboldt Hill 2013 (M_L=4.5)	20.8	0.009	0.008	0.019	0.014
Trinidad 2007 (M_L=5.1)	65.6	0.018	0.007	0.081	0.031
Ferndale 2010 Feb (M_w=5.9)	77.8	0.013	0.009	0.046	0.022
Willow Creek 2008 (M_w=5.4)	55.4	0.007	0.004	0.026	0.017
Ferndale 2007 (M_L=5.4)	63.3	0.005	0.006	0.021	0.014

[*]The January 2010 Ferndale Earthquake will be referred to as "the moderate event" in this study
[**]Large peak acceleration due to spikes from separation joints (Huang and Shakal 1995; Malhotra et al. 1995)
[***]Estimated after removing spikes using a band-pass filter

Eureka Channel Bridge and Pier E7

In this section representative responses of the bridge are presented. Figure 3 displays the bridge relative displacement referenced to the -16.46 m pile motion (essentially the ground motion at this depth) for the 2007 Ferndale event. All along the deck, predominant in-phase response is noted in both directions (TRAN defined as radially inward for this curved bridge). The bridge is seen to be noticeably more flexible in the mid-span zone (e.g. Channels 4 and 5 at Pier E-7), with the relatively tall compliant pier at this location (Figure 2).

Transverse displacement along Pier E-7 at the four instrumented elevations (Figure 2) is shown in Figure 4. In-phase response with a dominant fundamental period is evident (about 0.65 seconds). Furthermore, it can be seen (Figure 4) that the pile cap as well as the bridge deck displacements display a significant level of amplification. In general, the pier deformation is evenly accounted for by the column and the pile group deformations in both the transverse and longitudinal directions.

Pier E-7 Seismic Response

In an effort to gain preliminary insights, the transverse recorded seismic motion of Pier E-7 was studied, based on its tributary section of the bridge deck (Wang 2015). This idealization in the transverse direction is partially substantiated by presence of separation joints at the adjacent bents (Figure 2).

Utilizing the recorded motions, the dynamic transverse response is investigated to identify lateral stiffness of the E-7 column and the foundation at this location. A sub-structuring

approach (Elgamal et al. 1996) is adopted where motion at any given depth is taken to define the "input" for the overlying structural domain.

As such, using a beam-column pier E-7 Finite Element (FE) idealization from the deck, down to the pile cap (Figure 2), column flexural rigidity was identified $(EI)_{id}$ by minimizing the difference between the computed and recorded Channel 5 deck response with the aid of SNOPT (Appendix A) to estimate a secant flexural rigidity. For that purpose, the recorded pile cap motion (Chan 3) at the base of the column is employed as the input base excitation. On this basis (Wang et al. 2020), it was found that the identified flexural rigidity $(EI)_{id}$ of the column (Table 3) was about 0.6 EI for low amplitude earthquake events (where EI is the un-cracked section bending stiffness). This estimate compares well with practical guidelines (e.g., Caltrans 2013). During the moderate shaking event, $(EI)_{id}$ instantaneous values reached as low as about 0.25 EI, with no signs of permanent reduction as the drift ratio diminished towards the end of shaking.
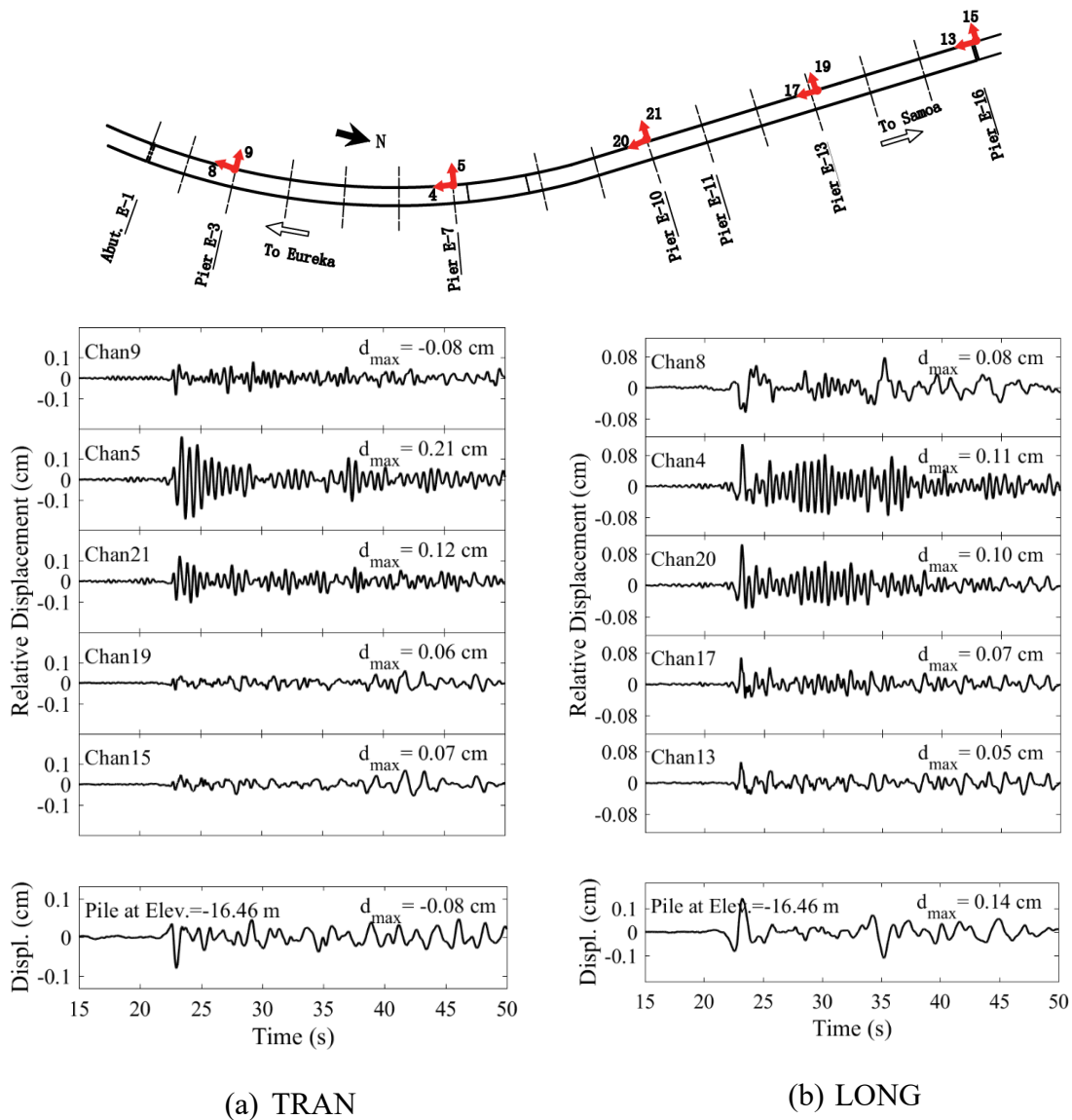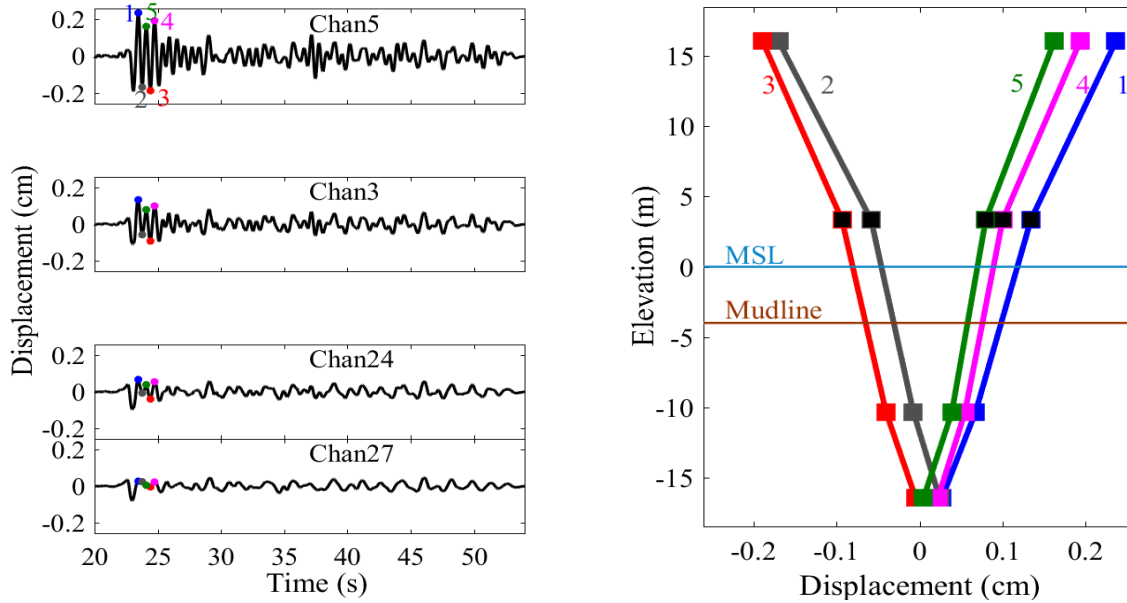

Figure 3. Relative displacement along the bridge deck during the 2007 Ferndale Earthquake
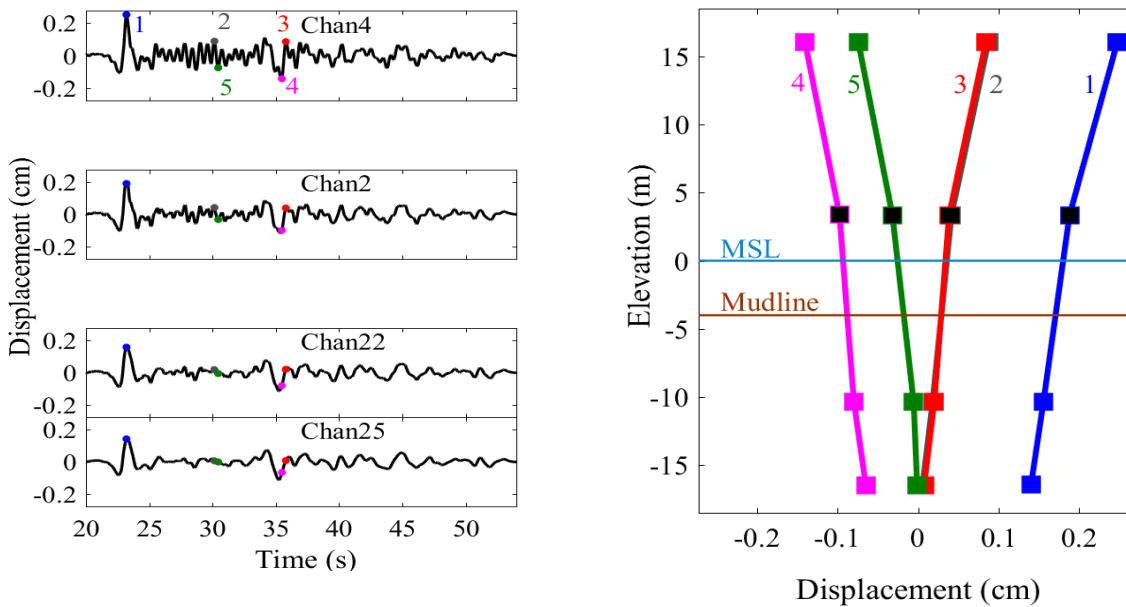
Figure 4. Time history of displacement and displaced configuration of Pier E7 at selected time instants during the 2007 Ferndale Earthquake

Using a similar approach, the estimated E-7 foundation stiffness clearly reflected the constraining effect of the soil surrounding the pile foundation. During the moderate event (Wang et al. 2020), instantaneous reductions in stiffness of about 50% were noted during the strongest phase of this shaking event.

6

Eureka Channel Bridge Lateral Foundation Stiffness

A beam-column model (202 elements) representing the entire Eureka Channel Bridge with its different column heights was developed (Wang et al. 2020). The graphical user interface MSBridge (Elgamal et al. 2014) was employed to generate the mesh for this curved bridge.

Focus was placed on the transverse response. Lateral springs were included at the base of the pier columns to account for stiffness of the underlying pile foundations and the associated soil-foundation-structure interaction (Lam and Martin 1986; Zafir 2002). These springs represent stiffness of the foundation down to an assumed uniform-excitation depth as defined by the recorded motion at -16.46 m. Using SNOPT (Appendix A), stiffness of the lateral springs was optimized so that the computed response is compatible with the recorded motions along the bridge super-structure (Wang et al. 2020). The results shown in Figure 5 suggest (compared to the Samoa Channel bridge scenario as reported in Wang et al. 2018):
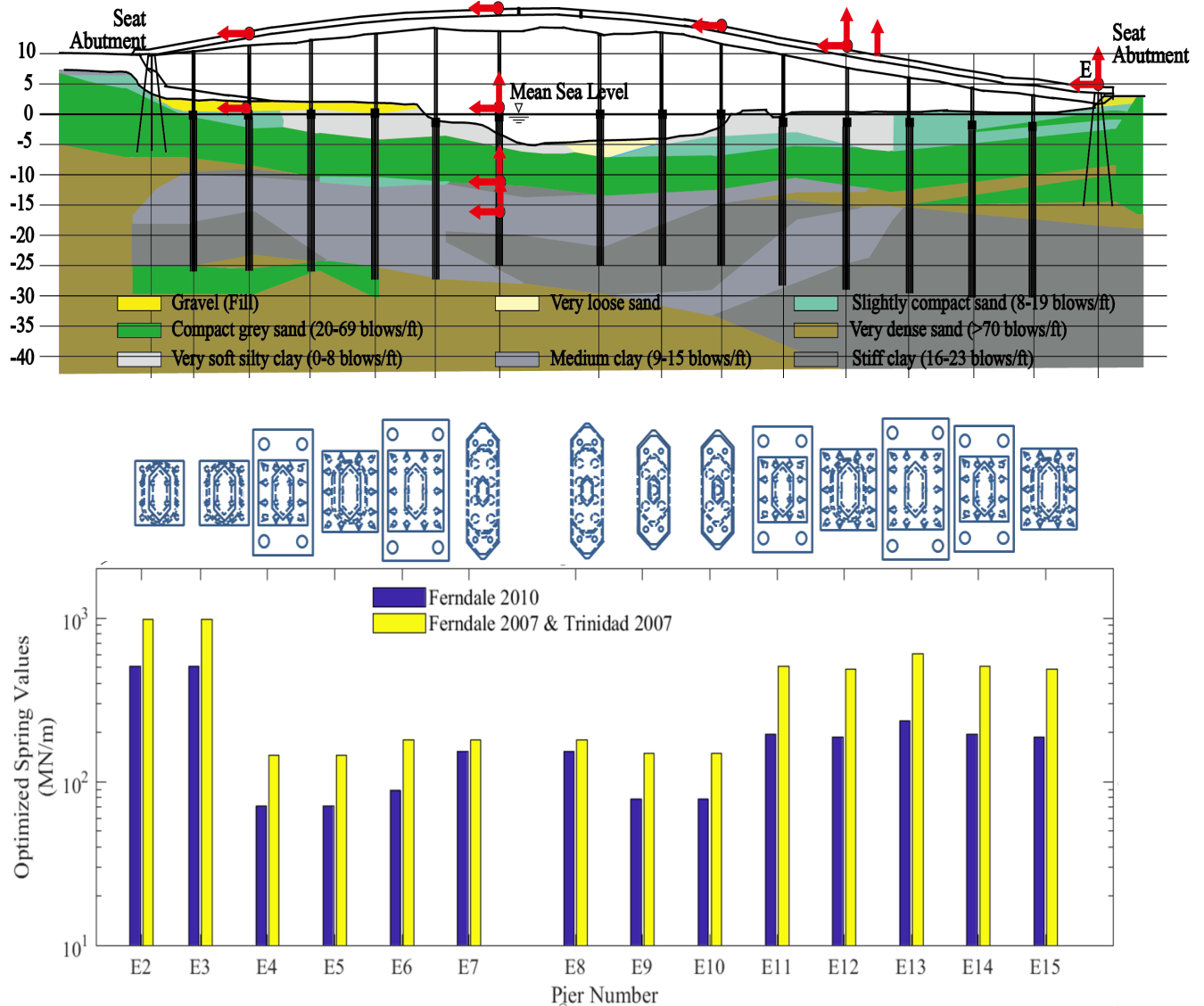
Figure 5. Identified Transverse direction base spring values along the Eureka Channel bridge

i) Foundation stiffness overall is higher,
ii) Reduction in stiffness during the strong shaking phase is pronounced, but to a lesser degree.
iii) Variability in stiffness along the bridge length is less pronounced.

Summary and Conclusions

The Eureka CSMIP seismic records (3 bridges and downhole array) constitute a unique invaluable resource for documentation of bridge and foundation response over a wide range of ground shaking scenarios. Inferred lateral stiffness of the involved pile-groups provides new insights about the actual foundation resistance at low and moderate levels of seismic excitation. These insights increase our confidence in current design/modeling assumptions, and allow for better understandings as relates to bridge response during strong earthquakes.

Acknowledgements

Appendix A

SNOPT (Sparse Nonlinear Optimization), a general-purpose numerical optimization code (Gill et al. 2002) was employed (Wang et al. 2020) to minimize the difference (Figure 6) between computed and recorded seismic response (Elgamal et al. 2004). The extended OpenSees-SNOPT framework, has been conveniently set up to perform this task (Gu 2008). For each earthquake simulation, OpenSees starts with a user-defined set of modeling parameters (initial guess), and an objective function Φ (measure of error) is computed using the recorded and computed responses. From there, SNOPT systematically conducts numerous OpenSees runs in which values of the modelling parameters are changed incrementally (re-computing Φ every time). Conceptually, if a lower Φ is found, values of the parameters are updated and the process continues until a minimum Φ is attained (thus defining optimal values of the numerical model parameters, Figure 6). A major advantage of SNOPT is that it requires relatively few evaluations of the objective function which helps speed up the time-consuming OpenSees simulations (Gu 2008).

The objective function was defined to be the sum of squared differences of computed and recorded seismic response at the sensor locations of interest (over any user-specified time interval):

$$\Phi = \sum_{i=1}^{Number\ of\ Sensors} \sum_{n=Start\ time\ step}^{End\ time\ step} (u_i(t_n) - u_i^{Rec}(t_n))^2$$

in which u is the OpenSees computed response (displacement or acceleration), u^{Rec} is the recorded instrumentation response, and t is time step (Wang et al. 2020).
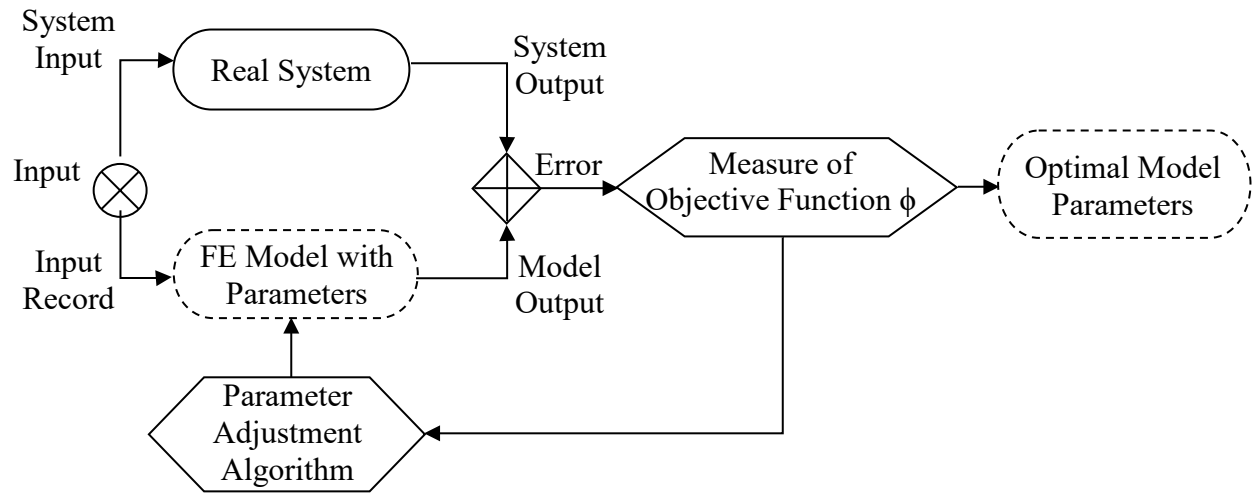
Figure 6. Block diagram illustrating the optimization procedure framework (after Zeghal 1990, Elgamal et al. 2004)

References

Caltrans (2002). "As-Built Plans, Earthquake Retrofit Project for Eureka Channel Bridge." California Department of Transportation, Sacramento, CA, [personal communication].

Caltrans (2013). "Seismic Design Criteria Version 1.7." California Department of Transportation, Sacramento, CA.

Elgamal, AW, Zeghal, M, Parra, E, Gunturi, R, Tang, HT, and Stepp, JC (1996). Identification and modeling of earthquake ground response - I. Site amplification. Soil Dynamics and Earthquake Engineering;15(8):499-522.

Elgamal A, Lai T, Gunturi R, Zeghal M. (2004). System identification of landfill seismic response. Journal of earthquake engineering;8(04):545-566.

Elgamal, A., Lu, J., and Mackie, K. (2014). "MSBridge: OpenSees Pushover and Earthquake Analysis of Multi-span Bridges - User Manual." Department of Structural Engineering, University of California, San Diego.

Gill, PE, Murray, W, and Saunders, MA (2002). SNOPT: An SQP algorithm for large-scale constrained optimization. SIAM Journal on Optimization;12(4):979-1006.

Gu Q. (2008). Finite element response sensitivity and reliability analysis of soil-foundation-structure-interaction (SFSI) systems, Doctor of Philosophy. University of California, San Diego, CA.

Huang, M. J., & Shakal, A. F. (1995). CSMIP strong-motion instrumentation and records from the I10/215 interchange bridge near San Bernardino. Earthquake spectra, 11(2), 193-215.

Lam, I. P., and Martin, G. R. (1986). "Sesimic Design of Highway Bridge Foundations." Federal Highway Administration, Washington D.C.

Malhotra, P. K., Huang, M. J., & Shakal, A. F. (1995). Seismic interaction at separation joints of an instrumented concrete bridge. Earthquake eng & structural dyn, 24(8), 1055-1067.

Storesund, R., Dengler, L., Mahin, S., Collins, B. D., Hanshaw, M., Turner, F., and Welsh, K. (2010). M6.5 Earthquake Offshore Northern California January 9, 2010. GEER Field Reconnaissance Summary.

Wang, N., Elgamal, A., & Lu, J. (2018). Assessment of the Samoa Channel Bridge-foundation seismic response. Soil Dynamics and Earthquake Engineering, 108, 150-159.

Wang, N., Elgamal, A., & Lu, J. (2020). Assessment of the Eureka Channel Bridge-foundation seismic response. (in preparation).

Zafir, Z. (2002). "Seismic Foundation Stiffness for Bridges." Proc., Deep Foundations 2002: An International Perspective on Theory, Design, Construction, and Performance, ASCE, GSP 116, Orlando, Florida, 1421-1437.

Zeghal, M. (1990). System identification of the nonlinear seismic response of earth dams, Ph.D. Thesis, Princeton University, Princeton, NJ.

VALIDATION OF CALTRANS ORDINARY BRIDGE MODELING APPROACH USING CSMIP DATA

Yijun Xiang, Jawad Fayaz, Farzin Zareian

Department of Civil & Environmental Engineering
University of California, Irvine

Abstract

This study aims at validating the modeling approaches of ordinary bridge structures suggested by Caltrans (SDC 2013; referred to as *SDC* models) and sophisticated models suggested by researchers, herein termed as *Stick* models. The validation is conducted using the CSMIP sensor data of four ordinary bridges in California with seat-type, and monolithic abutments. The backbone curves of the structural components of the *Stick* model including shear keys, abutment piles, and backfill soil are updated using Particle Swarm Optimization. This study yields the guidelines for calibration of parameters of bridge structural components and suggests improvements for modeling approaches of such bridges.

Introduction

Seat-type and monolithic box-girder bridges are among the most common types of highway bridges constructed in California. These bridges experienced different levels of damage such as rotation of decks, unseating of abutments, breakage of shear keys, and damage to columns during seismic events. As an essential part of public infrastructure, bridges are expected to be designed in a way that they survive and maintain functionality after major earthquake excitations. With this backdrop, advanced bridge modeling approaches along with nonlinear time-history analysis is needed to provide insight for the proper and safe design of bridge structures. There is a substantial body of research focusing on designing, modeling and nonlinear behavior of seat-type and monolithic bridges. Current bridge design specifications in California (Caltrans SDC, 2013) include seismic design criteria for Ordinary Standard bridges and their components including abutments, superstructure, substructure support systems and foundations. Caltrans SDC details how bridge design engineers should proportion bridge components, and conduct analyses to capture the bridge behavior at the component- and system-level during design level seismic excitations.

During the past decades, researchers have developed analytical models for bridge structures and investigated their behavior during seismic excitations. In particular, Mackie and Stojadinovic (2007) developed bridge structure design equations by considering uncertainty in the hazard, demand, damage, and loss to the bridge using performance-based methodologies. Kaviani et al. (2012) modeled reinforced concrete bridges with skewed-angled seat-type abutment; they concluded that bridges with large abutment skew angles bear a higher probability of collapse. Ramanathan et al. (2015) suggested finite element bridge modeling approaches for three types of bridges: straight, curved and skewed bridges. They compared analytical response with recorded sensor data and tested the fragility and seismic vulnerability among bridge

components for each bridge type. Choi (2002) investigated the nonlinear behavior and seismic capacity of monolithic bridges. By performing nonlinear static pushover analysis, they showed that the lateral displacement of monolithic bridge is reduced due to end-restraining effect of the abutment. Other researches have focused on the modeling of bridge components such as shear keys, abutments, elastomeric bearing, and backfill soil. Rollins and Jessee (2013) performed laboratory tests on abutment walls with several skew angles and developed an adjustment factor to account for the reduced capacity due to skew angles. Laboratory tests conducted by Kottari (2016) developed response curves of shear keys further improved the knowledge of modeling approaches of bridge structures. The recent modeling approach used by Fayaz et al. (2019) combines the latest literature on the bridge component models to develop a better representation of real bridges.

Since the goal of this study is to validate the bridge modeling approach by matching recorded data with analytical results from finite element models, engineering optimization approaches are utilized to estimate and evaluate the key bridge parameters of bridge components (e.g., yielding point of shear key, stiffness of abutment piles, stiffness of backfill soil). Although optimization methods are widely used in system identification and model updating of bridge and building structures (a list of previous research work is presented in the following), however, this study proposes an applied optimization method that is tailored for bridge structures with field data. Ebrahimian et al. (2017) updated a nonlinear finite element model of a frame-type structure by minimizing the discrepancies between predicted and measured response; their work, among others, are conducted using simulated data instead of recorded data. Nasrellah and Manohar (2011) proposed an identification method that uses particle filtering to capture the behavior of structures including both computational models and models from laboratory and field tests. Song and Dyke (2014) proposed a real-time dynamic model updating method to match a modified Bouc-Wen model using data from two shake table tests. Lagaros et al. (2002) investigated evolutionary algorithms including Genetic Algorithms and Evolution Strategies, and optimized the weight of two space structures with inter-story drift being the constraints. Yang and Soh (1997) used Genetic Algorithm with a tournament selection strategy for configuration optimization of truss structures with up to 112 members. Perez and Behdinan (2007) verified the effectiveness of Particle Swarm Optimization method on structural optimization tasks by estimating the cross-sectional area, allowable displacement, and stresses for members in a 25-bar truss system.

This research focuses on the validation of bridge modeling approaches, especially the parameters of the backbone curves of bridge components, by comparing the discrepancy between sensor recorded response and analytical response using two modeling approaches: *SDC* and *Stick* modeling approaches. *SDC* refers to the bridge modeling approach suggested in Seismic Design Criteria (SDC) (2013). The *Stick* modeling approach is presented in Fayaz et al. (2019) that is borrowed from a collection of bridge modeling approaches available in current literature. The difference in response data from these two models is analyzed, and the difference in the modeling of bridge components of these two modeling approaches are discussed. The *Stick* modeling approach is further updated using Particle Swarm Optimization to minimize the discrepancy between recorded and simulated response. This study assesses the appropriateness of the current *Stick* modeling approach and updates a better setting of key bridge parameters in terms of the match between analytical response using the modeling approach and the true recorded response.

Bridge Models

Finite Element models of the bridges were developed in *OpenSees* (McKenna et al., 2010). The finite element models are comprised of: abutments, shear keys, column bents, elastomeric bearing pads, backfill soil, and superstructure. An illustration of the model is provided in Figure 1 and Figure 2 for seat-type abutment bridges and monolithic abutment bridges, respectively. The models are based on the bridge models presented in Omrani et al. (2017); however, their structural component models are upgraded, and associated modeling parameters are updated (Fayaz et al., 2019).
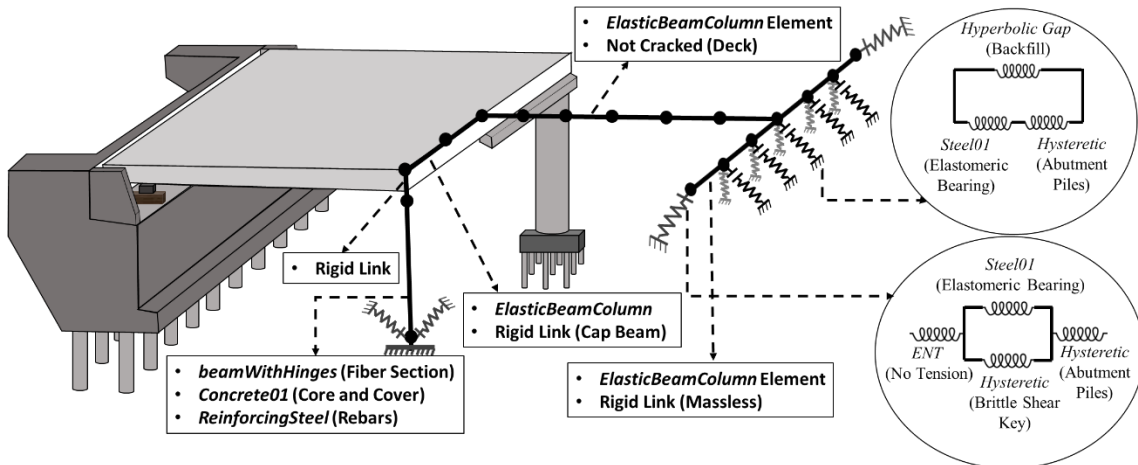
Figure 1: Illustration of the finite-element model of bridges with seat-type abutments
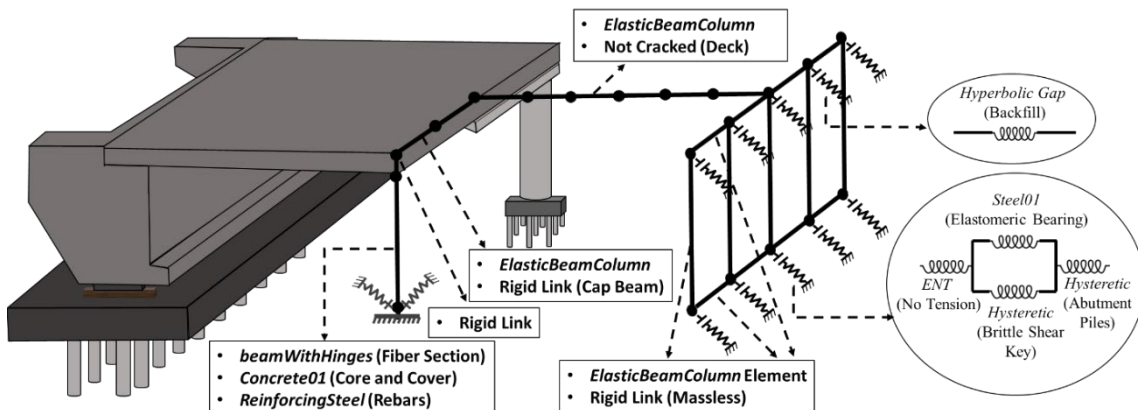
Figure 2: Illustration of the finite-element model of bridges with monolithic abutments

Caltrans SDC (2013) recommends the superstructure be designed to remain elastic during an event of Earthquake; therefore, the superstructure is modeled with `elasticBeamColumn` using uncracked section properties. To capture the dynamic response accurately, the mass of the superstructure is distributed throughout the length of the deck with each span's mass being distributed in ten intervals. The bridge columns are modeled using `beamWithHinges` element (two Gauss integration points) with fiber-discretized cross-sections to model confined concrete for the core, unconfined concrete for the cover and steel rebars. The nonlinear behavior of the columns is concentrated at two plastic hinges at the opposite ends connected by a linear elastic

element. The plastic hinge length is determined based on Caltrans SDC (2013). Assuming a monolithic construction of cap beam and columns, the cap beam is modeled as a rigid bent using `elasticBeamColumn` element with high torsional, in-plane, and out-of-plane stiffnesses. The concrete and steel are modeled using Concrete01 and `ReinforcingSteel` materials, respectively, which are available in *OpenSees*. The base of bridges is simulated as fixed and pinned connections for single-column bent and multiple-column bent, respectively, with the stiffness of connections arising from piles beneath. The piles under the bridge columns are modeled using elastic springs with the horizontal stiffnesses described as per Choi (2002).

Stick Modeling Approach

Shear keys are designed and modeled in a brittle/isolated manner using the `hysteretic` spring model available in *OpenSees*. The model is defined with a trilinear backbone curve as given in Figure 3d. The shear key is designed as per Caltrans SDC (2013) with area of vertical reinforcement (A_{vsk}) calculated as per Eq. 1, $P_{dl}{}^{sup}$ is the superstructure dead load reaction at the abutment and f_{ye} is the yield strength of steel rebars. Based on past experimental observations detailed in Kottari (2016), the sliding shear resistance of an isolated shear key is associated with two states: i) shear resistance at first sliding (V_{slid}) and ii) ultimate sliding shear resistance (V_u) right before the rupture of the dowel bars. Assuming a smooth construction joint is provided, the shear resistance due to the dowel action (F_d) of the vertical dowel bars is calculated using Eq. 2 which leads to the calculation of V_{slid} in Eq. 6 through Eqs. 3, 4, and 5. Based on the equilibrium of the horizontal and vertical forces (Bozorgzadeh et al., 2006). V_u is calculated as per Eq. 7.

$$A_{vsk} = \frac{\alpha \times P_{dl}{}^{sup}}{1.8 \times f_{ye}} \quad ; \qquad 0.5 < \alpha < 1 \qquad \text{Eq. (1)}$$

$$F_d = \sum^{\# \, of \, Vertical \, bars} \sqrt{2.\,M_{pl,i}.\,f_{cb,i}.\,d_{b,i}} \qquad \text{Eq. (2)}$$

$$M_{pl,i} = \frac{f_y.\,d_{b,i}{}^3}{6} \qquad \text{Eq. (3)}$$

$$f_{b,i} = a_i.\,f_c{}^{1.2} \qquad \text{Eq. (4)}$$

$$a_i = 2.0 + \frac{0.5}{d_{b,i}} \qquad \text{Eq. (5)}$$

$$V_{slid} = \frac{T + F_d}{\left(1 - \mu_f.\,tan\beta\right)} \qquad \text{Eq. (6)}$$

$$V_u = \frac{\mu_f.\,cos\gamma + sin\gamma}{1 - \mu_f.\,tan\beta}.\,A_{vsk}.\,f_{su} \qquad \text{Eq. (7)}$$

In these equations, $M_{pl,i}$ is the plastic moment capacity of bar i, and the compressive strength of confined concrete, $f_{cb,i}$, f_c is the uniaxial concrete compressive strength, $d_{b,i}$ is the diameter of bar i, β is the angle of the inclined face of the shear key with respect to a vertical plane, T is the cohesive force, and μ_f is the coefficient of friction of the smooth construction

joint ($\mu_f = 0.36$) (Kottari, 2016). γ is the angle of inclination of the vertical dowel bar (Angle of Kink). It is assumed that bond breaker is applied on the construction joint, hence $T = 0$ in Eq. 6. The value of γ is obtained from Kottari (2016) through interpolation for the provided diameter of dowel bars. The initial stiffness (k_1) of the backbone curve is computed through the summation of shear and flexural responses of the concrete cantilever action of the shear key (Omrani et al., 2017), while the stiffness of hardening (k_2) and softening (k_3) branches are expressed as a percentage of k_1 (ranging from 0.5 % to 2.5% for various rebar diameters) that are interpolated according to Kottari (2016).

The model of abutment comprises i) abutment piles, ii) backfill soil, and iii) elastomeric bearing pads. Piles of the abutments are modeled through a trilinear `hysteretic` spring model in *OpenSees* with the backbone curve defined as per Choi (2002). The backbone is presented in Figure 3b. The backfill soil is modeled using the `HyperbolicGapMaterial` material with a Generalized Hyperbolic Force-Deformation (GHFD) backbone (Shamsabadi and Kapuskar, 2006). The backbone is presented in Figure 3c. Hence, the active resistance of the abutment is provided by the piles while the passive action includes resistance due to the piles and backfill soil. The parameters described by Ramanathan (2012) are used to model the elastomeric bearing pads using the `Steel01` material, as shown in Figure 3a. The longitudinal behavior of the abutment is modeled using five springs in parallel connected by a rigid link while the transverse behavior is modeled using one spring on both ends of the abutment.
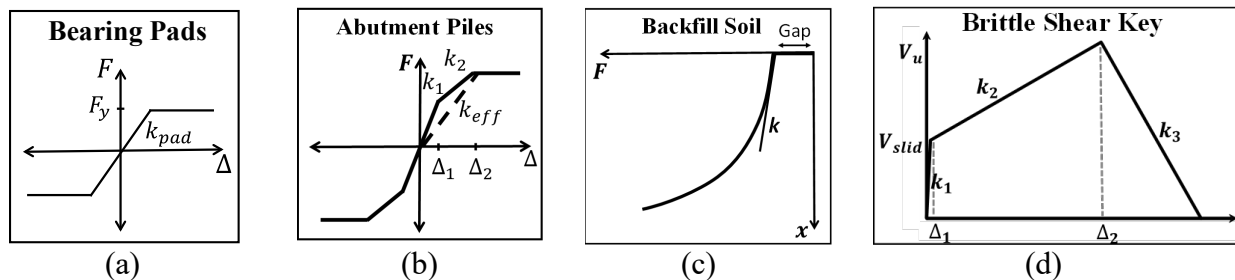

Figure 3: Details of the finite-element model of bridge structural components: a) Bearing pads response, b) Abutment pile response, c) Backfill soil response, and d) Shear key response

SDC Modeling Approach

Simplified analysis per Caltrans SDC (2013) requires the use of cracked flexural stiffness I_{eff} for ductile members. I_{eff} for reinforced concrete box girder sections are estimated between $0.5I_g$ to $0.75I_g$. This reduction factor is used for other superstructure types and cap beams. The torsional moment of inertia for columns is reduced to $0.2J_g$. Modeling of abutment longitudinal response is accomplished by a bilinear approximation of force-deformation relationship, including an effective abutment stiffness with expansion gaps considered for seat-type abutments and a realistic embankment fill response. The initial stiffness is proportional to the backwall/diaphragm height h, for seat-type and monolithic abutments, respectively, based on Eq. 8. In this equation, w is the projected width of backwall/diaphragm for seat-type and monolithic abutments, respectively. Eq. 9 yields the passive pressure force resisting the movement of the abutment, and Eq. 10 shows the effective abutment wall area for either seat-type or monolithic abutment type. For transverse abutment response, if the abutment is seat-type, a nominal transverse spring stiffness is taken as 50% of the elastic transverse stiffness of the adjacent bent.

While transverse stiffness of a monolithic type abutment is conservatively estimated as 40 kips/in per pile.

$$K_{abut} = \frac{50 kip/in}{ft}.w.\frac{h}{5.5ft}$$ Eq. (8)

$$P = A_e.5ksf.\frac{h}{5.5ft}$$ Eq. (9)

$$A_e = h.w$$ Eq. (10)

Bridge I

Bridge II
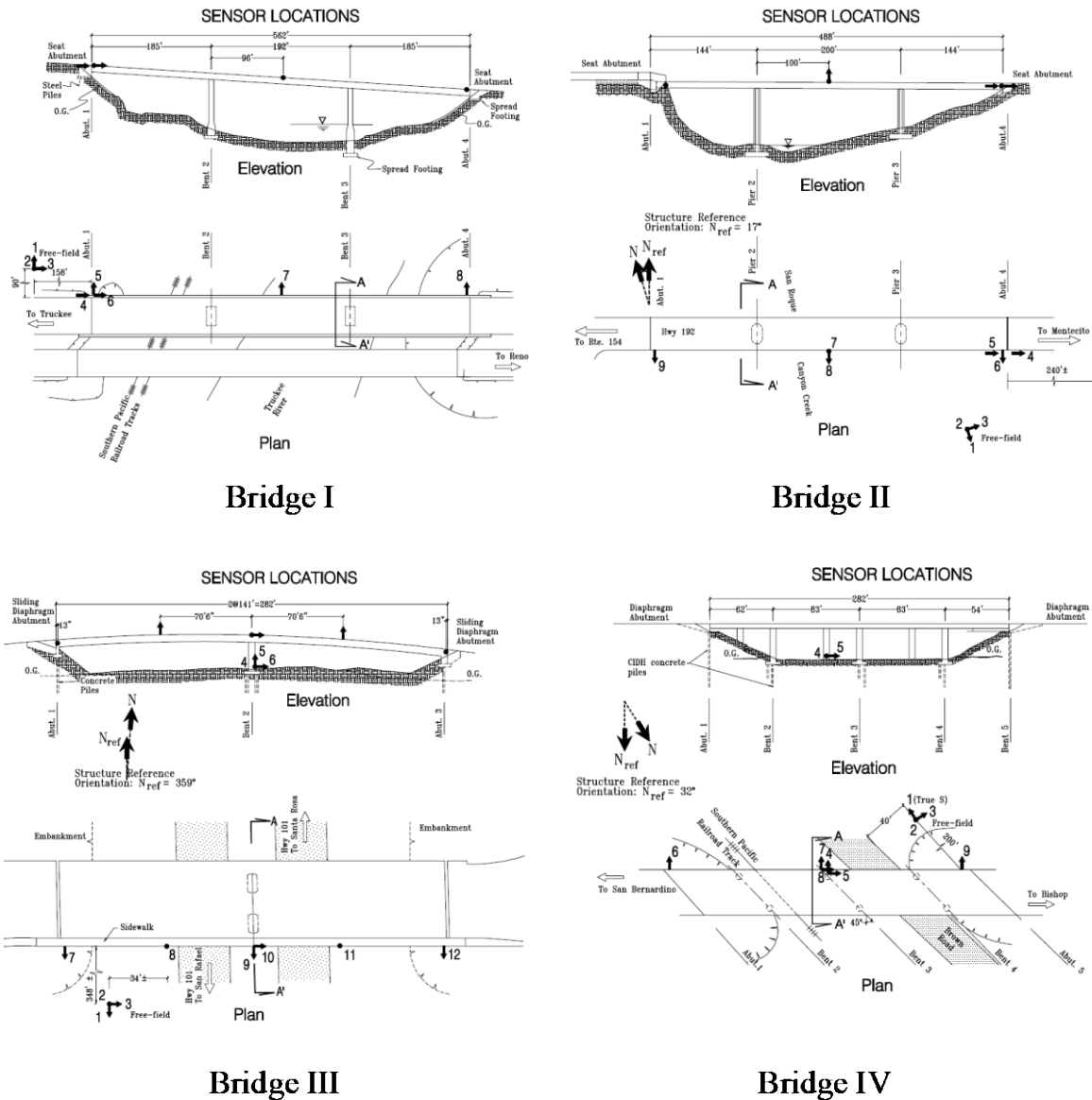
Bridge III

Bridge IV

Figure 4: Configurations of selected CSMIP instrumented bridges

Selected Bridges for Case Studies

Four CSMIP instrumented bridges are selected in this study: i) Truckee I-80 River Bridge, ii) Santa Barbara San Roque Canyon Bridge, iii) Rohnert Park Hwy 101 Bridge and iv) Ridgecrest-Hwy 395 Brown Road Bridge. Table 1 summarizes the basic information of the selected bridges, including the number of spans, the number of columns in each span, the skewness, and the abutment type. Figure 4 illustrates the configurations of bridge I, II, III and IV. Bridge I and II are selected to study the straight seat-type abutment bridges. Bridge III is a straight monolithic bridge, and bridge IV is a skewed-abutment monolithic bridge. All four bridges are modeled using both *Stick* and *SDC* modeling approaches (See Figure 1 and Figure 2) in *OpenSees* using the engineering drawings of the bridges. The key bridge components of bridge I and II include shear keys, backfill soil, abutment piles, elastomeric bearing pads, columns (with piles), and superstructure. Bridge III is modeled using foundational shear keys, backfill soil with the monolithic type abutment, abutment piles, elastomeric bearing pads, and columns (with piles). While bridge IV is modeled using backfill soil with the monolithic type abutment, abutment piles, and columns (with piles). Due to abutment skewness in bridge IV, the stiffness and force of backfill soil are reduced with reduction factors suggested by Rollins et al. (2013). The springs are altered as a function of the distance of the springs with respect to the center of the bridge (Kaviani et al. 2012) in the optimized *Stick* model.

Table 1. Selected bridges from CSMIP database

Bridge	I	II	III	IV
Name	Truckee I-80 River Bridge	Santa Barbara San Roque Canyon Bridge,	Rohnert Park Hwy 101 Bridge	Ridgecrest Hwy 395 Brown Road Bridge
Number of Spans	3	3	2	4
Column Bent	Single-column	Single-column	Two-column	Two-column
Skewness	Straight	Straight	Straight	Skewed
Abutment Type	Seat-type	Seat-type	Monolithic	Monolithic

Optimization Method

To obtain a better estimate of the key bridge parameters of the bridge components, Particle Swarm Optimization (PSO) is adopted in this study. The algorithm works by initializing a population of candidate particles, which move in the search space to minimize the objective function. Each particle will update itself based on its own local best-known position as well as the global best-known position found by the entire group. PSO is selected due to its convenience in implementation, the fewer number of hyperparameters, and the capability of dealing with high dimensional optimization problems. As a gradient-free algorithm, PSO does not require the objective function surface to be differentiable and is suitable in this study given that the objective function measures the discrepancy between recorded response and analytical response.

PSO Formula

As mentioned in Eq. 11, the velocity of particle i at dimension d at the kth step (i.e., v_{id}^k) is updated by three terms. The first term represents the velocity of particle i at the previous step

factored by w^k, where w (Eq. 13) decreases linearly as the algorithm carries on with index k (K is the total number of steps). The second term in Eq. 11 guides the particle's position (i.e., x_{id}^k) towards the local best position (i.e., x_{id}^{p-best}). The third term in Eq. 11 guides the particle towards the global best position (i.e., x_d^{g-best}), which is not a function of i. c_1 and c_2 are the hyperparameters that can be tuned as learning rates, and r_1 and r_2 are random variables ranging from 0 to 1 in order to increase uncertainty in the searching process. Finally, the position is updated by summing up the previous position and the velocity as shown in Eq. 12.

$$v_{id}^k = w^k v_{id}^{k-1} + c_1 r_1 \left(x_{id}^{p-best} - x_{id}^{k-1} \right) + c_2 r_2 \left(x_d^{g-best} - x_{id}^{k-1} \right) \qquad \text{Eq. (11)}$$

$$x_{id}^k = x_{id}^{k-1} + v_{id}^{k-1} \qquad \text{Eq. (12)}$$

$$w^k = w_{max} - (w_{max} - w_{min}) \frac{k}{K} \qquad \text{Eq. (13)}$$

The Objective Function and Updated Parameters

Several objective functions were implemented, tested, and critiqued. These objective functions were various combinations of the squared-sum-of-discrepancy between analytical response and recorded response. The discrepancies were measured in i) time history acceleration data, ii) acceleration data in the frequency domain using Fourier Transformation, iii) peak displacement value. The most representative objective function that maintains the signal signature was the one that measures the discrepancy in the time domain (see Eq. 14). The match in frequency domain leads to large errors due to the large fluctuation in frequency domain plus it will not include data seasonality that is evident in the time domain acceleration history of each bridge. The match in peak displacement compares only one data point and leads to an unrealistic estimation of parameters.

The measure of discrepancy between recorded acceleration response and simulated acceleration response in the time domain is shown in Eq. 14. The discrepancy is summed over all strong motion data points along time history and overall sensor locations where the recorded response is measured. Acceleration instead of displacement is picked as the response where the error is computed due to the rich information contained in acceleration data and its stationarity compared to displacement time history.

$$J(\boldsymbol{\theta}) = \sum_{j=1}^{N_{sen}} \sum_{l=1}^{\tau} \frac{[\ddot{u}_j(l\Delta t) - \ddot{\hat{u}}_j(l\Delta t)]^2}{\sum_{p=1}^{\tau}[\ddot{u}_j(p\Delta t)]^2} \qquad \text{Eq. (14)}$$

Objective functions are functions that vary with the change of the set of bridge parameters vector $\boldsymbol{\theta}$ ($\boldsymbol{\theta} = \{\theta_1, \cdots, \theta_d, \cdots, \theta_{D_B}\}$; $D_B \in \{D_I, D_{II}, D_{III}, D_{IV}\}$, see Table 2 for the definition of D_B). Given that the four selected bridges have different key bridge structure components, the selection of $\boldsymbol{\theta}$ and the optimization dimension also vary. Table 2 provides the key bridge parameters updated by the optimization method and the corresponding dimension

(number of parameters). The searching space is limited between $\theta_d/10$ and $10\theta_d$ for each dimension d, and a quadratic penalty is added to the objective function if constraints are violated.

Results and Discussion

The overall results of the match between recorded acceleration response and the simulated acceleration response imply the inappropriateness of the *SDC* modeling approach as well as the insufficiency in the *Stick* modeling approach. The performances of the modeling approaches vary with the type of bridges. The response from the models developed using the *SDC* modeling approach is closer to field data than the models based on the *Stick* modeling approach for seat-type abutment bridges; an opposite observation is made for monolithic abutment bridges. The results clearly show that the *SDC* modeling approach underestimates bridge stiffness in the longitudinal direction. The optimization method assists the *Stick* modeling approach, but the benefit of the optimization process is limited. That is because the dynamic properties of the bridge models highly depend on the model geometry and types of elements utilized (sufficiency of the analytical models).

Table 2. Bridge parameters updated using optimization method for four selected bridges

Bridge	Bridge parameters θ of key bridge structure components	Num. of Dim. (D_B)
I & II	Shear key sliding shear: V_{slid}, Deformation corresponding to Shear key sliding shear: u_1, Shear key ultimate shear: V_{usk}, Stiffness of backfill soil: K_{abut}, Force of backfill soil: f_{abut}, Stiffness of abutment piles: K_{eff}, Coefficient of friction for bearing pads: μ, Column moment of inertia: I_c, Damping Ratio: ξ	$D_I = D_{II} = 9$
III	Shear key sliding shear and corresponding deformation in transverse and longitudinal directions: V_{slid_T}, u_{1_T}, V_{slid_L}, u_{1_L}, Shear key ultimate shear in transverse and longitudinal directions: V_{usk_T}, V_{usk_L}, Stiffness and force of backfill soil: K_{abut}, f_{abut}, Stiffness of abutment piles: K_{eff}, Coefficient of friction for bearing pads: μ, Column moment of inertia: I_c, Damping Ratio: ξ	$D_{III} = 12$
IV	Backfill stiffness and force K_{abut}, f_{abut}, Stiffness of abutment piles: K_{eff}, Column moment of inertia I_c, Damping Ratio ξ	$D_{IV} = 5$

Seat-type Abutment Bridges

The performance of the two modeling approaches are investigated for Bridge I for illustration purposes; the same patterns and trends are found in Bridge II, whose results are omitted due to page limit. For simplicity, the results associated with the *SDC* and *Stick* modeling approaches are labeled as *SDC*, and *Stick*, respectively. The results associated with the optimized *Stick* modeling approach is labeled as *OptStick*. Figure 5 presents the response at the edge of the deck in the longitudinal direction, both in time domain and in frequency domain, for all three modeling approaches. In the frequency domain, *SDC* generates a spurious spike of frequency content near 1.8Hz, and this leads to the spurious low frequency waveform in time domain. *Stick*, applied with the same 5% damping ratio as *SDC*, captures the recorded waveform more accurately compared to *SDC*. This is mainly due to the inappropriateness of

longitudinal abutment modeling of *SDC*, where the longitudinal stiffness is unrealistically small. In this case, the improvement in performance from optimization method is very limited, as the response from *OptStick* and *Stick* are almost identical in longitudinal direction.
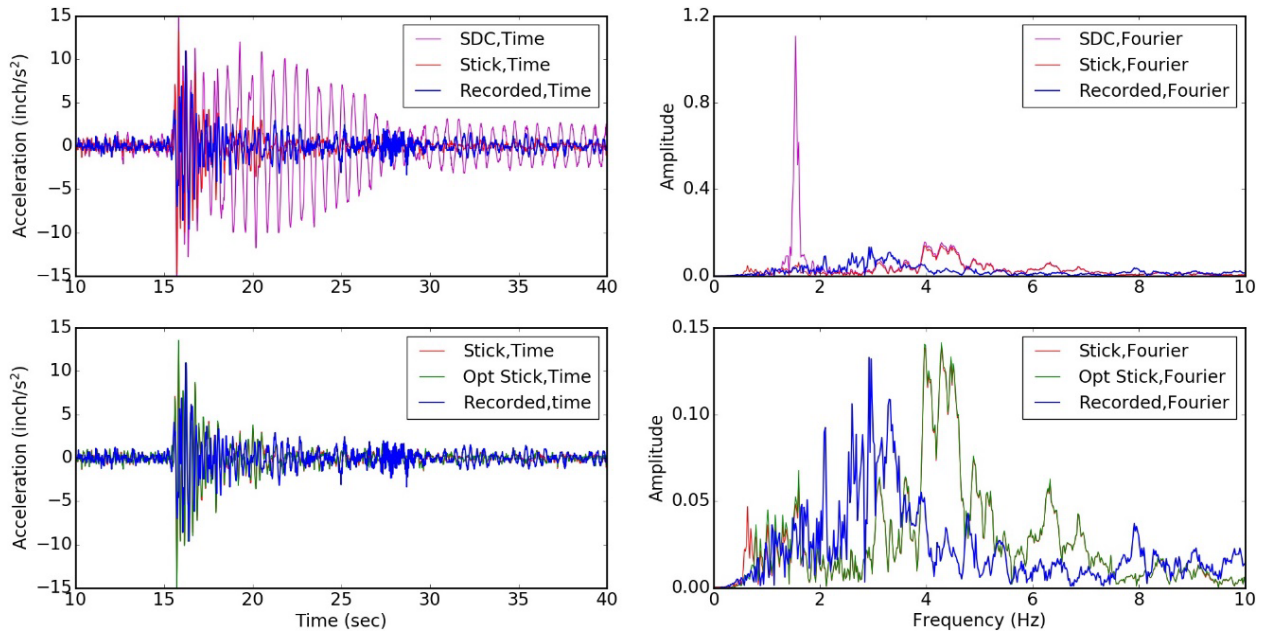

Figure 5: Deck response at the edge of Bridge I in longitudinal direction subject to Whitehawk Earthquake M_w = 4.7 occurred on Oct 26, 2011
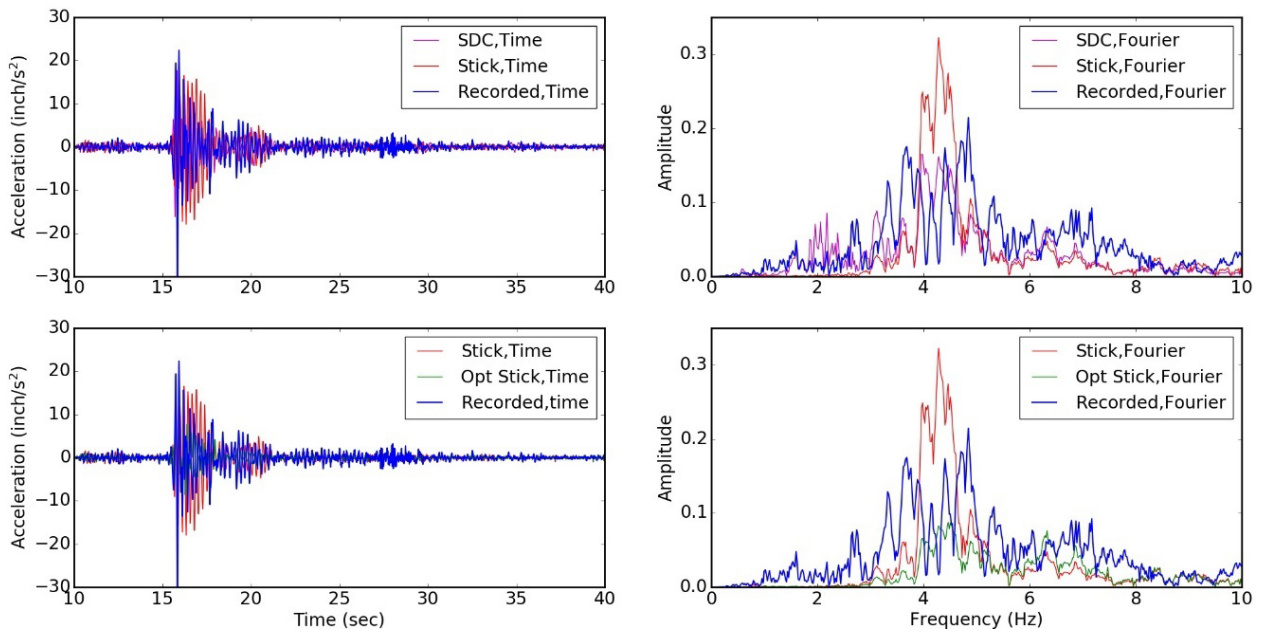

Figure 6: Deck response at the edge of Bridge I in transverse direction subjected to Whitehawk Earthquake M_w = 4.7 occurred on Oct 26, 2011
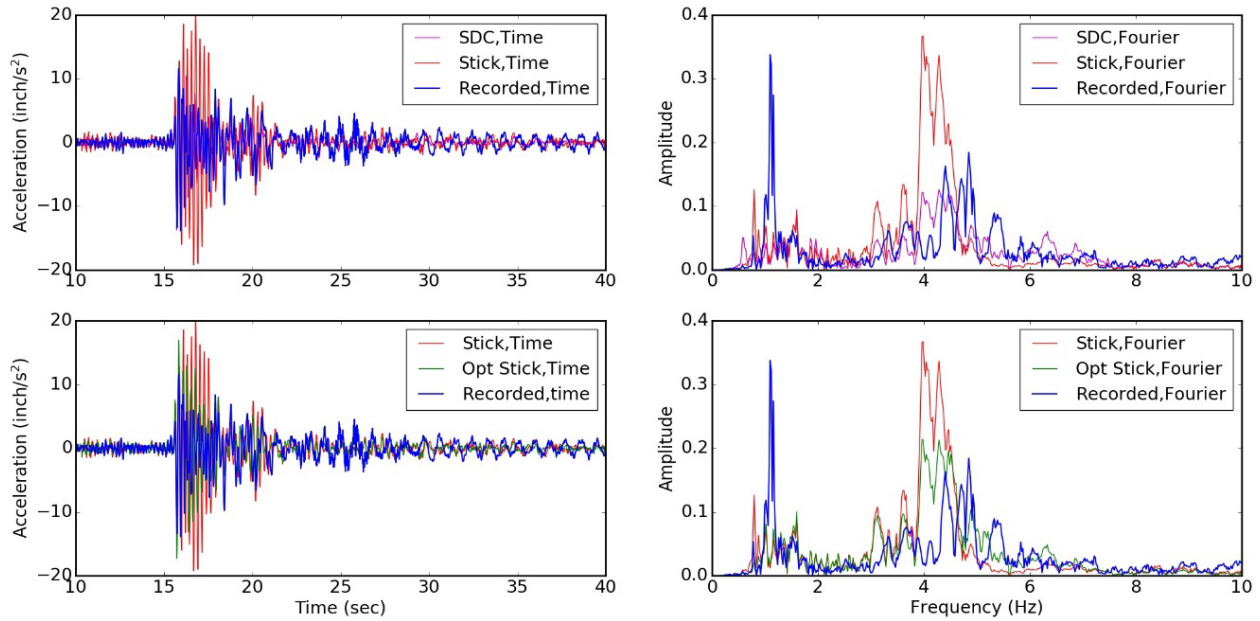
Figure 7: Deck response in the middle of Bridge I in transverse direction subject to Whitehawk Earthquake $M_w = 4.7$ occurred on Oct 26, 2011

Figure 6 shows the response of the edge of the deck in the transverse direction. In the frequency domain, all three modeling approaches are able to capture the main frequency content around 4Hz. Although the amplitude of the frequency content estimated from *Stick* is slightly higher than the recorded one, *OptStick* brings the amplitude in frequency domain down towards the recorded data, and this can be verified in the time domain as the higher amplitude in acceleration in *Stick* is reduced to the same level of the recorded data by *OptStick*. In this case, *SDC* successfully matches the recorded response in both time and frequency domain, which implies that *SDC* provides a relatively accurate modeling approach to capture the response at edge of the deck in the transverse direction.

Figure 7 shows the response in the middle of the deck in transverse direction. All three modeling approaches are able to capture the two main frequency contents at 1 Hz and 4 Hz. Although the amplitude of the first main frequency content (1 Hz) is underestimated by all three modeling approaches, and *Stick* overestimates the amplitude of the second main frequency content (4 Hz). Similar to the transverse response at the edge of the deck, *OptStick* helps in reducing the fictitious amplitudes generated by *Stick*, and this can be seen in both time domain and frequency domain results. *SDC* can still match the recorded response relatively well in the transverse direction.

Monolithic-type Abutment Bridges

Bridge IV is picked to demonstrate the difference in modeling approaches for monolithic bridges; the bridge was subjected to the Ridgecrest Earthquake that occurred on Jul 5, 2019, with $Mw = 7.1$. Figure 8 shows the abutment response in the transverse direction. In frequency domain, *Stick* and *Optstick* are both able to capture the frequency contents, and they both follow the trends of the recorded data, although there is a slight shift in *OptStick* around 2Hz, and the

estimated amplitude for that frequency content is much higher than the recorded amplitude. However, the performance of *SDC* is quite poor that it creates a fictitious frequency content around 1.8 Hz with a considerably large amplitude. This modeling inaccuracy can be confirmed in time domain, as *SDC* has a low-frequency waveform with higher amplitude. In this case, *Stick* performs slightly better than *SDC* in terms of amplitude estimation, while *OptStick* alleviates the overestimation of amplitude.

For the transverse response in the middle of the deck, as shown in Figure 8, while *SDC* has the same inaccurate estimate of the main frequency content, *Stick* and even *OptStick* are not able to capture the true frequency, which is around 3 Hz. In time domain, *SDC*, as expected, displays a low-frequency high-amplitude waveform, while *Stick* can match the recorded time history trend much more precisely. *OptStick* further updates *Stick* and make the fitting of response much closer to the recorded data.

Parameters of Three Modeling Approaches

Tables 3-5 summarized the key bridge parameters used in *SDC* and the key bridge parameters used in *Stick* and updated in *OptStick* for both seat-type and monolithic abutment bridges. Each bridge is tested with two ground motions, so that there are three sets of estimated parameter values: parameters of the original *Stick*, parameters updated using GM1 and parameters updated with GM2.
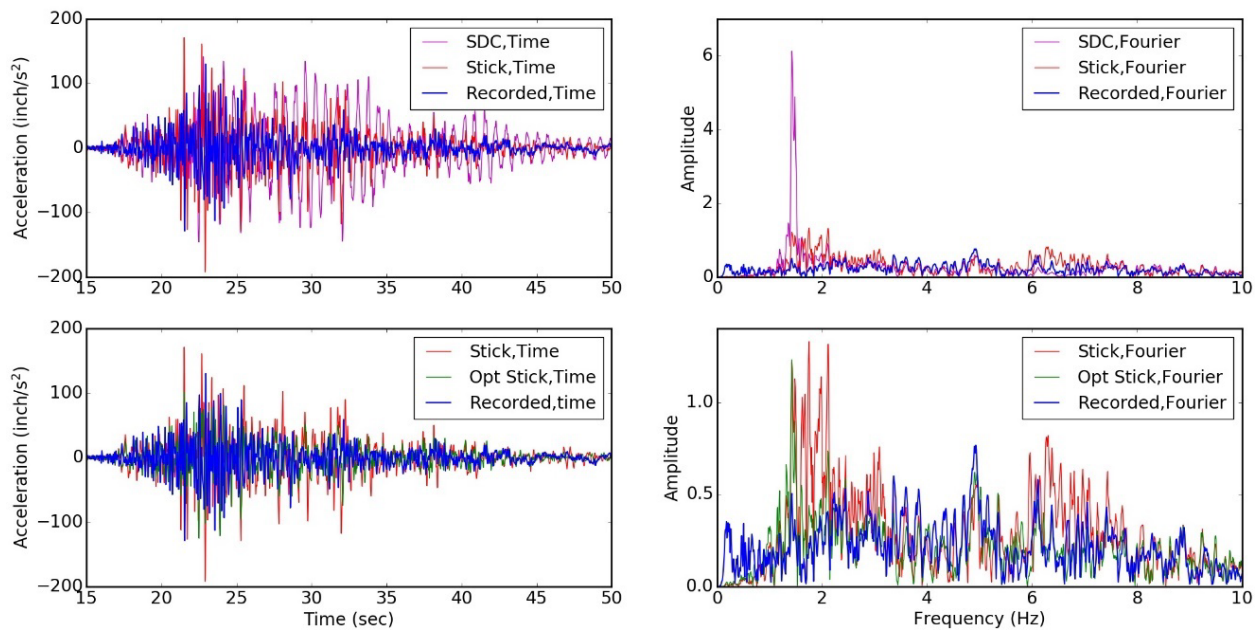

Figure 8: Abutment response of Bridge IV in transverse direction subject to Ridgecrest Earthquake $M_w = 7.1$ occurred on Jul 5, 2019
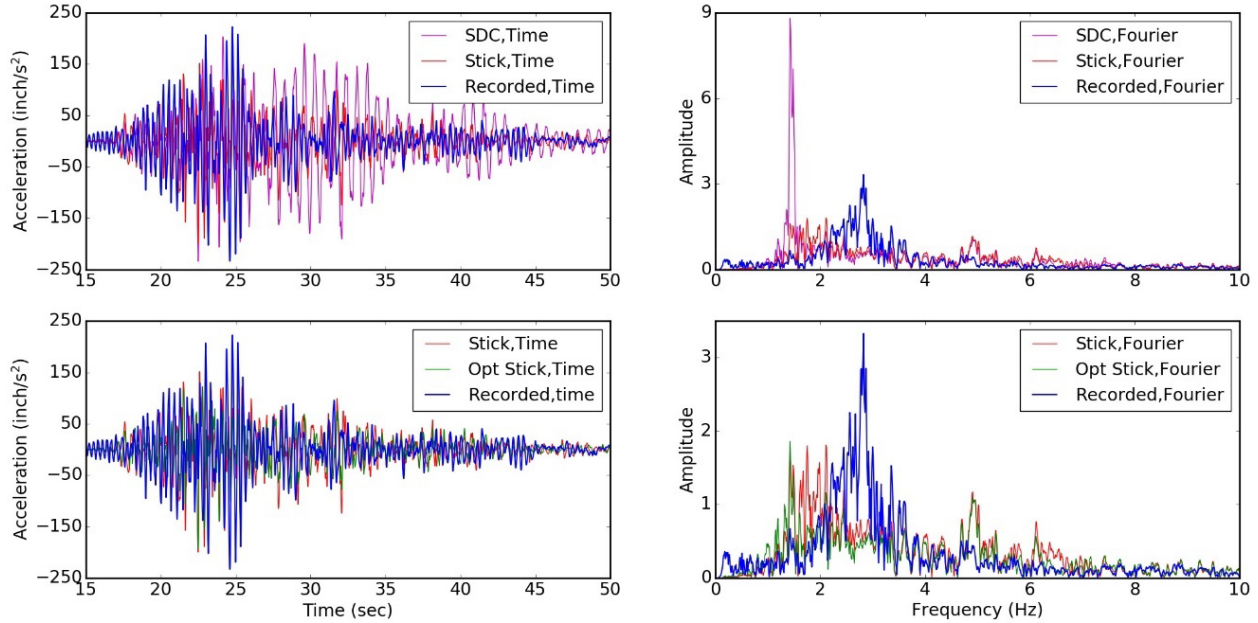
Figure 9: Deck response in the middle of Bridge IV in transverse direction subject to Ridgecrest Earthquake $M_w = 7.1$ occurred on Jul 5, 2019

Table 3. Bridge parameters used in *SDC* modeling approach

Bridge	I	II	III	IV
Abutment longitudinal stiffness K_{eff}(kips/in)	1675	1632	6854	1761
Backfill Passive Pressure Force P_{bw}(kips)	2763	2938	8910	1673
Transverse Spring Stiffness (kips/in)	242	1621	480	280
I_{col}(in^4)	23×10^6	34×10^6	2×10^6	4×10^5
J_{col}(in^4)	47×10^6	67×10^6	4×10^6	8×10^5
I_{deck} (in^4)	40×10^7	50×10^7	107×10^7	28×10^7
Damping Ratio ξ	0.05	0.05	0.05	0.05

Table 4. Seat-type bridge parameters in *Stick* modeling approach

Bridge	I			II		
Model	*Stick*	*OptStick*GM1	*OptStick*GM2	*Stick*	*OptStick*GM1	*OptStick*GM2
V_{slid}(kips)	249	132	158	158	246	272
V_{usk}(kips)	1055	959	1484	715	1423	1065
u_1(in)	0.006	0.004	0.002	0.007	0.004	0.008
K_{abut}(kips/in)	593	388	430	662	287	260
f_{abut}(kips)	291	340	225	366	502	271
K_{eff}(kips)	2000	3346	2842	1680	687	655
μ	0.189	0.042	0.112	0.192	0.495	0.551
I_c(in^4)	23×10^6	17×10^6	22×10^6	34×10^6	17×10^6	13×10^6
ξ	0.05	0.16	0.13	0.05	0.19	0.17

Table 5. Monolithic bridge parameters in *Stick* modeling approach

Bridge	III			IV		
Model	*Stick*	*OptStick*GM1	*OptStick*GM2	*Stick*	*OptStick*GM1	*OptStick*GM2
$V_{slid\,T}$(kips)	178	150	208			
$V_{usk\,T}$(kips)	904	1393	718		No Transverse Shear Key	
$u_{1\,T}$ (in)	0.03	0.07	0.04			
K_{abut}(kips/in)	876	1191	908	221	331	292
f_{abut}(kips)	700	322	470	129	163	48
K_{eff}(kips)	480	485	267	280	211	134
μ	0.148	0.343	0.378		No Bearing Pad	
I_c(in^4)	20×10^5	22×10^5	14×10^5	4×10^5	2×10^5	2×10^5
ξ	0.05	0.18	0.18	0.05	0.16	0.17
$V_{slid\,L}$(kips)	357	388	271			
$u_{1\,L}$(in)	0.014	0.002	0.01		No Longitudinal Shear Key	
$V_{usk\,L}$(kips)	1809	2250	1057			

Conclusion

Bridge modeling approaches are essentially important as they give guidance for the design and retrofit of bridge structures. This study investigated three bridge modeling approaches; namely, *SDC*, *Stick,* and *OptStick*, using four CSMIP instrumented bridge structures including: Truckee I-80 River Bridge, Santa Barbara San Roque Canyon Bridge, Rohnert Park Hwy 101 Bridge and Ridgecrest Hwy 395 Brown Road Bridge. The first two are seat-type abutment bridges, and the last two are monolithic abutment bridges.

SDC uses the simplified modeling approach per Caltrans SDC (2013) for the longitudinal and transverse abutment, as well as columns and structure by using cracked section properties. *Stick* combines backbone models of shear keys, abutment piles, elastomeric bearing pads, and backfill soil to represent a better configuration of bridge structures. *OptStick* stands for an optimized version of *Stick* via optimization techniques and updates the key bridge parameters of bridge components in *Stick.* Acceleration response generated from these three modeling approaches is compared with the recorded response obtained from the CSMIP database. Time history data is also transferred into frequency domain using Fourier transformation in order to have a better understanding of the different performances from different modeling approaches.

For bridges with seat-type abutments, the *SDC* model was superior to other modeling types, especially in capturing the transverse response at the middle and the edge of the deck. *SDC* is able to capture the main frequency content of recorded response, and *SDC* response is closer to the recorded response compared to the more sophisticated *Stick*. However, seismic response is inaccurately estimated using the *SDC* model in the longitudinal direction. This is due to the modeling requirements that lead to a low abutment longitudinal stiffness in the *SDC* model. Although *Stick* sometimes leads to more inaccurate dynamic response, optimization methods help correct those discrepancies by updating the key bridge parameters, and the results from *OptStick* can be as precise as those from the *SDC*.

For monolithic bridges, the response from *Stick* has a better match with recorded response compared to the *SDC* model. *SDC* models often estimate spurious frequency contents, and the amplitude estimation in both time and frequency domains could be very different from that of a recorded response. Although *Stick* has a slight overestimation in amplitudes, it can capture the trends of recorded response. *OptStick* is able to reduce the fictitious amplitude estimation from a *Stick* so that the predicted response can be much closer to the recorded response in both time and frequency domains.

However, given the best updated results, it can be argued that even *OptStick* cannot capture every component of a real bridge structure accurately. This implies that the underlying and fundamental modeling assumptions of all models (i.e., *Stick* and *SDC*) require a re-evaluation, and a new modeling approach is required that can sufficiently and efficiently estimate bridge response during seismic excitations.

Acknowledgments

Reference

Bozorgzadeh, A., Megally S., Restrpo J., Ashford S.A. (2006), Capacity Evaluation of Exterior Sacrificial Shear Keys of Bridge Abutments. Journal of Bridge Engineering, **11**, 555-565.

Caltrans SDC (2013), Seismic Design Criteria. Version 1.7, California Department of Transportation, Sacramento, CA.

Choi, E. (2002), Seismic analysis and retrofit of mid-America bridges. Ph.D. Thesis, Department of Civil and Environmental Engineering, Georgia Institute of Technology, Atlanta (GA).

Ebrahimian, H., Astroza, R., Conte, J.P.,de Callafon, R.A.(2017), Nonlinear Finite Element Model Updating for Damage Identification of Civil Structures using Batch Bayesian Estimation. *Mechanical Systems and Signal Processing* **84**, 194-222.

Fayaz, J, Xiang, Y., and Zareian, F. (2019), Performance Assessment of Bridges Under A Sequence of Seismic Excitations. *Computational Methods in Structural Dynamics & Earthquake Engineering* (*COMPDYN 2019*), Crete Island, Greece, June 2019

Kaviani, P., Zareian, F., Taciroglu, E. (2012), Seismic Behavior of Reinforced Concrete Bridges with Skew-anges Seat-type Abutments. *Engineering Structures* **45**, 137–150.

Kottari, A. (2016), Design and Capacity Assessment of External Shear keys in Bridge Abutments. Ph.D. Thesis, Department of Structural Engineering, University of California, San Diego, CA.

Lagaros, N.D., Papadrakakis, M., Kokossalakis, G. (2002), Structural Optimization using Evolutionary Algorithms. *Computers and Structures*, **80**, 571-589.

Mackie, K.R., Stojadinovic, B. (2007), Performance-based Seismic Bridge Design for Damage and Loss Limit States. *Earthquake Engineering and Structure Dynamics*, **36**,1953-1971.

McKenna, F., Scott, M. H., and Fenves, G. L. (2010), Nonlinear Finite Element Analysis Software Architecture using Object Composition. *Journal of Computing in Civil Engineering*, **24**(3), 95-107.

Nasrellah, H.A., Manohar, C.S. (2011), Finite Element Method Based Monte Carlo Filters for Structural System Identification. *Probabilistic Engineering Mechanics*, **26**, 294-307.

Omrani, R., Mobasher B., Sheikhakbari, S., Zareian, F., Taciroglu, E. (2017), Variability in the Predicted Seismic Performance of a Typical Seat Type California Bridge due to Epistemic Uncertainties in its Abutment Backfill and Shear-key Models. *Engineering Structures* **148**, 718–738.

Perez, R.E., Behdinan, K. (2007), Particle Swarm Approach for Structural Design Optimization. *Computers and Structures*, **85**, 1579-1588.

Ramanathan, K. (2012), Next generation seismic fragility curves for California bridges incorporating the evolution in Seismic design philosophy. Ph.D. Thesis, Department of Civil and Environmental Engineering, Georgia Institute of Technology, Atlanta (GA).

Ramanathan, K., Jeon, J., Zakeri, B., DesRoches, R., Padgett, J. (2015), Seismic Response Prediction and Modeling Considerations for Curved and Skewed Concrete Box-girder Bridges. Earthquake and Structures, **9**, 1153-1179.

Rollins, K., Jessee, S.J. (2013), Passive Force-Deflection Curves for Skewed Abutments. *Journal of Bridge Engineering* **18**, 1086-1094.

Shamsabadi, A, Kapuskar, M. (2006), Nonlinear Seismic Soil-abutment-structure Interaction Analysis of Skewed Bridges. In: *Proc 5th National Seismic conference on bridges and highways*, San Francisco, CA.

Song, W., Dyke, S. (2014), Real-time Dynamic Model Updating of a Hysteretic Structural System. Journal of Structural Engineering, **140**(3), 04013082.

Yang, J, Soh, C.K. (1997), Structural Optimization by Genetic Algorithms with Tournament Selection. *Journal of Computing in Civil Engineering*. **11**(3), 195-200.

DATA-DERIVED SITE RESPONSE AND ITS PREDICTABILITY USING ERGODIC AND SITE-SPECIFIC METHODS

Pengfei Wang and Jonathan P. Stewart

Department of Civil & Environmental Engineering
University of California, Los Angeles

Abstract

We derive non-ergodic site response for California sites using an expanded version of the NGA-West2 database. We then investigate the degree to which different site response analysis methods capture observations. An ergodic site term provides a baseline against which other models are compared. Here we emphasize site-specific ground response analysis for sites with in situ V_S measurements. We describe the assignment of damping to individual soil layers using geotechnical models and site-specific spectral amplitude decay parameter κ. We provide data-model comparisons for cases in which ground response analyses provide variable levels of effectiveness.

Introduction

Ergodic models for site response provide a mean estimate conditioned on certain site parameters (typically the time averaged shear wave velocity in the upper 30 meters of the site, V_{S30}, and basin depth). The ergodic estimate of site response includes all site amplification mechanisms (impedance, nonlinearity, resonance, two- and three-dimensional wave propagation in basins, etc.), but these effects are smoothed over a large number of sites with different characteristics. As such, the associated site-to-site uncertainties (denoted ϕ_{S2S}) are substantial, increasing mean or >50%tile ground motions at long return periods as derived from probabilistic seismic hazard analyses (PSHA) relative to what would be obtained with more accurate methods.

Site-specific or *non-ergodic* site response is intended to account for wave propagation mechanisms at a specific site that control site response. An unbiased estimate of site-specific site response, for example as derived from analysis of earthquake recordings, substantially reduces ϕ_{S2S} (e.g., Rodriguez-Marek et al., 2014; Stewart et al. 2017). For sites without recordings, many projects seek to estimate site response using ground response analyses, which consider the effects of one-dimensional (1D) shear wave propagation and soil nonlinearity. Open questions related to this common practice are (1) How effective are such methods at capturing observed behavior, and how does this change with period?; and (2) What levels of epistemic uncertainty (ϕ_{S2S}), associated with wave propagation mechanisms not considered in 1D analysis, should be used in PSHA when site response is estimated from ground response analyses?

A sensible means by which to answer these questions is through comparisons of predictions of ground response analysis results to data. Not surprisingly, this general line of research contains numerous contributions over many years, with a typical application taking various input motions, running them through 1D soil columns, and comparing resulting response

spectra to those from recordings (e.g., Chang, 1996; Dickenson, 1994; Idriss, 1993). However, with the exception of vertical arrays, this research approach has a limited ability to answer the above questions, because predicted ground surface motions are strongly dependent on input motions, which are often highly uncertain. As a result, the effectiveness of the site response prediction is somewhat obscured.

The use of vertical arrays overcomes this problem because of the availability of recorded input motions, and has produced interesting findings that illustrate limitations, biases, and uncertainties associated with ground response analyses (e.g., Kaklamanos et al. 2013; Zalachoris and Rathje, 2015; Kaklamanos and Bradley, 2018; Afshari and Stewart, 2019). However, there are limitations associated with the use of vertical arrays to validate ground response analyses. First, the number of vertical arrays with sufficient ground motion recordings and site characterization is limited (but certainly growing with time). Second, vertical arrays only measure site response over the length domain of the array; as such they are not useful for evaluating long-period features that involve wavelengths longer than array dimensions. Third, the within-motion boundary condition that is used in analysis of vertical array data does not match that used in typical forward applications, in which outcropping input motions are selected.

To address these limitations, we suggest an alternative method for validating ground response analyses using data from surface-only instruments. The concept is to use recordings to infer the non-ergodic site response over a wide frequency range. The effectiveness of ground response analysis, and other methods, is then assessed by comparing predicted levels of site response against observation. This departs from the aforementioned prior work in that model effectiveness is not based on ground motions from a particular event (or series of events), but on the site amplification relative to a reference condition.

This work is in-progress, so final results are not provided here. We describe the approach, and summarize data assembled for this and related research. We then describe protocols that have been developed for applying ground response analyses at sites with Vs profiles but little of the other information typically required for such analyses (mainly, soil type and its variation with depth). Example results are presented and discussed.

Proposed Approach

We suggest here a method that can be used to test the effectiveness of ground response analyses using the results of ground surface recordings. The method is substantially more robust when seismic velocity profiles are available at candidate sites, and we apply this constraint in the present work. The method has four components.

The first component is assembling the required data. If not already available from another project (such as NGA projects, which involve substantial data collection and synthesis), this is a substantial task. The information required is identical to that needed for ground motion model development, namely, a database that includes information on source attributes, site conditions at recording stations, and ground motions (with record-specific processing details). In this project, we supplemented the NGA-West2 database with additional sites and events, as described in the next section. A need for the present work that is not shared in ground motion model development

projects, is seismic velocity profiles at recording stations (particularly shear-wave velocity, Vs, vs depth profiles).

The second component consists of ground motion analyses targeted at extracting information on site responses at recording stations. The steps involved in developing these results are descried elsewhere (Stewart et al. 2017), so the procedure is not repeated here. What these analyses provide is an estimate of a site term, denoted η_S, for each site and response spectral oscillator period. This site term represents the mean difference between a regionally-unbiased ground motion model and observed motions at the site. For weak shaking conditions that do not induce soil nonlinearity, the sum of η_S and the ergodic site term for the site (F_S), comprises the mean non-ergodic site response (μ_{lnY}) relative to the ground motion model's reference condition:

$$\mu_{lnY} = F_S + \eta_S \qquad [1]$$

The third component consists of predicting site response for each site in the data inventory using available information on site conditions. In the case of ground response analyses, a Vs profile is required, and borehole data indicating soil stratigraphy and soil type characteristics for each layer is also useful (for estimation of modulus reduction and damping relations). Other methods may require different information, such as peak frequency from H/V spectral ratios (e.g., Kwak et al, 2017; Hassani and Atkinson, 2016).

The fourth component involves model-to-data comparisons in the form of residuals analyses, which can be used to estimate model bias and uncertainty. These procedures, and the interpretation of results, will be presented in subsequent publications.

Database

The approach described in the prior section requires a large database with many recordings for the second component (referred to here as *Full Database*). The database requirements for this component match those for ground motion model development projects. A subset of that database is used in components three and four (*Database Subset for Site Response Studies*).

Full Database

The database used in this study draws from an expanded version of the NGA-West2 database (Ancheta et al., 2014), which is a global database for active tectonic regions. There is a significant contribution of data from California to the NGA-West2 database (373 events, 1463 stations, 14231 recordings) over the time period 1938 to 2010. The site portion of the database (Seyhan et al. 2014) was developed to provide the principal site parameters used in model development − $Vs30$ and various depth parameters denoted as z_x. As part of this project and other complimentary projects, we converted the spreadsheet files that comprised the original NGA-West2 flatfile (pertaining to sources, sites, and ground motions) into tables within a relational database, which is housed on a local server. Data modifications and additions are made within

the relational database. The database is accessed using Python scripts within Jupyter notebooks on DesignSafe (Rathje et al. 2017).

We have identified earthquakes and recordings since 2011 in California, which significantly extend the NGA-West2 database. Figure 1 shows the locations of events sorted by magnitude, most of which occur in five main regions: Bay Area, Eastern Sierra and Nevada, central California, southern California, and Imperial Valley and northern Mexico. These five zones incorporate most of the urban areas in the state, and contain a large fraction of the ground motion stations. We focus here on the Bay Area and southern California regions. Moroever, since difficulties can be encountered in the analysis of site terms using small magnitude data, we only consider **M** >= 4.0 events (Stafford et al. 2017). The data from events within the Bay Area and southern California regions in Figure 1 is derived from 25 earthquakes that have produced about 9,300 three-component recordings within the distance cutoffs suggested by Boore et al. (2014). These data are screened for magnitude (requiring **M** > 4), to remove duplicate recordings (e.g., seismometers and accelerometers at the same location), and to remove recordings that appear to be unreliable from instrument malfunctions or similar. This leaves about 5873 usable three-component records. Figure 2 shows the locations of these events and of the 1185 recording stations with recordings.
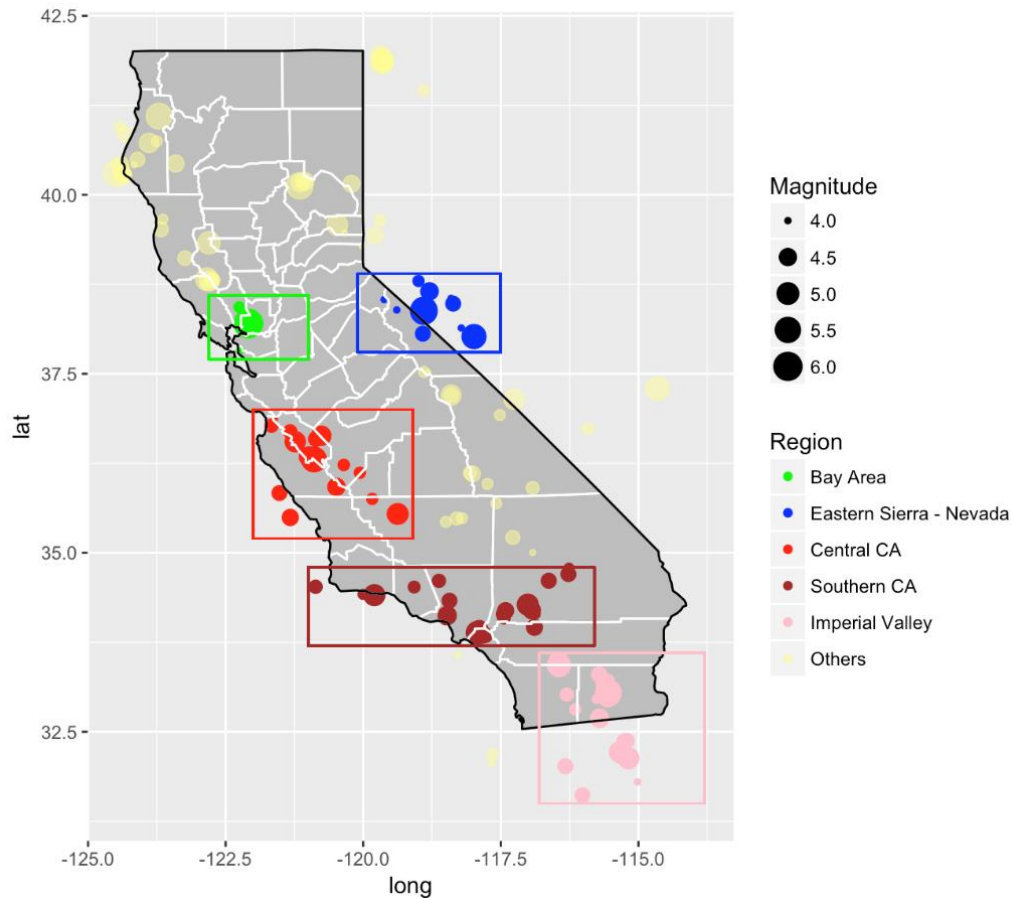

Figure 1. Locations of earthquakes in California and northern Mexico with **M** >= 4.0 since 2011 for which ground motion data has been compiled for addition to the NGA-West2 database
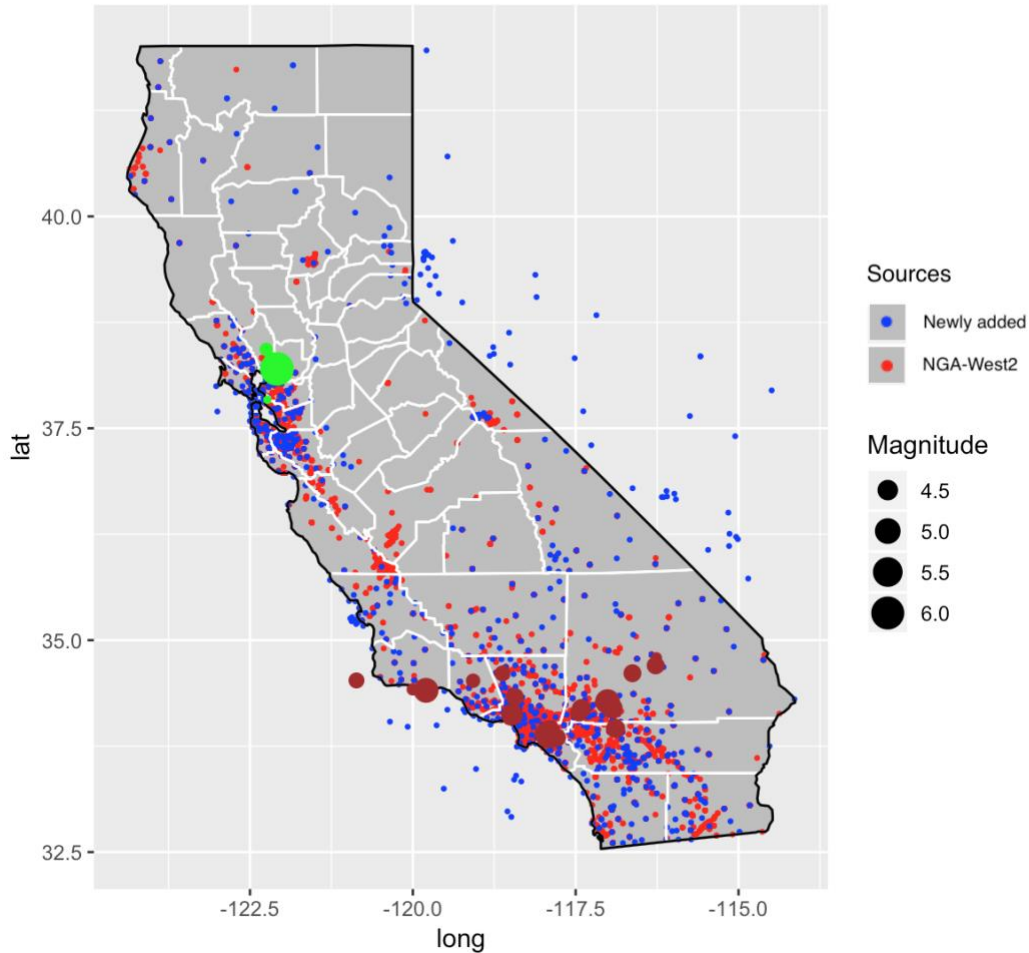
Figure 2. Map of California showing locations of considered earthquakes with **M** >= 4.0 since 2011 and locations of stations that recorded the events (blue – new stations, red – stations in NGA-West2 database)

Each of the three-component records has been processed according to standard protocols developed during Pacific Earthquake Engineering Research center (PEER)-NGA projects, as described in Ancheta et al. (2014). This processing provides a lowest usable frequency for each ground motion component. Horizontal ground motion components are combined to median-component (RotD50) as defined by Boore (2010) using the routines given in Wang et al. (2017). We take the lowest useable frequency for RotD50 as the higher of the two as-recorded values. Figure 3 shows the number of usable RotD50 horizontal-component ground motions as a function of oscillator period. The fall-off begins at about 1.0 sec and the data is reduced by 50% at 2.5 sec.
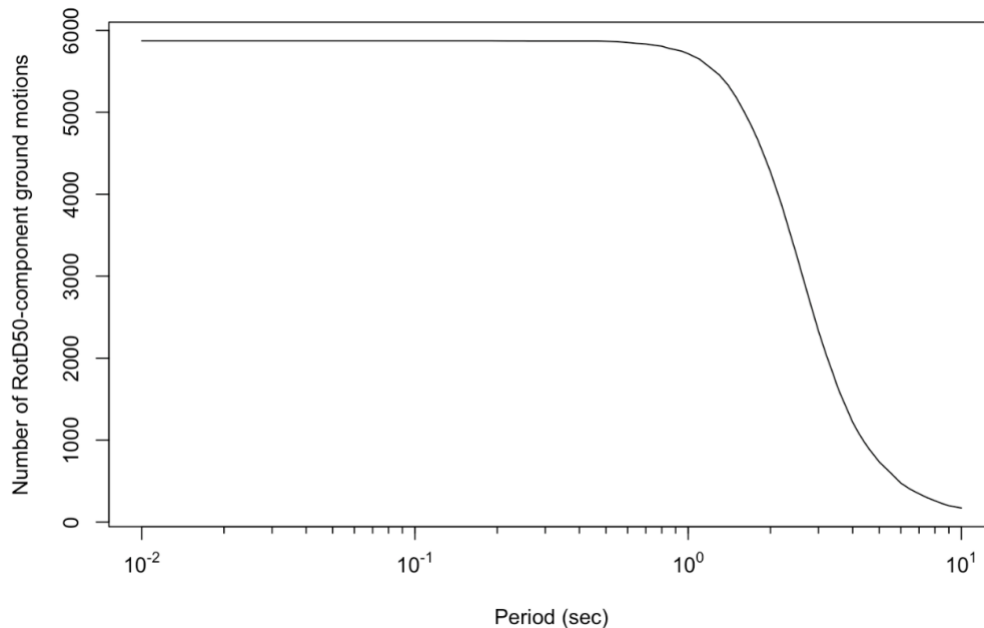
Figure 3. Number of usable RotD50-component ground motions as a function of oscillator period for the data added for the Bay Area and southern California regions.

Considering both the NGA-West2 data and new data, there are 1818 recording sites shown in Figure 2. Of those, 1340 are sites that were included in the NGA-West2 site database. Hence, there are 478 new sites that require assignment of site parameters. We use measured V_S profiles to compute V_{S30} when available, and in the absence of this data, we use proxies (slope gradient – Wald and Allen (2007); terrain category – Yong et al., 2012 and Yong 2016; surface geology – originally by Wills and Clahan (2006) and Kriging interpolated by Thompson et al 2014, and later updated by Wills et al. 2015 and Thompson 2018. We have evaluated correlations among these proxies and used this information to develop model weights in a manner similar to that described in Kwok et al. (2018). This work will be documented subsequently, and resulted in the following weights:

- Surface geology with local data adjustment: 0.665
- Terrain categories: 0.323
- Surface gradient: 0.012

Database Subset for Site Response Studies

A subset of the full database is applied for site response studies. The criteria used to define this subset are: (1) a minimum number of recordings per site of 10 (applied to ensure statistically robust estimates of site term, η_S); (2) availability of a V_S profile for the site.

Figure 4 shows a histogram of the number of recordings at stations in the full database. Of the 1818 sites in the full database, 366 meet the minimum recordings/site criterion.
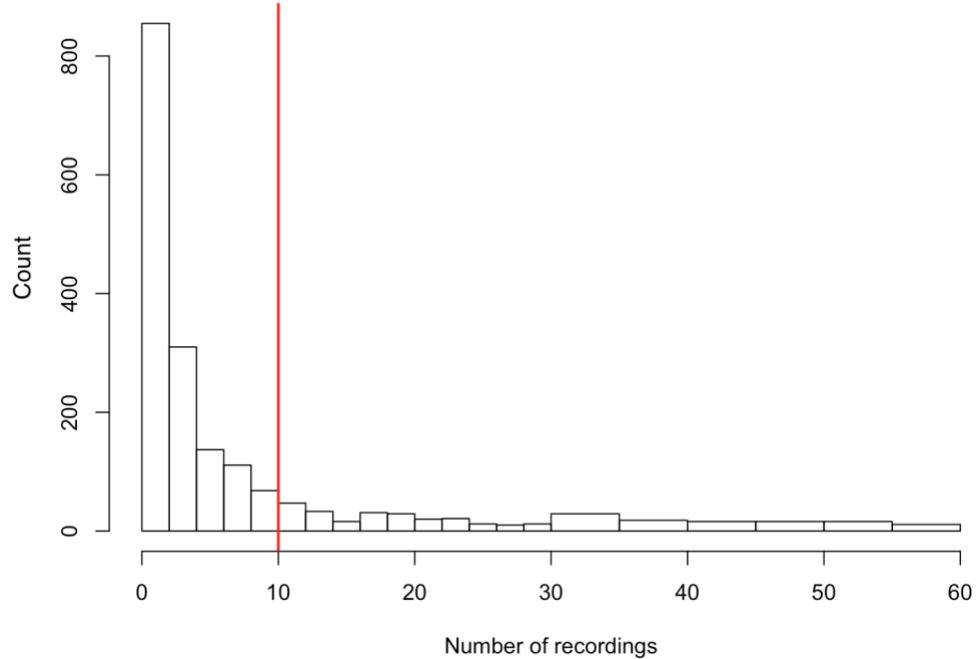
Figure 4. Histogram of number of recordings at stations in the full database. Ten is the minimum number of records/station for sites considered in the present research.

We performed a search for *Vs* profiles for each of the sites meeting the first criterion. This was done using the shear wave velocity profile database compiled for California by Ahdi et al. (2018). We find 149 sites with a *Vs* profile within around 200 m of the strong motion site. Many of these profiles are from Yong et al. (2013), which provides *Vs* profiles from various surface wave tests and H/V spectral ratios from microtremors. Of the 149 sites with *Vs* profiles, only 3 have a boring log that indicates stratigraphic details and soil/rock layer descriptions. This geotechnical data is needed to apply models for modulus reduction and damping as a function of shear strain.

Most of the recordings used in this research involve low ground motion amplitudes. Figure 5 shows a histogram of the ratio (strain index):

$$I_\gamma = \frac{PGV}{V_{S30}} \qquad [2]$$

where *PGV* is from the surface recording and is taken from the RotD50 component. This ratio provides an index related to shear strain (Idriss, 2011; Kim et al, 2016), and can be used to judge the degree to which soil responses are likely to be affected by nonlinearity. As shown in Figure 5, 97% of ground motions in the subset have $I_\gamma < 0.03\%$. We conclude that the soil responses are predominantly in the linear range, meaning that modulus reduction is unity and damping is at the minimum value. We refer to the minimum damping from geotechnical models (Darendeli 2001 for soils with fines; Menq 2003 for granular soils) as D_{min}^L. As a result, the primary need for stratigraphic and material description information is to define D_{min}^L as a function of depth.
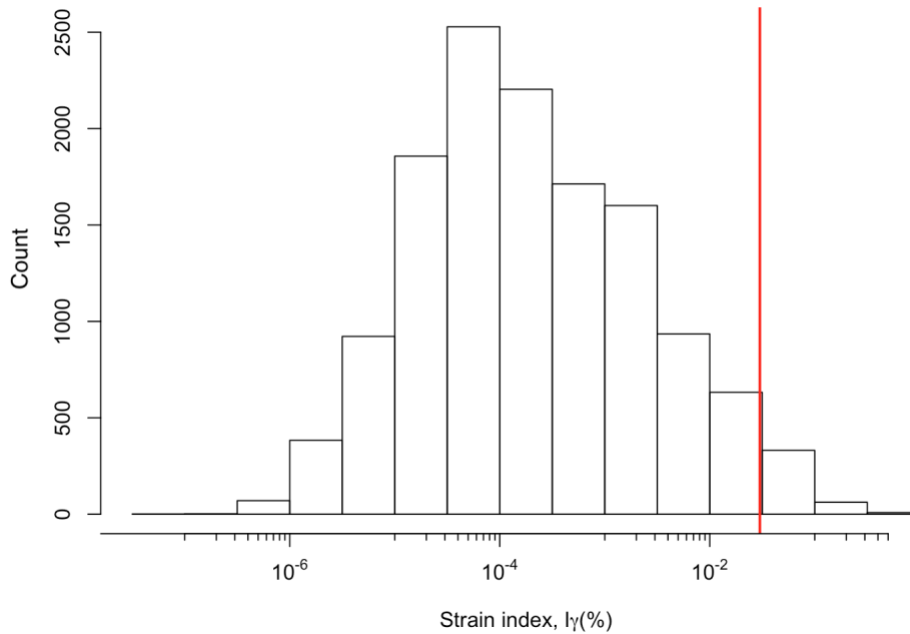
Figure 5. Histogram of strain index number of recordings at stations in the full database.

To derive D_{min} profiles for use in ground response analyses, the next two sections describe (1) how stratigraphy was inferred to enable estimates of D_{min}^L (for sites without borehole logs); and (2) how site spectral amplitude decay parameter (κ) was measured from recordings and then interpreted to constrain small-strain damping. As such, these sections support the development of alternative damping profiles, each of which are being considered in the validation analyses.

Inference of Unit Weight and Material Damping

Ground response analyses for linear conditions require shear wave velocity, unit weight, and D_{min} profiles. Shear wave velocity profiles are measured at each of the sites in the *Database Subset for Site Response Studies*. In most forward applications, geotechnical site characterization provides borehole logs that describe site stratigraphy and soil type information, which can be used to derive the input parameters used to predict unit weight and D_{min}^L. As described above, this is not the case for many of the sites considered in this research. This section describes how we estimate unit weight and soil parameters used to estimate material damping.

Unit Weight

For soil units, we estimate unit weight using phase relationships, which relate unit weight to void ratio, specific gravity, and saturation. Void ratio is taken from an empirical relationship with *Vs* shown in Figure 6 and given as (Rogers et al., 1985):

$$V_S = 42.9 + 94.1/e^2 \qquad [3]$$
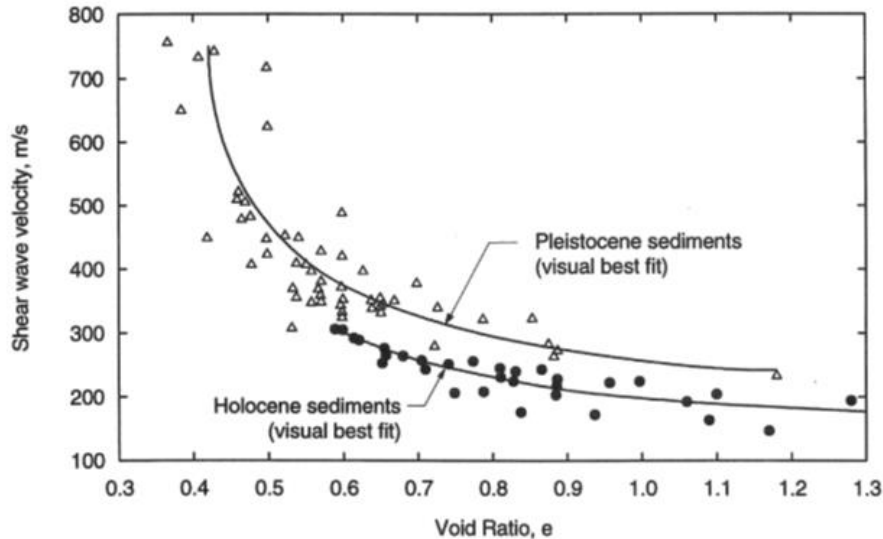
where *Vs* is in units of m/s.

Figure 6. Empirical relationships between void ratio, age, and shear-wave velocity for alluvial sediments in southern California (Fumal and Tinsley 1985). Eq. [3] fits the combined data (Rogers et al 1985)

Specific gravity is commonly taken as $G_S = 2.7$. Saturation (S) is taken as 1.0 below the first depth where V_P exceeds 1500 m/s. Above that depth, or over the full depth where V_P data is absent, saturation is assumed as 50%. Total unit is then computed as:

$$\gamma = \frac{G_S \gamma_w}{1 + e}\left(1 + \frac{eS}{G_S}\right) \quad\quad [4]$$

where γ_w is the unit weight of water (10 kN/m3).

For rock units, we assigned unit weight based on V_S as follows:

$$\gamma = \begin{cases} 20\ \text{kN/m}^3, & \text{if } 450 < V_S < 700\ \text{m/s} \\ 22\ \text{kN/m}^3, & \text{if } V_S > 700\ \text{m/s} \end{cases}$$

Stratigraphy and Soil Type to Estimate D_{min} in Soil Layers

Stratigraphic and soil type information is needed to apply the geotechnical model for D_{min} estimation by Darendeli (2001), which is conditioned on plasticity index (PI), over-consolidation ratio (OCR), and mean effective stress. Effective stress can be calculated using unit weights from the prior section and water table depth (as applicable). PI and OCR are generally derived from laboratory tests on samples retrieved from the field.

We consider two types of available information as potentially useful to assign stratigraphy and soil type information – the mapped surface geology and the V_S profile. Surface geology is used to estimate soil type near the ground surface. The V_S profile is used in combination with the surface unit assignment to estimate variations with depth.

Surface geology is taken from state-wide geologic maps by Wills and Clahan (2006) and Wills et al. (2015). We assume relationships between surface geological unit and PI/OCR, with details indicated in Table 1. Considerations in the development of the relationships in Table 1 include:

- Geologically young sediments (Holocene) are assumed to have low OCR, and older units are assumed to have relatively high OCRs. The rationale is that young deposits have relatively limited pseudo-overconsolidation from ageing and are unlikely to have experienced significant unloading from natural geological processes.
- Young sediments deposited in quiescent environments (e.g., bays, lakes, central/flat portions of alluvial basins) are assumed to be relatively fines- and clay-rich, thus having high PI. Young alluvial sediments deposited on steeper gradients are assumed to be relatively granular (PI = 0).
- Tertiary sedimentary bedrock units often carry information on rock type (e.g., shale, sandstone, etc.). We assume the bedrock units are similar to corresponding soil units (i.e., shale and sandstone interpreted as clay and sand, respectively).
- For pre-Quaternary units without information on material type or depositional environment, there is no basis for relatively coarse- or fine-grained behavior. We assume an intermediate condition in this case (roughly corresponding to low-plasticity silt).

Table 1 is organized in reference to 12 geological units that the stations in full database encountered and recommended by Wills and Clahan (2006): Qal1, Qal2, and Qal3 are relatively young alluvial sediments likely to be of Holocene age; Qoa is older alluvium of Pleistocene age; QT describes sediments in the early Pleistocene to Pliocene periods, for which the method of deposition is unknown; Tsh, Tss, and Tv comprise Tertiary age bedrock of consisting of shale, sandstone, or volcanic origin-materials (typically basalt or rhyolite), respectively; serpentine is a metamorphic rock of Tertiary age largely comprised of the clay mineral serpentinite; and Kss, Kjf, and crystalline are hard rock, typically of Cretaceous age.

Before assigning one of the hard rock classes (Kss, Kjf, crystalline), we perform a visual check of morphology using Google Earth™. When this check indicates that the surface appears to be soil, and if the velocity of the nearest-surface layer is compatible with soil, we assign a soil surficial unit and assign rock at greater depths where velocities become fast.

The soil property assignments in Table 1 apply for ground surface layers. The assignment of properties at depth is made in consideration of gradients in the *Vs* profile. If the surface layer consists of sediments or Tertiary rock, the soil index properties are not changed in successive layers absent sudden changes in velocity with depth. Sudden changes can trigger soil type changes – for example, when a granular layer is underlain by a much slower layer, the underlying unit is taken as clay. Similarly, when a fine-grained surface layer is underlain by a much stiffer layer, the underlying material is taken as granular. When a layer velocity exceeds 760 m/s, it is taken as rock. Figure 7 shows the flow chart used to assign soil type information as a function of depth.

Table 1. The list of 12 geological units and their corresponding PI and OCR. Ma indicates million years.

Geological age	Geol. unit	Description	Estimated Parameters
Holocene (< 0.011 Ma)	Qal1	Quaternary Holocene alluvium with flat gradients (< 0.5%).	PI = 30 OCR = 1.2
	Qal2	Quaternary Holocene alluvium with moderate gradients (0.5 - 2.0%).	PI = 10 OCR = 1.2
	Qal3	Quaternary Holocene alluvium with steep gradients (> 2%).	PI = 10 OCR = 1.2
Pleistocene (< 2.6 Ma)	Qoa	Quaternary Pleistocene alluvium. Soil composition unknown.	PI = 10 OCR = 2
Pliocene (2.6-5.3 Ma). Young era within the Tertiary.	QT	Quaternary to Tertiary deposits, including Saugus Fm. in So. CA, Paso Robles Fm. in central Coast Ranges, and Santa Clara Fm. in San Francisco Bay area. Soil composition unknown.	PI = 10 OCR = 2.5
Tertiary (2.6-66 Ma).	Tsh	Shale and siltstone units, such as the Repetto, Fernando, Puente, and Modelo Fms in So. CA.	PI = 15 OCR = 3
	Tss	Sandstone units, such as the Topanga Formation in So. CA and Butano Formation in San Francisco Bay area.	PI = 0 OCR = 3
	Tv	Volcanic units including the Conejo Volcanics in Santa Monica Mtns and the Leona Rhyolite in East Bay Hills.	PI = 15 OCR = 3
	Serpentine	Serpentine rock is clay-rich.	PI = 15 OCR = 3
Cretaceous	Kss	Cretaceous sandstone of the Great Valley Sequence	NA
	Kjf	Franciscan complex rocks, including mélange, sandstone, shale, chert, and greenstone.	NA
	crystalline	Crystalline rocks, including Cretaceous granitic rocks, Jurassic metamorphic rocks, schist, and Precambrian gneiss.	NA

***D*_{min} in Firm Rock Layers**

The Darendeli (2001) model cannot be used for pre-Tertiary rock (units Kss, Kjf, crystalline). Laboratory data on material damping for such materials is limited. A presumably judgement-based model was presented by Schnabel (1973) and has been widely used since that time. Choi (2008) performed testing on welded Bandelier Tuff and Topopah Spring Tuff and developed damping models. Models from these two sources are compared in Figure 8. The D_{min-} component from Topogah Spring Tuff is considered more representative of bedrock materials in our study region based on its unit weight (Bandelier Tuff has low unit weights). The D_{min} range for this material is about 0.2 – 1.0% (average = 0.3%). We have used the Choi model for the present work, but acknowledge that its use carries large uncertainty.
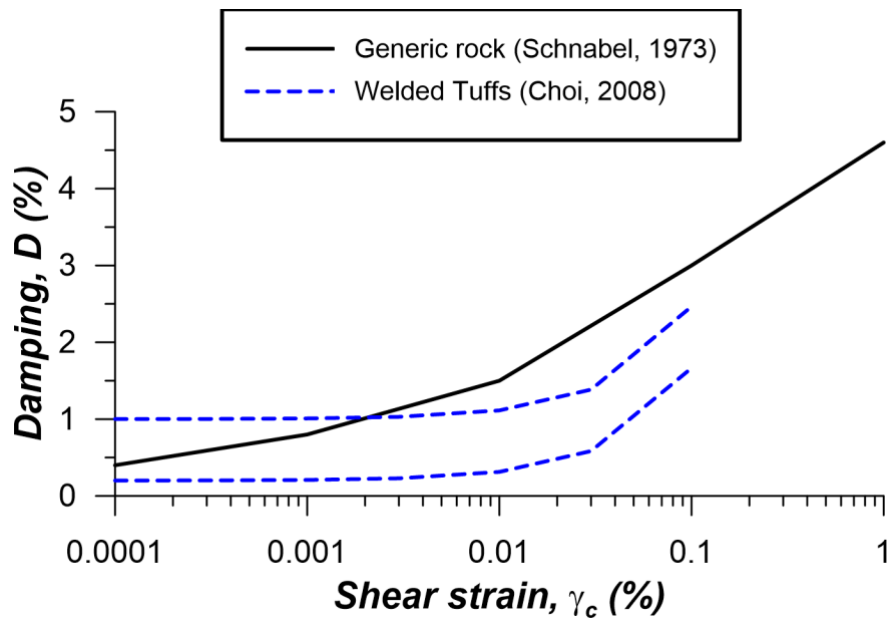

Figure 8. Comparison of rock damping model from Schnabel (1973) and range from Choi (2008).
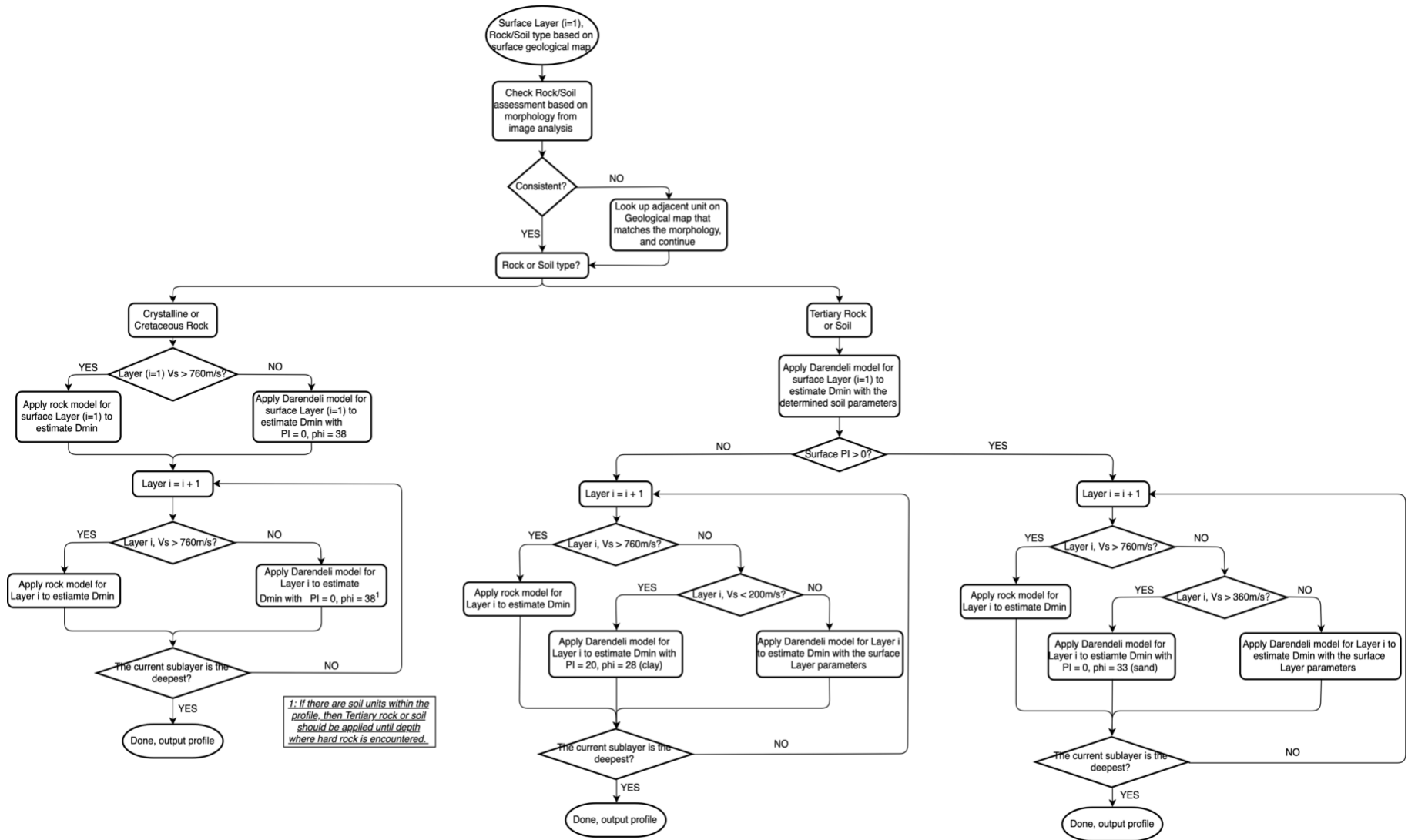
Figure 7. Flow chart used to assign soil type information as function of depth

κ-Informed Damping Model

Approach

Figure 9 shows Fourier amplitude spectra for ground motions at two examples sites in our database. The spectra show a characteristic feature, which is decay of Fourier amplitudes with increasing frequency for frequencies beyond the peak in the spectrum. This frequency-dependent decay can be described as:

$$D(f) = exp(-\pi\kappa f) \qquad [6]$$

where f is frequency in Hz and κ is a decay parameter that can be established through fits to data (e.g., Anderson and Hough, 1984).
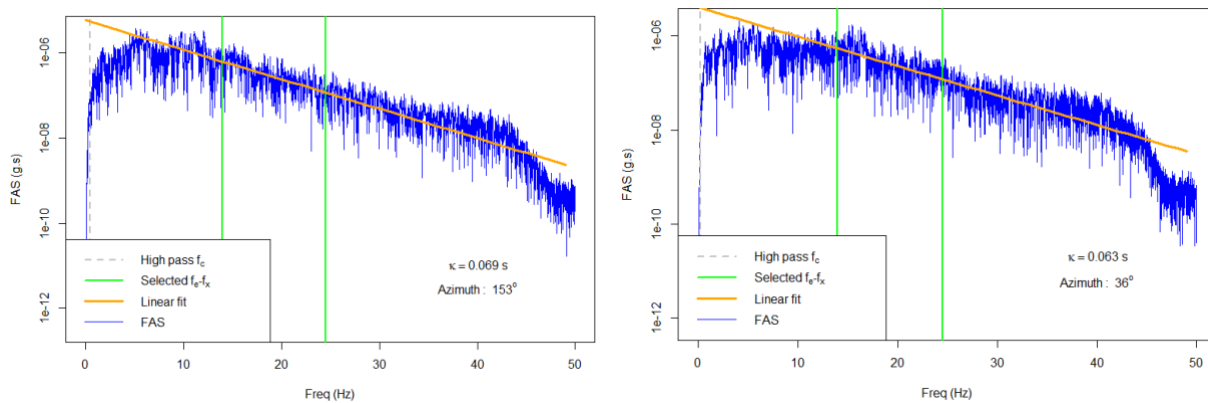
Figure 9. Analysis of κ from recordings at two example sites (left: AZ.KNW, right: AZ.PFO)

The decay parameter arises from material damping and wave scattering that occurs on the wave path from source-to-site, often including appreciable contributions from site response. The path and site response contributions to κ combine as (adapted from Anderson 1991):

$$\kappa = \kappa_0 + \kappa_R R \qquad [7]$$

where R is site-to-source distance, κ_R is the slope by which κ increases with distance, and κ_0 represents the cumulative effect of damping and wave scattering through the soil column.

The relationship between κ_0 and profile attributes can be expressed as (Hough and Anderson 1988; Chapman et al. 2003; Campbell 2009):

$$\kappa_0 = \int_0^{z_s} \frac{dz}{Q_{ef}(z)V_S(z)} \qquad [8]$$

where z_s is the site column thickness (depth to reference crustal rock) and $Q_{ef}(z)$ is the depth-dependent effective material quality factor, representing both the effects of frequency-dependent wave scattering and frequency-independent soil damping. Q_{ef} can be converted to an effective soil damping as follows (Campbell, 2009):

$$D_{ef}(\%) = \frac{100}{2Q_{ef}} \tag{9}$$

Measurements of κ from recordings can, in principal, inform levels of damping applied in ground response analyses as follows:

1. Measure κ for a set of sites from multiple earthquakes, as shown for example in Figure 9.
2. Develop a regionally appropriate model for κ_R.
3. Adjust each measured value of κ, for each event recorded at a given site, to estimate κ_0 by re-arranging Eq. (7) as $\kappa_0 = \kappa - \kappa_R R$.
4. Since the soil/rock column thickness analyzed in ground response analysis is typically smaller than the full profile to reference crustal rock ($Vs \approx 2.5$-3 km/s), adjust κ_0 from Step (3) as,

$$\Delta\kappa = \kappa_0 - \kappa_{0,b} = \int_0^{z_p} \frac{2D_{ef}(z)}{100} \frac{dz}{V_S(z)} \tag{10}$$

where $\kappa_{0,b}$ is the site decay parameter at the base of the profile and z_p is the depth of the analyzed soil column ($z_p < z_s$).

5. Modify the laboratory damping with a profile-specific adjustment factor F_D to match $\Delta\kappa$ from Step (5), which can be represented by re-writing Eq. (10) as:

$$\Delta\kappa = \int_0^{z_p} \frac{2D_{min}^L(z) \times F_D}{100} \frac{dz}{V_S(z)} \tag{11}$$

The depth-invariant value of F_D represents the means by which the field observations of kappa inform the damping model. In some cases, F_D may be unreasonably high. To constrain F_D so that it provides damping values within a realistic range, we have enforcea maximum value of $F_D = 5$. The approach maintains the scaling of damping with soil type and depth in the laboratory models, while adjusting for other effects encountered in field conditions (scattering).

Implementation of the above procedure requires several model components – distance correction term κ_R and site decay parameter for the base of profile condition $\kappa_{0,b}$. The following sub-sections describe the calculation of κ from recordings, models used for these components, and example results.

Fitting of κ from Ground Motions

We apply the κ-fitting procedures described in Afshari and Stewart (2019), which were adapted from Cabas et al. (2017) and Xu et al. (2020). The fit occurs over a range of frequencies from f_e to f_x (upper and lower bounds, respectively) that is selected for each record.

Search ranges for f_e and f_x are taken as 10-18Hz and 22-28Hz, respectively, each with 0.5Hz increments. For each possible combination of f_e and f_x, κ is computed for combinations of the two horizontal components rotated to various azimuths. The variability of κ with azimuth is computed for each f_e-f_x combination, which is expressed as a coefficient of variation (COV). We seek the combination of f_e and f_x that minimizes the azimuthal variability, and then take κ as the median. The Fourier amplitude spectra for two example sites shown in Figure 9 are for the azimuths and frequency ranges identified using this process.

Analysis of Path- and Site Contributions to κ

Rates of crustal attenuation vary spatially due to variations in geologic conditions. Conditions producing relatively fast ground motion attenuation rates (i.e., low crustal quality factor, Q) would be expected to increase κ_R. Insight into spatial variations of attenuation rates are provided by maps of frequency-independent Q (denoted Qs) by Eberhart-Phillips (2016) for Northern California and Hauksson and Shearer (2006) for Southern California. Figure 10 shows maps of California indicating variations of Qs at a depth of 10 km from the two sources. There are systematic differences between Qs, with southern California values being higher.
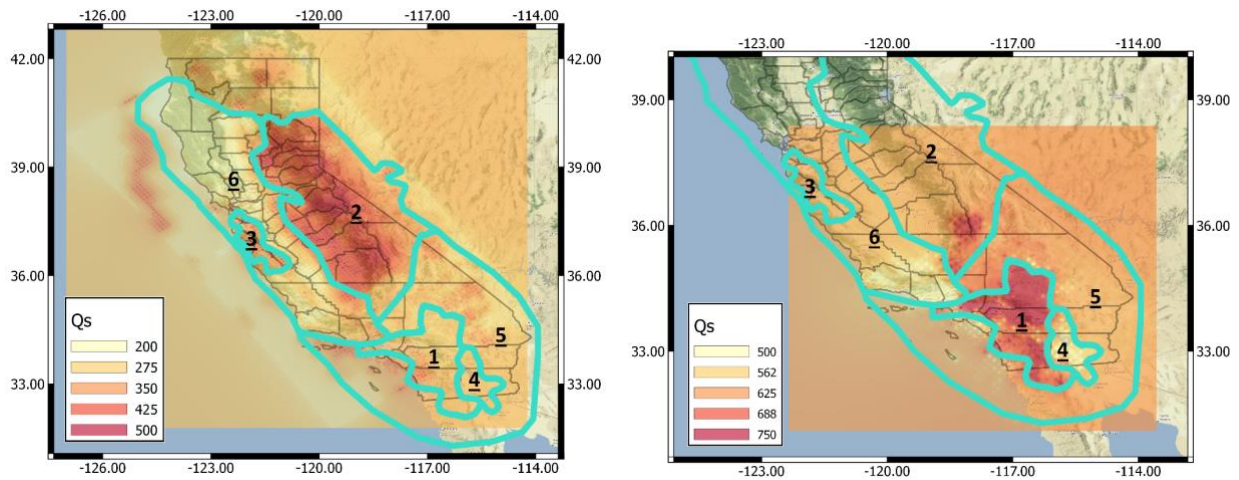
Figure 10. Spatial variation of frequency-independent quality factor (Qs) for California as derived from two models at a depth of 10 km. Zones considered in mixed-effects analysis of path κ are shown.

Allowing for differences in Qs between the two sources, and considering both maps, we have assigned six zones of approximately uniform Qs, with the intention of computing κ_R separately for each zone. If the value of κ_R for zone i is taken as $\kappa_{R,i}$, then the $\kappa_R R$ term in Eq. (7) is computed as:

$$\kappa_R R = \sum_i \kappa_{R,i} R_i \qquad [12]$$

where R_i is the path length (between source and site) through zone i. Distance R_i is zero if the path does not go through the zone i.

We use mixed-effects regression (more specifically, random intercept model) to obtain $\kappa_{0,j}$ for each station j and $\kappa_{R,i}$ for each zone i, by adapting Eq. (7) as follows:

$$\kappa_{k,j} = \kappa_{0,j} + \sum_{i=1}^{n} \kappa_{R,i} R_{k,i} \qquad [13]$$

where $\kappa_{k,j}$ is the measured κ from recording k at station j, $\kappa_{0,j}$ is the site-specific decay parameter at station j, n is the number of zones in California, and $R_{k,i}$ is the source-to-site path length for recording k that goes through zone i. Station terms $\kappa_{0,j}$ are taken as random effects and path terms $\kappa_{R,i}$ as fixed effects. Eq. (13) is solved using an equivalent matrix form. Regressions are performed in R [packages *nlme* (Pinheiro et al. 2019) or *lme4* (Bates et al., 2015)] using the full database (i.e., NGA-West2 stations and records in California as augmented here). The resulting κ_R values are shown for each zone in Figure 11, where they are plotted against the Qs values from the two references. The error bars shown in the figure indicate the estimation error for κ_R from the regressions and the within-zone ranges of Qs. Regressions provided negative κ_R in Zone 2, which is plotted instead at zero.
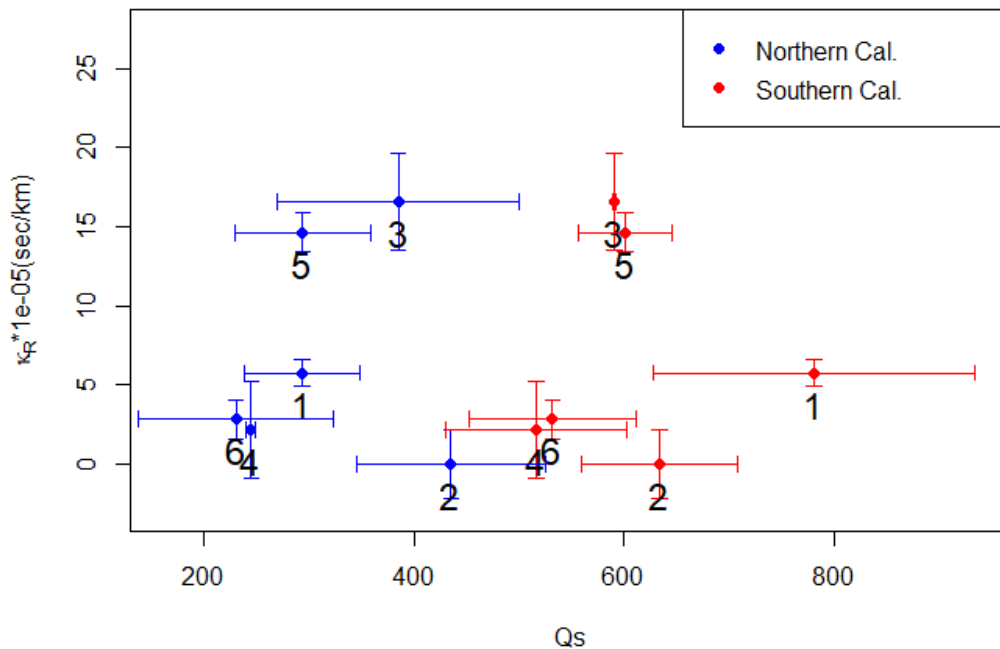
Figure 11. Variation of κ_R with average Qs within the six zones shown in Figure 10. Average Qs is taken from both Eberhart-Phillips (2016) for Northern California and Hauksson and Shearer (2006) for Southern California

Base of Profile Site Decay Parameter, $\kappa_{0,b}$

The base of profile site decay parameter $\kappa_{0,b}$ is needed to estimate the change in site kappa over the profile depth ($\Delta\kappa$) using Eq. (10). Because the sites considered in this research are surface-only instruments, $\kappa_{0,b}$ cannot be measured (i.e., from a downhole instrument) but instead is estimated from models. Several such models were considered.

Silva et al. (1998) used California data to relate κ_0 to V_{S30},

$$\kappa_0 = \begin{cases} 0.008 \text{ sec}, & V_{S30} > 1500 \text{ m/s} \\ 0.020 \text{ sec}, & 760 < V_{S30} < 1500 \text{ m/s} \\ 0.030 \text{ sec}, & 360 < V_{S30} < 760 \text{ m/s} \end{cases} \qquad [14]$$

Van Houtte et al. (2011) and Xu et al. (2000) used larger databases from the KiK-net array in Japan and NGA-West data to derive empirical relationships between κ_0 and V_{S30}. Van Houtte et al. (2011) proposed:

$$ln\kappa_0 = 3.490 - 1.062lnV_{S30} \qquad [15]$$

Xu et al. (2020) proposed:

$$ln\kappa_0 = \begin{cases} k_1(lnV_1)^2 + k_2lnV_1 + k_3, & 100\text{m/s} < V_{S30} < V_1 \\ k_1(lnV_{S30})^2 + k_2lnV_{S30} + k_3, & V_1 < V_{S30} < V_2 \\ k_1(lnV_2)^2 + k_2lnV_2 + k_3, & V_2 < V_{S30} < 3000\text{m/s} \end{cases} \qquad [16]$$

where k_1=0.18, k_2=1.816, k_3=-7.38, V_1=155 m/s, and V_2 = 2000 m/s. The units of κ_0 are sec in both Eq. (15) and (16).

We apply the Van Houtte et al. (2011) relationship in the present work. To obtain $\kappa_{0,b}$, we estimate the V_{S30} corresponding the base of the soil column by projecting vertically (constant velocity) the V_S at the deepest portion of the profile. We then enter this value into Eq. [15] to compute $\kappa_{0,b}$. Results of this process for the two example sites are shown in Table 2, as are derived values of $\Delta\kappa$ and F_D using Eqs [10-11].

Table 2. Site kappa results for the AZ.KNW and AZ.PFO sites

Site	κ_0 (sec)	$\kappa_{0,b}$ (sec)	$\Delta\kappa$ (sec)	F_D
Keenwild Fire Station, Mountain Center, CA (AZ.KNW)	0.059	0.009	0.050	5
Pinyon Flats Observatory, CA (AZ.PFO)	0.050	0.006	0.044	5

Data-to-Model Comparisons for Example Sites

Figure 12 compares the data-derived site amplification (labelled as "true site amp.") with estimates derived from ground response analyses ("GRA") and from an ergodic model (Seyhan and Stewart 2014) for the AZ.KNW site. The ground response analysis results shown here use laboratory-based damping models. The site exhibits a peak in the amplification at about 0.09 sec. This occurs because AZ.KNW is a rock site with a shallow surficial soil layer. Ground response analyses are able to capture this feature and provide a good representation of the frequency-dependent shape of the site amplification. In contrast, the ergodic model significantly misfits the observed site amplification. Figure 13 shows similar results for the AZ.PFO site, where ground

response analyses misfit the data, but still arguably improve upon the predictions of an ergodic model.

 The effects of a κ-informed damping model are modest for the two example sites examined here. The impacts of alternate damping models is being explored by applying these procedures to additional sites with thick soil columns.

Figure 12. Non-ergodic site response at the AZ.KNW site, compared with site response predictions obtained with use of ground response analysis and an ergodic model. The maximum period used in the plots is the median of the maximum usable periods from data processing. The ground response model provides a good estimate of the shape of the amplification function in this case.
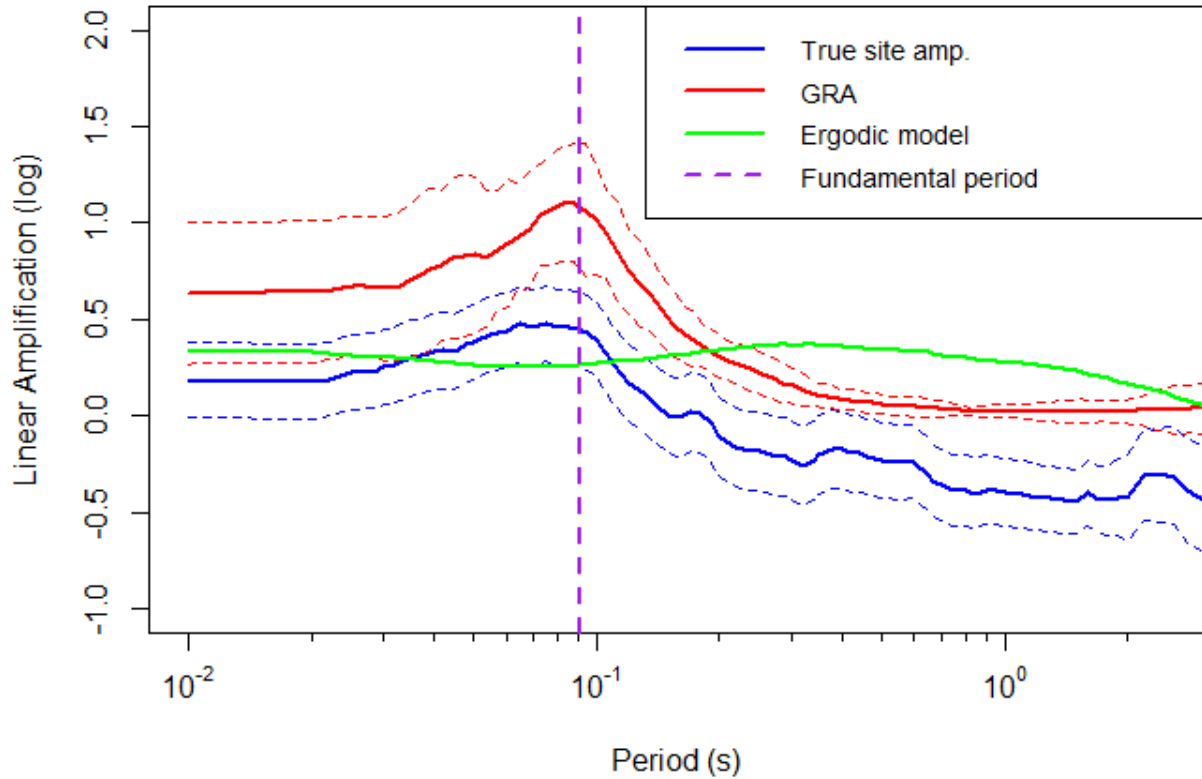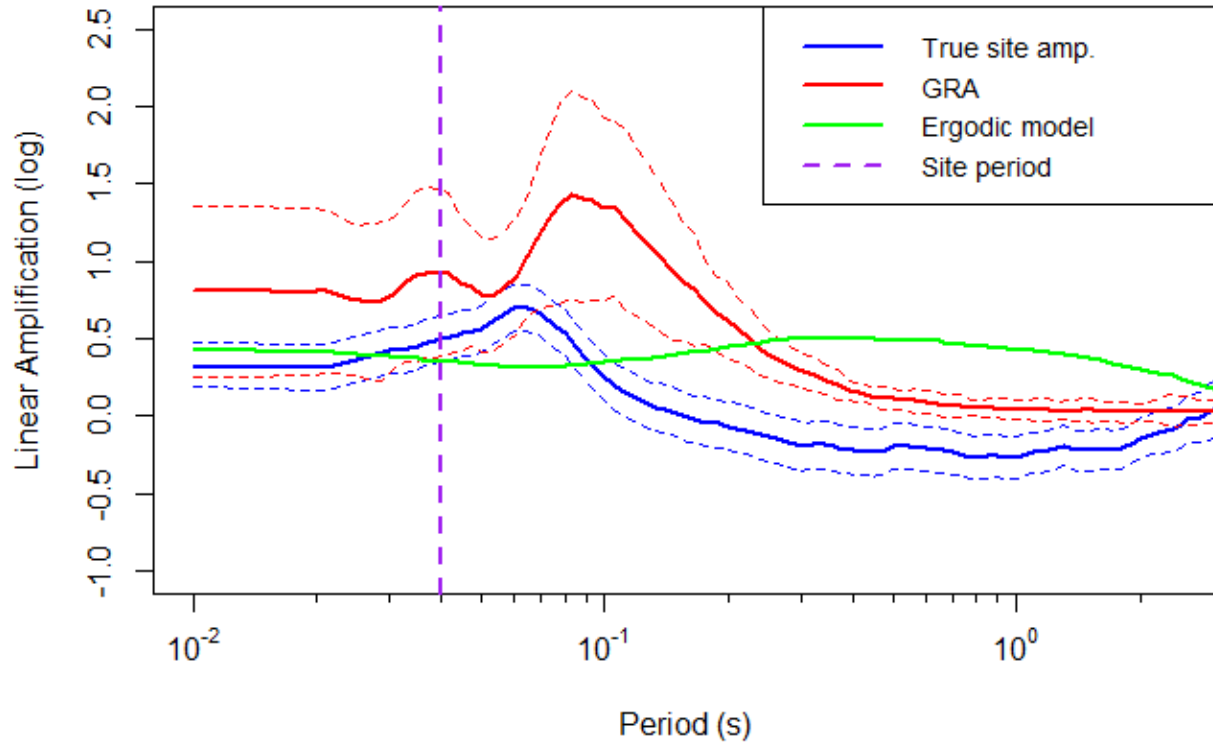
Figure 13. Non-ergodic site response at the AZ.PFO site, compared with site response predictions obtained with use of ground response analysis and an ergodic model. The ground response model provides a relatively poor estimate of the shape of the amplification function in this case.

Conclusions

This research has the broad objective of investigating the effectiveness of ground response analysis, and other methods of site response analysis, through comparisons to true site response as established from analysis of recordings. Effectiveness is judged, in this context, through bias and site-to-site uncertainty of predicted site response.

We describe a new approach using non-ergodic site responses derived from surface-only instruments as the basis for validation studies. This paper has the main objective of describing the methodology, particularly with regard to procedures that implement ground response analyses given limited available information. We illustrate the approach using two sites with shallow soil layers overlying firm rock materials. In these cases, ground response analyses provide improved estimates relative to ergodic models. The work for this project is ongoing and full results will be presented in a later report.

Acknowledgments

presented here represents the views and opinions of the authors and does not reflect the policy, expressed or implied, of the US Government.

References

Afshari, K., Stewart, J. P. (2019) Insights from California Vertical Arrays on the Effectiveness of Ground Response Analysis with Alternative Damping Models. *Bull. Seismol. Soc. Am.* DOI: 10.1785/0120180292

Ahdi, SK, S Sadiq, O Olhan, Y Bozorgnia, YMA Hashash, DY Kwak, D Park, A Yong, JP Stewart (2018). Development of a United States community shear wave velocity profile database, in Geotechnical Engineering and Soil Dynamics V: Seismic Hazard Analysis, Earthquake Ground Motions, and Regional-Scale Assessment, June 10-13, 2018, Austin, TX, ASCE Geotechnical Special Publication No. 291, S.J. Brandenberg and M.T. Manzari (eds.), pp 330-339.

Ancheta, T.D., Darragh, R.B., Stewart, J.P., Seyhan, E., Silva, W.J., Chiou, B.S.-J., Wooddell, K.E., Graves, R.W., Kottke, A.R., Boore, D.M., Kishida, T., and Donahue, J.L., (2014). NGA-West2 database, *Earthquake Spectra*, **30**, 989-1005.

Chapman, M. C., P. Talwani, and R. C. Cannon (2003). Ground-motion attenuation in the Atlantic Coastal Plain near Charleston, South Carolina, *Bull. Seism. Soc. Am.* **93**, 998–1011.

Anderson, J. G., and S. E. Hough (1984). A model for the shape of the Fourier amplitude spectrum of acceleration at high frequencies, *Bull. Seis- mol. Soc. Am.* **74**, 1969–1993.

Anderson, J. G. (1991). A preliminary descriptive model for the distance dependence of the spectral decay parameter in southern California, *Bull. Seism. Soc. Am*. **81**, 2186–2193.

Bates D., Maechler, M., Bolker, B., Walker, S. (2015). Fitting Linear Mixed-Effects Models Using lme4. *Journal of Statistical Software*. 67, 1-48.

Boore D.M. (2010). Orientation-independent, nongeometric-mean measures of seismic intensity from two horizontal components of motion, *Bull. Seismol. Soc. Am.*, **100**, 1830–1835.

Boore, D. M., Stewart, J. P., Seyhan, E., and Atkinson, G. M, (2014). NGA-West 2 equations for predicting PGA, PGV, and 5%-damped PSA for shallow crustal earthquakes, *Earthquake Spectra*. **30**, 1057–1085.

Cabas, A., Rodriguez-Marek, A. and Bonilla, L.F. (2017). Estimation of site-specific Kappa ($\kappa 0$)-consistent damping values at KiK-net sites to assess the discrepancy between laboratory-based damping models and observed attenuation (of seismic waves) in the field, *Bull. Seism. Soc. Am.* **107**, 2258-2271

Campbell, K.W., (2009). Estimates of shear-wave Q and $\kappa 0$ for unconsolidated and semiconsolidated sediments in Eastern North America. *Bull. Seismol. Soc. Am.*, **99**, 2365-2392.

Chang, S.W. (1996). Seismic response of deep stiff soil deposits, *Ph.D. Thesis*, Univ. of California, Berkeley.

Choi WK (2008) Dynamic properties of ash-flow tuffs. *Ph.D. thesis*, Department of Civil Engineering, University of Texas, Austin, Texas.

Darendeli, M. B., (2001). Development of a new family of normalized modulus reduction and material damping curves, *PhD Thesis*, Department of Civil Engineering, University of Texas, Austin, TX.

Dickenson, S.E. (1994). The dynamic response of soft and deep cohesive soils during the Loma Prieta earthquake of October 17, 1989, *Ph.D. Thesis*, Univ. of California, Berkeley.

Eberhart-Phillips, D. (2016). Northern California seismic attenuation: 3D QP and QS models. *Bull. Seismol. Soc. Am.* **106**, 2558-2573.

Fumal, TE and JC Tinsley (1985). Mapping shear wave velocities of near surface geologic materials, *Prof. Paper 1360*, US Geological Survey.

Hassani, B., and G. M. Atkinson (2016). Site effects model for central and eastern North America based on peak frequency, *Bull. Seismol. Soc. Am*., **106**, 2197–2213.

Hauksson, E., and P. Shearer (2006). Attenuation models (QP and QS) in three dimensions of the southern California crust: Inferred fluidsaturation at seismogenic depths, *J. Geophys. Res.* **111** (B05302).

Hough, S. E., and J. G. Anderson (1988). High-frequency spectra observed at Anza, California: Implications of Q structure. *Bull. Seismol. Soc. Am.* **78**, 692–707.

Idriss, I. M., 2011. Use of Vs30 to represent local site conditions, in *4th LASPEI/IAEE International Symposium Effects of Surface Geology on Strong Ground Motions*, Santa Barbara, CA.

Idriss, I.M. (1993). Assessment of site response analysis procedures, *Report to National Institute of Standards and Technology*, Gaithersburg, Maryland, Dept. of Civil & Environmental Eng., Univ. of California, Davis.

Kaklamanos, J, BA Bradley, EM Thompson, LG Baise. (2013). Critical parameters affecting bias and variability in site-response analyses using KiK-net downhole array data, *Bull. Seismol. Soc. Am.*, **103**, 1733–1749.

Kaklamanos, J, B Bradley, 2018. Challenges in predicting seismic site response with 1D analyses: Conclusions from 114 KiK-net vertical seismometer arrays, *Bull. Seismol. Soc. Am*., **108**, 2816-2838.

Kim, B., Y. M. A. Hashash, J. P. Stewart, E. M. Rathje, J. A. Harmon, M. I. Musgrove, K. W. Campbell, and W. J. Silva (2016). Relative differences between nonlinear and equivalent-linear 1D site response analyses. *Earthq. Spectra*, **32**, 1845–1865.

Kwak, DY, JP Stewart, S.-J. Mandokhai, D Park (2017). Supplementing *VS30* with H/V spectral ratios for predicting site effects, *Bull. Seism. Soc. Am.*, **107**, 2028-2042.

Kwok, AOL, JP Stewart, DY Kwak, P-L Sun (2018). Taiwan-specific model for VS30 prediction considering between-proxy correlations, *Earthquake Spectra*, **34**, 1973-1993.

Menq, F., (2003). Dynamic properties of sandy and gravelly soils, *PhD Thesis*, Department of Civil Engineering, University of Texas, Austin, TX.

Pinheiro J, Bates D, DebRoy S, Sarkar D, R Core Team (2019). nlme: Linear and Nonlinear Mixed Effects Models. R package version 3.1-140.

Rodriguez-Marek, A., Rathje, E. M., Bommer, J. J., Scherbaum, F., and Stafford, P. J.. (2014). Application of single-station sigma and site response characterization in a probabilistic seismic hazard analysis for a new nuclear site, *Bull. Seismol. Soc. Am.*, **104**, 1601–1619.

Rathje EM, Dawson C, Padgett JE, Pinelli JP, Stanzione D, Adair A, Arduino P, Brandenberg SJ, Cockerill T, Dey C, Esteva M. DesignSafe: new cyberinfrastructure for natural hazards engineering. *Natural Hazards Review*. 2017 Feb 21;**18**(3):06017001.

Rogers, A. M., J. C. Tinsley, and R. D. Borcherdt (1985). Predicting relative ground response, *U.S. Geol. Surv. Profess.* Paper 1360, 221-248.

Schnabel PB (1973) Effects of local geology and distance from source on earthquake ground motions. *Ph.D. thesis*, University of California, Berkeley.

Seyhan, E, JP Stewart, TD Ancheta, RB Darragh, and RW Graves (2014). NGA-West 2 site database. *Earthquake Spectra*, **30**, 1007-1024.

Silva, W., R. B. Darragh, N. Gregor, G. Martin, N. Abrahamson, and C. Kircher (1998). Reassessment of site coefficients and near-fault factors for building code provisions, Technical Report Program Element II: 98-HQ-GR-1010, Pacific Engineering and Analysis., El Cerrito, California USA.

Stafford, J.S., Rodriguez-Marek, A., Edwards, B., Kruiver, P.P., and Bommer, J.J., (2017). Scenario dependence of linear site-effect factors for short-period response spectral ordinates. *Bull. Seismol. Soc. Am.*, **107**, 2859–2872.

Stewart, JP, K Afshari, CA Goulet (2017). Non-ergodic site response in seismic hazard analysis, *Earthquake Spectra*, **33**, 1385-1414.

Thompson E. M., D. J. Wald, C. B. Worden. (2014) A Vs30 Map for California with Geologic and Topographic Constraints. *Bull. Seismol. Soc. Am.*, **104**, 2313–2321.

Thompson, E.M., (2018), An Updated Vs30 Map for California with Geologic and Topographic Constraints: U.S. Geological Survey data release. DOI: 10.5066/F7JQ108S.

Van Houtte, C., Drouet, C., Cotton, F. (2011). Analysis of the origins of κ (kappa) to compute hard rock to rock adjustment factors for GMPEs. *Bull. Seismol. Soc. Am.*, **101**, 2926–2941.

Wald, D. J., and T. I. Allen (2007). Topographic slope as a proxy for seismic site conditions and amplification, *Bull. Seismol. Soc. Am.*, **97**, 1379–1395.

Wang, P., Stewart, J.P., Bozorgnia, Y., Boore, D.M., and Kishida, T., (2017). "R" Package for computation of earthquake ground-motion response spectra. *PEER Report No. 2017/09*, Pacific Earthquake Engineering Research Center, Berkeley, CA.

Wills, C. J., and K. B. Clahan (2006). Developing a map of geologically defined site-condition categories for California, *Bull. Seismol. Soc. Am.*, **96**, 1483–1501.

Wills, C. J., C. I. Gutierrez, F. G. Perez, D. M. Branum. (2015). A Next Generation VS30 Map for California Based on Geology and Topography. *Bull. Seismol. Soc. Am*., **105**, 3083–3091.

Xu, B., EM Rathje, YMA Hashash, JP Stewart, KW Campbell, and WJ Silva (2020). κ_0 for soil sites: Observations from Kik-net sites and their use in constraining small-strain damping profiles for site response analysis, *Earthquake Spectra*, https://doi.org/10.1177/8755293019878188.

Yong, A., A. Martin, K. Stokoe, and J. Diehl (2013). ARRA-funded V S30 measurements using multi-technique approach at strong-motion stations in California and central-eastern United States, *U.S. Geol. Surv*. Open-File Rept. 2013-1102, 65 pp.

Yong, A., S. E. Hough, J. Iwahashi, and A. Braverman. (2012). A terrain- based site-conditions map of California with implications for the contiguous United States, *Bull. Seismol. Soc. Am.* **102**, 114–128.

Yong, A., (2016). Comparison of measured and proxy-based V$_{S30}$ values in California, *Earthquake Spectra*. **32**, 171-192.

Zalachoris, G, EM Rathje, 2015. Evaluation of one-dimensional site response techniques using borehole arrays, *J. Geotech. Geoenviron. Eng.*, **141**, 04015053.

IDENTIFICATION OF EARTHQUAKE INPUT EXCITATIONS FOR CSMIP-INSTRUMENTED BUILDINGS

S. F. Ghahari, and E. Taciroglu

Department of Civil & Environmental Engineering
University of California, Los Angeles

Abstract

This paper presents the results of a study on the identification of earthquake input excitations for CSMIP-Instrumented buildings. The true earthquake input motions exciting buildings may not be available for various reasons. For example, when there is Soil-Structure Interaction (SSI) effects, the recorded signal at the foundation level, which is commonly used as input excitation, is a part of the building's response. Also, the waves scattered from a vibrating building can alter the wave field around the building, so the so-called recorded Free-Field Motions (FFMs), another input motion candidate, could be polluted with these reflecting waves. Moreover, if there is significant Kinematic SSI, what actually a building experiences as input excitation is different from FFM and foundation response. These unmeasured motions are called Foundation Input Motions (FIMs) and have to be identified from recorded building's responses. In this paper, we propose various methods to carry out this task along with their verification, validation and real-life applications.

Introduction

Consideration of input excitations is an important ingredient of seismic design and assessment of building structures under earthquake hazards. Ground motions recorded on the ground surface—i.e., Free-Field Motions (FFMs)—have often been used as input excitations in seismic response analyses of structures. Such recordings are sometimes not true FFMs, in that they are polluted by waves scattered from nearby structures (see, e.g., [1]). More problematically, even the true FFMs are inherently different from what the subject structure experiences due to spatial variability as well as kinematic interaction effects (see, e.g., [2]). The other common option in dynamic analyses is to use the motion recorded at the foundation level as the input excitation. However, if there is an inertial interaction between the structure and the surrounding soil, the signal recorded at the foundation is part of the system's response [3], [4]. Such Soil-Structure Interaction (SSI) effects generally prevent the direct measurement of true input excitations. These true input excications are often referred to as Foundation input Motions (FIMs) [5]. The FIMs cannot be physically recorded unless there is a massless foundation without any building superstructure. **Figure 1** summarizes the aforementioned issues regarding the usage of various types recordings as earthquake input excitations. It is worth noting that even in the absence of SSI, for many real-life cases, the foundation responses are either at low Signal-to-Noise Ratio (SNR) levels or not recorded at all [6].
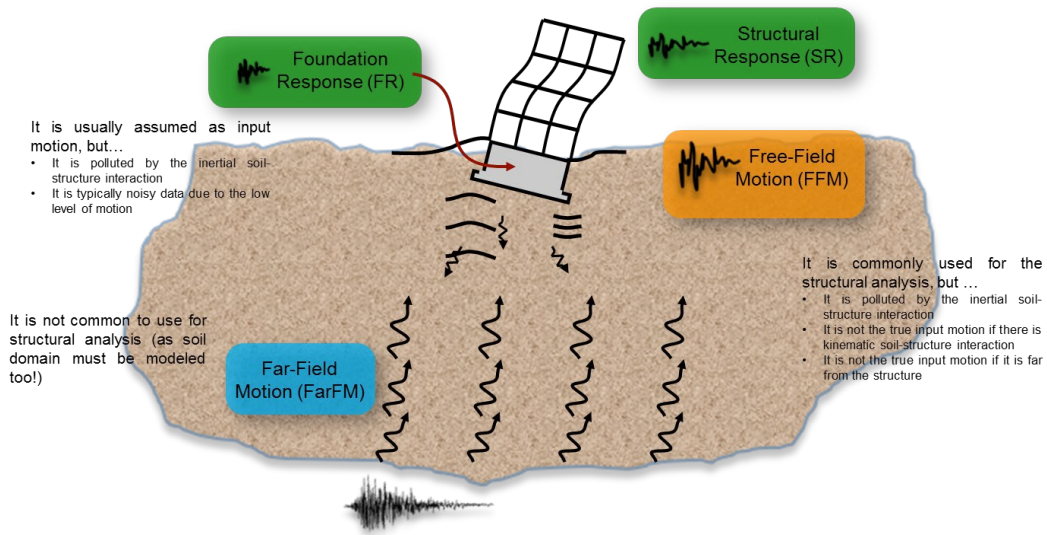
Figure 1. Available recording during an earthquake.

The back-calculation of FIMs from real-life data is a key capability for capturing actual earthquake input excitations and for validating new or existing procedures for considering SSI effects. The California Strong Motion Instrumentation Program (CSMIP) was established by California Geological Survey, in collaboration with various other agencies such as USGS and Caltrans in 1972 following the destructive 1971 San Fernando earthquake to obtain vital earthquake data for the engineering and scientific communities through a statewide network of strong motion instruments [7]. Through CSMIP, more than 900 stations were installed, including 650 ground-response stations, 170 buildings, 20 dams, and 60 bridges. A recent survey (**Table 1**) by the authors indicates that, at the present time, there are ~236 buildings with available instrumentation layouts and at least one earthquake dataset in the Center for Engineering Strong Motion Data (CESMD) [8]. The ~70% of the buildings are instrumented and maintained by the California Geological Survey (CGS) (**Figure 2**a) and this building inventory features various structural types as shown in **Figure 2**b.
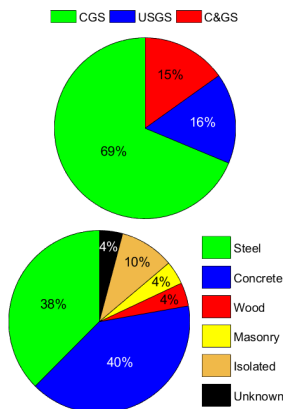
Figure 2. Distribution of CSMIP-instrumented buildings

Table 1. Available building data in CESMD.

Item Description	Number
Number of total records	1643
Number of buildings	377
Number of earthquakes	254
Number of earthquake sets	1588
Number of buildings with at least one earthquake	322
Number of buildings with at least one available earthquake	314
Number of buildings with the available layout	272
Number of buildings with the available layout and at least one recorded earthquake	243
Number of buildings with the available layout and at least one available earthquake	236

Identification Methods

The response of a building structure to a base excitation can be written as a time convolution as $x(t) = FIM(t) * h(t)$ where $FIM(t)$ and $h(t)$ are FIM signal and building's Impulse Response Function (IRF), respectively, and $*$ denotes time convolution. According to this relationship, an obvious way to recover FIM is through the deconvolution provided that building's IRF is known, while this is not the case for real problems because buildings are complex and unknown systems. Note that even having a building's IRF, the deconvolution process is a challenging task because the inverse of the IRF could (and mostly will) be an unstable filter which will be discussed later (see, e.g., [9]).

In a real-world scenario, the building is itself unknown and must be identified first or along with the FIMs. One way is to estimate the system (i.e., building's IRF) via numerical modeling. Despite the existing knowledge and tools for numerical modeling of structural systems, there are various sources of uncertainties (SSI, damping, non-structural, connections, etc.), which makes accurate modeling highly difficult even for very simple structures. Therefore, the building has to be identified. The simplest approach to identify building structures is through Operational Modal Analysis (OMA) for which large number of techniques have been developed in last few decades [10]–[14]. Yet, it is well accepted that the behavior of a structure during an earthquake would be different from its behavior under operational conditions. Also, the ambient data might be unavailable because the measurement system usually needs higher resolution and sensitivity. On the other hand, the identification of buildings using data recorded during strong seismic events without direct measurments of input excitations is challenging. This particular situation—namely, outout-only identification under strong excitations—has been a main focus of the authors in last decade.

The authors have developed a series of Blind[1] Modal Identification (BMID) methods for the aforementioned type of problems [15]–[21]. However, these methods nominally need dense instrumentation. Also, the level of uncertainty is not quantified because they are deterministic solutions. Another workaround is to use model-based solutions in which a numerical model with unknown parameter is assumed for the building under study. This model can be a simple Timoshenko beam as used by the authors [22]–[25] or a coupled beam used by Lignos and Miranda [6]. The problem with such solution is the potentially high level of modeling uncertainties that are not quantified in the mentioned studies. Recently, a series of output-only Bayesian Finite Element (FE) model updating methods have been proposed (see, e.g., [26]). In the present study, we used this method to estimate FIMs from real-life data recorded at the Millikan Library building [27]. While the results are promising, the computational cost is huge. to resolve this limiting fact, we developed a new series of solutions based on the Cross-Relation (CR) idea [28], [29]. The major idea behind this solution is to use response of several adjacent buildings that experience same excitation and extract input motion as common part. After presenting results of the Bayesian estimation of the Millikan Library, details of the proposed CR methods will be presented. A series of verification, validation, and application studies were

---

[1] Output-only

conducted by using these new solutions which are presented in this paper. To see a summary of the available FIM identification solutions discussed above **Figure 3** is presented.
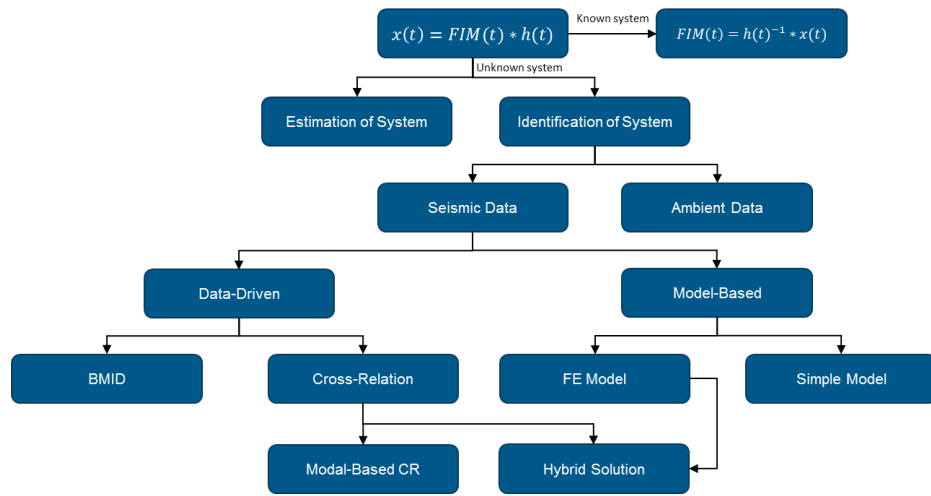
Figure 3. Available/developed solutions for FIM identification.

Output-Only Bayesian Estimation

The overall procedure of the output-only Bayesian estimation method is shown in **Figure 4** [30]. In this method, we assume a prior normal distribution for the unknown parameter vector $\mathbf{\psi}$ (collection of FE model's uncertain parameters and inputs) and propagate this uncertainty through the FE model. Based on the Bayes' rule, the posterior distribution is obtained by calculating the difference between the prediction and measurement (collected through sensors). This process sequentially continues in time. The details of the method are presented in Appendix A.

Figure 4. The output-only Bayesian estimation.

The method is already verified in various publications [31]. Herein, the method is used to estimate parameters of the FE model of the Millikan Library (**Figure 5**left) as well as unmeasured FIMs using real-life response signals during the 2002 Yorba Linda earthquake [27]. Using the available structural drawings, a detailed FE model of the structural system is developed [21]. We used the graphic-user-interface of SAP2000 software [32] to develop the initial geometry of the model. The SAP2000 model was then transferred to OpenSees [33]. The model uses linear-elastic beam-column elements to model beams and columns, and quadrilateral shell elements with linear-elastic section to model shear walls and slabs. The kinematic interaction of precast claddings installed on the north and south faces of the building with the structural system is modeled using diagonal brace elements. The damping energy dissipation for the time history analysis is defined using mass- and stiffness-proportional Rayleigh damping. The Rayleigh damping parameters are treated as unknowns to be estimated. The 3D model of the superstructure is shown in **Figure 5**right. Different colors in this figure present different material properties.
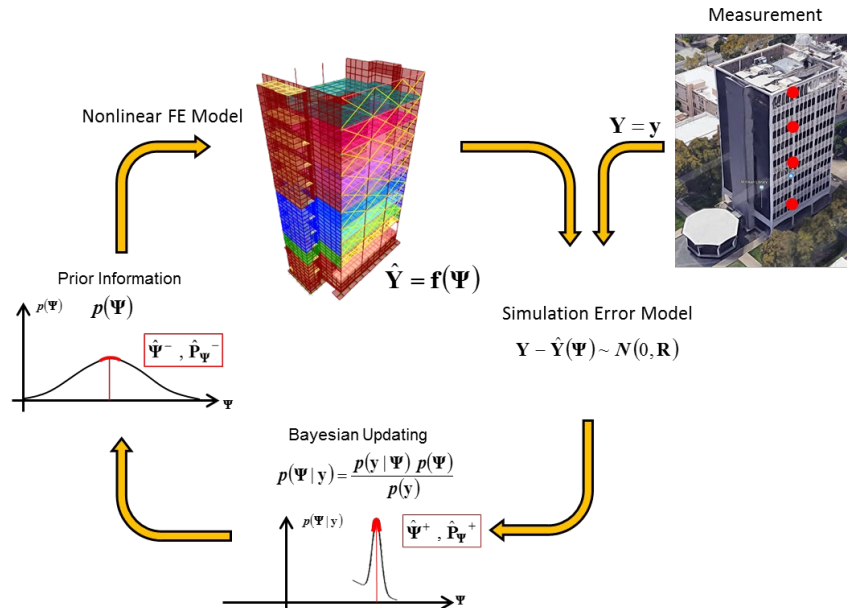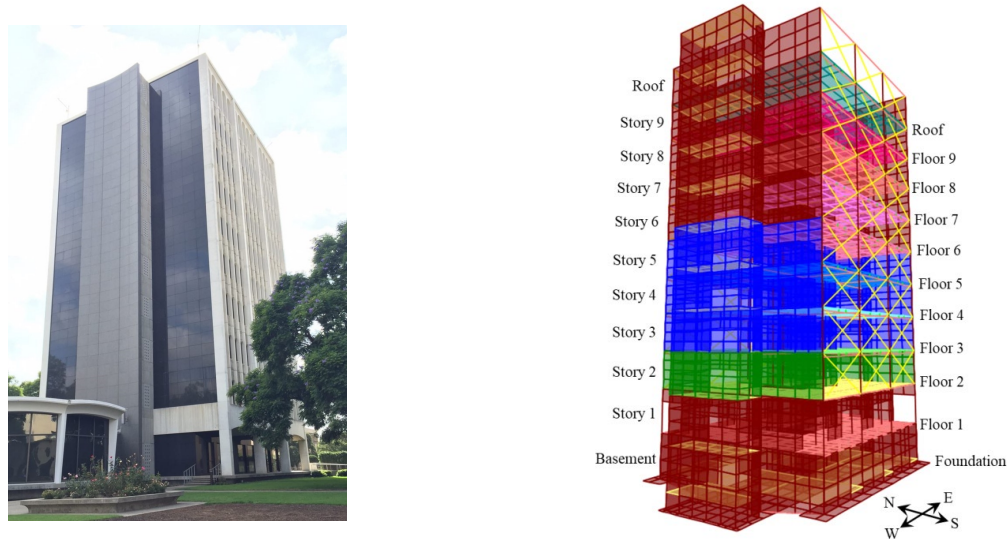

Figure 5. Developed the FE model of the Millikan Library structure.

To include SSI effects, distributed linear soil springs and dashpots are added underneath the foundation slab of the FE model as shown in **Figure 6**. As seen, the building has a two-level foundation system consisting of a central pad and two north and south foundation strips. Six unknown stiffness parameters, namely $k_x, k_{y1}, k_{y2}, k_{z1}, k_{z2}, k_{z3}$ are defined for different foundation regions. Likewise, six (unknown) parameters, namely $c_x, c_{y1}, c_{y2}, c_{z1}, c_{z2}, c_{z3}$, are used to define the damping.

The Bayesian estimation is carried out in two steps: In the first step, the foundation-level motions are used as uniform base input excitations to estimate the model parameters characterizing the structural model regardless of the soil subsystem. In this step, the torsional and rocking components of the foundation-level motion are also assumed as unknown input motions and estimated jointly with structural model parameters. In the second step, the identified structural model parameters are fixed at their mean estimates obtained from the first step, and the

three translational components of the FIM and parameters characterizing the soil-structure model and overall Rayleigh damping are estimated jointly. The second step comprises an output-only FE model updating.
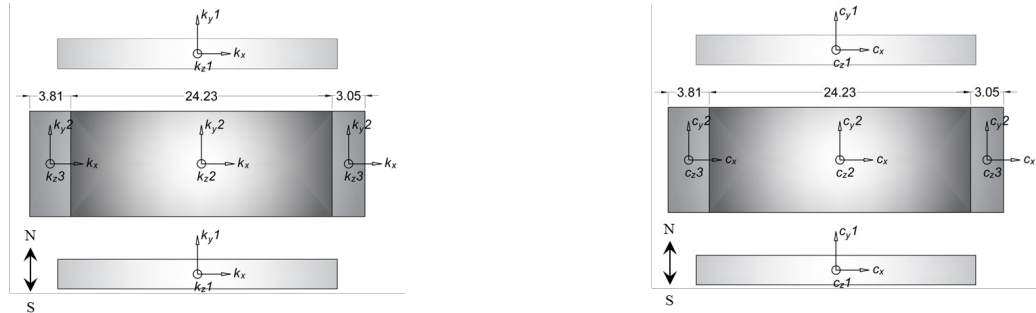
Figure 6. Foundation plan of the Millikan Library with six unknown subgrade stiffness (left) and damping (right) parameters.

Table 2 shows the initial and final estimate of the six model parameters along with their final estimated coefficient of variation (COV) at the end of the first step. The small values of the COVs denote that the identified values are reliable.

Table 2. Initial and final estimates of the model parameters along with the estimated coefficient of variation (COV).

| Parameter ID	Description	Initial	Estimated	COV
1	Elastic modulus of brace elements (E_{Clad})	$20\ GPa$	$16.7\ GPa$	2.6%
2	Effective Elastic modulus of column/wall concrete at basement and 1st story ($E_{W\&C1}$)	$17.3\ GPa$	$33.6\ GPa$	1.0%
3	Effective Elastic modulus of column/wall concrete at 2nd story to Roof ($E_{W\&C2}$)	$17.3\ GPa$	$23.9\ GPa$	0.8%
4	Mass-proportional Rayleigh damping coefficient (a)	0.4	0.36	4.1%
5	Stiffness-proportional Rayleigh damping coefficient (b)	5.3×10^{-3}	1.4×10^{-3}	1.9%
6	Distributed floor mass on 1st to Roof floors (m)	$250\ kg/m^2$	$278.5\ kg/m^2$	2.0%

In the second step, we fix above mentioned six parameters in their identified values and identify 12 soil subsystem's parameters, the elastic modulus of the foundation (E_{Found}), and three translational FIMs. However, the identifiability study showed that not all 12 parameters are identifiable by using available instrumentation layout and stiffness and damping parameters in x and y directions must be reduced to one [27]. Also, a new set of Rayleigh damping parameters are identified, as those parameters identified in the first step represent a fixed-base system. The identified parameters of the soil subsystem are shown in **Table 3**. To evaluate how well the updated model prediction matches the measurement records, **Figure 7** compares the measured acceleration response time histories at the selected measurement channels with those estimated using the final estimates of the model parameters and FIMs. This figure shows a remarkable match between the estimated and measured acceleration responses.

Finally, **Figure 8** shows the time history of the posterior mean and standard deviation (SD) of the three components of the FIM.

Table 3. Initial and final estimates of the soil-structure parameters along with estimated COVs. Stiffness and damping parameters are in MN/m^3 and KNs/m^3, respectively, and E_{Found} is in GPa.

	k_x	k_{y1}	k_{z1}	k_{z2}	k_{z3}	c_x	c_{y1}	c_{z1}	a	b	E_{Found}
Initial	65	40	20	22.5	37.5	700	700	1000	0.36	1.4×10^{-3}	7.5
Estimated	158.7	73.4	139.0	93.5	111.9	685	1748	4126	0.01	1.0×10^{-3}	32.5
COV	5.4%	4.4%	1.0%	4.1%	2.9%	16.8%	3.3%	1.2%	55.4%	3.3%	3.6%

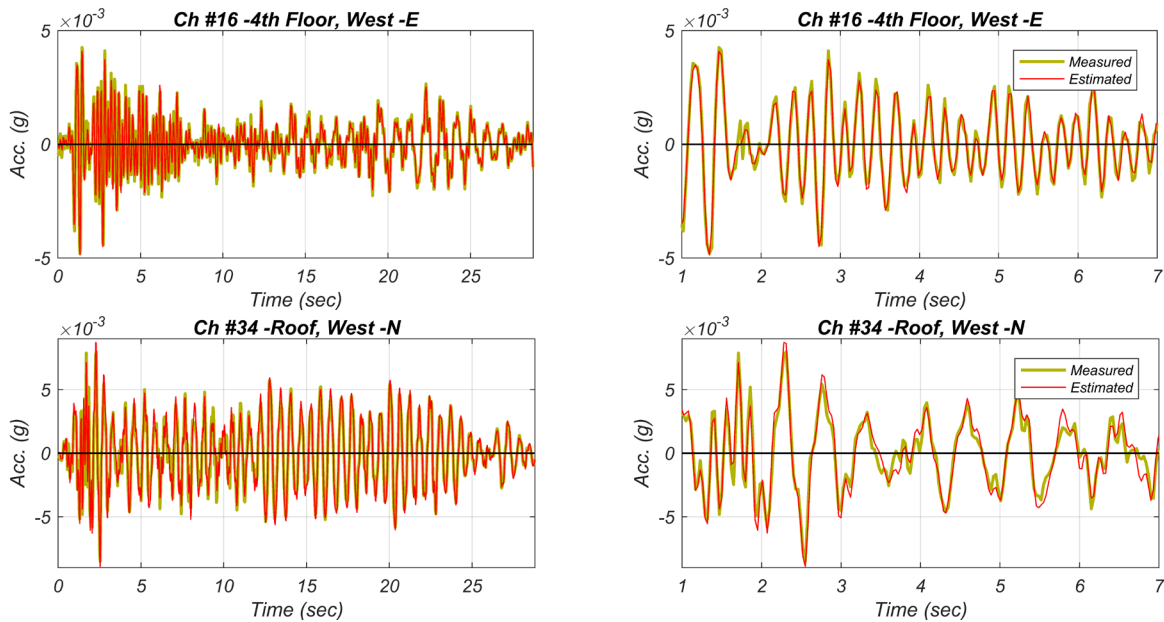**Figure 7.** Comparison of the measured predicted responses. The right-hand-side plots magnify the response time history between 1-7 sec.
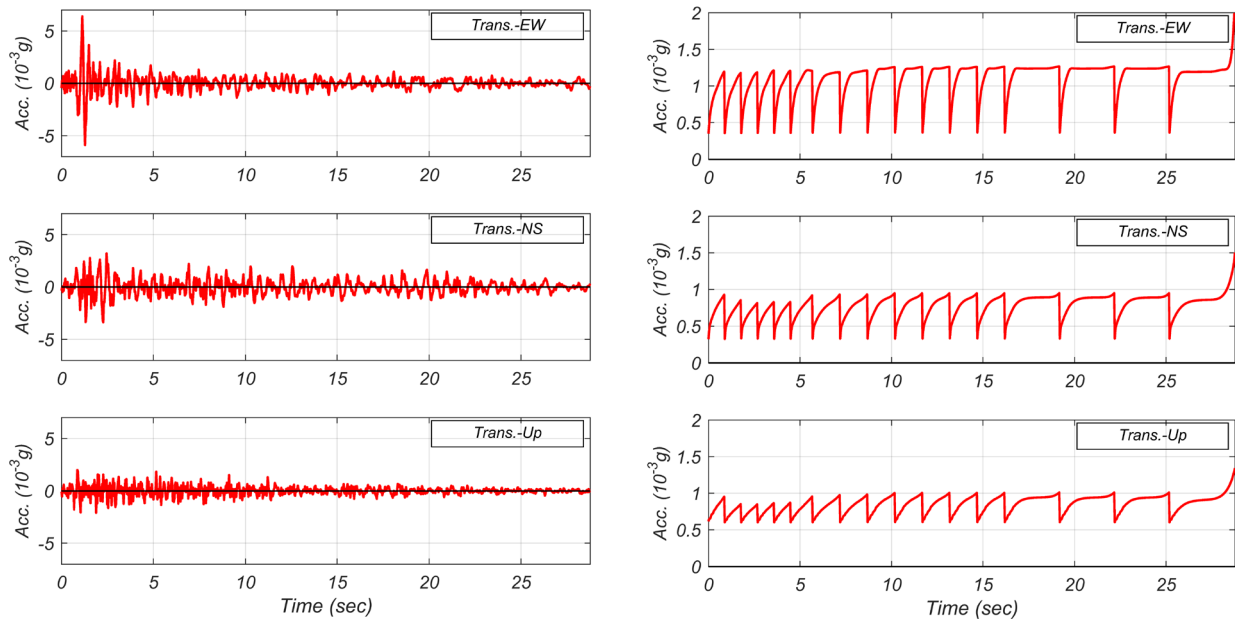
Figure 8. Estimated FIMs (left) and their standard deviation (right).

57

Cross-Relation Method

The model-based method presented in the previous section works very well and provides us with promising results along with the estimation uncertainties. However, it needs an initial numerical model free from modeling uncertainty, which may not available. Also, the method needs relatively dense instrumentation, and more importantly it is computationally very demanding because each time sample of the input motions is treated as an uncertain parameter. The authors have recently proposed a data-driven solution ([28], [29]) for site effect identification which works based on the Cross-Relation (CR) idea [34]. The method can be adopted to solve the present output-only system identification and FIM estimation as follows.

Assume that two adjacent buildings are excited under a similar input acceleration s. The response of Buildings 1 and 2 can be written as a linear convolution of this input motion and each building's IRF as

$$x_1 \cong h_1 * s \tag{1}$$

$$x_2 \cong h_2 * s \tag{2}$$

where h_1 and h_2 are buildings' IRFs, respectively. Convolving both sides of Eqs. (1) and (2) by h_2 and h_1, respectively, we have

$$x_1 * h_2 - x_2 * h_1 = 0 \tag{3}$$

As seen, the equation above is a system of N equations (N is the total number of samples) with at most $2L$ unknown where L is the length of the longer IRF. So, provided that $N \geq 2L$, IRFs can be theoretically estimated. Once IRFs are estimated, unknown FIM can be backcalculated through the deconvolution.

The CR solution is simple and practical for CSMIP instrumented buildings, as our survey shows that even by imposing limiting criteria like distance less than 1 km (see, e.g., [35]) and similarity of the soil types, there are 29 and 23 candidate sets in Southern and Northern California, respectively, as shown in **Figure 9**.

Figure 9. Potential candidate sets for CR application in Southern (left) and Northern California (right).

While the CR method seems doable, there are some major challenges. The length of the IRFs for typical structures is not short which makes the estimation problem severely ill-conditioned. Also, the length is not a priori known. The CR method work based on the assumption that systems (here buildings) are dissimilar. So, if there is any similarity between these two adjacent buildings cannot be identified. Specifically, systems are unidentifiable at common zeros. To show this, let's assume that z-Transform [36] of IRFs can be factorized as $H_1(z) = (z - z_0)\bar{H}_1(z)$ and $H_2(z) = (z - z_0)\bar{H}_2(z)$. Then, Eq. (3) can be written as

$$X_1(z)(z - z_0)\bar{H}_2(z) - X_2(z) * (z - z_0)\bar{H}_1(z) = 0 \tag{4}$$

Obviously, systems are not identifiable at the common zero z_0. This issue is a critical issue when we notice that the length of IRFs is long and zeros of random polynomials cluster uniformly near the unit circles [37], which means lots of common zeros. In addition to these major problems, some minor issues like measurement noise, input excitation spatial variability, number of adjacent buildings, etc. must be addressed. In what follows, we propose various versions of the CR method whose applications depend on the complexity of the problem and the needed accuracy and reliability.

CR Method using Rational Transfer functions

Adding independent white Gaussian measurement noises $\boldsymbol{v}_1$ and $\boldsymbol{v}_2$ to Eqs. (1) and (2), Eq. (3) is rewritten as

$$\boldsymbol{x}_i * \boldsymbol{h}_j - \boldsymbol{x}_j * \boldsymbol{h}_i = \tilde{\boldsymbol{v}}_{ij} \tag{5}$$

where we used indices i and j, respectively, instead of 1 and 2 to be able to extend the solution to many buildings as will be discussed later. Also, $\tilde{\boldsymbol{v}}_{ij} = \boldsymbol{h}_j * \boldsymbol{v}_i - \boldsymbol{h}_i * \boldsymbol{v}_j$. Linear discrete-time convolution of Eq. (5) can be converted to multiplication by using the z-Transform as in

$$X_i(z^{-1}) H_j(z^{-1}) - X_j(z^{-1}) H_i(z^{-1}) = V_{ij}(z^{-1}) \tag{6}$$

In Eq. (6), H_i and H_j are z-Transforms of IRFs and are referred to as Transfer Functions (TFs) or System Functions [38], while X_i, X_j, and V_{ij} are the z-Transforms of $\boldsymbol{x}_i$, $\boldsymbol{x}_j$, and $\tilde{\boldsymbol{v}}_{ij}$, respectively. Theoretically, the IRFs have infinite length, but they can be recast as Infinite Impulse Response (IIR) filters by representing their corresponding TFs in the format of the ratio of complex polynomials

$$H(z^{-1}) = \frac{b_0 + b_1 z^{-1} + \cdots + b_{n_b} z^{-n_b}}{1 + a_1 z^{-1} + \cdots + a_{n_a} z^{-n_a}} \tag{7}$$

where the numerator $N(z^{-1}) = b_0 + b_1 z^{-1} + \cdots + b_{n_b} z^{-n_b}$ is an n_b-order polynomial with $n_b + 1$ parameters b_k $(k = 0, \dots, n_b)$ representing a Moving Average (MA) part, and the denominator $D(z^{-1}) = 1 + a_1 z^{-1} + \cdots + a_{n_a} z^{-n_a}$ is an n_a-order polynomial with n_a parameters a_k $(k = 1, \dots, n_a)$ representing an Autoregressive (AR) part. As seen, while the IRFs in their original MA form are infinitely long, their IIR representations have a finite length in both the numerator and the denominator. Using Eq. (7), the CR defined in Eq. (6) can be expressed as

$$X_i N_j D_i - X_j N_i D_j = V_{ij} D_i D_j, \tag{8}$$

where we dropped (z^{-1}) for simplicity. Eq. (8) can be further restated in a simplified form as

$$X_i G_{ij} - X_j G_{ji} = E_{i,j} \tag{9}$$

where $G_{ij} = N_j D_i$ and $G_{ji} = N_i D_j$ are two Finite Impulse Response (FIR) filters with orders $n_{b_j} + n_{a_i}$ and $n_{a_j} + n_{b_i}$, respectively, and $E_{i,j}$ is the noise residual, which must be perfectly zero in an ideal scenario.

If we now define $L_{ij} = n_{b_j} + n_{a_i} + 1$ and $L_{ji} = n_{a_j} + n_{b_i} + 1$, then it is trivial to show that $X_i G_{ij}$, for example, would be an $(L_{ij} + N - 2)$th-order polynomial in z^{-1}. Using the z-Transform definition, $X_i G_{ij}$ can be calculated as

$$X_i G_{ij} = \begin{bmatrix} x_i[0] & 0 & \cdots & 0 \\ \vdots & \cdots & \cdots & \vdots \\ x_i[L_{ij}-2] & x_i[L_{ij}-3] & \cdots & 0 \\ x_i[L_{ij}-1] & x_i[L_{ij}-2] & \cdots & x_i[0] \\ x_i[L_{ij}] & x_i[L_{ij}-1] & \cdots & x_i[1] \\ \vdots & \vdots & \ddots & \vdots \\ x_i[N-1] & x_i[N-2] & \cdots & x_i[N-L_{ij}] \\ 0 & x_i[N-1] & \cdots & x_i[N-L_{ij}+1] \\ \vdots & \cdots & \ddots & \vdots \\ 0 & \cdots & 0 & x_i[N-1] \end{bmatrix} \begin{bmatrix} G_{ij}[0] \\ G_{ij}[1] \\ \vdots \\ G_{ij}[L_{ij}-1] \end{bmatrix} \tag{10}$$

where $G_{ij}(z^{-1}) = G_{ij}[0] + G_{ij}[1]z^{-1} + \cdots + G_{ij}[L_{ij}-1]z^{-(L_{ij}-1)}$. A similar matrix representation can be written for $X_j G_{ji}$ as well. It is trivial to show that to satisfy Eq. (9), both $X_i G_{ij}$ and $X_j G_{ji}$ must have the same length. So, we can discard a few terms at the beginning and the end of signals $X_i G_{ij}$ and $X_j G_{ji}$, and rewrite Eq. (9) as

$$[\mathbf{X}_{ij} \quad -\mathbf{X}_{ji}]\begin{bmatrix} \mathbf{G}_{ij} \\ \mathbf{G}_{ji} \end{bmatrix} = E_{i,j} \tag{11}$$

where

$$\mathbf{X}_{ij} = \begin{bmatrix} x_i[n_0^{i,j}] & x_i[n_0^{i,j}-1] & \cdots & x_i[n_0^{i,j}-L_{ij}+1] \\ \vdots & \vdots & \ddots & \vdots \\ x_i[n_0^{i,j}+W^{i,j}-1] & x_i[n_0^{i,j}+W^{i,j}-2] & \cdots & x_i[n_0^{i,j}+W^{i,j}-L_{ij}] \end{bmatrix}_{W^{i,j} \times L_{ij}} \tag{12}$$

$$\mathbf{X}_{ji} = \begin{bmatrix} x_j[n_0^{i,j}] & x_j[n_0^{i,j}-1] & \cdots & x_j[n_0^{i,j}-L_{ji}+1] \\ \vdots & \vdots & \ddots & \vdots \\ x_j[n_0^{i,j}+W^{i,j}-1] & x_j[n_0^{i,j}+W^{i,j}-2] & \cdots & x_j[n_0^{i,j}+W^{i,j}-L_{ji}] \end{bmatrix}_{W^{i,j} \times L_{ji}} \tag{13}$$

and $\boldsymbol{G}_{ij} = [G_{ij}[0] \quad G_{ij}[1] \quad \cdots \quad G_{ij}[L_{ij}-1]]^T$ and $\boldsymbol{G}_{ji} = [G_{ji}[0] \quad G_{ji}[1] \quad \cdots \quad G_{ji}[L_{ji}-1]]^T$. The term $\boldsymbol{E}_{i,j}$ is an $(L_{ij} + L_{ji}) \times 1$ vector containing noise errors. Start time $(n_0^{i,j})$ and time window $(W^{i,j})$ can be chosen any value greater than $\max(L_{ij}, L_{ji})$ and less than $W^{i,j} \leq N - 1 - n_0^{i,j}$, respectively.

Such CR expressions like Eq. (11) can be written between any pair of buildings. That is, we have a total of $n_p = P(P-1)/2$ CRs that can be stated as

$$\mathbf{X}\,\boldsymbol{G} = \boldsymbol{E} \tag{14}$$

where

$$\mathbf{X} = \begin{bmatrix} \mathbf{X}_{12} & -\mathbf{X}_{21} & & & \\ & & \mathbf{X}_{13} & -\mathbf{X}_{31} & \\ & & & \ddots & \\ & & & & \mathbf{X}_{(P-1)P} & \mathbf{X}_{P(P-1)} \end{bmatrix} \tag{15}$$

$$\boldsymbol{G} = \left[\boldsymbol{G}_{12}{}^T, \boldsymbol{G}_{21}{}^T, \boldsymbol{G}_{13}{}^T, \boldsymbol{G}_{31}{}^T, \dots, \boldsymbol{G}_{(P-1)P}{}^T, \boldsymbol{G}_{P(P-1)}{}^T\right]^T \tag{16}$$

$$\boldsymbol{E} = \left[\boldsymbol{E}_{1,2}{}^T \quad \boldsymbol{E}_{1,3}{}^T \quad \cdots \quad \boldsymbol{E}_{(P-1),P}{}^T\right]^T \tag{17}$$

In Eq. (14), matrix $\mathbf{X}$ is constructed by the building's response signals available through measurement, while vector $\boldsymbol{G}$ is composed of a_k and b_k coefficients of TFs of all buildings which are unknown and are going to be identified. Vector $\boldsymbol{E}$ is a noise vector. For simplicity, we select an equal time-window length W for all pairs, so matrix $\mathbf{X}$ is an $(n_p \times W) \times \left(\sum_{i=1}^{P}\sum_{j=i+1}^{P}(L_{ij} + L_{ji})\right)$ and set the start time index equal to $n_0 = \max(L_{ij})$ for $i,j = 1:P$ and $i \neq j$.

To solve the Eq. (14) we exactly use the Bayesian estimation introduced in Appendix A in which the Eq. (14) plays the role of the observation equation and $\boldsymbol{\theta}$ contains all unknown a_k and b_k coefficients of TFs of all buildings.

Deconvolution

Once the buildings are identified, it may look trivial to recover input excitations through deconvolution. That is,

$$S(z^{-1}) = \frac{X_i(z^{-1})}{H_i(z^{-1})} \tag{18}$$

and then

$$s[n] = \frac{1}{2\pi\sqrt{-1}} \oint S(z^{-1})\, z^{n-1} dz \tag{19}$$

where $n = t/\Delta t$ is discrete-time index and varies from 0 to $N-1$ with t and Δt denoting the time and sampling time interval, respectively. However, this inversion problem is only possible

if the system $1/H_i(z^{-1})$ is stable[2]. To satisfy this condition, the system $H_i(z^{-1})$ must not have any zeros outside of the unit circle, or in other words, it must be minimum phase [38], while it is most probably non-minimum phase.

A conventional way to calculate the inverse of a non-minimum phase system is through the Least-Squares Error (LSE). According to Eq. (1), we need to design an inverse FIR filter, $\boldsymbol{g}_{i_{n_{g_i} \times 1}}$, which satisfies

$$\boldsymbol{d} = \boldsymbol{h}_i * \boldsymbol{g}_i \tag{20}$$

where $\boldsymbol{d}_{\left(n_{h_i} + n_{g_i} - 1\right) \times 1} = \begin{bmatrix} 1 & 0 & \cdots & 0 \end{bmatrix}^T$. Convolving this filter with $x_i[n]$ results in recovering input motion. The Eq. (20) can be expressed in a matrix form as

$$\mathbf{H}_i \, \boldsymbol{g}_i = \boldsymbol{d} \tag{21}$$

with

$$\mathbf{H}_{i_{\left(n_{h_i} + n_{g_i} - 1\right) \times n_{g_i}}} = \begin{bmatrix} h_i[0] & & & \\ h_i[1] & h_i[0] & & \\ & h_i[1] & \ddots & \\ h_i[n_{h_i} - 1] & & & h_i[0] \\ & h_i[n_{h_i} - 1] & & h_i[1] \\ & & \ddots & \\ & & & h_i[n_{h_i} - 1] \end{bmatrix}, \tag{22}$$

As the number of the columns of the matrix $\mathbf{H}_i$ is less than that of the rows, the coefficients of the FIR filter are computed in an approximate LSE way as $\boldsymbol{g}_i = \mathbf{H}_i^\dagger \boldsymbol{d}$ where † is the Moore-Penrose pseudo-inverse operator. Therefore, it is impossible to realize the exact inverse of a linear FIR system using this method. Moreover, because $\boldsymbol{g}_i$ is non-minimum phase the error energy $(\boldsymbol{d} - \mathbf{H}_i \, \boldsymbol{g}_i)^T (\boldsymbol{d} - \mathbf{H}_i \, \boldsymbol{g}_i)$ does not converge to zero [39].

Fortunately, as the input excitation is measured by at least another building, there is a possibility to exactly recover it. For example, if we can identify inverse filters $\boldsymbol{g}_i$ and $\boldsymbol{g}_j$ satisfying the following equation

$$\boldsymbol{d} = \boldsymbol{h}_i * \boldsymbol{g}_i + \boldsymbol{h}_j * \boldsymbol{g}_j \tag{23}$$

we can recover common input excitation through

$$\boldsymbol{s} = \boldsymbol{x}_i * \boldsymbol{g}_i + \boldsymbol{x}_j * \boldsymbol{g}_j \tag{24}$$

To identify these inverse filters, let's set $n_{g_i} = n_{h_j} - 1$ and $n_{g_j} = n_{h_i} - 1$. Then, we have

---

[2] Bounded-Input Bounded-Output (BIBO) condition.

$$[\mathbf{H}_i \quad \mathbf{H}_j] \begin{bmatrix} \boldsymbol{g}_i \\ \boldsymbol{g}_j \end{bmatrix} = \boldsymbol{d} \tag{25}$$

in which matrix $[\mathbf{H}_i \quad \mathbf{H}_j]$ is square and the exact solution can be recovered through matrix inversion [39]. However, the solution is only available if these two buildings do not share common zeros, which is not the case in our problem as discussed before. Herein, we propose a modification to the deconvolution to reduce the chance of having common zeros [40].

Time convolution of the Eq. (1) can be expressed in the time-frequency domain using Short-Time-Fourier-Transform (STFT) as follows [41]

$$\underline{x}_i[p, k] = \sum_{k'=0}^{N_w-1} \sum_{p'=0}^{Q_i-1} \underline{s}[p - p', k'] \underline{h}_i[p', k, k'] \tag{26}$$

where underbar represents STFT representation, N_w is the number of frequencies, and Q_i is the length of IRF in STFT domain. The IRF in the STFT domain ($\underline{h}_i[p', k, k']$) is called a cross-band filter. Neglecting effects of the neighbor frequencies, we can approximate response at each frequency using its band-to-band version ($\underline{\tilde{h}}_i[p', k]$) which is Convolutive Transfer Function (CTF) as

$$\underline{x}_i[p, k] \approx \sum_{p'=0}^{Q_i-1} \underline{s}[p - p', k] \underline{\tilde{h}}_i[p', k] \tag{27}$$

which is a convolution at each frequency index of k as

$$\underline{\boldsymbol{x}}_i \approx \underline{\tilde{\boldsymbol{h}}}_i * \underline{\boldsymbol{s}} \tag{28}$$

which is similar to the time convolution. So, we can follow the same approach described above to recover $\underline{\boldsymbol{s}}$ at each frequency and then transform the solution to the time domain through inverse STFT. That is, we are looking for $\boldsymbol{g}_i$s filters which satisfy the following relationship

$$\boldsymbol{d} = \sum_{1}^{n_B} \underline{\tilde{\boldsymbol{h}}}_i * \underline{\boldsymbol{g}}_i \tag{29}$$

where n_B is the number of buildings. Now a similar solution introduced in Eq. (25) can be used to estimate inverse CTFs and consequently recover input excitation. Contrary to the time domain solution, the CTFs have very short length and the chance of having common zero among the buildings significantly reduces.

Verification

To verify the method, the response of four shear buildings with a various number of stories from 3 to 7 are generated under Elcentro ground acceleration. **Figure 10** shows the recorded time histories and the exact Transfer Functions (green curves). We carried out the proposed TF-based CR method by starting at those red initial TFs. The final results are shown in blue and black. The blue curves show the TFs constructed by mean values of the coefficients,

while the black curves are the means of the TFs. As seen, the estimated TFs (black and blues curves) are perfectly matched to the exact TFs except very high-frequency region. Note that the response signals are polluted with random noises with Root-Mean-Squares (RMS) equal to 5% of the RMS of the noise-free signals. As the solution is obtained through a stochastic filtering approach, the variance of the estimated results is also shown in **Figure 10** through mean ±1 standard deviation. As seen, the estimated results are highly reliable. We then employed the proposed STFT deconvolution solution to recover common input motion. A comparison between the recovered one and the exact one is shown in **Figure 11**. As seen, the input motion is almost identical to the exact time history.
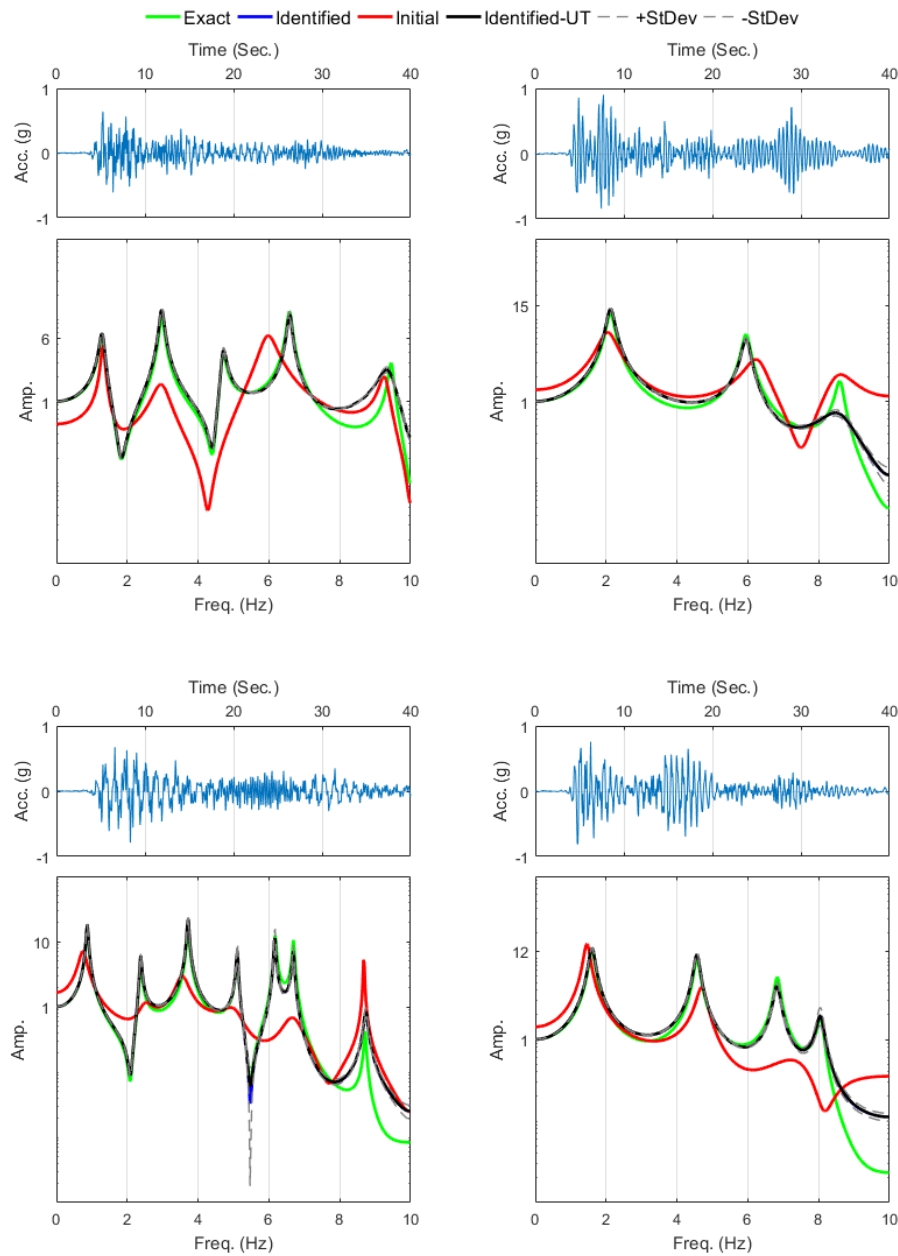
Figure 10. Results of the verification study.
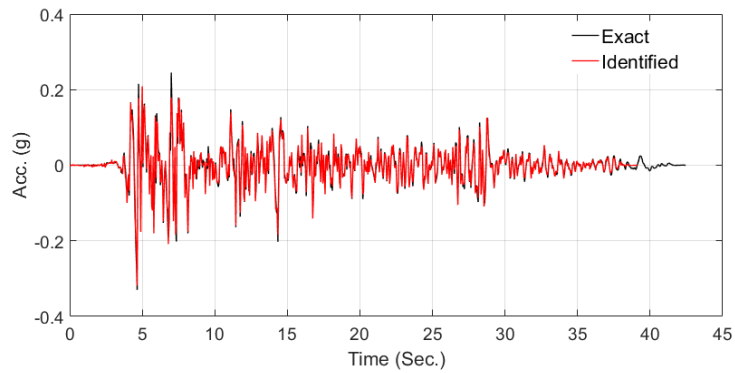
Figure 11. Comparison between exact and recovered input motion.

Validation

To validate the method, data recorded on two neighboring buildings in downtown San Francisco (CSMIP stations #58411 and #58412 are used (see **Figure 12**). Data recorded in the East-West direction during the recent 2014 South Napa earthquake is studied here. **Figure 13** displays a comparison between the recorded signals at the foundation levels of these two buildings, both of which are assumed here to be input motions. As seen, these two signals are quite similar and have a correlation coefficient [42] >76%, and as such, they satisfy the major assumption of the proposed method.
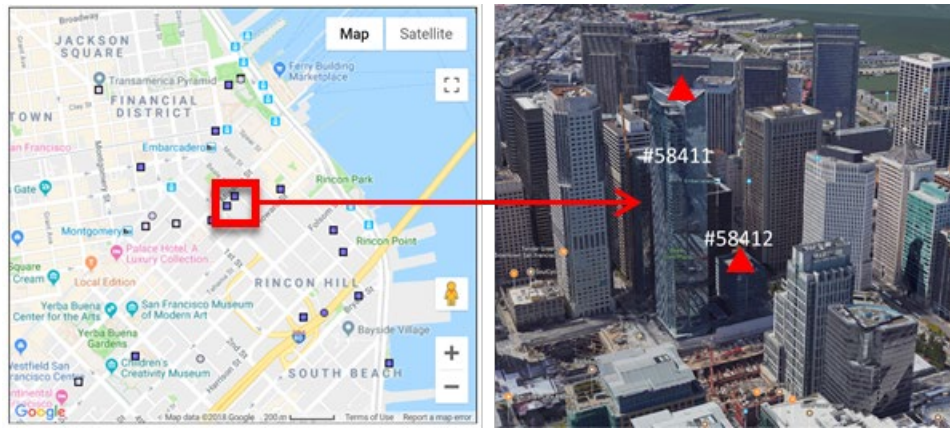
Figure 12. Chosen buildings for the validation study.
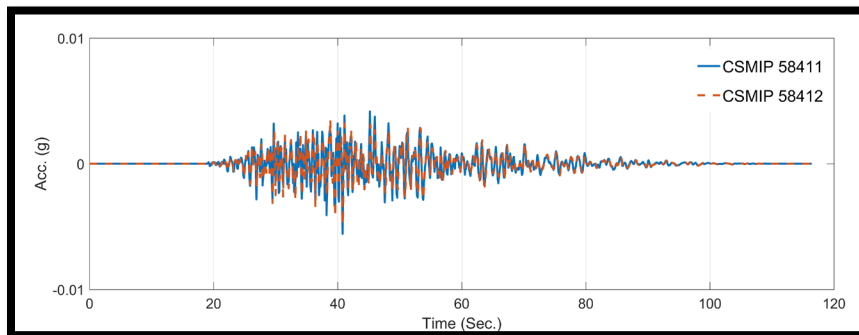
Figure 13. 76% similarity between recorded signals at the foundations of two buildings.

To carry out the identification process, we use signals recorded at the roof level—i.e., channel #29 for CSMIP58411, and the average of channels #11 and #12 for CSMIP58412, which are located at the two opposing ends of roof floor. We only use 50 seconds of the intense portion of the signals, because the level of vibration is too low during other times. **Figure 14** shows again the exact TFs in green which are empirically calculated using input and output signals, the initial TFs in red, and the identified TFs in black and blue. As seen, the final results are quite matched to the exact ones with a negligible variation.

Finally, we extracted common input excitation which is compared to the measured foundation responses (assumed here as exact input motions) in **Figure 15**. It is quite interesting to note that there is almost a 76% similarity between the recovered input motion and each of these foundation responses, showing the method works very well.
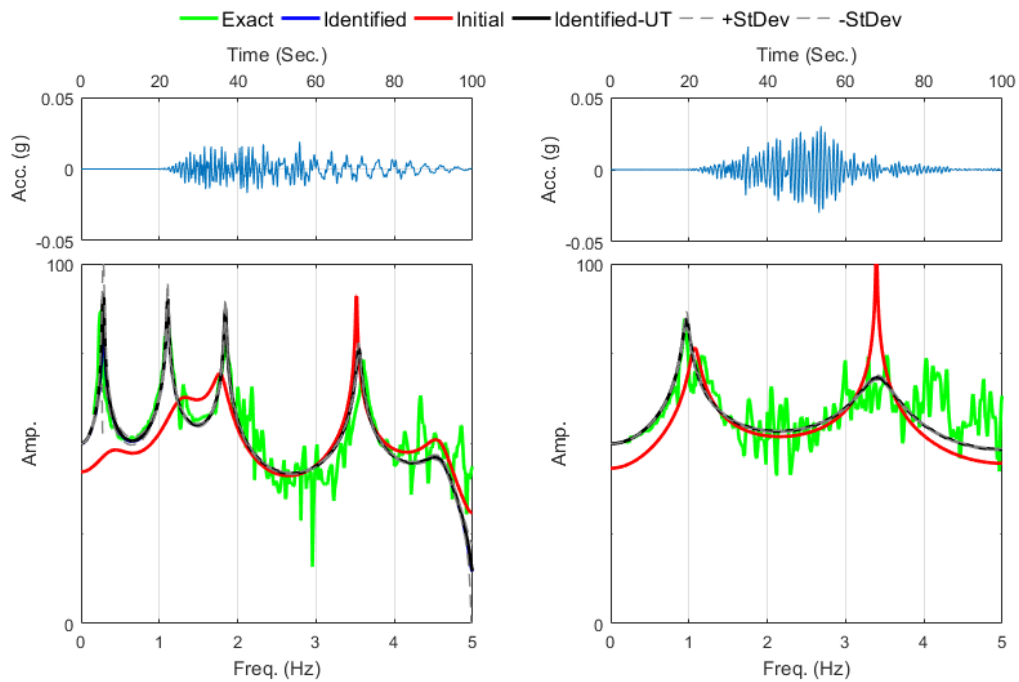
Figure 14. Results of the validation study.
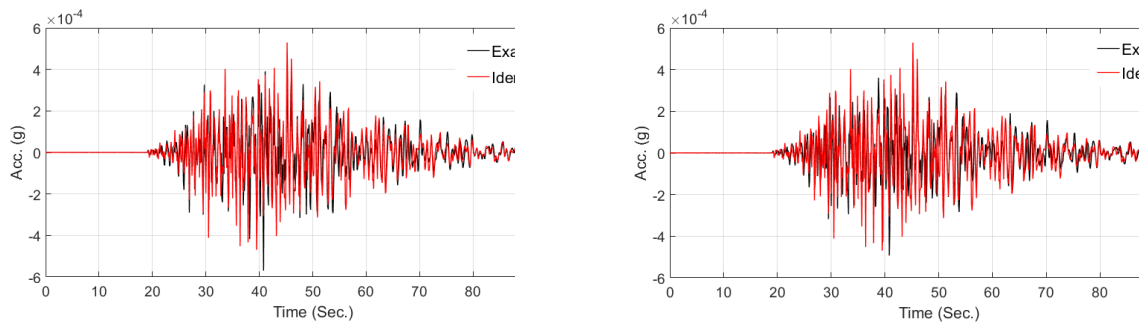
Figure 15. Comparison between recovered input motion and recorded foundation responses.

Modal-Based CR Method

The initial guess in the proposed CR method is sometimes important because the problem is not convex and could have various local solutions. To make the method more robust we replaced the Transfer Function formula with an IRF constructed using superposition of analytical modal IRFs as shown in the following equation

$$h[k\Delta t] = \Delta t \sum_{m=1}^{n_m} \frac{\beta_m \varphi_{r,m}}{\omega_{d_m}} e^{-\xi_m \omega_{n_m} k\Delta t} \left[\left(\omega_{d_m}^2 - \xi_m^2 \omega_{n_m}^2 \right) \sin(\omega_{d_m} k\Delta t) \right. \\ \left. + 2\xi_m \omega_{n_m} \cos(\omega_{d_m} k\Delta t) \right] \tag{30}$$

where ω_{n_m}, ξ_m, β_m, and $\varphi_{r,m}$ are m-th mode natural frequency, damping ratio, contribution factor, and modal deformation, respectively, and $\omega_{d_m} = \omega_{n_m}\sqrt{1 - \xi_m^2}$. By using this closed-form solution, we now have parameters with physical meaning. So, we can set initial point more accurately. More importantly, we can put constraints on the parameters. For example, we know that natural frequencies and damping ratios are positive. Or natural frequencies must be increasing values. Also, we can limit the frequency of interest according to the frequency content of the recorded responses.

Verification

To verify the modal-based version of the CR method, we simulated the response of a 5-story and a 3-story shear buildings whose modal properties are reported in **Table 4**. The responses ate the roof were polluted with random noises to have signals with Signal-to-Noise Ratio (SNR) of 40. Before carrying out the identification, signals were filtered by a low-pass filter with cut-off frequency of 15 Hz, as there is no energy above this frequency in the 3-story response.

Table 4. Analytical modal properties.

	5-Story Building					3-Story Building		
Modes	1	2	3	4	5	1	2	3
$f_n (Hz)$	2.22	5.12	8.09	11.33	16.27	3.17	8.88	12.83
$\xi_n (\%)$	5.00	4.18	5.00	6.26	8.42	5.00	4.21	5.00
$\varphi_{rn}\beta_n$	1.41	-0.54	0.15	-0.02	0.0006	1.22	-0.28	0.06

To see the accuracy of the identified modal properties or actually systems, simulated responses are compared with the responses predicted by using exact input motion and identified modal properties in **Figure 16**. As seen, both buildings are identified perfectly. The recovered input motion is compared with the exact one in **Figure 17** in the frequency domain. As observed, the recovered input motion is highly accurate.
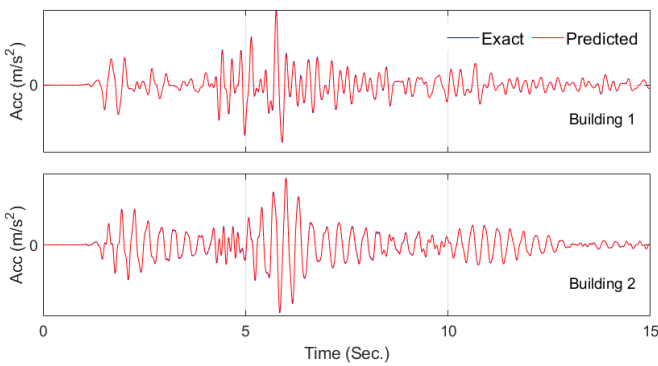
Figure 16. Comparison between simulated responses with predicted responses using identified modal properties and exact input motion.
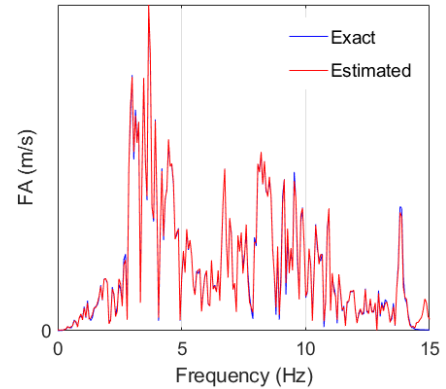
Figure 17. Comparison between exact and recovered input motion in the frequency domain.

Validation

To validate the method, we used a new set of buildings not to be limited to a specific case. **Figure 18** shows these two buildings with less than 500 meters distance. They are oriented in the same direction, so we can use our 2D modal-based CR approach. There are two nearby free-field stations, but one of them is no longer working. We use data recorded in the NS directions of these buildings at the roof level during July 5th 2019 Ridgecrest earthquake. In the first step, we need to specify the frequency range of interest and the probable number of modes. **Figure 19** shows the Fourier spectra of the two signals. As seen, we may be able to recover input motion up to 6 Hz. In this frequency range, the CSMIP24517 building seems to have 2 modes while the other building could have up to 3 modes. Using two response signals, we carried out the estimation and **Figure 20** shows a comparison between the recovered FIM in time and frequency domains with the recorded FFM. As seen, these two signals are very similar, which validates the performance of the proposed method.
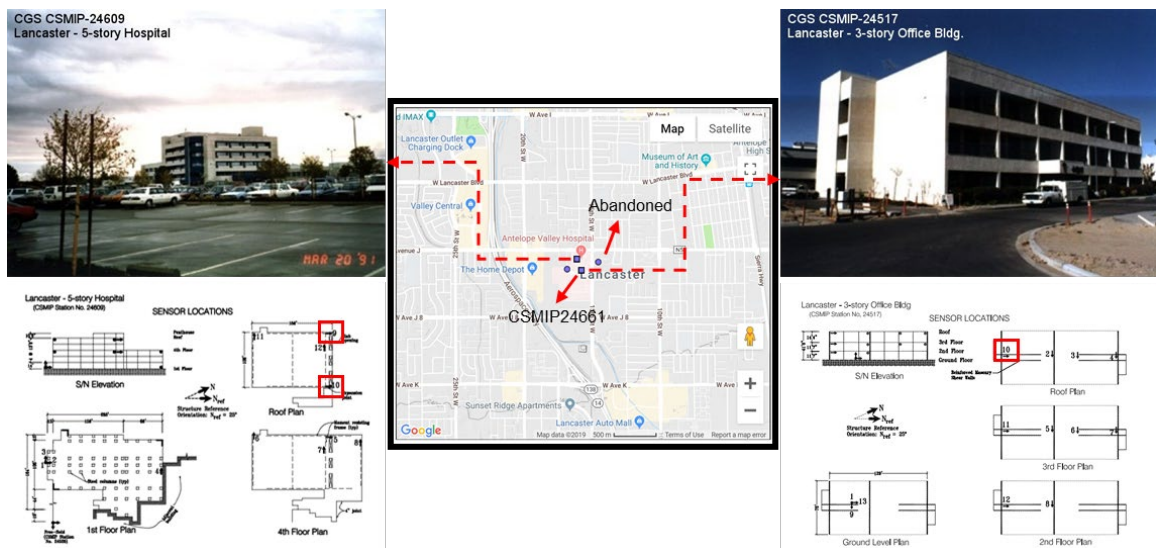
Figure 18. Buildings used for validation of the modal-based CR method.
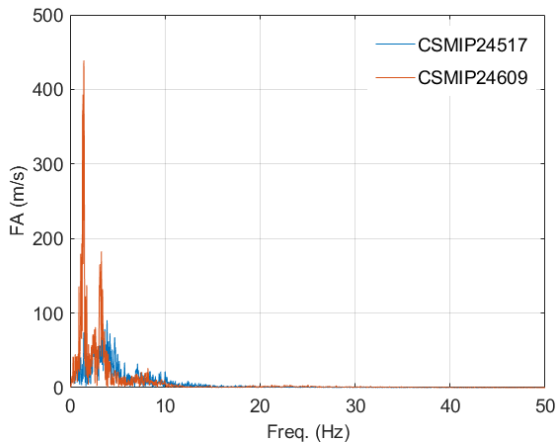
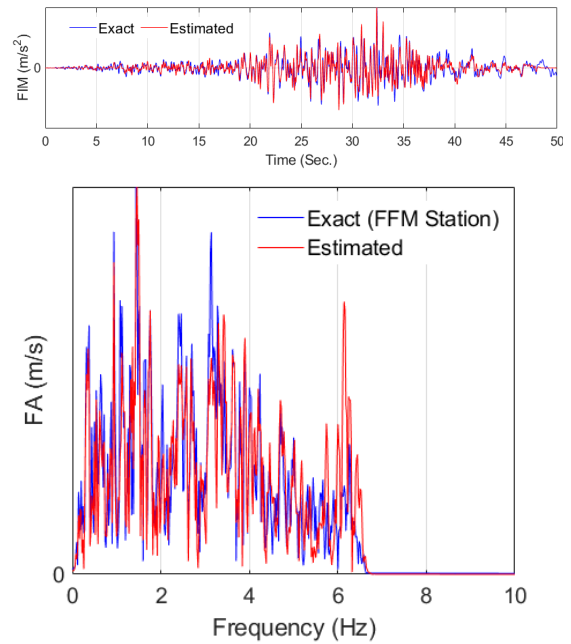**Figure 19.** Fourier spectra of the response of two buildings.

Figure 20. Comparison between identified input motion and recorded FFM in (top) time and (bottom) frequency domain.

Application

As another example, **Figure 21** shows two buildings with almost 500 meters distance. We use their roof response in NS direction recorded in Alumrock 2007 earthquake. Based on the Fourier spectra (not shown here), we consider frequencies below 10 Hz to make sure both signals have enough energy. Five and four modes are considered for CSMIP57355 and CSMIP57356 buildings, respectively.

Figure 21. Buildings used for application study of the modal-based CR method.

As no FFM is recorded, a comparison between identified input motion and recorded foundation responses is shown in **Figure 22** in time and frequency domains. The correlation analysis shows that there is almost 80% similarity between foundation responses and this identified input motion.
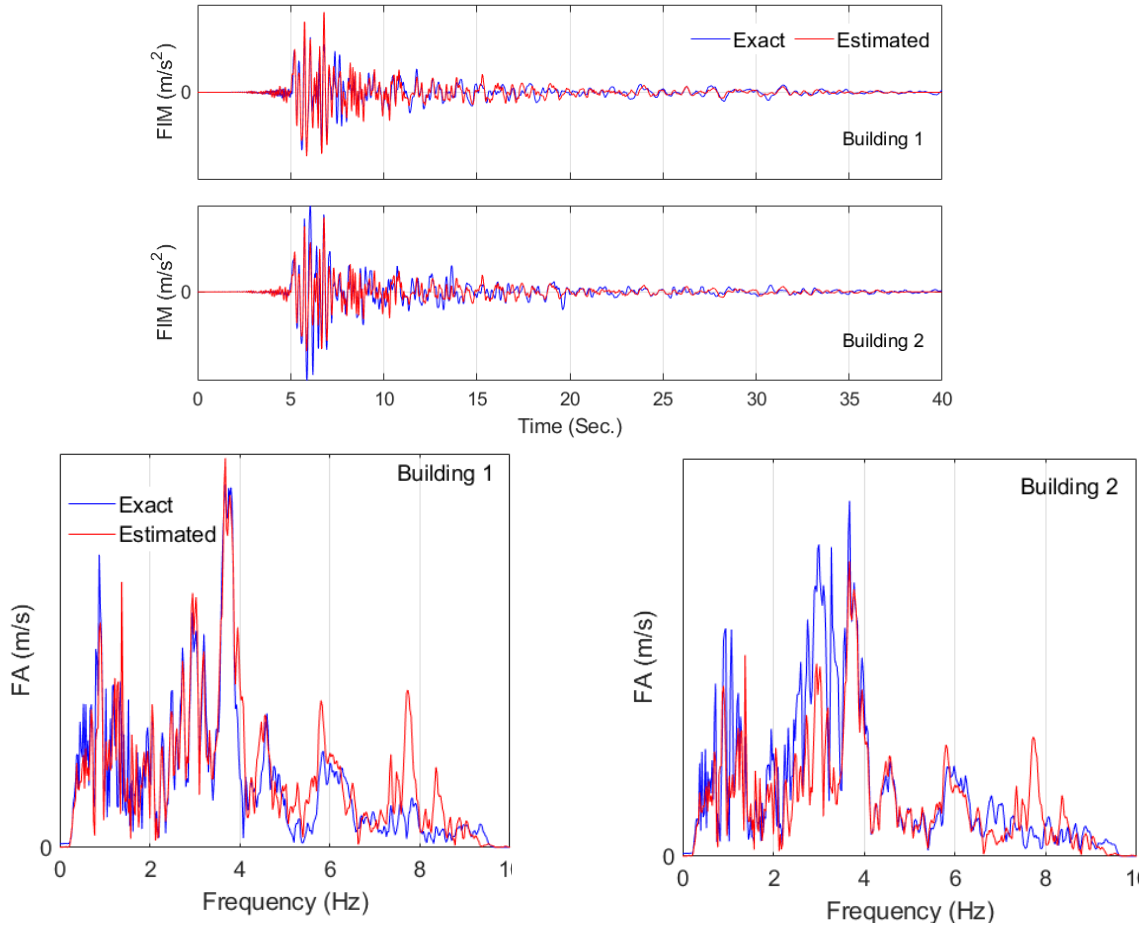
Figure 22. Comparison between recorded foundation responses (blue) and the identified input motion. Building 1 is CSMIP57355 and Building 2 is CSMIP57356.

Model-Based CR Method

In real-life, there is no guarantee to have adjacent buildings aligned in the same direction. So, the CR method should be extended to a more general 3D problem. While it is theoretically possible to use the TF-based or modal-based CR solutions to the 3D cases, the number of parameters to be estimated will be huge. In this section, a hybrid solution is proposed in which model-based Bayesian estimation is combined with the original CR solution to take advantage of benefits of each one [43].

Assume that two buildings are excited under similar bidirectional ground accelerations $\ddot{x}_g$ and $\ddot{y}_g$. Assume that the buildings remain linear-elastic, do not exhibit lateral-torsional

coupling, and are instrumented in their local principal directions x and y as shown in **Figure 23**. The recorded absolute acceleration responses of Building 1 can be written as a linear discrete convolution of the input motions and the building's IRF as

$$\ddot{x}_1 = h_1^x * \left[\ddot{x}_g \cos\alpha + \ddot{y}_g \sin\alpha \right] + v_1, \tag{31}$$

$$\ddot{y}_1 = h_1^y * \left[-\ddot{x}_g \sin\alpha + \ddot{y}_g \cos\alpha \right] + w_1, \tag{32}$$

where h_1^x and h_1^y are the building's IRFs in local x and y directions, respectively; and v_1 and w_1 represent the corresponding measurement noises, which are assumed to be zero-mean, spatially uncorrelated Gaussian white signals.
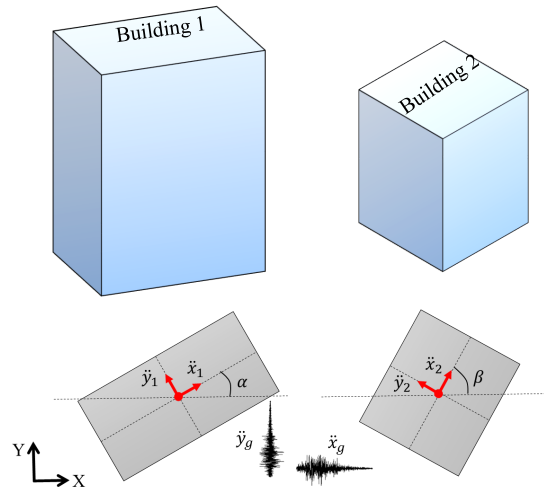
Figure 23. Two adjacent instrumented buildings under a bidirectional seismic excitation.

It is straightforward to combine Eqs. (1) and (2) to come up with equations that contain only a unidirectional earthquake excitation as follows

$$\ddot{x}_1 * h_1^y \sin\alpha + \ddot{y}_1 * h_1^x \cos\alpha = h_1 * \ddot{y}_g + \bar{v}_1 + \bar{w}_1 \tag{33}$$

$$\ddot{x}_1 * h_1^y \cos\alpha - \ddot{y}_1 * h_1^x \sin\alpha = h_1 * \ddot{x}_g + \tilde{v}_1 + \tilde{w}_1, \tag{34}$$

where

$$h_1 = h_1^x * h_1^y, \tag{35}$$

and $\bar{v}_1 = v_1 * h_1^y \sin\alpha$, $\bar{w}_1 = w_1 * h_1^x \cos\alpha$, $\tilde{v}_1 = v_1 * h_1^y \cos\alpha$ and $\tilde{w}_1 = -w_1 * h_1^x \sin\alpha$ are colored noises. Similar equations can be written for the other building by replacing the subscript "1" with "2" and the orientation angle α with β as

$$\ddot{x}_2 * h_2^y \sin\beta + \ddot{y}_2 * h_2^x \cos\beta = h_2 * \ddot{y}_g + \bar{v}_2 + \bar{w}_2 \tag{36}$$

$$\ddot{x}_2 * h_2^y \cos \beta - \ddot{y}_2 * h_2^x \sin \beta = h_2 * \ddot{x}_g + \tilde{v}_2 + \tilde{w}_2, \tag{37}$$

where $h_2 = h_2^x * h_2^y$, $\bar{v}_2 = v_2 * h_2^y \sin \beta$, $\bar{w}_2 = w_2 * h_2^x \cos \beta$, $\tilde{v}_2 = v_2 * h_2^y \cos \beta$, and $\tilde{w}_2 = -w_2 * h_2^x \sin \beta$. Following the CR method, we convolve both sides of Eqs. (33)/(34) and (36)/(37), respectively, by h_2 and h_1, to get

$$\{\ddot{x}_1 * h_1^y \sin \alpha + \ddot{y}_1 * h_1^x \cos \alpha\} * h_2 - \{\ddot{x}_2 * h_2^y \sin \beta + \ddot{y}_2 * h_2^x \cos \beta\} * h_1 = \bar{r} \tag{38}$$

$$\{\ddot{x}_1 * h_1^y \cos \alpha - \ddot{y}_1 * h_1^x \sin \alpha\} * h_2 - \{\ddot{x}_2 * h_2^y \cos \beta - \ddot{y}_2 * h_2^x \sin \beta\} * h_1 = \tilde{r}, \tag{39}$$

where

$$\bar{r} = h_2 * (\bar{v}_1 + \bar{w}_1) - h_1 * (\bar{v}_2 + \bar{w}_2) \tag{40}$$

$$\tilde{r} = h_2 * (\tilde{v}_1 + \tilde{w}_1) - h_1 * (\tilde{v}_2 + \tilde{w}_2). \tag{41}$$

In Eqs. (40) and (41), $\bar{r}$ and $\tilde{r}$ are the remainders that represent the difference between the ideal case of noiseless measurements and the realistic case of noisy measurements. We assume that initial numerical models of the two buildings are available, and our objective is to identify/update their corresponding model parameters. Based on this assumption, Eqs. (3) and (39) can be rewritten as

$$\{y_1\langle\ddot{x}_1 \sin \alpha \rangle + x_1\langle\ddot{y}_1 \cos \alpha\rangle\} * h_2 - \{y_2\langle\ddot{x}_2 \sin \beta\rangle + x_2\langle\ddot{y}_2 \cos \beta\rangle\} * h_1 = \bar{r} \tag{42}$$

$$\{y_1\langle\ddot{x}_1 \cos \alpha \rangle + x_1\langle-\ddot{y}_1 \sin \alpha\rangle\} * h_2 - \{y_2\langle\ddot{x}_2 \cos \beta\rangle + x_2\langle\ddot{y}_2 \sin \beta\rangle\} * h_1 = \tilde{r}, \tag{43}$$

where, for example, $y_1\langle\ddot{x}_1 \sin \alpha \rangle$ stands for the response of Building 1 in its y direction under the input excitation $\ddot{x}_1 \sin \alpha$. The components of Eqs. (42) and (13) can be derived easily. For example, the first part of Eq. (42)—i.e., $\{y_1\langle\ddot{x}_1 \sin \alpha \rangle + x_1\langle\ddot{y}_1 \cos \alpha\rangle\} * h_2$—can be calculated as follows: First, $y_1\langle\ddot{x}_1 \sin \alpha \rangle$ and $x_1\langle\ddot{y}_1 \cos \alpha\rangle$ are estimated. Then, they are used as input excitation in the x-direction of Building 2. The resulting response time history is then used as input excitation for Building 2 in the y-direction, since $h_2 = h_2^x * h_2^y$. The resulting response time history of Building 2 in the y-direction represents the first part of the Eq. (42).

Eqs. (42) and (13) are used as the observation equation within the Bayesian estimation framework where FE models are used to carry out all the predictions and the vector θ parameters of the structural models. Through this hybrid solution, we avoid adding unknown input motions to the updating parameters which substantially reduces computational cost. Also, the Fe models provide the opportunity to reduce number of structural parameters to be estimated.

Deconvolution

Since the two buildings have been fully identified, the common ground motions, $\ddot{x}_g$ and $\ddot{y}_g$, can be recovered from the buildings' responses via deconvolution. Herein, we suggest another deconvolution approach because we have two input motions. Let us assume a noise-free version of the discrete-time convolution in Eq. (31) in the matrix form as

$$\mathbf{A}_{N\times N}\, \boldsymbol{x}_{N\times 1} = \boldsymbol{b}_{N\times 1} \tag{44}$$

with

$$\boldsymbol{b} = [\ddot{x}_1[0] \quad \cdots \quad \ddot{x}_1[N-1]]^T \tag{45}$$

$$\boldsymbol{x} = [\ddot{x}_g[0]\cos\alpha + \ddot{y}_g[0]\sin\alpha \quad \cdots \quad \ddot{x}_g[N-1]\cos\alpha + \ddot{y}_g[N-1]\sin\alpha]^T \tag{46}$$

$$\mathbf{A} = \begin{bmatrix} h_1^x[0] & & & & & \\ h_1^x[1] & h_1^x[0] & & & & \\ \vdots & & \ddots & & & \\ h_1^x[L_1^x-1] & h_1^x[L_1^x-2] & \cdots & h_1^x[0] & & \\ 0 & h_1^x[L_1^x-1] & \ddots & \cdots & h_1^x[0] & \\ \vdots & & & & & \ddots \\ 0 & \cdots & 0 & h_1^x[L_1^x-1] & h_1^x[L_1^x-2] & h_1^x[0] \end{bmatrix}, \tag{47}$$

wherein L_1^x is the effective length of the first building's IRF in its local x-direction. The matrix $\mathbf{A}$ can be ill-conditioned, which means that the vector $\boldsymbol{x}$ cannot be recovered by a matrix inversion [44]. To resolve the ill-conditioning problem of matrix $\mathbf{A}$, we have to replace this matrix with its closest well-conditioned approximation.

Matrix $\mathbf{A}$ has a Toeplitz structure; that is, it has equal elements across the main diagonal and the sub-diagonals parallel to the main diagonal (our systems are causal, so their matrices are lower triangular). It has been shown [45] that for each Toeplitz matrix, a well-conditioned circulant matrix can be found that is asymptotically equivalent to the Toeplitz matrix. To recover the ground motions from each building's response, we invert the asymptotically equivalent circulant matrix corresponding to $\mathbf{A}$. By constructing another similar matrix representation—as Eq. (44) corresponds to Eq. (2)—, we can backcalculate the ground motion vectors $\ddot{x}_g$ and $\ddot{y}_g$ in the global coordinate system as follows

$$\begin{bmatrix} \ddot{x}_g \\ \ddot{y}_g \end{bmatrix} = \begin{bmatrix} \cos\alpha & \sin\alpha \\ -\sin\alpha & \cos\alpha \end{bmatrix}^{-1} \begin{bmatrix} \left(\mathbf{C}_{1,x}^{-1}\,\ddot{x}_1\right)^T \\ \left(\mathbf{C}_{1,y}^{-1}\,\ddot{y}_1\right)^T \end{bmatrix} \tag{48}$$

where $\mathbf{C}_{1,x}$ and $\mathbf{C}_{1,y}$ are the circulant matrices constructed using matrix $\mathbf{A}$ for the local x and y directions [45], respectively. Indeed, the ground motions can also be recovered from responses of the second building, which must be identical in ideal conditions (noise-free and perfect identification results).

Verification

To verify the proposed identification method, we created two three-dimensional building models using SAP2000 [32] as shown in **Figure 24**. The details of these models can be found in [43]. To simulate the seismic responses of the two buildings, we applied the East-West (EW) and the North-South (NS) ground motions recorded at the El Centro station during the 1940 Imperial Valley earthquake in the global X and Y directions, respectively. The roof absolute acceleration response time histories in local x and y directions of the two buildings are used for the

identification. Independent random noises with $0.005 \ m^2/sec^4$ variance (corresponding to signals with $0.7\%g$ root mean square amplitude) is added to the simulated time histories to mimic in noisy measurements.

The proposed system identification is utilized to estimate the unknown parameters, which consist of parameters characterizing the soil-foundation impedance functions and superstructure's parameters as

$$\boldsymbol{\theta} = \left[K_x^1, K_y^1, K_{xx}^1, K_{yy}^1, C_x^1, C_y^1, W_w^1, \alpha_1, \beta_1, K_x^2, K_y^2, K_{xx}^2, K_{yy}^2, C_x^2, C_y^2, W_w^2, \alpha_2, \beta_2 \right]^T \tag{49}$$

where K and C represent soil spring stiffness and soil dashpot viscosity, and superscripts and subscripts denote the building number and the direction, respectively. W_w^1 and W_w^2 are the equivalent widths of the infill walls in Buildings 1 and 2, respectively. Also, parameters α_1, β_1, and α_2, β_2 are mass- and stiffness-proportional Rayleigh damping coefficients of Buildings 1 and 2, respectively. The "true" values of these parameters are provided in **Table 5**.

Table 5. Exact values of the updating parameter candidates.

Building No.	1	2	3	4	5	6	7	8	9
	K_x	K_y	K_{xx}	K_{yy}	C_x	C_y	W_w	α	β
1	(GN/m)	(GN/m)	(GNm)	(GNm)	(MNs/m)	(MNs/m)	(m)	(1/s)	(1000s)
	3.33	3.44	156	283	89	89	0.5	0.90	0.27
Building No.	10	11	12	13	14	15	16	17	18
	K_x	K_y	K_{xx}	K_{yy}	C_x	C_y	W_w	α	β
2	(GN/m)	(GN/m)	(GNm)	(GNm)	(MNs/m)	(MNs/m)	(m)	(1/s)	(1000s)
	1.93	2.05	25	69	30	30	0.5	0.83	0.26
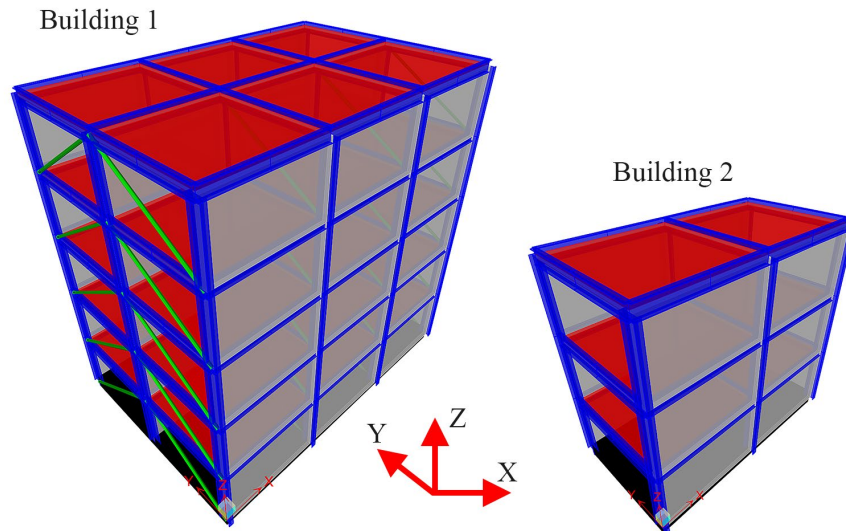
Figure 24. Two adjacent buildings used for verification study.

After carrying out an extensive identifiability study, which is another specific benefit of the proposed method and can be found in the original reference [43], the list of updating parameters was reduced to $\boldsymbol{\theta} = [K_x^1, K_{xx}^1, W_w^1, \alpha_1, K_x^2, K_{xx}^2, W_w^2, \alpha_2]^T$ and other parameters fixed at

their true values. **Table 6** shows the results of the identification along with the estimation Coefficient of Variation (COV). As seen, all unknown parameters, except K_x^2 , are identified with small final errors and near-zero COVs. K_x^2 is the parameter that we added to our updating parameters list despite the fact that it had a relatively strong dependence on W_w^2. As seen in **Table 6**, this dependency results in an inaccurate estimation of W_w^2 as well. The estimated COVs can be used to assess the estimation uncertainties, the higher the COV, the less reliable the estimation is. **Table 6** shows that the COV of K_x^2 is approximately 3 times larger than other parameters, which means that the identified parameter value for K_x^2 is relatively less reliable than other parameters.

Table 6. Identified mean errors and COVs through.

ID No.	1	3	7	8	10	12	16	17
Parameters	K_x^1	K_{xx}^1	W_w^1	α_1	K_x^2	K_{xx}^2	W_w^2	α_2
Final Error (%)	0.96	−0.57	−0.15	3.08	23.29	−2.07	−5.25	1.49
Final COV (%)	0.96	0.55	0.51	1.04	3.90	0.57	0.99	0.92

To evaluate the accuracy of the identification results and the effects of estimation errors, the response of buildings are generated using the identified parameters and using exact ground motions. The responses are compared with the noise-free measured (simulated using exact parameter values) responses in **Figure 25**. As can be seen, the predicted responses match the exact responses. This means that the combined effects of 23% error in K_x^2 and 5% error in W_w^2 do not significantly affect the response of Building 2 in its x-direction.

Finally, having identified the FE models of the buildings, we recover the input ground motions in global directions using the deconvolution approach. The input motions backcalculated using each building's recoded responses are shown in **Figure 26**. As seen, the recovered ground motions from both buildings' responses match the exact input motions.
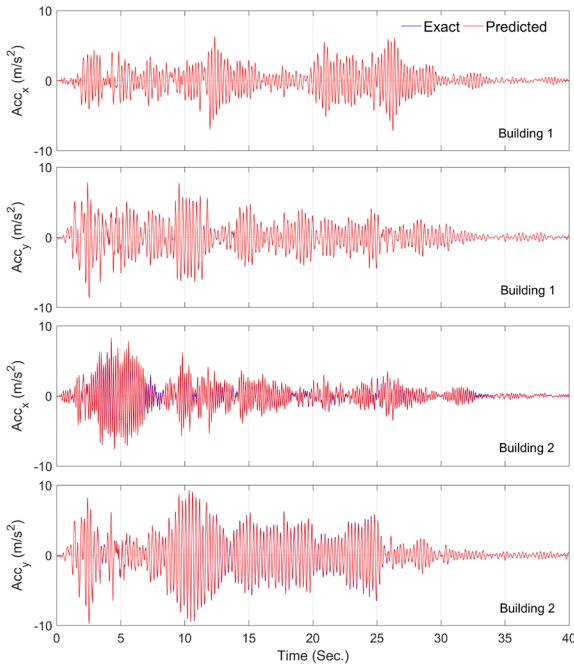
Figure 25. Comparison of the predicted and exact building responses.
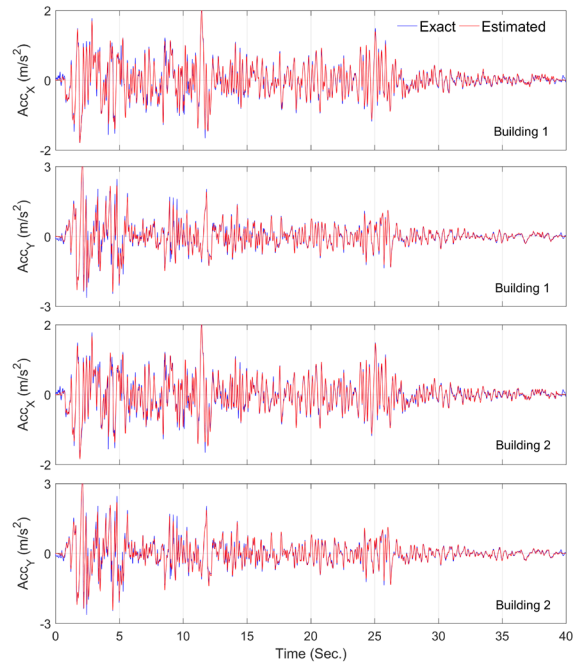
Figure 26. Comparison of the recovered and exact input motions.

Conclusions

Earthquake input excitation to the building structures may be unavailable in various conditions. Soil-Structure Interaction (SSI) effects may prevent measuring true input excitation through both inertial and kinematic effects. Also, input excitation may be lost due to sensor malfunctioning or recorded with low resolution. The present study proposed various methods to be able to extract input excitation from responses recorded by instrumented buildings like CSMIP buildings. The proposed methods range from sophisticated and computationally demanding model-based output-only Bayesian estimation to simple but practical data-driven Cross-Relation (CR) method in which needed additional information is taken from response of the adjacent buildings. We successfully verified and validated all these methods using simulated and real-life data, respectively. A hybrid method was also proposed by a combination of these two mentioned methods to take advantage of benefits of either method to solve more complex 3D problems. We also developed two deconvolution techniques to fix the stability problems commonly observed in recovering input motions.

Acknowledgment

References

[1]   M. R. Gallipoli, M. Mucciarelli, F. Ponzo, M. Dolce, E. D'Alema, and M. Maistrello, "Buildings as a seismic source: Analysis of a release test at Bagnoli, Italy," *Bull. Seismol. Soc. Am.*, 2006.

[2]   A. Zerva and V. Zervas, "Spatial variation of seismic ground motions: An overview," *Appl. Mech. Rev.*, vol. 55, no. 3, p. 271, 2002.

[3]   J. P. Wolf and A. J. Deeks, Foundation vibration analysis: A strength of materials approach. Butterworth-Heinemann, 2004.

[4]   J. P. Stewart, R. B. Seed, and G. L. Fenves, *Empirical evaluation of inertial soil-structure interaction effects*. Pacific Earthquake Engineering Research Center, 1998.

[5]   A. L. Pais and E. Kausel, "On rigid foundations subjected to seismic waves," *Earthq. Eng. Struct. Dyn.*, vol. 18, no. 4, pp. 475–489, 1989.

[6]   D. G. Lignos and E. Miranda, "Estimation of base motion in instrumented steel buildings using output-only system identification," *Earthq. Eng. Struct. Dyn.*, vol. 43, no. 4, pp. 547–563, 2014.

[7]   M. J. Huang and A. F. Shakal, "Structure Instrumentation in the California Strong Motion Instrumentation Program," in *Strong Motion Instrumentation for Civil Engineering Structures*, 2011.

[8]   S. F. Ghahari and E. Taciroglu, "IDENTIFICATION OF DYNAMIC FOUNDATION STIFFNESSES AND INPUT MOTIONS FROM STRONG MOTION DATA RECORDED AT CSMIP INSTRUMENTED BUILDINGS," *Conf. Pap. · Oct. 2016 CITATIONS*, 2017.

[9]   P. C. Hansen, "Deconvolution and regularization with Toeplitz matrices," *Numerical Algorithms*. 2002.

[10]   R. Brincker, L. Zhang, and P. Andersen, "Modal identification of output-only systems using frequency domain decomposition," *Smart Mater. Struct.*, vol. 10, no. 3, pp. 441–445, 2001.

[11]   P. Van Overschee and B. De Moor, "Subspace algorithms for the stochastic identification problem," *Automatica*, vol. 29, no. 3, pp. 649–660, 1993.

[12]   F. Abazarsa, S. F. Ghahari, F. Nateghi, and E. Taciroglu, "Response-only modal identification of structures using limited sensors," *Struct. Control Heal. Monit.*, vol. 20, no. 6, 2013.

[13]   S. F. Ghahari, M. A. Ghannad, and E. Taciroglu, "Blind identification of soil-structure systems," *Soil Dyn. Earthq. Eng.*, vol. 45, 2013.

[14]   F. Abazarsa, F. Nateghi, S. F. Ghahari, and E. Taciroglu, "Blind modal identification of non-classically damped systems from free or ambient vibration records," *Earthq. Spectra*, vol. 29, no. 4, 2013.

[15]   E. Taciroglu, F. Abazarsa, and S. F. Ghahari, "Response-only identification of torsionally coupled buildings using strong motion data," in *9th International Confernce on Urban Earthquake Engineering/4th Asia Conference on Earthquake Engineering*, 2012.

[16]   S. F. Ghahari, F. Abazarsa, M. A. Ghannad, M. Celebi, and E. Taciroglu, "Blind modal identification of structures from spatially sparse seismic response signals," *Struct. Control Heal. Monit.*, vol. 21, no. 5, 2014.

[17]   S. F. Ghahari, F. Abazarsa, and E. Taciroglu, "Blind modal identification of non-classically damped structures under non-stationary excitations," *Struct. Control Heal. Monit.*, 2016.

[18]   S. F. Ghahari, F. Abazarsa, M. A. Ghannad, and E. Taciroglu, "Response-only modal identification of structures using strong motion data," *Earthq. Eng. Struct. Dyn.*, vol. 42, no. 8, 2013.

[19]   S. F. Ghahari, M. A. Ghannad, J. Norman, A. Crewe, F. Abazarsa, and E. Taciroglu, "Considering wave passage effects in blind identification of long-span bridges," in *Conference Proceedings of the Society for Experimental Mechanics Series*, 2013, vol. 5.

[20]   F. Abazarsa, F. Nateghi, S. F. Ghahari, and E. Taciroglu, "Extended blind modal identification technique for nonstationary excitations and its verification and validation," *J. Eng. Mech.*, vol. 142, no. 2, 2016.

[21]   S. F. Ghahari, F. Abazarsa, O. Avci, M. ??elebi, and E. Taciroglu, "Blind identification of the Millikan Library from earthquake data considering soil-structure interaction," *Struct. Control Heal. Monit.*, vol. 23, no. 4, pp. 684–706, 2016.

[22]   E. Taciroglu, M. Çelebi, S. F. Ghahari, and F. Abazarsa, "An investigation of soil-structure interaction effects observed at the MIT green building," *Earthq. Spectra*, vol. 32, no. 4, pp. 2425–2448, 2016.

[23]   E. Taciroglu and S. F. Ghahari, "Identification of soil-foundation dynamic stiffness from seismic response signals," in *American Concrete Institute, ACI Special Publication*, 2017, vol. 2017–Janua, no. SP 316.

[24]   N. Shirzad-Ghaleroudkhani, M. Mahsuli, S. F. Ghahari, and E. Taciroglu, "Bayesian identification of soil-foundation stiffness of building structures," *Struct. Control Heal. Monit.*, 2017.

[25]   E. Taciroglu, S. F. Ghahari, and F. Abazarsa, "Efficient model updating of a multi-story frame and its foundation stiffness from earthquake records using a timoshenko beam model," *Soil Dyn. Earthq. Eng.*, vol. 92, 2017.

[26]   H. Ebrahimian, R. Astroza, J. P. Conte, and C. Papadimitriou, "Bayesian optimal estimation for output-only nonlinear system and damage identification of civil structures," *Struct. Control Heal. Monit.*, vol. 25, no. 4, 2018.

[27]   E. Ebrahimian, H.;Ghahari, S.F.;Asimaki, D.;Taciroglu, "Estimation of the Soil-Structure Model Parameters for the Millikan Library Building Using a Sequential Bayesian Finite Element Model Updating Technique," *Earthq. Eng.& Struct. Dyn.*, 2019.

[28]   S. F. Ghahari, F. Abazarsa, and E. Taciroglu, "Probabilistic blind identification of site effects from ground surface signals," *Bull. Earthq. Eng.*, 2017.

[29]   S. F. Ghahari, F. Abazarsa, C. Jeong, A. Kurtulus, and E. Taciroglu, "Blind identification of site effects and bedrock motion from surface response signals," *Soil Dyn. Earthq. Eng.*, vol. 107, pp. 322–331, 2018.

[30]   R. Astroza, H. Ebrahimian, Y. Li, and J. P. Conte, "Bayesian nonlinear structural FE model and seismic input identification for damage assessment of civil structures," *Mech. Syst. Signal Process.*, vol. 93, pp. 661–687, 2017.

[31]   H. Ebrahimian, R. Astroza, J. P. Conte, and C. Papadimitriou, "Bayesian optimal estimation for output-only nonlinear system and damage identification of civil structures," *Structural Control and Health Monitoring*, 2018.

[32]   S. V CSI, "8, 2002. Integrated Finite Element Analysis and Design of Structures Basic Analysis Reference Manual," *Comput. Struct. Inc., Berkeley, California, USA*, 2010.

[33]   F. McKenna, "OpenSees: a framework for earthquake engineering simulation," *Comput. Sci. Eng.*, vol. 13, no. 4, pp. 58–66, 2011.

[34]   G. Xu, H. Liu, L. Tong, and T. Kailath, "A least-squares approach to blind channel identification," *IEEE Trans. Signal Process.*, vol. 43, no. 12, pp. 2982–2993, 1995.

[35]   N. A. Abrahamson, J. F. Schneider, and J. C. Stepp, "Empirical Spatial Coherency Functions for Application to Soil-Structure Interaction Analyses," *Earthq. Spectra*, vol. 7, no. 1, pp. 1–27, 1991.

[36]   J. R. Ragazzini and L. A. Zadeh, "The analysis of sampled-data systems," *Trans. Am. Inst. Electr. Eng. Part II Appl. Ind.*, vol. 71, no. 5, pp. 225–234, 1952.

[37]   C. P. Hughes and A. Nikeghbali, "The zeros of random polynomials cluster uniformly near the unit circle," *Compos. Math.*, 2008.

[38]   A. V Oppenheim, R. W. Schafer, and J. R. Buck, *Discrete Time Signal Processing*, vol. 1999. 1999.

[39]   M. Miyoshi and Y. Kaneda, "Inverse Filtering of Room Acoustics," *IEEE Trans. Acoust.*, 1988.

[40]   X. Li, S. Gannot, L. Girin, and R. Horaud, "Multisource mint using convolutive transfer function," in *ICASSP, IEEE International Conference on Acoustics, Speech and Signal Processing - Proceedings*, 2018.

[41]   Y. Avargel and I. Cohen, "System identification in the short-time fourier transform domain with crossband filtering," *IEEE Trans. Audio, Speech Lang. Process.*, 2007.

[42]   J. Bendat and A. Piersol, Engineering applications of correlation and spectral analysis. 1993.

[43]   E. Ghahari, S.F., Abazarsa, F., Ebrahimian, H., Taciroglu, "Output-only model updating of adjacent buildings from sparse seismic response records and identification of their common excitation," *Struct. Control Heal. Monit.*, vol. submitted, 2018.

[44]   S. Hashemi and J. K. Hammond, "The interpretation of singular values in the inversion of minimum and non-minimum phase systems," *Mech. Syst. Signal Process.*, 1996.

[45]   R. Gray, "On the asymptotic eigenvalue distribution of Toeplitz matrices," *IEEE Trans. Inf. Theory*, 1972.

[46]   H. Ebrahimian, R. Astroza, J. P. Conte, and R. A. de Callafon, "Nonlinear finite element model updating for damage identification of civil structures using batch Bayesian estimation," *Mech. Syst. Signal Process.*, vol. 84, pp. 194–222, 2017.

[47]   S. Haykin, *Kalman Filtering and Neural Networks*, vol. 5, no. 3. 2001.

[48]   S. J. Julier and J. K. Uhlmann, "New extension of the Kalman filter to nonlinear systems," in *Signal Processing, Sensor Fusion, and Target Recognition VI*, 1997, vol. 3068, p. 182.

Appendix A: Output-Only Bayesian Estimation

The response of the Finite Element (FE) model of a building at each time step to a multi-directional earthquake excitation can be expressed as a (nonlinear) function of the model parameter vector, $\boldsymbol{\theta}$, and the time history of the base input motions, $\ddot{\boldsymbol{u}}_{1:i}^g$, i.e.,

$$\widehat{\boldsymbol{y}}_i = h_i\left(\boldsymbol{\theta}, \ddot{\boldsymbol{u}}_{1:i}^g\right), \tag{A1}$$

where $h_i(.)$ is the nonlinear response function of the FE model at time step i, encapsulating all the dynamics of the model from time step 1 to i. The measured response vector of the structure, $\boldsymbol{y}_i$, is related to the FE predicted response, $\widehat{\boldsymbol{y}}_i$, as

$$\boldsymbol{v}_i\left(\boldsymbol{\theta}, \ddot{\boldsymbol{u}}_{1:i}^g\right) = \boldsymbol{y}_i - \widehat{\boldsymbol{y}}_i\left(\boldsymbol{\theta}, \ddot{\boldsymbol{u}}_{1:i}^g\right), \tag{A2}$$

in which $\boldsymbol{v}_i \in \mathrm{R}^{n_y \times 1}$ is the simulation error vector and accounts for the misfit between the measured and FE predicted response of the structure. The simulation error is ideally modeled as a zero-mean Gaussian white noise vector (i.e., $\boldsymbol{v}_i \sim N(\mathbf{0}, \mathbf{R})$) by neglecting the effects of modeling error [46]. The objective of the estimation problem is to find the estimates of the unknown parameter vector, i.e., $\boldsymbol{\psi}_i = \left[\boldsymbol{\theta}^T, \ddot{\boldsymbol{u}}_{1:i}^{g\ T}\right]^T$, for which the discrepancies between the measured and FE predicted responses are minimized in a probabilistic sense. Since the estimation problem is highly nonlinear, a sequential estimation approach is used in this study to improve estimation efficiency. In this approach, the time domain is divided into successive overlapping time windows, referred to as the estimation windows. The estimation problem is solved at each estimation window to estimate the unknown parameter vector. Assume that the m-th estimation window spans from time step t_1^m to time step t_2^m. Therefore, the unknown parameter vector at this estimation window is defined as $\boldsymbol{\psi}_m = \left[\boldsymbol{\theta}^T, \ddot{\boldsymbol{u}}_{t_1^m:t_2^m}^{g,m\ T}\right]^T$, where $\boldsymbol{\psi}_m \in \mathrm{R}^{(n_\theta + t_l \times n_{\ddot{u}^g}) \times 1}$, in which $t_l = t_2^m - t_1^m$ is the estimation window length, and $n_{\ddot{u}^g}$ is the number of unknown components of the base input motions. The unknown parameter vector, $\boldsymbol{\psi}_m$, is estimated using a parameter-only Kalman filtering method. To this end, the unknown parameter vector is modeled as a random vector, the evolution of which is characterized by a Gaussian Markov process – also known as a random walk. Then, a state-space model is set up, in which the state equation governs the evolution of the random parameter vector and the measurement equation corresponds to the discrepancies between the measured and FE predicted structural responses [47], i.e.,

$$\boldsymbol{\psi}_{m,k+1} = \boldsymbol{\psi}_{m,k} + \boldsymbol{\gamma}_{m,k}, \tag{A3}$$

$$\boldsymbol{y}_{t_1^m:t_2^m} = \widehat{\boldsymbol{y}}_{t_1^m:t_2^m,k+1}\left(\boldsymbol{\psi}_{m,k+1}\right) + \boldsymbol{v}_{t_1^m:t_2^m,k+1}, \tag{A4}$$

in which $\boldsymbol{\gamma}_{m,k} \sim N(\mathbf{0}, \mathbf{Q})$, $\boldsymbol{v}_{t_1^m:t_2^m,k+1} \sim N(\mathbf{0}, \widetilde{\mathbf{R}})$, where $\widetilde{\mathbf{R}} \in \mathrm{R}^{(t_l \times n_y) \times (t_l \times n_y)}$ is a block diagonal matrix, whose block diagonals are the simulation error covariance matrix $\mathbf{R}$. In Eqs. (A3) and (A4), k denotes the iteration number. As can be observed, the estimation process at each estimation window is iterative, i.e., the mean vector and covariance matrix of the unknown parameter vector is iteratively updated based on the discrepancies between the time histories of the measured and estimated responses.

An Unscented Kalman Filtering (UKF) method is used to update the unknown parameter vector at each iteration. In this method, the nonlinear FE model is evaluated separately at a set of deterministically selected realizations of the unknown parameter vector, which are referred to as the sigma points (SPs) denoted by $\boldsymbol{\vartheta}^j$. The sigma points are selected around the prior mean estimate $\widehat{\boldsymbol{\psi}}^-$. In this study, a scaled Unscented Transformation (UT) based on $2n_\psi + 1$ sigma points (i.e., $j = 1,2,\dots,2n_\psi + 1$) is used, where n_ψ denotes the size of the extended parameter vector. The mean and covariance matrix of the FE predicted structural responses, and the cross-covariance matrix of $\boldsymbol{\psi}$ and $\boldsymbol{y}$ are respectively computed using a weighted sampling method as

$$\overline{\boldsymbol{y}} = \sum_{j=1}^{2n_\psi+1} W_m^j \, \widehat{\boldsymbol{y}}_i(\boldsymbol{\vartheta}^j), \tag{A5}$$

$$\widehat{\mathbf{P}}_{yy} = \sum_{j=1}^{2n_\psi+1} W_e^j \left[\widehat{\boldsymbol{y}}_i(\boldsymbol{\vartheta}^j) - \overline{\boldsymbol{y}} \right]\left[\widehat{\boldsymbol{y}}_i(\boldsymbol{\vartheta}^j) - \overline{\boldsymbol{y}} \right]^T + \mathbf{R}, \tag{A6}$$

$$\widehat{\mathbf{P}}_{\psi y} = \sum_{j=1}^{2n_\psi+1} W_e^j \left[\boldsymbol{\vartheta}^j - \widehat{\boldsymbol{\psi}}^- \right]\left[\widehat{\boldsymbol{y}}_i(\boldsymbol{\vartheta}^j) - \overline{\boldsymbol{y}} \right]^T, \tag{A7}$$

where W_m^j and W_e^j denote weighting coefficients [48]. Now, the UKF prediction-correction procedure can be employed to estimate the posterior parameter mean vector $\widehat{\boldsymbol{\psi}}^+{}_{m,k+1}$ and covariance matrix $\widehat{\mathbf{P}}^+_{\psi,m,k+1}$ at each iteration. The identification algorithm is summarized in **Table A1**.

Table A1. Identification algorithm for joint estimation of the model parameters and the FIM time history.

1. Set the estimation window length t_l, and the start and end points of each estimation window.
2. Set the initial mean vector and covariance matrix of the unknown parameter vector as $$\widehat{\boldsymbol{\psi}}^+{}_0 = \left[\widehat{\boldsymbol{\theta}}_0{}^T, \ddot{\boldsymbol{u}}^{g,0}_{t_1^0:t_2^0}{}^T \right]^T, \text{ and } \mathbf{P}^+_{\psi,0} = \begin{bmatrix} \widehat{\mathbf{P}}_{\theta\theta,0} & \mathbf{0} \\ \mathbf{0} & \widehat{\mathbf{P}}_{\ddot{u}^{g,0}} \end{bmatrix}.$$
3. Define the process noise covariance matrix $\mathbf{Q}$ and the simulation error covariance matrix $\mathbf{R}$. Set up matrix $\widetilde{\mathbf{R}}$.
4. For the m-th estimation window:
4.1. Retrieve the posterior estimates of the mean vector and covariance matrix of the unknown parameter vector from the last estimation window (i.e., $\widehat{\boldsymbol{\psi}}^+{}_{m-1}$, and $\mathbf{P}^+_{\psi,m-1}$). Set up $\widehat{\boldsymbol{\psi}}^+{}_{m,0}$ and $\mathbf{P}^+_{\psi,m,0}$ based on $\widehat{\boldsymbol{\psi}}^+{}_{m-1}$ and $\mathbf{P}^+_{\psi,m-1}$.
4.2. Iterate ($k = 1, 2, \dots$):
a. Set $\widehat{\boldsymbol{\psi}}^-{}_{m,k+1} = \widehat{\boldsymbol{\psi}}^+{}_{m,k}$, $\mathbf{P}^-_{\psi,m,k+1} = \mathbf{P}^+_{\psi,m,k} + \mathbf{Q}$.
b. Generate sigma points. Run the FE model for $(2n_\psi + 1)$ sigma points. Derive $\overline{\boldsymbol{y}}$, $\widehat{\mathbf{P}}_{yy}$, and $\widehat{\mathbf{P}}_{\psi y}$ using Eqs. (A5)-(A7).
c. Compute the Kalman gain matrix: $\mathbf{K} = \widehat{\mathbf{P}}_{\psi y}\left(\widehat{\mathbf{P}}_{yy}\right)^{-1}$.
d. Find the corrected estimates of the mean vector and covariance matrix of the unknown parameter vector: $$\widehat{\boldsymbol{\psi}}^+{}_{m,k+1} = \widehat{\boldsymbol{\psi}}^-{}_{m,k+1} + \mathbf{K}\left(\boldsymbol{y}_{t_1^m:t_2^m} - \overline{\boldsymbol{y}}\right), \ \mathbf{P}^+_{\psi,m,k+1} = \mathbf{P}^-_{\psi,m,k+1} - \mathbf{K}\left(\widehat{\mathbf{P}}_{yy} + \widetilde{\mathbf{R}}\right)\mathbf{K}^T.$$
e. Check for convergence: if $\left\|\widehat{\boldsymbol{\psi}}^+{}_{m,k+1} - \widehat{\boldsymbol{\psi}}^+{}_{m,k}\right\| < 0.02 \times \widehat{\boldsymbol{\psi}}^+{}_{m,k-1}$ or $k + 1 > 10$, then move to the next estimation window ($m = m + 1$, go to step 4); otherwise, iterate again at the current estimation window ($k = k + 1$, go to step 4.2).

GEOLOGIC OBSERVATIONS ASSOCIATED WITH THE
JULY 2019 Mw 6.4 AND Mw 7.1 RIDGECREST EARTHQUAKE SEQUENCE

Janis L. Hernandez

Department of Conservation, California Geological Survey
Los Angeles, California

Extended Abstract

The Ridgecrest Earthquake Sequence began on July 4, 2019 with a M_w 6.4 earthquake at 10:33 am PDT at a depth of 8.7 km. The epicenter was located about 18 km east-northeast of the City of Ridgecrest within the Naval Weapons Station China Lake (NWSCL) property. This event was preceded by several small foreshocks a few days prior to the event. Surface rupture from this event was expressed as a zone of surface faulting over 17 km long, consisting of several strands with en-echelon stepovers, striking northeast-southwest with left-lateral displacement of the ground surface. Rupture appears to have propagated from the epicenter toward the southwest.

Figure 1 – Seismicity pattern from Ridgecrest July 4, 2019 Mw 6.4 earthquake (SCEDC, 2013). Epicenter location (green star) and aftershocks, including M4.9 (orange star) prior to Mw7.1 event. Geologic map shows the area is underlain by granitic bedrock (pink polygons) surrounded by younger alluvial valley deposits in yellow. Bright yellow polygons surrounding faults are Alquist-Priolo fault zone boundaries for Holocene faults.

Aftershock patterns following the M_w 6.4 event followed the northeast-southwest trend, however a perpendicular northwest-southeast L-shaped pattern developed near the epicenter at the north end of the fault zone (Figure 1).

This northwest-southeast aftershock pattern appeared to be weakly coincident with a discontinuous zone of northwest striking, previously mapped Holocene-active faults. The pattern of faulting and seismicity hinted at the possibility of cross-fault triggering, similar to what was observed in other earthquake sequences such as the 1987 Elmore Ranch - Superstition Hills earthquake sequence (Hudnut and others, 1989).

About 34 hours after the M_w 6.4 event and numerous aftershocks, some of which were M5+, the M_w 7.1 mainshock event occurred at 8:19pm PDT. The epicenter of this mainshock was located approximately 10 km northwest of the Mw 6.4 epicenter, at a depth of 10 km (Figure 2). Surface rupture from this event occurred along a northwest-southeast striking fault zone, roughly coincident with the northwest -southeast seismicity observed north of the M 6.4 rupture prior to the mainshock. Displacement was right-lateral and extended bilaterally away from the epicenter over a distance of ~50 km.
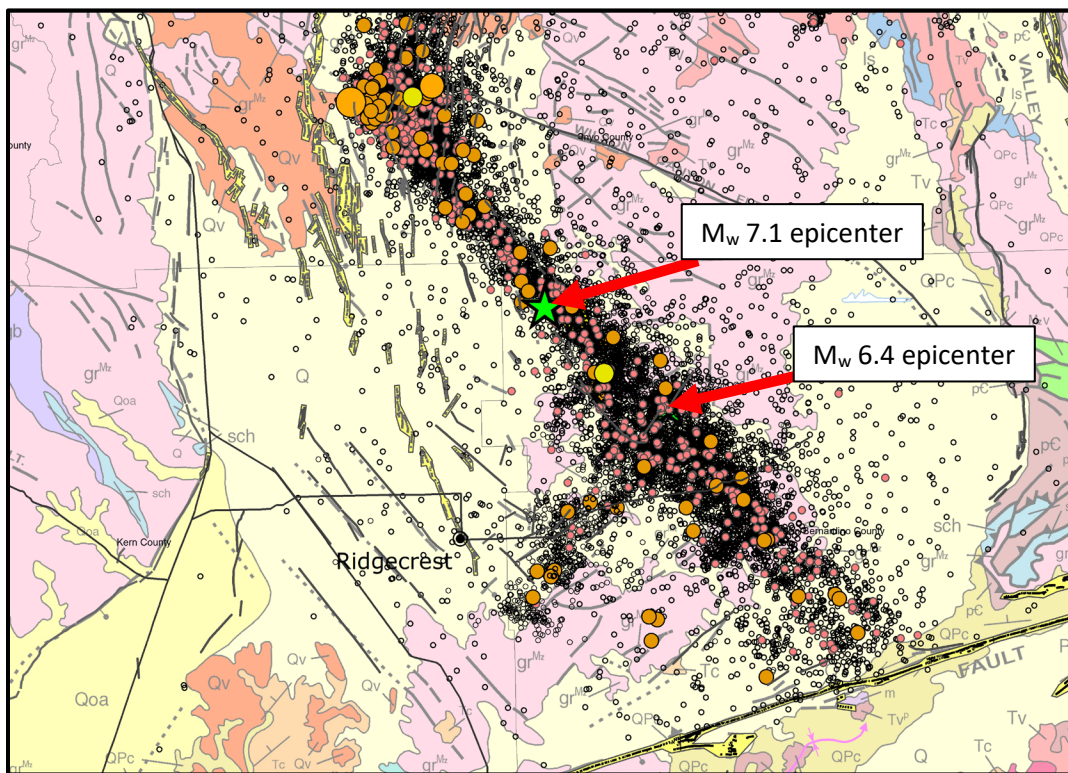
Figure 2 – Seismicity pattern from post-Mw 6.4 and 1-week post-Mw 7.1 earthquake events (SCEDC, 2013). Surface rupture from both large earthquake events occurred on faults that were either not previously mapped, or on faults with discontinuous mapped traces.

The Ridgecrest Earthquake Sequence is located within the Eastern California Shear Zone, which is dominated primarily by active, steeply-dipping, right-lateral, strike-slip and oblique-slip faults that are overall part of the system of the San Andreas Fault and North American plate

boundary. The Ridgecrest area and the greater Indian Wells Valley have experienced numerous historic earthquake swarms.

Previous events that produced surface rupture include: Indian Wells Valley M 5.2 earthquake event on October 1, 1982, (Roquemore, and Zellmer, 1983), and the Ridgecrest M_L 5.8 earthquake on September 20, 1995 (Hauksson and others, 1995). Surface rupture from these two events occurred on the Little Lake and Airport Lake Faults, where they exhibited minor right-lateral and vertical displacements. Observations from the 1982 event included 4mm of separation, distributed along en-echelon fault segments over a distance of ~10km. The 1995 event generated about 1cm of right oblique slip on a fault segment about 3km long. These fault traces were subsequently zoned by the State as part of the Alquist-Priolo Earthquake Fault Zoning program.

Field observations of surface rupture were made starting on July 4, 2019 immediately after the M 6.4 event by the Ridgecrest Rupture Mapping Group (Kendrick and others, 2019). Methods of collecting data included; helicopter overflights, field mapping, UAV (drone) imagery, ground-based lidar, and review of digital satellite imagery, much of which was available within a few days after the first earthquake event. Social media postings were also helpful in documenting surface rupture, in some cases prior to road repairs were made on public right of ways. Much of the surface rupture documentation was done on iPad tablets using ArcCollector application, and later compiling data into ArcGIS platform.

Documented surface rupture from the Mw 6.4 event extended a distance of ~ 17 km, with up to 1.5 m of left-lateral displacement, and about 15 cm of vertical displacement. At the southwest termination of the M 6.4 rupture, distributed faulting is present on multiple strands. Left-lateral displacements on these distributed faults are typically less than 5 cm, and increase to tens of cms as the fault zone integrates into a single strand about 1 km northeast of Randsburg Wash Road.

Surface rupture from the Mw7.1 event extended a distance of ~50 km with up to 5 m of right-lateral displacement, and about 1.5m of vertical displacement. Maximum displacements were noted within China Lake playa, near the epicenter. The principle surface rupture is variably expressed as a single fault with knife-edge vertical scarps and narrow fault zone, to multiple strand, left-stepping en-echelon ruptures with conjugate faults that splayed away from the main strand, continuing over a significant distance.

Analysis of the surface ruptures and fault geometry is ongoing. There are multiple sources of high precision data that are currently being analyzed, and field mapping that is continuing to be performed in areas where complexities occur and digital analysis methods need to be field verified. Lidar was flown in early August by the National Center for Airborne Laser Mapping (NCALM) and was funded by the National Science Foundation, the U.S. Geological Survey, with support from the Southern California Earthquake Center. The lidar data is expected to be released in late 2019, after processing by NCALM and a review by the U.S. Navy.

In conclusion, the Ridgecrest Earthquake Sequence is one of the most complex modern set of earthquakes to date, and it produced extensive surface rupture in a fairly remote area of southern California. Having the benefit of advanced technology and rapid assessment by a team of geologists, we anticipate learning much from these earthquake events.

References

Hudnut, K.W., Seeber, L., and Pacheco, J., 1989, Cross-fault triggering in the November 1987 Superstition Hills earthquake sequence, southern California: Geophysical Research Letters, v. 16, no. 2, p. 199-202.

Kendrick, K. J., Akciz, S. O., Angster, S. J., Avouac, J., Bachhuber, J. L., Bennett, S. E., Blake, K., Bork, S., Brooks, B. A., Burgess, P., Chupik, C., Dawson, T., DeFrisco, M. J., Delano, J., DeLong, S., Dolan, J. F., DuRoss, C. B., Ericksen, T., Frost, E., Gold, R. D., Graehl, N. A., Haddon, E. K., Hatem, A. E., Hernandez, J. L., Hitchcock, C., Hudnut, K. W., Koehler, R. D., Kozaci, O., Ladinsky, T., Madugo, C. M., Mareschal, M., McPhillips, D., Milliner, C., Morelan, A. E., Nevitt, J., Olson, B., Padilla, S. E., Patton, J. R., Philibosian, B., Pickering, A., Pierce, I., Ponti, D. J., Pridmore, C., Rosa, C., Roth, N., Scharer, K. M., Seitz, G. G., Spangler, E., Swanson, B. J., Thomas, K., Thompson Jobe, J., Treiman, J. A., Williams, A. M., & Oskin, M. E., 2019, Geologic observations of surface fault rupture associated with the Ridgecrest M6.4 and M7.1 earthquake sequence by the Ridgecrest Rupture Mapping Group. Poster Presentation #217 at 2019 Southern California Earthquake Center (SCEC) Annual Meeting.

SCEDC (2013): Southern California Earthquake Center. Caltech.Dataset, doi:10.7909/C3WD3xH1.

Stewart, J.P. (ed.), Brandenberg, S.J., Wang, Pengfei, Nweke, C.C., Hudson, K., Mazzoni, S., Bozorgnia, Y., Hudnut, K.W., Davis, C.A., Ahdi, S.K., Zareian, F., Fayaz, J., Koehler, R.D., Chupik, C., Pierce, I., Williams, A., Akciz, S., Hudson, M.B., Kishida, T., Brooks, B.A., Gold, R.D., Ponti, D.J., Scharer, K.M., McPhillips, D.F., Ericksen, T.., Hernandez, J., Patton, J., Olson, B., Dawson, T., Treiman, J., Duross, C.B., Blake, K., Buchhuber, J., Madugo, C., Sun, J., Donnellan, A., Lyzenga, G., and Conway, E., 2019, Preliminary report on engineering and geological effects of the July 2019 Ridgecrest Earthquake sequence: Geotechnical Extreme Events Reconnaissance Association Report GEER-064, https://doi.org/10.18118/G6H66K.

RIDGECREST EARTHQUAKE SEQUENCE: STRONG MOTION DATA AND GEOTECHNICAL ENGINEERING IMPACTS

Jonathan P. Stewart, Ph.D., P.E.

Geotechnical Extreme Events Reconnaissance Association

See GEER Report for full list of contributors

Abstract

The Ridgecrest Earthquake sequence included a foreshock event on July 4 2019 (**M**6.4) and a **M**7.1 mainshock event on July 5 2019. These events occurred in the Eastern California Shear Zone, near Indian Wells Valley, south of China Lake and west of Searles Valley. GEER partnered with several organizations to collect perishable data and document the important impacts of these events, including the US Geological Survey, the California Geological Survey, the US Navy, the Southern California Earthquake Center, and local utilities. Critical geotechnical features of this event are extensive left-lateral (**M**6.4 event) and right-lateral (**M**7.1 event) surface ruptures over fault segments of variable complexity and width as well as across extensional and compressive step-over zones. We also document lifeline performance at fault crossings (gas, water, electrical), mainshock slip and afterslip, liquefaction and lateral spreading features, and liquefaction effects on structures. These effects are documented using field (ground) mapping and aerial imagery that will support subsequent development of high-resolution digital elevation models. Over 1200 ground motions were recorded from the foreshock and mainshock alone, with many additional aftershock records. The data demonstrate significant impacts of site response and rupture directivity on ground motion attributes.

GEER Report

Stewart, J.P. (ed.), Brandenberg, S.J., Wang, Pengfei, Nweke, C.C., Hudson, K., Mazzoni, S., Bozorgnia, Y., Hudnut, K.W., Davis, C.A., Ahdi, S.K., Zareian, F., Fayaz, J., Koehler, R.D., Chupik, C., Pierce, I., Williams, A., Akciz, S., Hudson, M.B., Kishida, T., Brooks, B.A., Gold, R.D., Ponti, D.J., Scharer, K.M., McPhillips, D.F., Ericksen, T.., Hernandez, J., Patton, J., Olson, B., Dawson, T., Treiman, J., Duross, C.B., Blake, K., Buchhuber, J., Madugo, C., Sun, J., Donnellan, A., Lyzenga, G., and Conway, E., 2019, Preliminary report on engineering and geological effects of the July 2019 Ridgecrest Earthquake sequence: Geotechnical Extreme Events Reconnaissance Association Report GEER-064, https://doi.org/10.18118/G6H66K.

CHARACTERIZATION OF THE AMPLIFICATION OF FORCES TO NONSTRUCTURAL COMPONENTS USING RECORDED EARTHQUAKE DATA

Xiang Wang and Tara Hutchinson

Department of Structural Engineering
University of California, San Diego

Abstract

The overall scope of this study is to evaluate the acceleration amplification effects of nonstructural components using recorded earthquake responses of buildings and nonstructural components. Specifically, two separate, yet complementary efforts are undertaken, namely: 1) characterizing nonstructural component amplification effects using a large set of building earthquake responses that are available in the CESMD strong motion database, and 2) identifying the dynamic characteristics of instrumented nonstructural components integrated within a full-scale building shake table test program. Findings from this study are intended to supplement current seismic design provisions of nonstructural systems with evidence obtained from recorded data.

Introduction

Nonstructural components and systems account for 70-80% of the overall investment to a building and are critical to their post-earthquake functionality and survivability (Taghavi and Miranda, 2003; FEMA E-74, 2012). In this regard, seismic design recommendations for nonstructural systems have evolved substantially over the past few decades (e.g. ATC 1978, BSSC 1995; BSSC 1998; CEN, 2004; NZS1170.5, 2004). In US practice, design of NCSs is subdivided into acceleration and displacement sensitive systems (ASCE 7, 2016). Design of the former currently relies on a set of simplified equations to determine the seismic design force demand to the NCS, denoted as F_p. The force F_p is primarily a function of the design spectral acceleration, location of the NCS (building height) and component amplification effects bounded within two limit values (Drake and Bachman, 2006):

$$F_p = \frac{0.4 a_p S_{DS} W_p}{R_p / I_p} (1 + 2\frac{z}{h})$$ ASCE 7-16 Equation 13.3-1

$$F_p \leq 1.6 S_{DS} W_p I_p$$ ASCE 7-16 Equation 13.3-2

$$F_p \geq 0.3 S_{DS} W_p I_p$$ ASCE 7-16 Equation 13.3-3

where W_p is the component operating weight; S_{DS} is the short period spectral acceleration; z is the height in structure of attachment point; h is the total height of structure; a_p is the component amplification factor taken as 1.0 for rigid components and 2.5 for flexible components; I_p and R_p are component importance factor and response modification factor, respectively. It is noted that the supporting structures' acceleration amplification factor is empirically defined as *1+2z/h*. This represents a linear (first mode assumed) distribution of the acceleration amplification over the

height of the building (from 1 at the ground level to 3 at the top of the building), irrespective of the height and lateral force resisting system of individual buildings.

With the objective of assessing the robustness of current code equations (ASCE-7, 2016), the Applied Technology Council recently initiated a multi-phased project, with the second phase particularly focused on undertaking a comprehensive study to investigate the influence of a wide variety of parameters that may affect the estimation of seismic forces to nonstructural components (e.g., building lateral force system, building ductility, component damping, component ductility, and etc.). The project, ATC-120, led to a proposal for an improved equation (NIST, 2018; Lizundia, 2019):

$$\frac{F_p}{W_p} = PGA \times \left[\frac{\left(\dfrac{PFA}{PGA} \right)}{R_{\mu bldg}} \right] \times \left[\frac{\left(\dfrac{PCA}{PFA} \right)}{R_{pocomp}} \right] \times I_p \qquad \begin{array}{c} \text{ATC-120 Equation 4-2} \\ \text{(NIST, 2018)} \end{array}$$

The above equation assumes that the design force demand to a nonstructural component is determined by two separate amplification effects: a) amplification of the peak ground acceleration (PGA) induced by the supporting structure (terms in the first bracket), and b) amplification of the peak floor acceleration (PFA) induced by the nonstructural component (terms in the second bracket). Major improvements offered by this equation relative to the existing code equation (ASCE-7, 2016) are summarized as follows:

- The PFA/PGA distribution adopts a nonlinear equation as proposed by Alonzo-Rodrigues and Miranda (2016) to address the linear distribution simplification that is generally considered to be conservative (Fathali and Lizundia, 2011).
- Building ductility $R_{\mu bldg}$ is explicitly considered in the equation to account for the reduced building acceleration responses induced by building ductility (Kazantzi et al., 2018).
- The component amplification factor (denoted as PCA/PFA) incorporates the effects of component inherent damping and component ductility. The PCA/PFA ratio ranges between 1.4 for high-ductility components and 4.0 for elastic components with an assumed damping ratio of 5%.

Complementing the research initiative on the nonstructural seismic design force evaluation led by the ATC-120 project (NIST, 2017 and 2018), the overall scope of the present study aims at exploring the acceleration amplification effects of nonstructural components using recorded earthquake responses of buildings and nonstructural components. This study involves two separate yet complementary efforts are undertaken, namely: 1) characterizing nonstructural component amplification effects using a large set of building earthquake responses that are available in the CESMD strong motion database[1], and 2) identifying the dynamic characteristics of instrumented nonstructural components integrated within a full-scale building shake table test program (Hutchinson et al., 2014; Chen et al., 2016; Pantoli et al., 2016). Findings from the

---

[1] https://www.strongmotioncenter.org

analysis of these recorded datasets are intended to provide evidence and guidance to current nonstructural seismic design provisions.

Recorded Building Response Analysis

The metadata of all instrumented buildings and the associated earthquake records from the CESMD strong motion database[1] were analyzed to guide the selection of buildings and earthquake records of interest. This database included 581 records for reinforced concrete (RC) buildings and 655 records for steel buildings (as of 6/12/18). The instrumented buildings under each category were further classified based on their story numbers and lateral resisting systems. Using these selection criteria, this study focused on four representative building groups, namely: *RC shear wall*, *RC moment frame*, *steel moment frame*, and *steel braced frame* groups. Moreover, earthquake events with a PGA less than 0.05 g in at least one horizontal direction were excluded due to their very low amplitude. Details of the proposed building groups and the resulting number of associated earthquake records are summarized in Table 1.

Table 1. Summary of building groups and the associated earthquake record per group.

Building lateral system & Earthquake records	Low-rise (1-4)	Mid-rise (5-8)	High-rise (>=9)	Total Number
RC shear wall	11	6	10	**27**
# of earthquake records	22	17	24	**63**
RC moment frame	2	6	3	**11**
# of earthquake records	4	14	8	**26**
Steel moment frame	13	7	10	**30**
# of earthquake records	17	13	14	**44**
Steel braced frame	3	3	4	**10**
# of earthquake records	10	4	7	**21**

Individual Building Analysis Procedures

Figure 1 summarizes the analysis procedures for assessing the component amplification effects of individual buildings using recorded floor acceleration responses. The floor response spectra characteristics serve as critical indicators for the evaluation of the seismic demands of nonstructural components. In ***Step 1***, we employ the deterministic-stochastic identification method (Van Overschee and De Moor, 1996) using the recorded acceleration responses of individual buildings to estimate the modal parameters of the buildings (i.e., periods, damping ratios, and mode shapes). In this step, the system input and output involve the building responses at the two horizontal directions. These estimated periods are used to initiate the structural dynamic parameters optimization (in ***Step 2***). In ***Step 2***, we follow the optimization method proposed by Cruz and Miranda (2016 and 2019) to update the building periods and damping ratios associated with individual earthquake events. The proposed modal inclusion criteria allow for enhanced reliability estimation regarding the identified modal parameters of the buildings, particularly the damping ratios. ***Step 3*** involves evaluating the building floor response spectra

---

[1] https://www.strongmotioncenter.org

using the recorded floor accelerations as well as component amplification factors (denoted as a_p = PCA/PFA), which are obtained by normalizing the floor response spectra against the associated peak floor accelerations. It is noted that the building responses in the two orthogonal horizontal directions are investigated separately, and therefore the building torsional effects are not explicitly considered within the scope of the present study. An example of the resulting component amplification factors of a 5-story hospital building (CSMIP Station #: 23634) and the associated modal characteristics obtained using the proposed analysis procedures are presented in Figure 2.

Step 1: Deterministic-Stochastic Identification
- *Input & output involve building responses in the two horizontal directions (allows for torsional vibration identification)*
- *Extract building periods & damping ratios (initial values for optimization in **step 2**)*

Step 2: Modal Parameters Optimization
- *Optimize building periods & damping ratios using the method proposed in **Cruz & Miranda (2016 and 2019)***
- *Modal inclusion criteria: spectra ratio, modal contribution, reliability intervals*

Step 3: Floor Response Spectra Characterization
- *Evaluate floor response spectra & component amplification*
- *Extract spectral peaks associated with the building vibration modes*

Figure 1. Data analysis procedures for individual buildings.

5-story Hospital Building
(CSMIP #23634)

Component Amplification Factor
– *floor response spectra normalized by peak floor acceleration*
– *denoted as a_p (= PCA / PFA)*
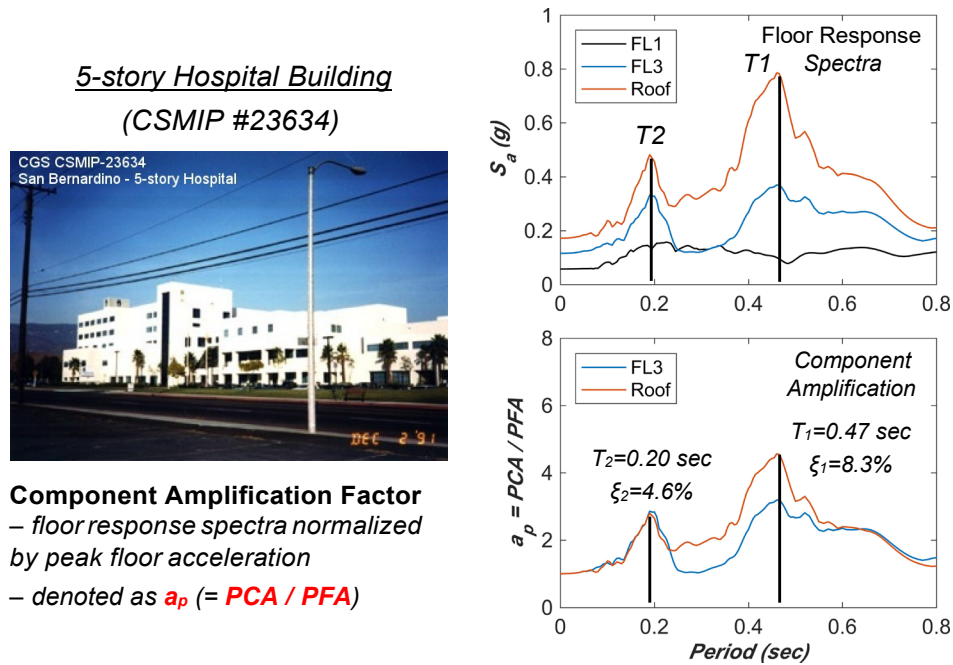
Figure 2. Floor response spectra and component amplification factors a_p of a 5-story hospital building (photograph on left courtesy of CSMIP, Station #: 23634). The floor response spectra represent elastic acceleration spectra with a 5% damping ratio.

Component Amplification of Steel Moment Frame Buildings

The results presented in this section focus on the steel moment frame buildings (see Table 1), whereas those of the remaining building groups will be included in the final project report.

The steel moment frame building group includes a total of 30 buildings subjected to 44 earthquake records with PGA>0.05 g in at least one horizontal direction. With the aim of statistically analyzing the component amplification effects of this building group, the following criteria are adopted in the statistical assessment:

- The analysis of the building responses is decoupled along the two orthogonal directions with no account of the building torsional effects.
- The analysis focuses on the first two building vibration modes (sufficient for low- and mid-rise buildings).
- An upper bound component period is assumed as 0.75 seconds per OSHPD datasets (Watkins et al., 2010). This assumption excludes the fundamental modes of high-rise buildings that are considered unlikely to be tuned with the periods of most nonstructural components.
- The component inherent component damping is assumed to range between 2% ~ 5% (consistent with the range considered by ATC-120).

Following these criteria, the steel moment frame building dataset involves 41 data points for the first modal peaks and 43 data points for the second mode. The component amplification factor (denoted as a_p=PCA/PFA) vs normalized period curves of the roof level associated with the two modes are shown in Figure 3. It is noted that the normalized period represents the ratio of the component period over that of a specific building vibration mode. The component period normalization allows for extraction of the peak component amplification factor associated with individual building vibration modes (within an assumed window of 0.9 ~ 1.1 times the normalized period). Figure 4 presents the relationship between the peak component amplification factors associated with the first and second vibration modes and the identified structural damping ratios related to the corresponding modes. The resulting highly dispersed data points in the plots indicate that the component amplification factors associated with each of the two modes are not well correlated with the damping ratios of the supporting structures. When the assumed component damping ratio reduces from 5% to 2%, comparison of the mean values of the peak component amplification factors reveals that these amplification factors increase by about 50% ~ 60% for both the first and second modes. In addition, the mean peak component amplification factor of the first mode is about 50% larger than that of the second mode.

Figure 5 presents the peak component amplification factors along the height of the buildings. Each data point represents the peak at a specific vertical location (represented by relative height) of an individual building. The color code indicates the building with different stories. It is noted the first mode peaks solely consist of the contribution from the low- and mid-rise buildings. This is due to the fact that all the first mode periods of the high-rise buildings (with 9 stories or more) exceed the upper bound component period of 0.75 second. To facilitate the interpretation of the component amplification distribution along the building height, these data points are grouped into 4 evenly spaced bins according to their relative heights (the center of the representative bins are defined as 0.25, 0.5, 0.75 and 1). Although the bin numbers may not be sufficient for capturing the actual shape associated with the higher modes of mid-rise buildings, a refined binning strategy may not be feasible due to the relative data scarcity in the relative height range between 0.6 and 0.9 (particularly for mid- and high-rise buildings).
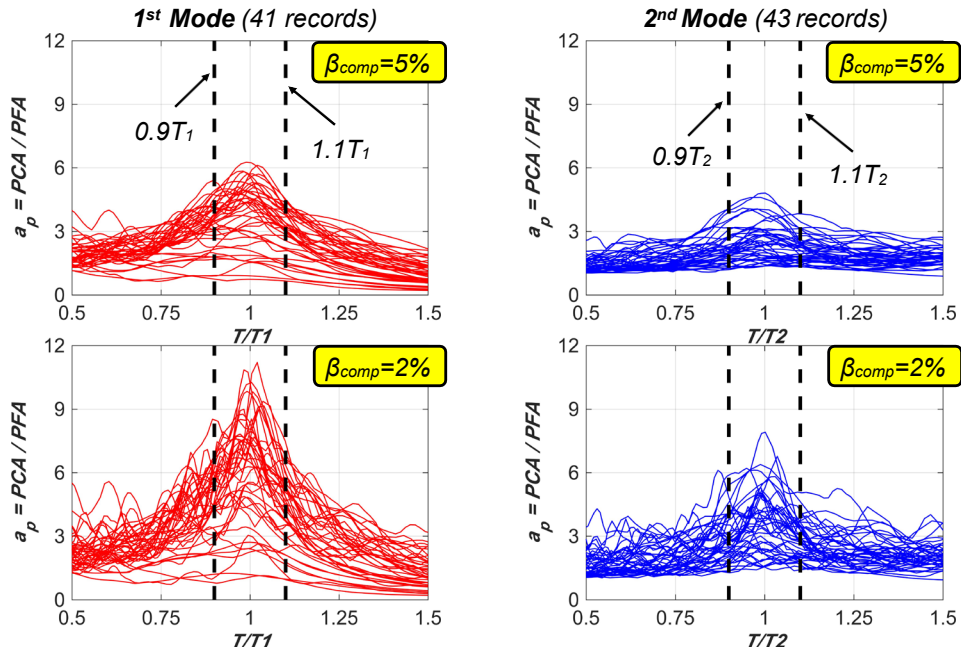
Figure 3. Roof level component amplification factor a_p vs normalized period for: first mode (left), and second mode (right). Upper plots assume a component damping β = 5%, while the lower pair of plots assume β = 2%.
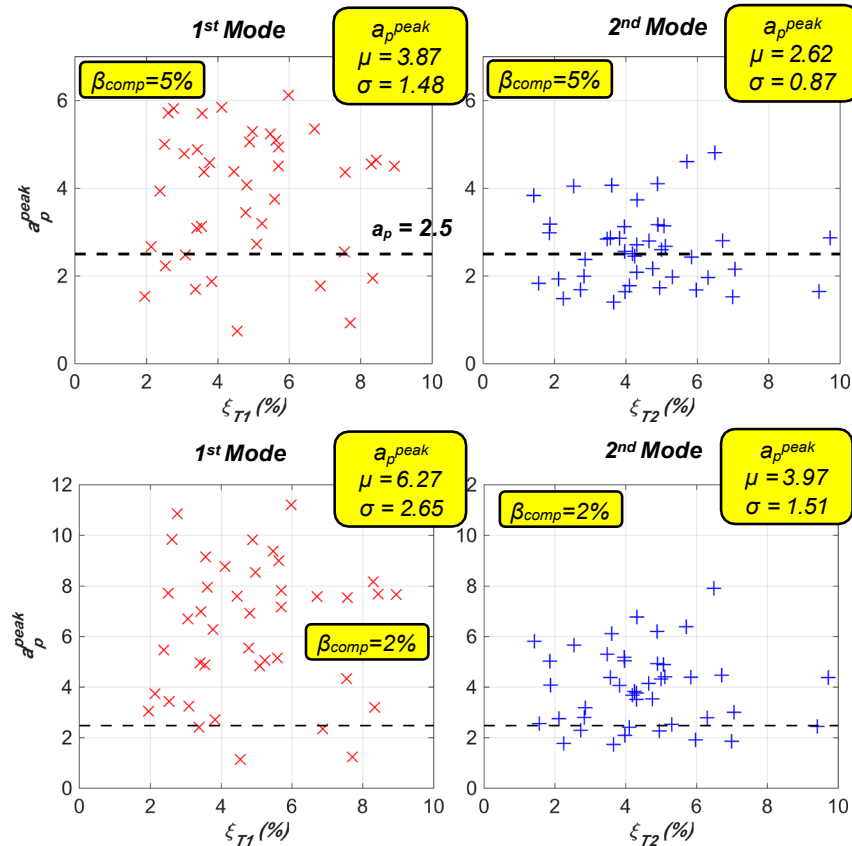
Figure 4. Roof level peak component amplification factor vs structural damping ratio: first mode (left column), and second mode (right column). Upper plots assume a component damping β = 5%, while the lower pair of plots assume β = 2%.

93
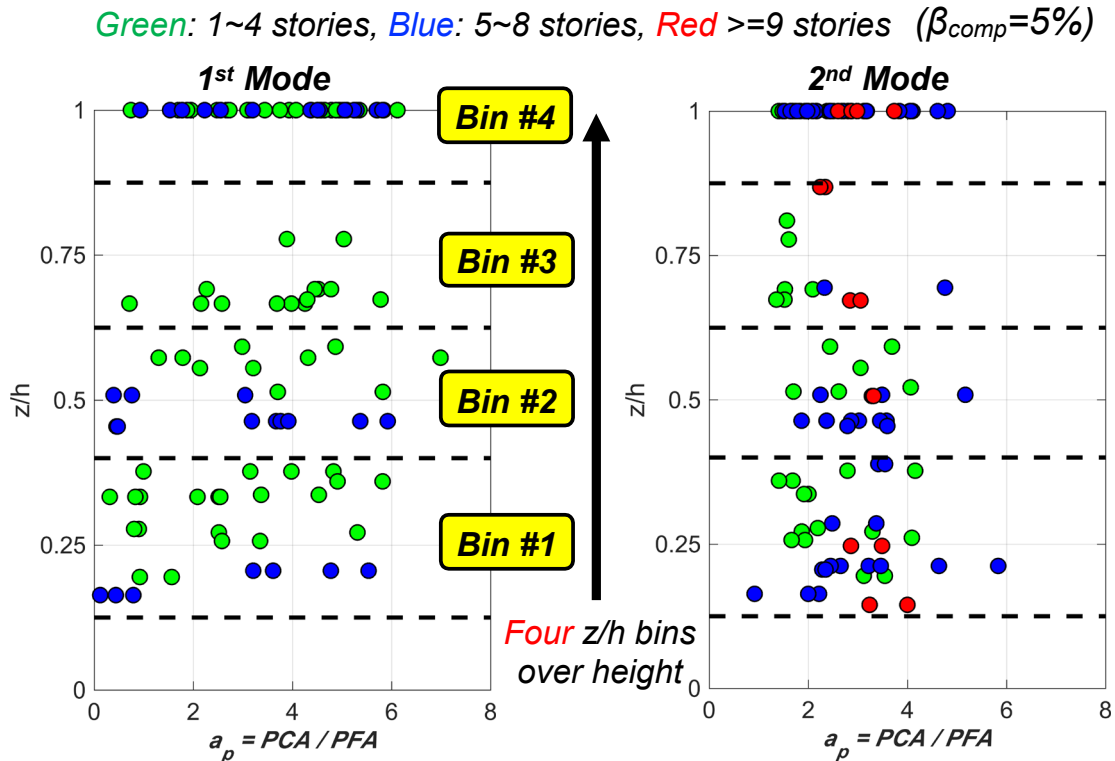
Figure 5. Peak component amplification factor distribution along the height of the buildings (steel moment frame dataset only): first mode (left), and second mode (right).
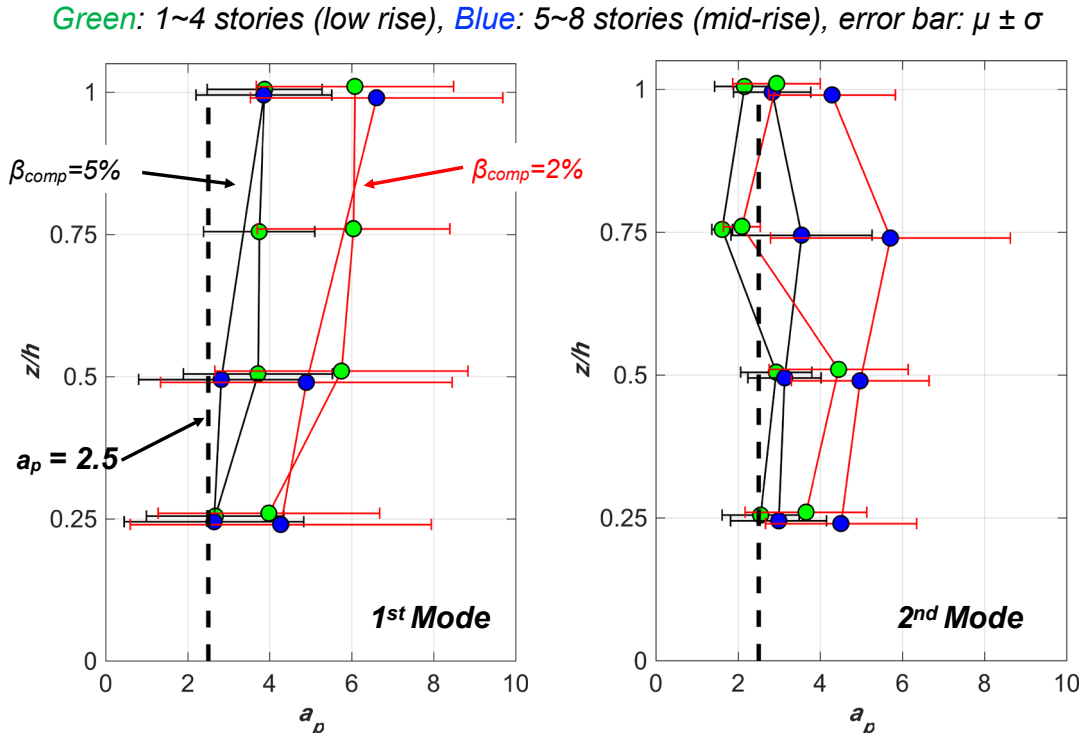
Figure 6. Peak component amplification factor distribution along the height of the buildings: first mode (left), and second mode (right).

Figure 6 summarizes the statistics (i.e., mean and standard deviation) of the vertical distributions of the peak component amplification factors of the low- and mid-rise buildings obtained using the clustered data points. The first mode amplification factors of the low- and mid-rise buildings both increase monotonically and attain the largest values at the roof level. The dispersion of the amplification factors appears comparable at different vertical locations, since the coefficient of variation is $0.5 \sim 0.6$ along the height. In contrast, the vertical distribution of the component amplification factors associated with the second mode differs significantly from that of the first mode. For the low-rise buildings, the mean amplification factor reaches the smallest value at the three-quarter building height ($z/h = 0.75$), which corresponds to the nodal point of the vibration modal shape of the second mode. The differences of the vertical distribution profiles associated with the two modes clearly demonstrate that the component amplification factor is also a function of the specific building mode shape and the relative height.

Recorded Nonstructural Component Response Analysis

Investigating component amplification effects using recorded building responses relies on the evaluation of floor response spectra, which a priori defines nonstructural components as generic linear oscillators given the building floor accelerations. However, the dynamic characteristics (i.e., period and damping ratio) of nonstructural components remains largely unexplored due to the scarcity of measurements during earthquakes, either simulated in the laboratory or obtained in the field (NIST, 2017 and 2018). In a recent experimental program, system-level building shake table tests were conducted at the University of California, San Diego (Chen et al., 2016; Pantoli et al., 2016). These tests provided a unique set of recorded responses of the test building as well as a broad variety of nonstructural components installed within the building (Hutchinson et al., 2014). In this section, the recorded nonstructural seismic responses are analyzed to expand understanding of the dynamic characteristics and the amplification effects of the nonstructural components utilized in this test program under simulated earthquake loading scenarios.

Shake Table Test Program

The test structure was a full-scale five-story reinforced concrete building outfitted with a variety of nonstructural components and systems, including two operable egress systems (elevator and steel stairs), a complete exterior façade system, a broad array of architectural layouts, as well as simulated medical compartments at the upper two floors of the building (Figure 7). In the experimental program, the test building was subjected to a sequence of earthquake tests in two test phases: (i) the building was first tested in base isolated (BI) configuration with seven earthquake tests, and (ii) subsequently in fixed base (FB) configuration with six earthquake tests. It is noted that the earthquake input motions were all applied along the longitudinal axis of the test building using the single-axis shake table.

In the FB test phase, the six earthquake motions were applied with increasing intensity to progressively damage the structure. The first two tests (FB-1 and FB-2) were serviceability earthquake events that the seismic demands of the test structure were sufficiently low (roof peak floor acceleration ~0.4 g). Seismic demands increased moderately in tests FB-3 and FB-4, as the peak acceleration reached ~0.7 g at the roof level. It is noted that test FB-5 is considered as

design event for the test building with the attainment of a peak story drift of ~2.8% at level 2 and a peak floor acceleration of ~1.0 g at the roof, whereas the final test (FB-6) represented a well above design event scenario as the achieved PIDR was as much as 6%. Additional details of the shake table test program, testing protocol, and test results may be found in the technical report series (Chen et al., 2013; Pantoli et al., 2013).

Figure 7. Shake table tests of a five-story reinforced concrete building outfitted with a variety of nonstructural components: test building (left), cooling tower and penthouse of the roof level (top middle left), medical ultrasound imagers of level 4 (bottom middle left), medical equipment of level 4 (top middle right), medical equipment of level 5 (bottom middle right), and computer server at level 3 (right).

Table 2. Description of floor-mounted nonstructural components in the shake table test program.

Nonstructural component	Attachment location	Geometry L x W x H [1] (in)	Operating weight (lb)	Attachment details	Physical observation
Computer server #1 (strong axis shaking)	Floor 3	50 x 30 x 80	3000	(8) M16-25 heavy duty anchors	No damage
Computer server #2 (weak axis shaking)	Floor 3	30 x 50 x 80	3000	(8) M16-25 heavy duty anchors	Incipient screw popping during test FB-4
Ultrasound imager #1	Floor 4	28 x 22 x 58	~300	(4) 1/2" x 3-1/4" expansion anchors	No damage
Ultrasound imager #2	Floor 4	28 x 22 x 58	~300	(4) 1/2" x 3-1/4" expansion anchors	No damage
Medical freezer	Floor 5	30 x 36 x 80	550	(3) 1/2" x 3-1/4" expansion anchors	No damage
Cooling tower [2]	Roof	88 x 108 x 128	6300	(4) snubber spring bearings	Water splashing
Air handling unit	Roof	100 x 58 x 68	1500	(10) 1/2" x 3-1/4" expansion anchors	No damage

[1] H = height, L = length (along shaking direction), W = width (transverse to shaking direction);
[2] Operating weight of the cooling tower consisted of its net weight of 3500 lbs and ~2800 lbs of water during the shake table tests.

Among the nonstructural components and systems installed within the test building, seven pieces of floor-mounted equipment are of interest in this study, since they represented typical acceleration-sensitive components that can be properly simulated as linear oscillators subjected to single-support floor excitations. Detailed descriptions of individual nonstructural components (e.g., geometry, weight, mounting location, attachment details, and etc.) are summarized in Table 2. It is noted that the attachment (or anchor) design of these components conformed to the ASCE-7 (2010 edition) code provisions (ASCE-7, 2010).

Identification of Dynamic Characteristics

The natural periods (or frequencies) and damping ratios of the nonstructural components are identified using the time-domain optimization method with the assumption that they behave as single degree-of-freedom linear oscillators in response to floor excitations. In the optimization algorithm, the objective function is defined as the root mean square error between the simulated response of the oscillator given the measured floor acceleration and the measured response of the nonstructural component (normally at the top of the component). The optimized natural period and damping ratio are obtained by minimizing the objective function (errors between simulated and measured responses). It is noted that the identified damping ratio obtained using this method may be interpreted as an equivalent damping ratio that lumps all possible energy dissipative sources (e.g., friction, contact, yielding). However, the nonstructural components selected for this study did not attain substantial damage during the shake table test sequence, and therefore the hysteretic energy dissipation is not likely to contribute heavily to the damping effects of the components considered in this study.

To demonstrate the effect of nonstructural dynamic characteristics, the two computer servers (see Figure 7 – image on the right) floor-mounted on the slab at level 3 are discussed and compared in detail. Figure 8 shows the time histories of the recorded floor acceleration and the component accelerations of individual units during the first fixed-base test. It is noted that the two servers were identical units but placed in different orientations with respect to the direction of shaking. Whereas Server 1 (strong-axis shaking unit) was oriented with its longitudinal axis was in parallel with the direction of shaking, Server 2 (weak-axis shaking unit) was oriented with its transverse axis in parallel with the direction of shaking (see floor plan layout in Figure 8). Comparison of the acceleration histories indicates that Server 2 underwent substantial amplification relative to the floor excitation, whereas the response of Server 1 remained nearly identical to the floor excitation. In fact, their sharply different dynamic behavior given the identical earthquake excitation results from the distinction of their natural frequencies (or periods) in the direction of shaking. The transfer functions clearly demonstrate that Server 1 was much stiffer than Server 2, since the natural frequency was ~20 Hz for Server 1 and <5 Hz for Server 2.
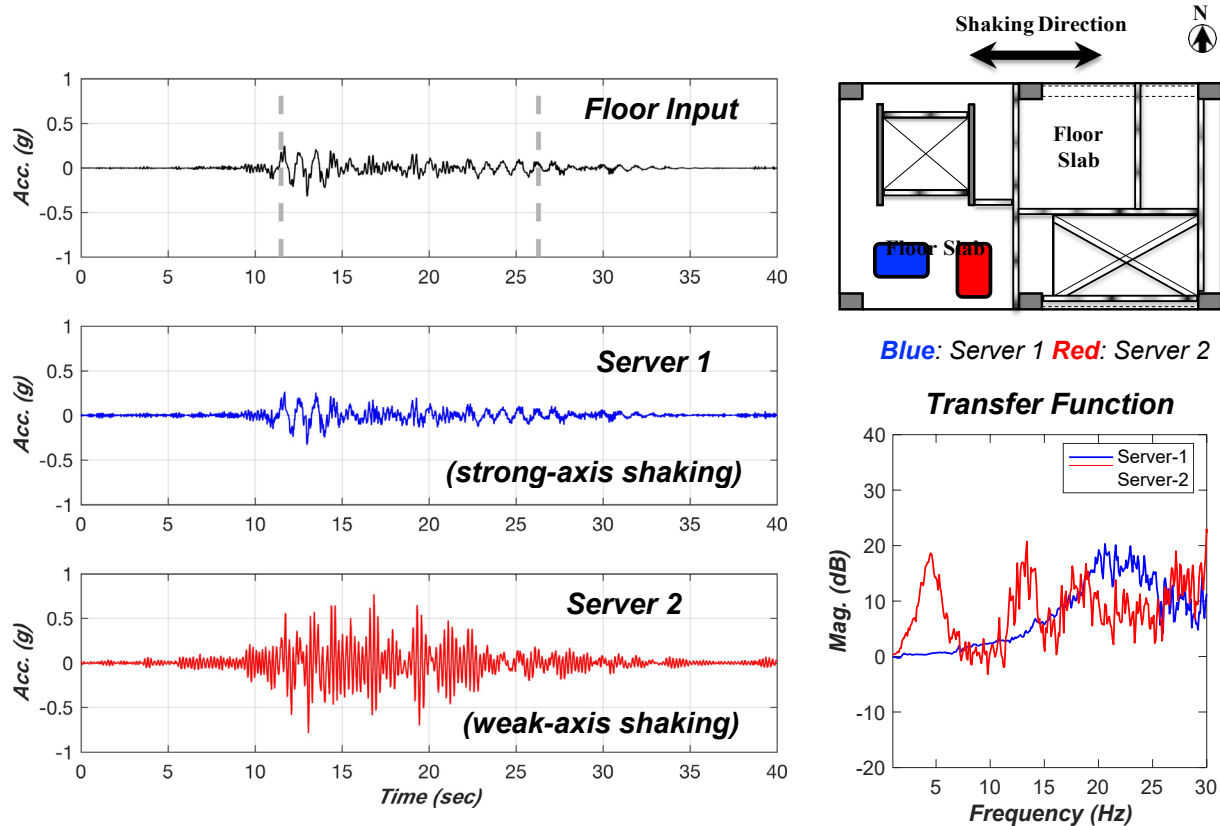
Figure 8. Acceleration time histories of floor 3 and the top of computer servers during the first fixed-base test (left); floor plan layout of level 3 and computer server locations (top right); and the associated transfer functions (bottom right).

The estimated frequencies obtained from the transfer functions provide the initial values for the optimization algorithm. Figure 9 provides the comparison of the recorded and measured component acceleration responses as well as the sensitivity of the identified parameters with respect to the objective function (root mean square error between the measured and simulated responses). Since the minima of the sensitivity curves represent the optimal parameters for the corresponding server unit, the frequency and damping ratio obtained using the optimization method are 25.2 Hz and 9.8% for Server 1 (strong axis shaking) and 4.5 Hz and 6.2% for Server 2 (weak axis shaking). However, it is important to note that both the frequency and damping ratio sensitivity curves for Server 1 appear rather flat in the vicinity of the minima, indicating that the objective function (error) becomes insensitive to the dynamic parameters. In other words, the dynamic parameters obtained from the optimization become less reliable in the case of insignificant component amplification effect. Under such scenarios, the natural frequency of the nonstructural component is determined from the spectral peak of the associated transfer function, whereas its damping ratio is considered as unidentifiable.

Server 1 (strong axis shaking)   *Server 2 (weak axis shaking)*
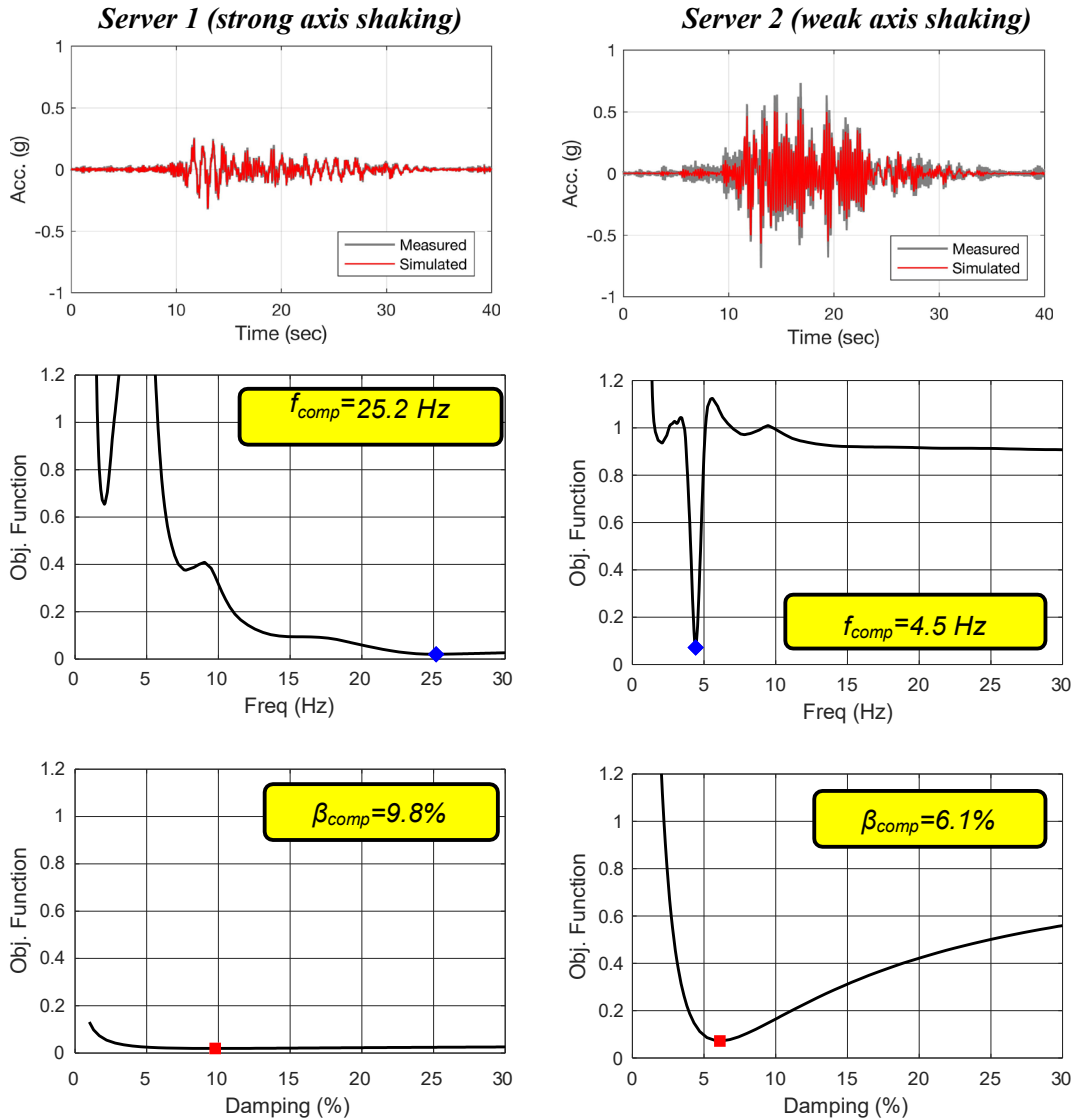
Figure 9. Time-domain dynamic characteristics optimization: measured and simulated component acceleration responses (top); frequency sensitivity curves (middle); and damping ratio sensitivity curves (bottom).

Table 3 summarizes the dynamic characteristics (frequencies and damping ratios) of all nonstructural components considered in this study, as well as the amplification factors as observed from the measured responses during the fixed-base test phase up to design event (FB-1 to FB-5). Results from final test FB-6 are excluded since it represents an extreme event that is normally not considered by the nonstructural design provisions. Among the seven nonstructural components considered in this study, computer server #1 and the air handling unit were rigid components (natural frequencies >20 Hz). The remaining five components were non-rigid components with their natural frequencies range between 4 and 9 Hz. It is noted that the identified damping ratios of these components were between 4.5 and 11, which is larger than the range of 2% and 5% as typically considered in the prior studies (NIST, 2018). Consistent with the ASCE 7 code provisions (ASCE, 2016), the two rigid components (computer server #1 and air handling unit) underwent only very limited acceleration amplification (1.3 as the maximum).

Of the five non-rigid components (with their natural frequencies less than 15 Hz), the measured amplification factors of the computer server #2 and the cooling tower (between 2 and 3) were larger than those of the remaining three components, with values less than 2. The differences in the amplification effects may be attributed to the following two aspects associated with their dynamic characteristics: (1) the natural frequencies of the computer server #2 and the cooling tower were closer to the second mode frequency of the building (~5 Hz during FB-1 but varied at different stages of the test sequence as a result of accumulated structural damage), and (2) the identified damping ratios of the computer server #2 and the cooling tower were moderately smaller than the remaining components.

Table 3. Dynamic characteristics and the component amplification factors of the nonstructural components achieved during the fixed-base tests.

Nonstructural component	Frequency (Hz)	Damping ratio (%)	PCA/PFA
Computer server #1 (strong axis shaking)	22~25	unidentifiable	1.0~1.3
Computer server #2 (weak axis shaking)	4.1~4.6	6.2~7.5	2.0~3.2
Ultrasound imager #1	5.6~7.2	8.5~11.3	1.1~1.6
Ultrasound imager #2	6.5~8.0	7.3~10.8	1.2~1.8
Medical freezer	7.7~9.1	7.1~10.5	1.2~1.5
Cooling tower	4.8~5.6	4.5~5.8	1.9~2.8
Air handling unit	20~22	unidentifiable	1.0

Conclusions and Future Work

With the overall scope of exploring the acceleration amplification effects of nonstructural components using recorded earthquake responses of buildings and nonstructural components. this study focuses on two separate yet complementary tasks: a) characterizing the component amplification effects using a large set of building earthquake responses that are available in the CESMD strong motion database and b) identifying the dynamic characteristics and the amplification effects of nonstructural components during a full-scale building shake table test program. Key findings from this study thus far are summarized as follows:

1. Component amplification effects are not well correlated with the damping ratios of their supporting structures.
2. The vertical distribution profiles of the peak component amplification factors of the first and second modes clearly demonstrate that the component amplification factor is a function of the specific building mode shape and the relative height. This observation corroborates a number of prior studies.
3. According to a limited set of recorded nonstructural seismic responses (five non-rigid components), it appears too conservative to assume an equivalent damping ratio of 2% for nonstructural components during earthquake loads, and in fact in the present study a damping ratio of 5% may be considered as the lower bound value, although some components may attain values as large as 10%.

4. The component amplification effects are highly dependent on the dynamic characteristics of the nonstructural components. The nonstructural components that underwent the largest amplification effects were those with their natural frequencies close to that of a building vibration mode and with smaller damping ratios. The measured amplification factors of these components ranged between 2 and 3 during the earthquake tests.

It is noted that the recorded building responses data analysis currently focuses on the steel moment frame buildings. Investigation of the recorded earthquake responses of the remaining building groups (reinforced concrete shear wall, reinforced concrete moment frame, braced steel frame) is ongoing. The effects of different lateral structural systems on the component amplification effects will be discussed in detail and the results will be included in the final project report.

Acknowledgments

References

Alonso-Rodríguez, A., and Miranda, E. (2016). "Dynamic behavior of buildings with non-uniform stiffness along their height assessed through coupled flexural and shear beams." *Bulletin of Earthquake Engineering*, *14*(12), 3463-3483.

ASCE (2010). *Minimum Design Loads and Associated Criteria for Buildings and Other Structures*, ASCE/SEI 7-10, Structural Engineering Institute of American Society of Civil Engineers, Reston, Virginia.

ASCE (2016). *Minimum Design Loads and Associated Criteria for Buildings and Other Structures*, ASCE/SEI 7-16, Structural Engineering Institute of American Society of Civil Engineers, Reston, Virginia.

Applied Technology Council (ATC). (1978). "Tentative provisions for the development of seismic regulations for buildings." *ATC Rep. No. 3-06*, Palo Alto, CA.

Building Seismic Safety Council (BSSC). (1995). *NEHRP recommended provisions for the development of seismic regulations for new buildings*, 1994 Ed., *FEMA 222A*, Federal Emergency Management Agency, Washington, D.C.

Building Seismic Safety Council (BSSC). (1998). *NEHRP recommended provisions for the development of seismic regulations for new buildings*, 1997 Ed., Part 1: Provisions, *FEMA 302*, Federal Emergency Management Agency, Washington, D.C.

CEN (2004). *Eurocode 8: design of structures for earthquake resistance – Part 1: general rules, seismic actions and rules for buildings.* EN 1998-1. Brussels, Belgium.

Chen, M.C., Pantoli, E., Wang, X., Astroza, R., Ebrahimian, H., Mintz, S., Hutchinson, T., Conte, J., Restrepo, J., Meacham, B., Kim, J., and Park, H., 2013a. *BNCS Report #1: Full-scale structural and nonstructural building system performance during earthquakes and post-earthquake fire - specimen design, construction and test protocol.* Report No. SSRP 13/9. University of California San Diego, La Jolla, CA.

Chen, M.C., Pantoli, E., Wang, X., Astroza, R., Ebrahimian, H., Hutchinson, T.C., Conte, J.P., Restrepo, J.I., Marin, C., Walsh, K.D. and Bachman, R.E. (2016). "Full-scale structural and nonstructural building system performance during earthquakes: Part I–Specimen description, test protocol, and structural response." *Earthquake Spectra*, *32*(2), 737-770.

Cruz, C., and Miranda, E. (2016). "Evaluation of damping ratios for the seismic analysis of tall buildings." *ASCE Journal of Structural Engineering*, 143(1), 04016144.

Cruz, C., and Miranda, E. (2019). "Reliability of damping ratios inferred from the seismic response of buildings." *Engineering Structures*, 184, 355-368.

Drake, R.M. and Bachman, R.E. (1996). "NEHRP provisions for 1994 for nonstructural components." *Journal of Architectural Engineering*, 2(1), 26–31.

Fathali, S., and Lizundia, B. (2011). "Evaluation of current seismic design equations for nonstructural components in tall buildings using strong motion records," *The Structural Design of Tall and Special Buildings*, Vol. 20, No. S1, pp. 30-46.

FEMA E-74 (2012). *Reducing the Risks of Nonstructural Earthquake Damage — A Practical Guide.* Federal Emergency Management Agency, Washington, DC.

Hutchinson, T., Restrepo, J., Conte, J., Pantoli, E., Chen, M., Wang, X., Astroza, R., and Ebrahimian, H. (2014). Shake table testing of a five story building outfitted with NCSs (BNCS project). *Network for Earthquake Engineering Simulation (distributor), Dataset, DOI*, *10*, D38W38349.

Kazantzi, A., Vamvatsikos, D., and Miranda, E. (2018). "The effect of yielding on the seismic demands of nonstructural elements," *Proceedings of the 16th European Conference on Earthquake Engineering*, Thessaloniki, Greece.

Lizundia, B. (2019). "Proposed nonstructural seismic design force equations." *Proc., 2019 SEAOC Convention,* Squaw Creek, CA.

NIST (2017). *Seismic Analysis, Design, and Installation of Nonstructural Components and Systems – Background and Recommendations for Future Work*, NIST GCR 17-917-44, National Institute of Standards and Technology, Gaithersburg, Maryland.

NIST (2018). *Recommendations for Improved Seismic Performance of Nonstructural Components*, NIST GCR 18-917-43, National Institute of Standards and Technology, Gaithersburg, Maryland.

NZS1170.5 (2004). *Structural Design Actions Part 5: Earthquake Actions – New Zealand*. Standards Council of New Zealand, Wellington, New Zealand.

Pantoli, E., Chen, M.C., Wang, X., Astroza, R., Ebrahimian, H., Mintz, S., Hutchinson, T., Conte, J., Restrepo, J., Meacham, B., Kim, J., and Park, H., 2013a. *BNCS Report #2: Full-scale structural and nonstructural building system performance during earthquakes and post-earthquake fire - test results.* Report No.SSRP 13/10. University of California San Diego, La Jolla, CA.

Pantoli, E., Chen, M.C., Wang, X., Astroza, R., Ebrahimian, H., Hutchinson, T.C., Conte, J.P., Restrepo, J.I., Marin, C., Walsh, K.D. and Bachman, R.E. (2016). "Full-scale structural and nonstructural building system performance during earthquakes: Part II–NCS damage states." *Earthquake Spectra*, *32*(2), 771-794.

Taghavi, S. and Miranda, E. (2003). *Response assessment of nonstructural building elements*. Report No. PEER-2003/05, Pacific Earthquake Engineering Research Center, Berkeley, CA.

Van Overschee, P., and De Moor, B. (1996). *Subspace system identification for linear systems.* Kluwer Academic Publishers, Boston, MA.

Watkins, D., Chui, L., Hutchinson, T., and Hoehler M. (2010). *Survey and Characterization of Floor and Wall Mounted Mechanical and Electrical Equipment in Buildings*, Report No. SSRP-2009/11, Department of Structural Engineering, University of California, San Diego.

BUILDING RESPONSE ANALYSIS AND DAMAGE DETECTION USING SUBSPACE IDENTIFICATION METHODS

Kenneth J. Loh and Chin-Hsiung Loh

Department of Structural Engineering
University of California, San Diego

Abstract

The overarching goal of this research is to derive innovative methodologies for analyzing diverse sensing streams to yield actionable information that directly support post-earthquake response, emergency management, and disaster recovery. As a step towards this goal, the objective of this study is to use data collected from the California Strong Motion Instrumentation Program (CSMIP) to demonstrate that a particular class of system identification (SI) techniques – namely, subspace identification (SI) or recursive subspace identification (RSI) – is especially suitable for rapid, post-disaster, structural health assessment. The advantage of SI/RSI is that it is an input-output and data-driven method, where only structural response records (*e.g.*, acceleration records) are needed for extracting dynamic properties of the structure. In this paper, both SI and RSI were be applied to assess CSMIP-instrumented buildings with acceleration records from past ground motion events. The result verified that building dynamic characteristics (*i.e.*, natural frequencies and mode shapes) could be clearly identified using all the recorded data simultaneously. In addition, the RSI algorithm was also employed for analyzing data recorded from the Northridge earthquake event. Time-varying modal properties of the building were also examined.

Introduction

Strong motion data acquired from structures during seismic events can play a vital role in gaining insights into the behavior of these systems if a systematic procedure is adopted in analyzing the acquired data. This process, known as system identification (ID), is an inverse problem in structural dynamics that involves the determination of mathematical models and the estimation of structural parameters based on measured responses under known excitations. Several methods, from the simple transfer function to the more sophisticated output error methods, have been devised [1]. In general, two different approaches have been used to assess the behavior of structures (*i.e.*, most commonly bridges) from their recorded data. The first approach is to develop a finite element model (FEM) and to modify the FEM parameters to match the measured response. This approach looks very attractive but has a major pitfall, since the FEM parameters have to be updated by a trial-and-error process. The second approach is to identify the modal parameters of the system and to study the changes in the structural dynamic characteristics. In this study, the inverse problem (*i.e.*, identification of the system state) will be used.

Many offline system identification algorithms that can be implemented for time-invariant systems with constant modal parameters were developed in the past (*e.g.*, the Kalman filter technique, Eigensystem realization algorithm (ERA) [2], and autoregressive exogenous (ARX) model [3]). Over the past few years, various system ID algorithms have been successfully applied, many of which uses both input and output data [4-7]. Several well-known offline system ID algorithms, including canonical variable analysis (CVA), numerical algorithms for subspace state space system identification (N4SID), multivariable output-error state space algorithm (MOESP), and Instrumental Variable-subspace state space system identification (IV-4SID) [8-10], have been developed.

Traditional system ID algorithms for analyzing building seismic response data and extracting system dynamic characteristics have predominantly been based on multi-input multi-output (MIMO) ARX models. However, they do suffer from several disadvantages:
- It is difficult to determine the model order of multivariate ARX model, and further optimization of parameters needs to be performed.
- There are too many unknown parameters to be estimated, where convergence in optimization may take time and require significant computational effort.
- While it is easy to estimate the frequency response function (FRF) between each pair of response measurements, but it is difficult to estimate the system mode shapes and natural frequencies.

Therefore, in this study, the subspace identification (SI) algorithm was used to analyze the seismic response data of two buildings, namely, the seven-story Van Nuys building and the 13-story Sherman Oaks building. The objective was to examine the dynamic characteristics of these buildings when they were subjected to different earthquake excitations. Furthermore, the recursive subspace identification (RSI) algorithm was also applied to the data collected from these two buildings during the Northridge earthquake. Unlike conventional system ID, SI has the following advantages:
- A good initial model can be quickly obtained with subspace methods, since the linear state space model is employed.
- SI provides simple parametrization for MIMO systems as well as robust noniterative numerical solutions.
- The reliable numerical tool-based methods, such as LQ decomposotion and singular value decomposition (SVD), are employed in the algorithm.
- SI provides rapid adoption in application through the use of stabilization diagrams to reliably estimate system dynamic characteristics.

Subspace Identification using Both Input and Output Measurements

In this section, data-driven subspace identification (SI-DATA) was used to extract the system dynamic characteristics seismic response data of the structure. First, consider a discrete time, state-space, dynamic system with n degree-of-freedoms (DOF). The system equation can be represented as [9]:

$$\mathbf{X}_{k+1} = \mathbf{A}_d \mathbf{X}_k + \mathbf{B}_d \mathbf{u}_k + \mathbf{w}_k \tag{1a}$$
$$\mathbf{y}_k = \mathbf{C}_c \mathbf{X}_k + \mathbf{D}_c \mathbf{u}_k + \mathbf{v}_k \tag{1b}$$

with $\mathbf{A}_d = \text{expm}(\mathbf{A}_c \Delta t) \in \mathbb{R}^{2n \times 2n}$, $\mathbf{B}_d = (\mathbf{A}_d - \mathbf{I}_{2n})\mathbf{A}_c^{-1}\mathbf{B}_c \in \mathbb{R}^{2n \times m}$. $\mathbf{A}_d$ is called the discrete-time state matrix, $\mathbf{B}_d$ is the discrete-time input matrix, $\mathbf{X}_k = \mathbf{X}(k\Delta t)$ is the discrete-time state vector, Δt is the sample time, and $k \in \mathbb{N}$. Here, $\mathbf{w}_k \in \mathbb{R}^{2n \times 1}$ is the process noise due to disturbances or modeling error, and $\mathbf{v}_k \in \mathbb{R}^{l \times 1}$ is the measurement noise due to disturbances or malfunction of the sensing nodes. Equation 1 is also known as a discrete-time combined deterministic-stochastic system, because it is a combination of a deterministic system and a stochastic system by combining the state $\mathbf{X}_k$ and output $\mathbf{y}_k$ individually. For subspace identification, the input and output measurements should be arranged into the format of a "data Hankel matrix". If the modal properties (*i.e.*, natural frequency, damping ratio, and mode shape) of the structure are needed, the Multivariable Output-Error State Space algorithm (MOESP) can be employed to extract the column space of the extended observability matrix from the LQ decomposition of the Hankel matrix [10].

Implementation of the Stabilization Diagram for SI

When applying SI-DATA for structural system identification, the method does not yield exact values for the parameters but only estimates with uncertainties. These uncertainties are responsible for the appearance of spurious modes. One of the important challenges is to remove these spurious modes. For this purpose, the stabilization diagram is used. The stabilization diagram has frequencies plotted in the horizontal axis and model orders plotted in the vertical axis. The quality of the stabilization diagram depends on the values of the input parameters of the algorithm and the noise ratio of the time series under analysis. In order to present a better visualization using stabilization diagram, certain criteria to remove the spurious modes need to be defined. In this study, four criteria were used and are described next.

First, the duration of the recorded data was selected. Since the seismic response data collected from the structure may contain pre-event memory data as well as the coda wave, therefore, the criterion to select the duration of data for SI must be defined. The initial time from the recorded data can be determined from the concept of a P-wave picker by using the following equation for calculating the Arias Intensity Criterion (AIC) [12]:

$$AIC(t) = t \log(\text{var}(a[1:t])) + (N - t + 1)\log(\text{var}(a[t+1:N])) \tag{2}$$

where t is the time moving window length, and N is entire time length. In addition, $\text{var}(a[1:t])$ is the variance of the data $a(t)$. The initial starting time can be determined from the time when the rate of slope of AIC values change dramatically, as is shown in Figure 1 and corresponding to when t is 15.0 s. Besides, the end point of the data can be determined from the plot of Arias Intensity when it reaches 99.5% (also shown in Figure 1 and when t is 56.5 s).

Second, depending on the quality of the data, a low-pass filter may be applied. Here, a Butterworth filter with order 10 was employed to filter out the high frequency signals so as to enhance the quality of the stabilization diagram. Third, for each model order, the identified mode shapes of the structure was identified. To ensure that these were the correct mode shapes, the modal assurance criterion (MAC) was applied between two different model orders:

$$MAC(\Phi^*_j \cdot \Phi_i) = \frac{\left|\Phi^*_j \cdot \Phi_i\right|^2}{(\Phi^*_j \cdot \Phi_j)(\Phi^*_i \cdot \Phi_i)} \geq MAC_\phi \tag{3}$$

The value of $MAC(\Phi^*_j \cdot \Phi_i)$ is a user-defined value (*e.g.*, by setting the threshold to 95%).
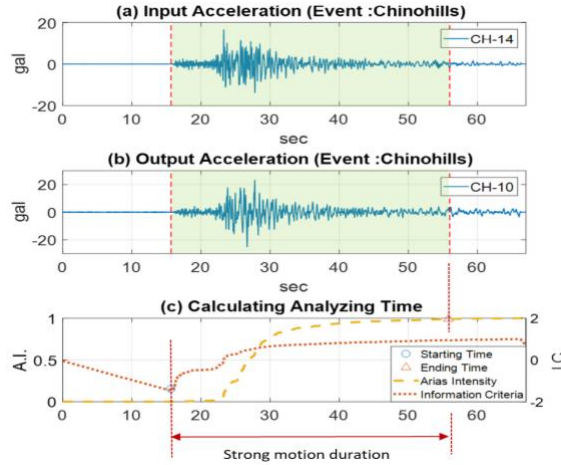
Figure 1. Plot of AIC and normalized Arias intensity to identify the strong motion duration

Last, the modal phase collinearity (MPC) could be calculated. For each particular identified mode, it was necessary to check the phase collinearity among each measurement node. The phase vector Ψ_k of a k_{th} mode from l measurement nodes is shown as:

$$\text{phase}(\boldsymbol{\psi}_k) = [b_{k,1} \quad b_{k,2} \quad \cdots \quad b_{k,l}]^T \in \mathbb{R}^{l \times 1} \quad (-\pi \leq b < \pi) \tag{4}$$

To ensure that it is the correctly identified mode, the phase difference among each measurement node should be either in-phase or out-of-phase:

$$|b_{k,q} - b_{k,r}| = 0 \quad \text{or} \quad \pi \quad (q \neq r) \tag{5}$$

Figure 2 shows an example of a stabilization diagram that compares different criteria applied. For all cases, a low-pass filter with a cutoff frequency of 50 Hz was implemented. In general, it can be observed that the consideration of both criteria (*i.e.*, MAC of 0.95 and MPC of 0.90) resulted in clear modes being identified (*i.e.*, green circles in Figure 2). Besides, with increasing model order, more noise modes can be observed.

Figure 2. Example of a stabilization diagram with different criteria applied to remove spurious modes.

Figure 3. Layout of strong motion instrumentation in the 7-story Van Nuys building.

Table 1: List of earthquake event from Van Nuys building for analysis.

Date	Earthquake	Epic.(Fault) Dist.(km)	Peak Acceleration (g)		Data
			Ground	Struct.	Raw data
1994/6/17	Northridge #	7.0 (1.7)	0.47	0.59	V(broken)
2008/7/29	Chinohills #	71.5 (--)	0.054	0.14	v(missing CH:8,13)
2010/7/7	BorregoSprings #	203.8 (--)	0.004	0.016	V(Missing CH:8,13)
2014/3/17	Encino #	9.8 (--)	0.144	0.219	v(Missing CH:8,13)

Building Seismic Response Analysis using SI-DATA

Analysis of the 7-Story Van Nuys Building

The Van Nuys building was instrumented with 16 accelerometers in 1980 and by CSMIP. Figure 3 shows the instrument layout in the building with 16 accelerometers distributed across five levels. The building was repaired and strengthened with concrete shear walls after the 1994 Northridge earthquake. Among all the seismic event recorded from the building, four seismic events (as shown in Table 1) were selected for the analysis conducted in this study. Prior to SI analysis, the time-frequency analysis on the roof response data of the building was generated. The modified complex Morlet wavelet with variable central frequency was used to generate the spectrogram [14]. Figure 4a shows the spectrograms calculated using Channels 9 and 3 of the Northridge earthquake data, while Figure 4b shows the spectrograms for the Encino earthquake data; all these channels corresponded to the roof response data. A comparison between these two sets of event data shows a significant change in the fundamental dominant frequency from about 0.5 Hz to 2.0 Hz. This result is expected and is consistent with the retrofit performed after the Nothridge earthquake, which would increase the stiffness of the structure and hence its dominant frequency.

Figure 4. Spectrograms of Channels 3 and 9 of the Van Nuys building corresponding to two seismic events: (top) Northridge earthquake and (bottom) Encino earthquake

Before using SI to determine the dynamic characteristics of the Van Nuys building, the sensitivity of model order according to the stabilization diagrams was examined. Figure 5 shows two stabilization diagrams computed using two different model orders (*i.e.*, based on *cl* values 120 and 160) corresponding to the Northridge earthquake data. Since a larger model order would include more data in each column of the data Hankel matrix, more noisy modes would appear. However, at the same time, a larger model order also means that some extra modes could be identified. For the case of the Northridge earthquake dataset, one could identify the torsional mode at frequency of 0.697 Hz. This mode can not be observed for the case when the *cl* value was set to 120. Using the spectrogram corresponding to a *cl* value of 160, three fundamental modes from the Northridge earthquake record was constructed, as is shown in Figure 6. The first mode is the longitudinal mode, the second mode is a combination of longitudinal and transverse modes, and the third mode is the torsional mode.
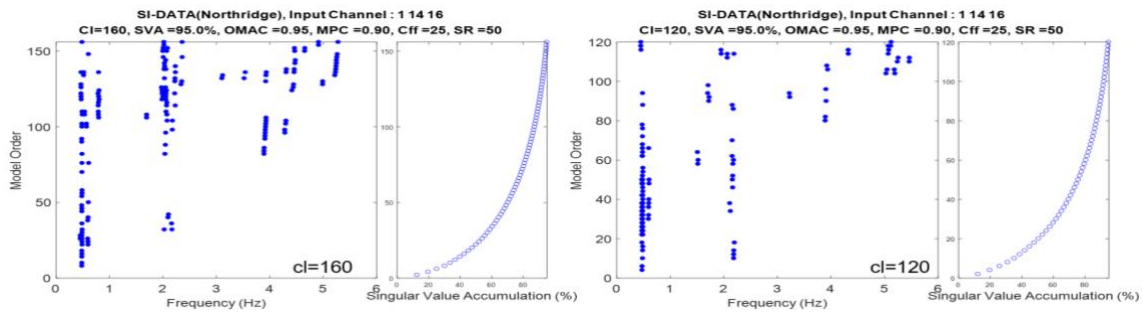
Figure 5. Comparison of stabilization diagrams using two different *cl* values.
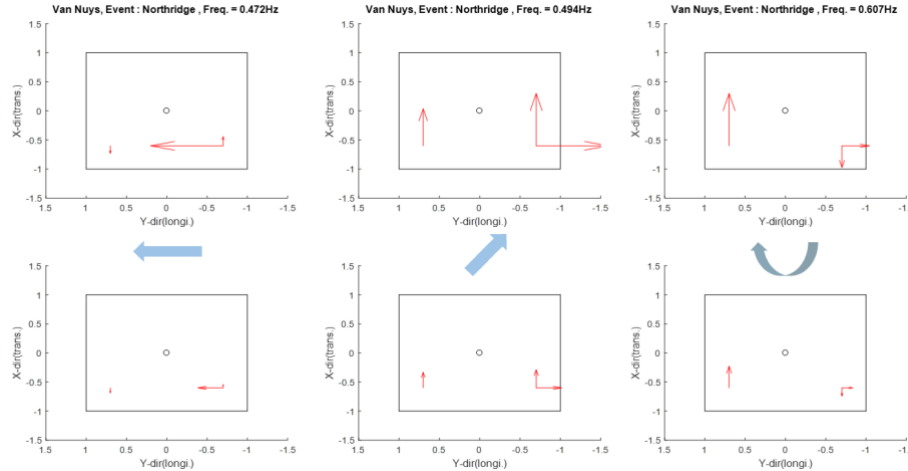
Figure 6. The three fundamental modes of the Van Nuys building was identified using SI (corresponding to data from the Northridge earthquake).

A similar approach was also employed for the other three earthquake events selected for this study. Figure 7 shows the stabilization diagrams from the other three small earthquake event datasets. It can be observed that the identified dominant frequencies are quite consistent among these events. Table 2 shows the comparison of the three identified fundamental frequencies of the building. Furthermore, the differences of these modal frequencies with respect to the result from Northridge earthquake is significant. As mentioned earlier, this result is expected and is due to the influence of retrofitting the building after the Northridge earthquake. The identified mode shapes from the Chino Hills earthquake is shown in Figure 8. The major difference observed between the Northridge and Chino Hills event is the second mode. For the small earthquake event, one can identify the transverse mode, while, for the larger Northridge earthquake, the second mode appears to be a combination of longitudinal and transverse motions.
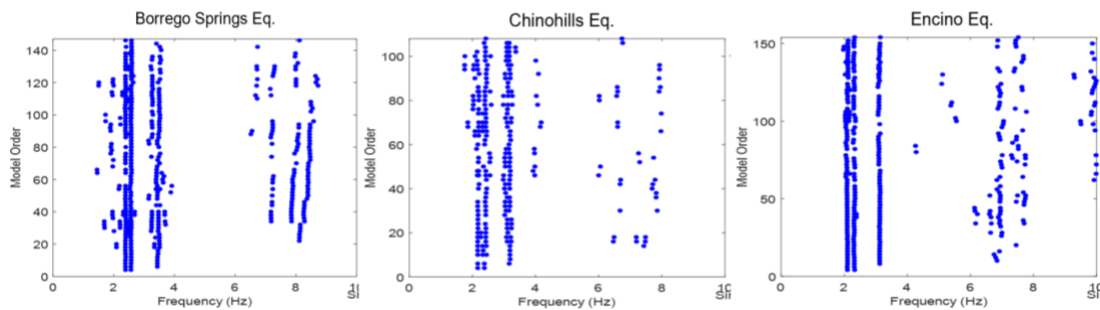
Figure 7. Stabilization diagrams from three earthquake events, namely, the Borrego Spring, Chino Hills, and Encino earthquakes

Table 2. Identified modal frequencies of the Van Nuys building

Event\Mode	1st mode (Longitudinal)	2nd mode (Transverse)	3rd mode (Torsion)
Northridge	0.468	0.487	0.697
Chinohill	2.174	2.382	3.172
BorregoS.	2.388	2.577	3.442
Encino	2.111	2.327	3.133
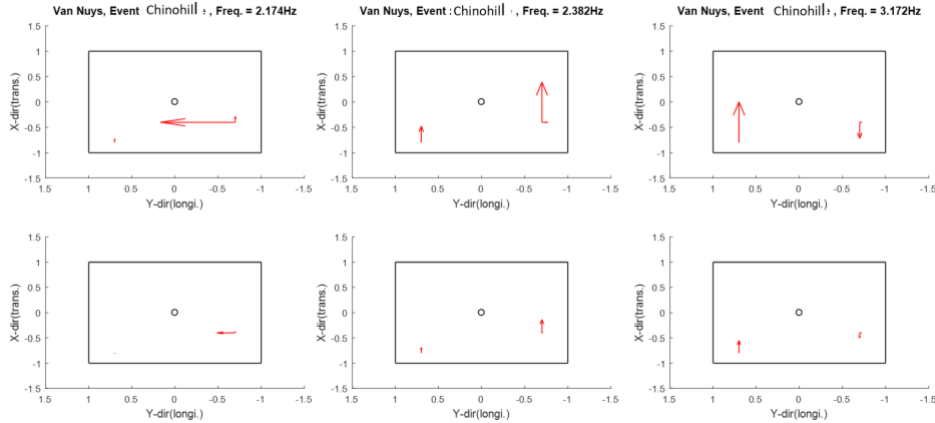
Figure 8. The identified three fundamental modes using data from the Chino Hills earthquake

Analysis of the 13-Story Sherman Oaks Building

In 1977, the 13-story Sherman Oaks building was instrumented with 15 accelerometers across five different levels. This building was also retrofitted with friction dampers after the 1994 Northridge Earthquake. Figure 9 shows the instrument layout in the building. Among all the recorded earthquake events from this building, five event datasets were selected for this study. SI analysis was performed using the same procedure as was described in the previous section and, specifically, for identifying the system natural frequencies.

Figure 10 shows the comparison of the stabilization diagrams corresponding to three different seismic events. It can be observed that the differences among these three stabilization diagrams are quite significant. First, the change in modal frequencies among these three dataset are obvious. One reason is because both the Whittier and Northridge earthquakes induced significant structural response, and this could have caused the structural system to undergo inelastic deformation. Second, the other reason is because the building was retrofitted with friction dampers after the 1994 Northridge earthquake.
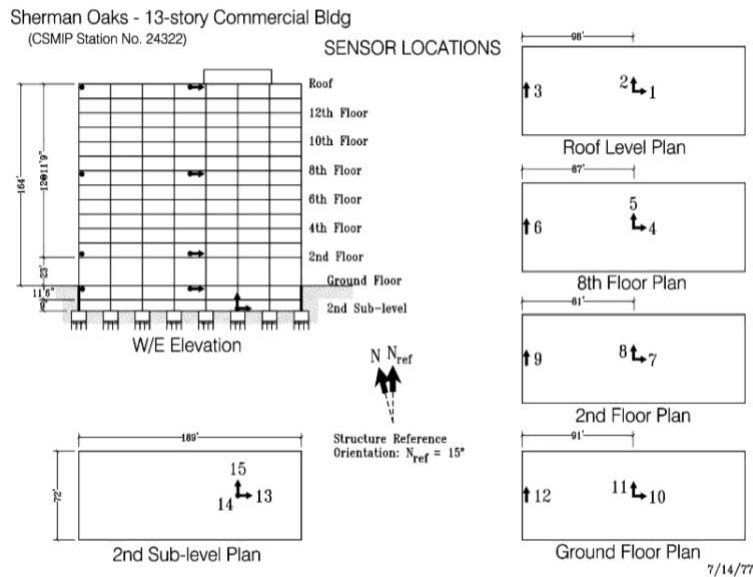
Figure 9. Strong motion instrumentation layout in the 13-story Sherman Oaks building
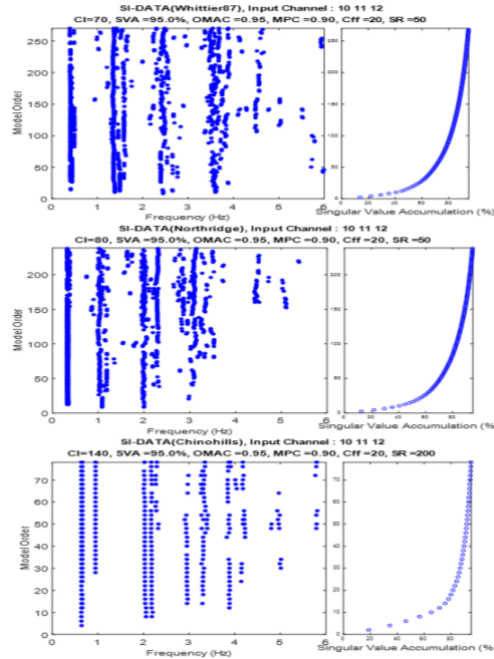
Figure 10. Stabilization diagrams corresponding to three different seismic events (*i.e.*, the Whittier, Northridge, and Chino Hills earthquakes).

Table 3 summarizes the identified natural frequencies of the Sherman Oaks building when SI was performed using five different earthquake datasets. In addition, the identified mode shapes from Whittier, Northridge, and Chino Hills earthquakes are shown in Figure 11. The mode shapes extracted from the two large earthquake excitations are significantly different than the mode shapes identified from the other smaller event datasets.

Table 3. Identified modal frequencies of the Sherman Oaks 13-story building.

Shenman Oak 13-story Building	Horizontal Peak Acceleration (g)		Identified system natural frequency (Hz)								
	Groiund	Structture	1st -Trans.	1st -Long.	2nd -Trans.	2nd -Long.	3rd -Trans.	4th -Trans.	1st -Tor.	2nd -Tor.	3th -Long.
Whittire87 EQ	0.15	0.17	0.408	0.448	1.368	1.501	2.398	3.534			
Northridge EQ	0.46	0.90	0.327	0.348	1.09		2.001				
Chinohills EQ	0.049	0.094	0.644	0.664	2.034	2.178	3.313		0.952	2.956	3.885
Calexico EQ	0.004	0.02	0.958	0.657	2.08	2.213		3.425	3.036		3.927
Encino EQ	0.242	0.538	0.634	0.656	1.953	2.155		3.23	2.918		3.841

Figure 11. The identified modes shapes of the 13-story Sherman Oaks building using three earthquake event datasets (*i.e.*, Whittier, Northridge, and Chino Hills earthquakes).
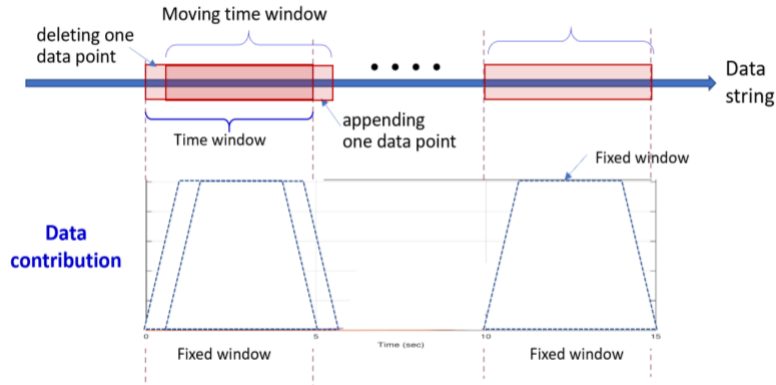
Figure 12. Concept of the moving window used in recursive subspace identification

Recursive Subspace Identification (RSI) with BonaFide LQ Renewing Algorithm

Despite the advantages of the SI-DATA algorithm, a disadvantage is that it is an offline identification technique and that it can only estimate the time-varying state of a structure. In order to track the time-varying modal properties of the system during strong earthquake excitations, recursive (or online) subspace identification needs to be used. The concept of recursive subspace identification is similar to moving time window system ID, as is illustrated in Figure 12. The analysis of the initial time window is the same as that of the SI-DATA algorithm (as was described in the previous section). When a new set of input and output data are appended, the RSI-BonaFide is applied. Furthermore, the RSI-BonaFide-Oblique algorithm is a projection matrix renewing method based on an oblique projection accomplished by LQ decomposition performed on the data Hankel matrix. One of the most significant points about the RSI-BonaFide-Oblique method is that it utilizes a fixed-length moving window technique that keeps the analyzed length of input and output data as a constant; therefore, there is no forgetting factor used in this particular algorithm [15].

Building Response Seismic Analysis using RSI

Since the peak ground acceleration and the peak acceleration response recorded from the 7-story Van Nuys building during Northridge earthquake excitation were 0.47 g and 0.59 g, respectively, it was believed that the building was most likely experienced inelastic response. Thus, the RSI-BonaFide method was used to investigate the time-varying modal parameters of the building. In order to simplify the analysis, instead of using all of the recorded data from the building, only the basement and roof acceleration records in longitudinal and transverse directions were used. The window length was selected and fixed as 4 s, and the duration of the window shift was set as 0.5 s. Figure 13 shows the identified time-varying modal frequencies in the longitudinal and transverse directions. It should be clarified that the result only provides the natural frequencies and their change with respect to time, and there it is not possible to detect the change of stiffness in the structure.
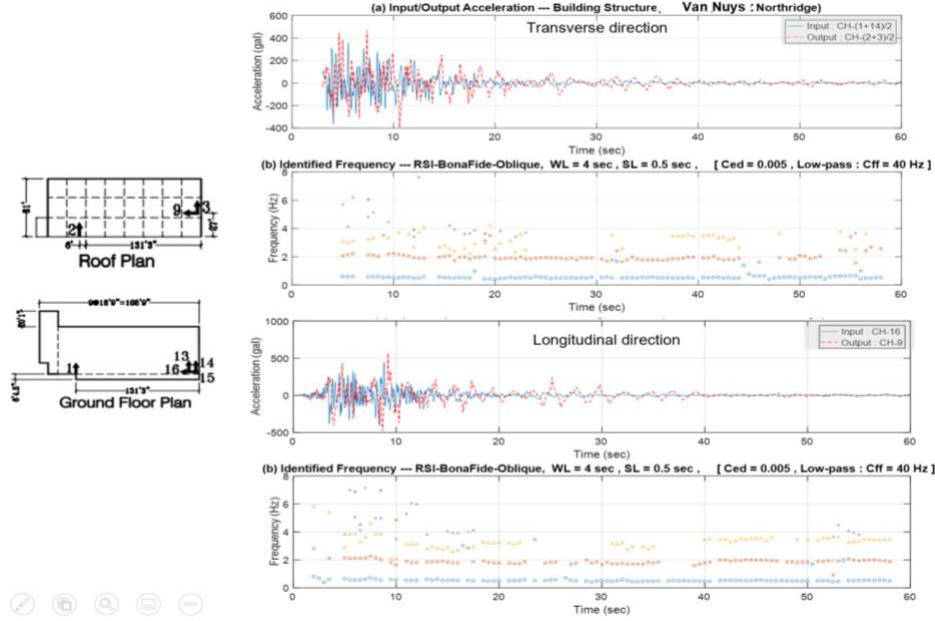
Figure 13. The identified time-varying modal frequencies of the Van Nuys building during the Northridge earthquake as determined using RSI-BonaFide algorithm

According to Caicedo *et al.* [16], a least squares optimization was developed to estimate the inter-story stiffness of each DOF using the identified modal parameters, such as by using the modal frequencies and mode shapes. Consider an *n*-story shear-type structure with one translational DOF on each floor (*i.e.*, 1 DOF per floor). The method was derived from the eigen-equation of this *n*-DOF system (where $n = 1\text{x}N$). At each time instant $t = k$ s, one can define the eigen-equation of the r_{th} mode according to Equation 6:

$$K_{System}\Phi_{r,(t=k)} = \omega^2_{r,(t=k)}M_{System}\Phi_{r,(t=k)} \tag{6}$$

where $r = 1, 2, 3, \ldots, s$, and s is the number of the identified modes ($s \leq n$) from RSI. By assuming that the structural model is a lumped-mass system, the mass and stiffness matrices can be expressed as:

$$M_{System} = \begin{bmatrix} m_1 & 0 & 0 & 0 \\ 0 & m_2 & 0 & 0 \\ 0 & 0 & \ddots & 0 \\ 0 & 0 & 0 & m_n \end{bmatrix} \tag{7}$$

$$K_{System} = \begin{bmatrix} k_1 + k_2 & -k_2 & 0 & 0 \\ -k_2 & k_2 + k_3 & \ddots & 0 \\ 0 & \ddots & \ddots & -k_n \\ 0 & 0 & -k_n & k_n \end{bmatrix} \tag{8}$$

It is assumed that the system mass matrix is known *a priori*. Then, the only unknown variables become the inter-story stiffness of each floor, namely $k_1, k_2, \ldots k_n$. At each time instant "k", the equation can be re-organized as shown in Equation (9).

$$\begin{bmatrix} \Delta_1 \\ \Delta_2 \\ \vdots \\ \Delta_s \end{bmatrix}_{(s\times n)\times n} \times \begin{bmatrix} k_1 \\ k_2 \\ k_3 \\ \vdots \\ k_n \end{bmatrix}_{(n\times 1)} = \begin{bmatrix} \Lambda_1 \\ \Lambda_2 \\ \vdots \\ \Lambda_s \end{bmatrix}_{(s\times n)\times 1} \tag{9}$$

The identified mode shapes can then be allocated into a matrix. $\Delta_{(t=k)}$ is allocated with the identified mode shapes with a dimension of $(s \times n) \times n$. The multiplication of modal frequency, mode shape, and floor mass also needs to form a single vector, namely $\Lambda_{(t=k)}$, with a dimension of $(s \times n) \times 1$. It should be mentioned that the number of identified modes is usually less than the number of exact modes in the structural system (*i.e.*, $s \leq n$). Nevertheless, the inter-story stiffness can then be estimated. In general, the result can provide a first stage safety assessment of the building by using the identified time-varying inter-story stiffnesses. Besides, to update the mass and stiffness matrices and make them compatible with both the measured eigenvalues and eigenvectors computed at each time instant, a model updating technique called efficient model correction method (EMCM), proposed by Yuen [17], can be applied.

For detecting the time-varying stiffness of the 7-story Van Nuys during an earthquake, a simplified lumped mass model needs to be assumed. This assumption needs to incorporate the distribution of the instrumented earthquake monitoring system. For simplicity, this building was assumed to be a 2-DOF system with mass $m_1 = 4M$ and $m_2 = 3M$, as is shown in Figure 14. The identified time-varying stiffness (stiffness index) of this 2-DOF simplified model is also shown in Figure 14. It should be mentioned that the variation of the stiffness index with respect to time does not indicate the dramatic change of stiffness at every instant of time during the earthquake excitation. As described earlier, this is the result of an equivalent linear stiffness index (secant stiffness) within the preselected and designated time window. For safety assessment of the structure, one should first apply the same approach to assess the time-varying stiffness of the structure using datasets corresponding to smaller seismic events, where the structure performed linearly. In doing so, the dynamic characteristics of the system can be acquired in a more stable fashion to build up a correct nominal model (*i.e.*, corresponding to the undamaged case). This approach was also applied to the 13-story Sherman Oaks building, and the result is shown in Figure 15.
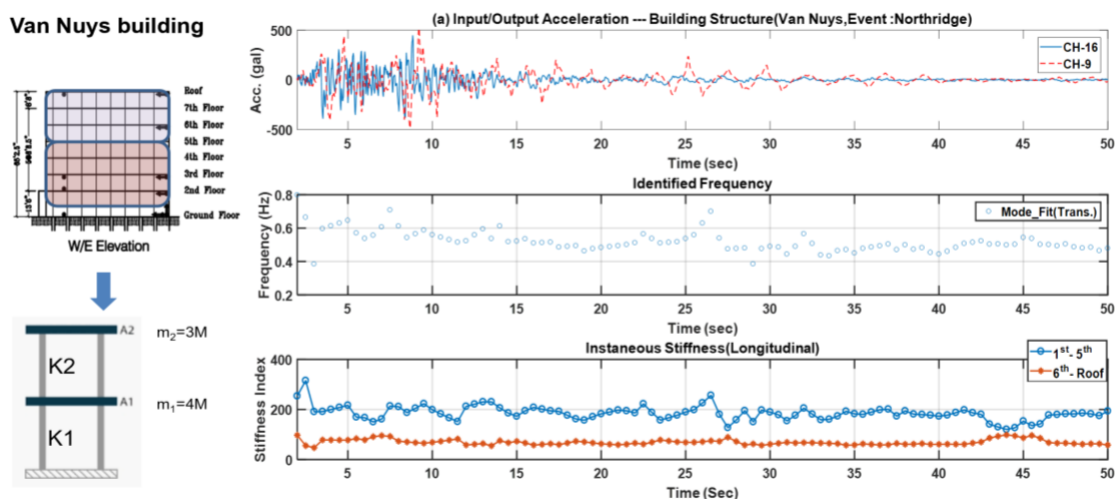
Figure 14. The identified time-varying stiffness index from the simplified model of the 7-story Van Nuys building
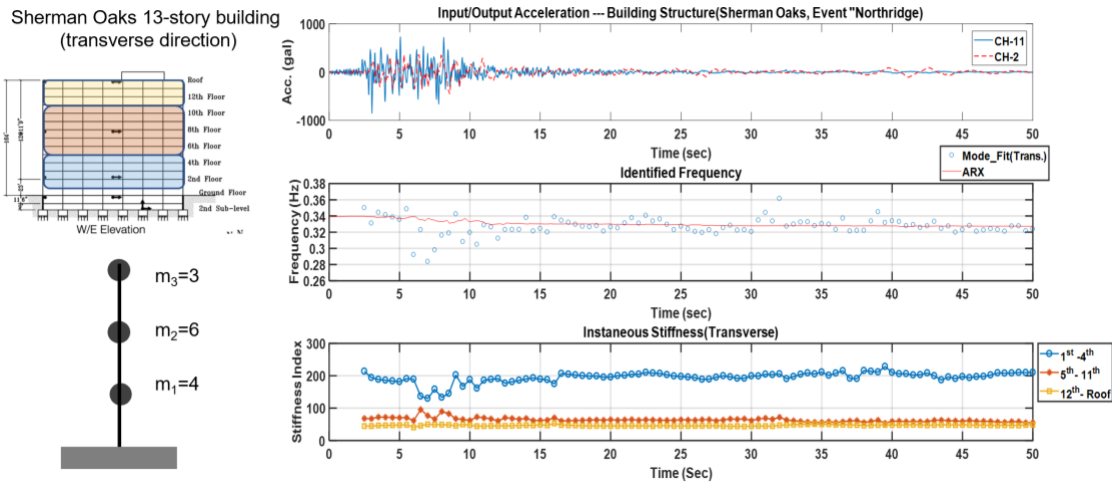
Figure 15. The identified time-varying stiffness index from the simplified model of the 13-story Sherman Oaks building

Conclusions

In this study, both subspace identification and recursive subspace identification with BonaFide LQ renewing algorithm (*i.e.*, incorporating a moving window technique) were utilized to identify the modal parameters (namely the natural frequencies and mode shapes) of two buildings during strong earthquake excitations. For SI, the stabilization diagram played an important role for extracting the real structural modes while removing the spurious modes. For RSI, based on strong seismic response datasets collected from the two buildings (*i.e.*, 7-story Van Nuys and 13-story Sherman Oaks buildings), one could identify their time-varying modal frequencies during these events. The least squares stiffness method was used to estimate the system stiffness matrix using simplified models of these structures. In general, the conclusion was that SI could provide a convenient and systematic multivariate system identification method for estimating the dynamic characteristics of these buildings. By combining the result from RSI (corresponding to when the structure was subjected to strong motion) and by developing a nominal model (corresponding to the undamaged case), one can potentially conduct damage assessment.

Acknowledgments

This research was supported by the Department of Conservation for the California Strong Motion Instrumentation Program (CSMIP) data interpretation project no. 1018-567.

References

[1]   C. R. Farrar, S. W. Doebling, and D. A. Nix, 2001, "Vibration-based structural damage identification," *Philosophical Transactions of the Royal Society A*, **359**(1778): 131-149.

[2]   J. N. Juang, *Applied System Identification*. Prentice Hall: Upper Saddle River, NJ (1994).

[3]   L. Lennart, *System Identification: Theory for the User, 2nd edition*. Prentice Hall: Upper Saddle River, NJ (1999).

[4]   B. D. Rao and K. S. Arun, 1992, "Model based processing of signals: a state space

approach," *Proceedings of the IEEE*, **80**(2): 293-309.

[5]   A-J. van der Veen, E. F. Deprettere, and A. L. Lee Swindlehurst, 1993, "Subspace based signal analysis using singular value decomposition," *Proceedings of the IEEE*, **81**(9): 1277-1308.

[6]   M. Viberg, 1994, "Subspace methods in system identification," *IFAC Proceedings Volumes*, **27**(8): 1-12.

[7]   P. van Overschee and B. De Moor, *Subspace Identification for Linear Systems: Theory-Implementation-Applications*. Kluwer Academic Publishers: Dordrecht, Netherlands (1996).

[8]   W. E. Larimore, 1994, "The optimality of canonical variate identification by example," *Proceedings of SYSID*, **94**: 151-156.

[9]   P. van Overschee and B. De Moor, 1994, "N4SID: Subspace algorithms for the identification of combined deterministic-stochastic systems," *Automatica*, **30**(1): 75-93.

[10]   M. Verhaegen, 1994, "Identification of the deterministic part of MIMO state space models given in innovations form from input-output data," *Automatica*, **30**(1): 61-74

[11]   J. C. Willems, 1986, "From time series to linear systems, part I," *Automatica*, **22**(5): 561-580.

[12]   H. Zhang, C. Thurber, and C. Rowe, 2003, "Automatic p-wave arrival detection and picking with multiscale wavelet analysis for single-component recordings," *Bulletin of the Seismological Society of America*, **93**(5): 1904-1912.

[13]   J-H. Weng, C-H. Loh, and J. N. Yang, 2009, "Experimental study of damage detection by data-driven subspace identification and finite-element model updating," *Journal of Structural Engineering*, **135**(12): 1533-1544.

[14]   W. Hsueh and C-H. Loh, 2017, "Damage detection of structures by wavelet analysis: application to seismic response of steel frames," *Proceedings of SPIE – Sensors and Smart Structures Technologies for Civil, Mechanical, and Aerospace Systems*, **10168**: 1016811.

[15]   K. Kameyama, A. Ohsumi, Y. Matsuura, and K. Sawada, 2005, "Recursive 4SID-based identification algorithm with fixed input-output data size," *International Journal of Innovative Computing, Information and Control*, **1**(1): 17-33.

[16]   J. M. Caicedo, S. J. Dyke, and E. A. Johnson, 2004, "Natural excitation technique and eigensystem realization algorithm for phase I of the IASC-ASCE benchmark problem: simulated data," *Journal of Engineering Mechanics*, **130**(1): 49-60.

[17]   K. V. Yuen, 2010, "Efficient model correction method with modal measurement," *Journal of Engineering Mechanics*, **136**(1): 91-99.

ESTIMATION OF COLUMN BASE FLEXIBILITY IN INSTRUMENTED BUILDINGS

Amit Kanvinde[1], Tomasz Falborski[2], Ahmad Hassan[1]

[1]Department of Civil and Environmental Engineering, University of California, Davis
[2]Faculty of Civil and Environmental Engineering, Gdansk University of Technology, Poland

Abstract

The rotational fixity of column base connections in Steel Moment Resisting Frames (SMRFs) strongly influences their seismic response. However, approaches for estimating base fixity have been validated only against laboratory test data. In the present study these approaches are examined based on strong motion recordings from two instrumented SMRF buildings in California. Three-dimensional simulation models are constructed for these buildings, including the gravity framing and nonstructural stiffness. For each building, the base fixities are parametrically varied. These include pinned and fixed bases, as well as intermediate fixities determined from previously developed models that are appropriate to simulate the specific types of base connections used in the buildings. The simulated response of these buildings is compared to strong motion recordings to inform optimal approaches for simulating column bases.

Introduction

Steel Moment Resisting Frames (SMRFs) are popular lateral load resisting systems in seismically active regions, due to their ductility and the architectural versatility offered by unbraced bays. Consequently, research studies pertaining to SMRFs are very extensive – addressing member, connection, as well as system response. These studies have resulted in well-established design procedures for SMRFs, including for overall system design and member selection (AISC 341-16 [1]), beam-to-column connections (AISC 358-16 [2]), and column base connections (AISC *Design Guide One* – Fisher and Kloiber [3]). Despite these advances, one area (in the context of SMRFs) where the guidance is relatively less developed is the simulation of column base connections. This is because research on column base connections has lagged other SMRF connections (e.g., beam-column connections), such that the focus in the context of base connections has been on developing strength models (AISC *Design Guide One* – Fisher and Kloiber [3]) rather than stiffness or load-deformation response. The lack of research has been further fueled by the presumption that base connections respond either as fixed (if capacity designed to be stronger than the attached column) or as pinned (if designed otherwise). Following this presumption, base connections are simulated as either fixed or pinned in current design and performance assessment practice (Zareian and Kanvinde [4]). Recent research has shown this practice to be highly problematic for two reasons. First, experiments on various types of column base connections (shown in Figures 1a-c) ranging from exposed base plate connections (Gomez et al. [5]), slab-overtopped base plate connections (Barnwell [6]) and embedded base connections (Grilli et al. [7]) indicate that base connections exhibit partial fixity, which contravenes both the fixed and pinned assumptions. Second, the erroneous characterization of fixity (as either fixed or pinned) has significant implications for structural

response. For both these reasons, structural response is sensitive to estimates of base fixity, underscoring the need for its accurate characterization. Motivated by this, base fixity models have been proposed for various base connection details, including for exposed (Grilli et al. [7]), slab-overtopped (Tryon [8]), and embedded (Torres-Rodas [9]). Each of these models has been developed using (and validated against) a limited set of laboratory test data, typically associated with the research group that developed the models. Consequently, results from each model provide excellent agreement with laboratory data it is developed from (and moderately good agreement against other sets of data – see Torres-Rodas [9]). However, applying these models with confidence to simulate the rotational fixity of as-built field details is challenging for the following reasons: (1) the laboratory specimens investigate only a limited set of configuration details, i.e., anchor rod configurations, base plate shape and aspect ratio, surrounding reinforcement, such that extrapolation of the models to field details that are different has not been verified, (2) all laboratory specimens are loaded laterally under a constant axial load, whereas in the field, the axial load varies due to seismic motions – this is an important effect because axial load has a strong effect on the fixity of exposed base plate connections – Kanvinde et al. [10], (3) in practice, base connections are loaded under biaxial bending, whereas none of the models or tests have interrogated the effect of biaxial bending on rotational fixity, and (4) the laboratory specimens are anchored to a strong floor, such that the effect of soil deformations is not reflected in the test data.

Against this backdrop, this paper seeks to inform best practices for simulation of column base fixity in SMRFs using recorded time history data from two buildings instrumented as part of the California Strong Motion Instrumentation Program (Naeim et al. [11]). Sophisticated 3-dimensional frame models of these buildings are constructed, and various options (including the previously published models introduced above) for simulating column bases are evaluated by comparing the simulated response of these buildings to the recorded response under the recorded seismic excitations. To maximize confidence in the findings, the paper relies on objective error measures to compare the recordings with simulations, and highly detailed structural simulations including a process to independently evaluate the stiffness of nonstructural components.

Types of Column Base Connections and Flexibility Models

Referring to Figure 1 shown below, SMRF column base connections in seismically active regions of the US take numerous forms, depending on the loading, soil type, system design and architectural considerations, and local economies. Broadly, these may be categorized into exposed base plate connections, or embedded connections, with detailing variations (e.g., placement of anchor rods) within each form. The following subsections describe these connections, outlining the physical mechanisms by which they deform and resist loads, along with the models proposed to estimate their flexibility.
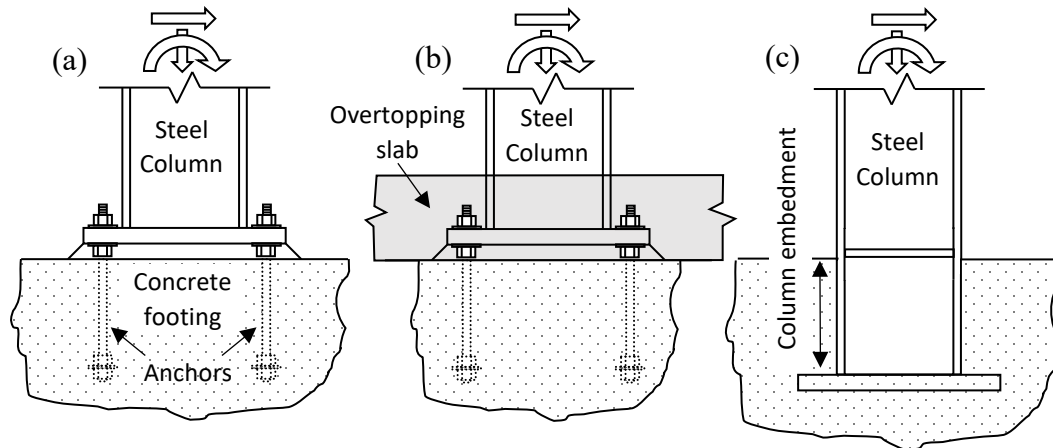
Figure 1. Common types of column base connections: (a) exposed base plate, (b) slab-overtopped exposed connections (c) embedded column base.

Exposed Base Plate Connections

Figure 1a shown previously schematically illustrates an exposed base plate connection in which the column is welded to a base plate, which is anchored to a footing using anchor rods, or post installed anchors (Gomez et al. [5]). The connection resists applied axial forces and moments through a combination of upward bearing on the compressive side of the connection and tensile forces in the anchor rods. In modern construction, usually a minimum of four anchor rods (near the corners of the connection) are provided to maintain erection stability as per OSHA [12]; these provide some degree of fixity even if the connection is not designed to carry significant moment. Additional anchor rods are often provided for supplemental strength. The connection itself is designed for the limit states of flexural yielding of the base plate, bearing failure in the footing, or anchor rode failure – by yielding, pullout or breakout (Steel Design Guide One [3]). Kanvinde et al. [10] presented a model to estimate the rotational flexibility of laboratory specimens with good accuracy (average test-predicted ratio $k_{base}^{test}/k_{base}^{model} = 0.89$). Subsequent research by Trautner [13] corroborates the validity of this model for other laboratory test data. Exposed base plate type connections are preferred for low- to mid-rise (less than 3-4 stories) SMRFs because it is economically unfeasible to transfer larger base moments through anchor rods; in such cases embedded base connections are typically specified.

Sometimes, exposed base connections are overtopped with a slab on grade (see Figure 1b); this is often the case in residential or commercial (as opposed to industrial) construction. The slab-on-grade is usually not considered in design, assuming that the connections respond in a manner similar to exposed base plate connections. However, studies by Barnwell [6] indicate that although the primary mechanism of load resistance is similar to the exposed base plate connections, the slab on grade (which is typically in the range of 150-200mm) increases the rotational fixity and provides additional strength as well. Tryon [8] proposed a model to estimate the rotational fixity of slab-overtopped connections. This model this model does not incorporate the effect of axial load since none of the laboratory specimens used for validation featured axial load.

Embedded Base Plate Connections

In contrast to slab-overtopped exposed base plate connections (Figure 1b) where in the embedment due to the slab is incidental, columns are often embedded in the footing by design (Figure 1c), to provide resistance through concrete bearing when exposed base plate connections with anchor rods become economically unfeasible. These connections are typically specified in mid- to high-rise buildings in which the moment demands are high. Referring to Figure 1c which shows such a connection, the load is resisted through a combination of horizontal bearing of the footing against the column flange, and vertical bearing against the embedded base plate. These mechanisms (identified by Grilli et al. [7] based on full-scale experiments) are the basis for a fixity model proposed by Torres-Rodas et al. [9] Although this model is able to characterize the stiffness of the experimental specimens with good accuracy (average test-predicted ratio $k_{base}^{test}/k_{base}^{model}$ =1.15), the experimental data set itself is relatively small (5 tests) and represents only one type of detail – similar to the one shown in Figure 1c. Variants of this configuration (for example using anchor rods in the embedded plates, or welded reinforcement attached to the column) are also prevalent. No test data exists for these, and consequently the efficacy of fixity models (Torres-Rodas et. al. [9]) is unknown as well.

Finally, none of these models (for any type of base connections) explicitly address the rotation of the footing itself, considering this to be a geotechnical/soil-structure interaction issue. This is because various footing designs (e.g., pedestal, raft, pile-cap) and soil types may be present along with features such as grade beams that connect the footings. Zareian and Kanvinde [4] proposed some recommendations for addressing these situations. Collectively, these models represent the state of the art for estimating base fixity in SMRFs. As described in a subsequent section, these models are used within frame models to examine their efficacy in reproducing recorded building motions.

Table 1. Building and CSMIP data characteristics.

Bldg	Location (all in CA)	CSMIP station	Stories	Square footage	Period (NS, EW, Estimate)	Base and foundation type	Sensors	Number of records and intensities $(S_a(T_1)/S_a^{DBE})$
1	Richmond	58506	3	37500 ft²	0.60s, 0.76s, 0.59s	Exposed base plates with overtopping slabs concrete pile caps and grade beams	12	8 (0.162; 0.033; 0.017; 0.011; 0.008; 0.006; 0.005; 0.005)
2	Burbank	24370	6	86500 ft²	1.29s, 1.33s, 0.96s	Embedded column bases connected to concrete pile caps and grade beams	13	7 (0.109; 0.085; 0.034; 0.011; 0.011; 0.003; 0.002)

Characteristics of Instrumented Buildings and Motions

Two SMRF buildings instrumented as part of the CSMIP were selected for analysis in this study. Table 1 shown above summarizes key characteristics of these buildings as well as the base connections used in these frames. Figures 2a-b illustrate these frames – each row of tiles within the figure represents one building (as indicated in the figure), whereas the columns show the photographs and structural models (first column), the moment frames (second column), and the gravity frames and the nonstructural components represented as braces (third column). Table 1 also indicates the normalized value of the geometric mean spectral acceleration for each of the records used in this study $S_a^{GM}/S_a^{10/50}$. This spectral acceleration is normalized by the design spectral acceleration (corresponding to a 10% probability of exceedance in 50 years) to provide a

sense of the intensity of the ground motions relative to building strength/design characteristics. Referring to these values, the intensity of ground motions is well below the design level, suggesting that that inelastic response is highly unlikely; this is later verified through the time history simulations. In each of the buildings, multiple accelerometers (oriented in orthogonal directions) are located on most story levels as well as at the ground level, enabling monitoring of effects such as torsion or unsymmetric response. In addition to the accelerograms recovered from these sensors, the CSMIP database also includes baseline corrected displacement time histories. The next section describes the frame models constructed to simulate these buildings.
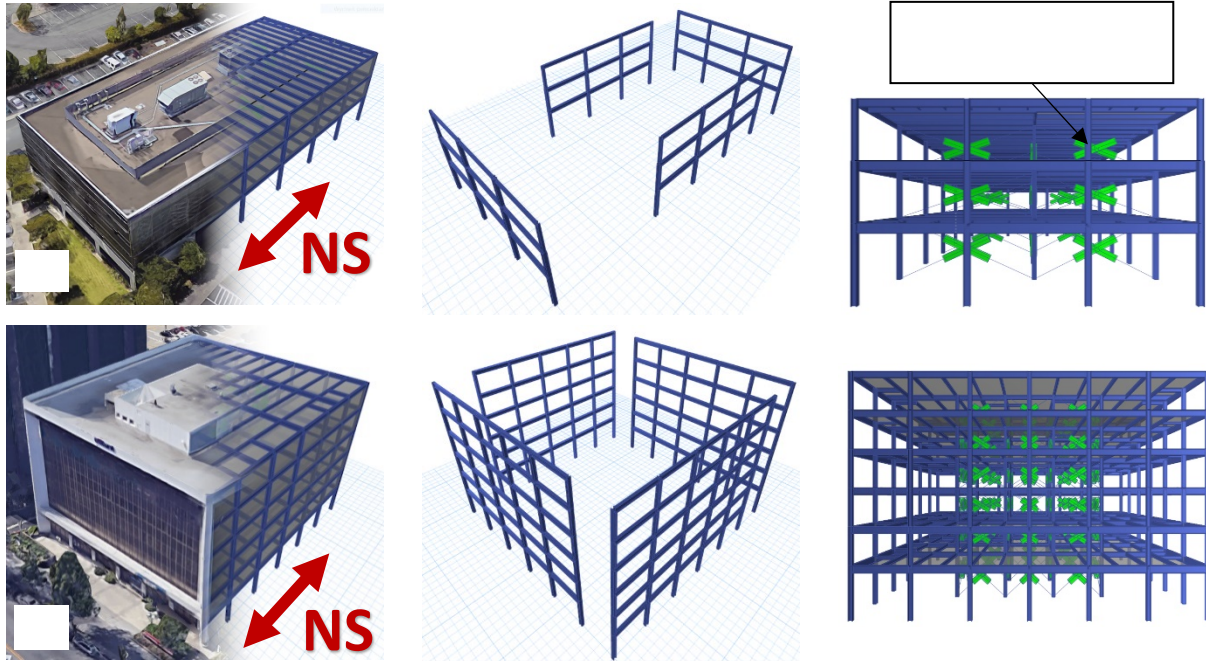
Figure 2. Selected buildings: (a) Building 1, (b) Building 2. Photograph and ETABS models (left column), Steel Moment Frames (middle column), and nonstructural bracing locations (right column).

Building Simulation Models

The main objective of the building simulations is to inform modeling practice for the column base connections, by varying column base fixity and examining the agreement between simulated and recorded response. To this end, it is especially important to minimize inaccuracies in the simulated frame/building response simulated by the building model such that the effect of base fixity may be evaluated with greater confidence. The building simulations are based on building drawings obtained from CSMIP; these drawings contain information regarding structural as well as nonstructural components, foundations, as well as connection details, including column base connections.

General Modeling Assumptions and Considerations

Three dimensional simulation models were constructed for all buildings using the software program ETABS [14]. In addition to the moment frames, the models included the

gravity frames, nonstructural components (i.e., partition and exterior walls) as well as diaphragms.

- All frames were simulated using 3-d elastic beam-column elements. The absence of inelastic response in all simulations was confirmed by performing post facto yielding checks in all members.
- Although inelastic response was not simulated, geometric nonlinearity was simulated to appropriately reflect P-Δ effects (due to the leaning effect of gravity frames) and the associated period elongation.
- Diaphragms were simulated as semirigid, accounting for the actual properties of the diaphragm including the steel decking and concrete.
- In the moment frames (indicated in Figure 2, second column), the beam-column connections were simulated as rigid, whereas in the gravity frames (Figure 2, third column), the beam-column connections were simulated as pinned; in both cases the columns were simulated as continuous through the height of the building.
- Finite joint size was modeled, along with panel zone flexibility.
- Seismic masses were assigned at each story level based on estimated dead loads as determined from the structural and nonstructural building drawings, as well as descriptions of finishes, as well as attached equipment and other masses that would contribute to seismic response. Over each story, the mass was uniformly distributed over the area of the diaphragm.
- The applied gravity loads reflect best estimates of both the dead and live loads. The total gravity loads are pertinent for accurate simulation of: (1) the leaning column or P-Δ effects, and (2) simulation of column base flexibility, especially for Building #1 with exposed column base plates whose fixity is sensitive to axial forces.
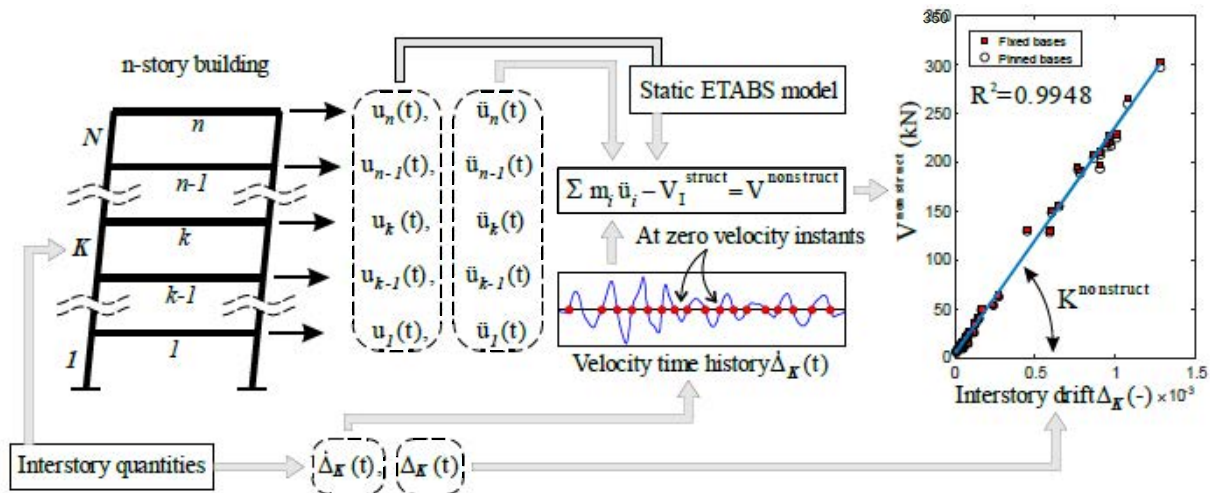
Figure 3. Process used for estimation of nonstructural stiffness.

Estimation of Nonstructural Stiffness

Nonstructural components (i.e., partition walls, cladding) contribute significantly (up to 40%) to the elastic stiffness of the building (NIST GCR 917 44 [15]), significantly affecting dynamic response. Thus, accurate characterization of nonstructural component stiffness is

essential for effective simulation of building response. The nonstructural stiffness within each story of the building may be estimated based on configuration of partition/external walls and cladding, based on test data (e.g., McMullin and Merrick [16]) and stiffness models (e.g., Kanvinde and Deierlein [17]) for similar types of nonstructural components. The stiffness of nonstructural wall and cladding details is sensitive to their geometry, the presence of doorways, captive ends, as well as construction details, e.g., type of studs (cold formed or wood), nail/screw patterns, sill plates (Kanvinde and Deierlein [17]; Jampole et al. [18]). As a result, literature-based estimates of nonstructural stiffness are approximate at best. Consequently, a direct approach for estimation of nonstructural stiffness was developed in this study, whose components are schematically illustrated in Figure 3.

Referring to this figure, this approach is based on the following observations and assumptions:

- During any ground motion, the instantaneous horizontal components of the story shear may be represented as $V_I^{story}{}_{x,y}(t)$ in which the subscript (Roman) I represents the Ith story, located directly below the ith floor (see Figure 3). The subscripts x and y represent the two horizontal directions.
- This instantaneous story shear may be decomposed into into three components, which must equilibrate the inertial forces of all the floors above story I:

$$V_I^{story}{}_{x,y}(t) = V_I^{NS}{}_{x,y}(t) + V_I^{struct}{}_{x,y}(t) + C_I^{damping}{}_{x,y} \cdot \dot{u}_{I,x,y}(t) = \sum_{i=I}^{N} m_i \cdot \ddot{u}_{i,x,y}(t) \qquad (1)$$

In the above equation, the terms $V_I^{NS}{}_{x,y}(t)$ and $V_I^{struct}{}_{x,y}(t)$ represent the instantaneous story shears (in the x and y directions) carried by the nonstructural and structural (i.e., SMRF and gravity frames) elements, respectively, whereas $C_I^{damping}{}_{x,y} \cdot \dot{u}_{x,y}(t)$ is the instantaneous damping force in which the term $\dot{u}_{x,y}(t)$ represents the instantaneous interstory velocities in the x and y directions. The term on the right hand side represents the inertial forces of all the floors above story I, in which $\ddot{u}_{i,x,y}(t)$ represents the instantaneous accelerations of these floors.

Following the observations above, the instantaneous force carried by the nonstructural elements $V_I^{NS}{}_{x,y}(t)$ may be determined if the remaining quantities in Equation 1 are estimated. To accomplish this, the following process is implemented for each building:

1. For a given story and direction within the building (e.g., the top story and x-direction), recorded time histories of interstory deformation (i.e., $u_{I,x,y}(t)$, interstory velocity $\dot{u}_{I,x,y}(t)$, and acceleration for all floors above the story (i.e., $\ddot{u}_{i,x,y}(t)$) are obtained. This process is conducted for multiple ground motions.
2. From these time histories, time instants at which the interstory velocity $\dot{u}_{I,x,y}(t)$, equals zero (or is negligible) are selected. At these instants, the damping force within the story is zero. Consequently, at each of these instants, the sum of the story shears carried by the structural frames and the nonstructural components must equal the inertial forces induced by stories above. This leads to the following equation:

$$V_I^{NS}{}_{x,y}(t) = \sum_{i=I}^{N} m_i \cdot \ddot{u}_{i,x,y}(t) - V_I^{struct}{}_{x,y}(t) \qquad (2)$$

3. The term $V_I^{struct}{}_{x,y}(t)$ on the right-hand side denotes the shear force carried in the structural frames in story I. This shear force may be determined as follows. For the time instants selected above in Step 1, instantaneous values of the floor lateral displacements (i.e., $u_{I,x,y}(t)$) represent the deformations of the structural (i.e., SMRF and gravity frames) as well. Consequently, the story shear carried by these frames may be suitably estimated by applying these displacements in a static manner to the simulation model of the building (described earlier). In this context, it is important to note that the shear carried by the structural frames depends on lateral displacements as well as rotations of the joints at each story. For all joints except at the base, this may be addressed by allowing the joints to rotate freely following physical response (i.e., a statically condensed situation). However, the rotation of the base joint is not known; recall that examining base fixity is the main objective of this paper. This is problematic because from a theoretical standpoint, the base rotation influences the deformed shape of the entire structure, affecting the relationship between the story shears and the applied displacements. Nonetheless, from a practical standpoint only the story shears in the first story are sensitive to the base rotational flexibility. This is verified through a parametric study in which the base flexibility is varied from pinned to fixed, with the resulting variation in story shears being less than 5% (for all stories except for the first story). Given this observation the shears in the upper stories may be directly determined as $V_I^{struct}{}_{x,y}(t)$.

4. Once all the terms in Equation 2 are estimated as above, for each selected instant within each ground motion, the force in the nonstructural elements $V_I^{NS}{}_{x,y}(t)$ may be computed, and plotted against the corresponding interstory deformation $u_{I,x,y}(t)$ at that instant within the same ground motion. Figure 3 illustrates such a plot (for the top story of Building #1). The plot includes data from 8 ground motions, and a total of 60 data points, each corresponding to a time instant when velocity $\dot{u}_{I,x,y}(t)$ equals zero (or is negligible).

Referring to the scatter plot in Figure 3, two observations may be made: (1) a strong linear correlation is apparent between the interstory deformation $u_{I,x,y}(t)$ and the force carried by the nonstructural components, suggesting that the nonstructural elements may be appropriately represented as linear elastic elements within the building simulation, (2) the figure overlays data points from 8 ground motions – it is encouraging to note that the relationship has minimal variability between ground motions. These observations are consistent across all buildings and ground motions. Consequently, the nonstructural stiffness for each story within each building is determined through regression fitting of this data (in all cases, the R^2 value is not less than 0.98 indicating a strong linear trend). As an additional point of reference, the nonstructural stiffnesses determined in this study are similar to those for similarly sized buildings as reported in literature (Davies et al. [19]). Once determined in this way, the nonstructural stiffness is applied in the form of equivalent bracing members (see Figure 2, third column). These bracing members (whose cumulative stiffness equals the estimated story nonstructural stiffness) are inserted into bays where nonstructural elements (e.g., partition walls) are present. The process outlined in this section maximizes the accuracy of the building model itself, such that it may be used to

effectively interrogate the effect of column base flexibility. This is the subject of the next section.

Results and Discussion

Once the building models have been developed as described in the previous section, they are used to examine the effect of base fixity on seismic response. For this purpose, a parametric study is conducted; this includes the following:

1. For each of the buildings, column base connections are represented in five alternate ways. These include pinned (denoted k_0 to indicate zero fixity), fixed (denoted k_∞ to indicate infinite fixity) and three intermediate values. These values denoted k_{model}, $0.5k_{model}$, and $1.5k_{model}$ represent the model-based estimates of base fixity. Of these, the first k_{model} is the best-estimate of base fixity estimated using the appropriate model for each base detail within each building (referring to Table 1). Specifically, the model by Kanvinde et al. [10] is used to estimate the fixity of exposed base plate details (in Building #1), whereas the model by Torres-Rodas et al. [9] is used to estimate the fixity of embedded base connections (in Building #2). The estimates $0.5k_{model}$, and $1.5k_{model}$ (in which the base fixity is set to ±50% of the best estimate) are also queried to examine the sensitivity of frame response to uncertainty in base fixity estimates. Zero-length rotational springs with properties corresponding to each of these stiffness estimates are provided at the column bases. Two such springs are provided at each base, to represent the flexibility in either direction; these springs are calibrated to reflect the dimensions/anchor rod placement in each direction. Interaction between the two directions is not simulated.

2. The parametrization outlined above results in 10 building simulation models; five of these models (with k_0, k_∞, k_{model}, $0.5k_{model}$, and $1.5k_{model}$) correspond to each of the two buildings. All 10 models are subjected to all ground motions (see Table 1) available for the corresponding building.

3. Each of the 75 NLTHA runs (obtained from two buildings) produces acceleration time histories (at each story and in both directions) that may be directly compared to recordings from the instrumented buildings. Depending on the number of stories and density of instrumentation (e.g., not all stories are instrumented in all buildings), each of the buildings has a different number of acceleration time histories. As an illustrative example, Figure 4 shows graphical comparisons of recorded and simulated acceleration histories for Building #1.
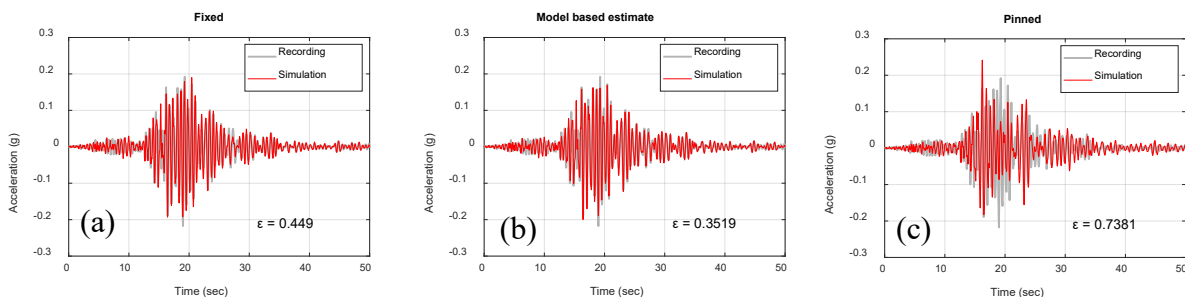
Figure 4. Sample recorded and simulated acceleration time histories for Building #1.

Each column overlays the simulated acceleration history corresponding to one representation of base fixity. Specifically, the recorded time histories in Figures 4a-c are identical, and correspond to the an accelerometer on the 3rd floor in the NS direction, whereas the simulated histories in each are different, corresponding to the k_0, k_{model}, and k_∞ base fixities. Significant torsional response was not noted in any of the buildings, such that the peak torsional rotation (in all cases/ground motions) was less than 2×10^{-4} rad.

Referring to Figure 4, it is observed that simulations with the fixed base k_∞ and the model based best-estimate k_{model} cases appear to track the recorded most closely, whereas simulations with the pinned base, i.e., k_0 show greater error. Although such visual assessment are informative, an objective error measure is needed to quantify agreement between simulated and recorded time histories, and to examine trends across various buildings or base details, and inform modeling practices in general. Naeim et al. [11] provide best practices for such quantification, in the specific context of utilizing CSMIP data; consequently, these practices are selected for this study. Specifically, the error between any pair of recorded and simulated time histories may be expressed as follows:

$$\varepsilon_{i,x,y} = \sum_{j=1}^{k} \frac{\int |\ddot{u}_{i,x,y,recorded} - \ddot{u}_{i,x,y,simulated}| \cdot dt}{\int |\ddot{u}_{i,x,y,recorded}| \cdot dt} \tag{3}$$

In the above equation, $\ddot{u}_{i,x,y,recorded}$ and $\ddot{u}_{i,x,y,simulated}$ refer to the recorded and simulated accelerations, respectively, at the ith story (in two orthogonal directions, i.e. N-S and E-W) at a given time instant j, whereas dt represents the time step. The error $\varepsilon_{i,x,y}$ is determined numerically. The error $\varepsilon_{i,x,y}$ calculated in this manner for the recorded and simulated time history pairs in Figures 4a-c is also shown on the corresponding figures. This provides a visual interpretation of the numerical value of the error as defined by Equation 3. The error measure $\varepsilon_{i,x,y}$ defined as above, is computed for all acceleration time history pairs arising from the 75 simulations and 15 recordings (obtained from two buildings). Figures 5a-b plot this error for all buildings versus the five levels of base fixity. Each of these figures contains two graphs. One represents the error (calculated as per Equation 3 above) from the acceleration time histories averaged over all instruments within the building – see graph denoted e_{total}. The second graph, denoted $e_{10\%}$ represents the error calculated by considering only the strong motion portion of each time history. Specifically, Equation 3 above is applied to all the time histories for only those values of acceleration that exceed 10% of the maximum acceleration within a time history. This provides a possibly more refined estimate, by discounting the error accumulated over low accelerations.
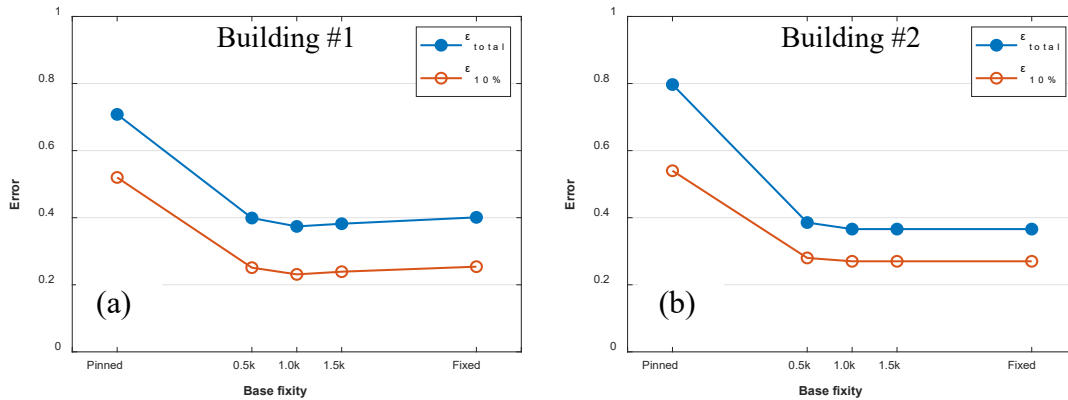
Figure 5. Error between simulated and recorded acceleration time histories.

Referring to Figures 5a-b, the following observations may be made:

- The pinned base assumption results in the greatest value of error. This suggests that simulating bases as pinned is grossly inaccurate. In fact, this error is quite large, i.e., both e_{total} and $e_{10\%}$ are greater than 0.5 even for Building #1 which includes only exposed type base connections. This suggests that the practice of simulating exposed base connection as pinned is not well-founded, and that the connection has significant rotational fixity, which is possibly enhanced by various factors including the presence of axial force as well as the overtopping slab.

- For Building #1 (i.e., Figure 5a), which features exposed base plate connections, the lowest error corresponds to k_{model}, such that the error increases as the fixity is increased beyond this value. Specifically, the simulations with k_∞ result in roughly 2.5% more error (for both e_{total} and $e_{10\%}$) as compared to the simulations with k_{model}. This is unsurprising, given the higher flexibility of exposed base plate connections and suggests that for these connections, simulating the bases with model-based estimates of stiffness is appropriate.

- For Building #2 (i.e., Figure 5b), the errors (both e_{total} and $e_{10\%}$) decrease substantially as the base fixity is increased, and saturate around the fixity corresponding to k_{model} – such that increasing the stiffness to infinity (i.e., a fixed base) results in essentially the same response. Referring to Table 1, Building #2 has embedded base connections. This suggests that embedded base connections may be suitably represented either based on the appropriate model (i.e., Torres-Rodas et al. [9]) or even as fixed, especially since the former requires more effort and familiarity with the model.

- The lowest errors for Building #1 with the exposed bases are in the range of e_{total} 0.374, and $e_{10\%}$ 0.231; these are obtained using k_{model}. The lowest errors obtained for Building #2 with the embedded bases are e_{total} 0.366, and $e_{10\%}$ 0.27; as noted above, these are obtained for base stiffness between k_{model} and k_∞. In absolute terms these errors may be considered low/acceptable, considering the following: (1) Previous work, e.g., Naeim et al. [11] used genetic algorithms to tune building properties to minimize errors between CSMIP recordings and simulations – these algorithms resulted in errors (defined similarly) not significantly lower than the ones reported in Figures 5a-b. The simulations in this study were not optimized in this manner, and used best estimates of structural

properties, to provide a realistic assessment of expected errors in building simulation. From this standpoint, the error values noted above are encouraging, and (2) Referring to Figure 4b, the error corresponding to values in this range represents good visual agreement between the recordings and simulations.

- In all cases, the sensitivity of error to the base flexibility in the neighborhood of k_{model} is modest (as illustrated by the errors for the $0.5k_{model}$, and $1.5k_{model}$ simulations).
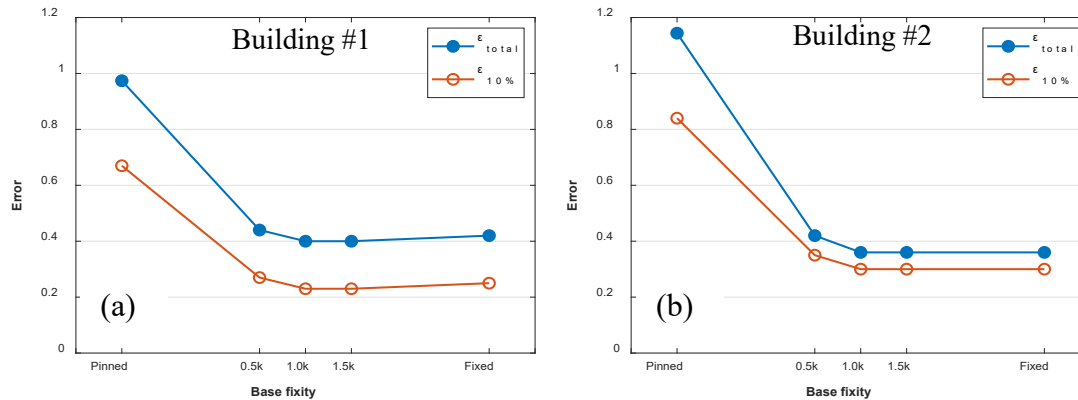
Figure 6. Error between simulated and recorded displacement time histories.

Figures 6a-b are similar to Figures 6a-b, except that they indicate errors for the recorded displacement time histories at each sensor. Such displacement time histories are provided by CSMIP and are based on integration as of the acceleration time histories as well as baseline corrections (Naeim et al. [11]). Both qualitatively and quantitatively, errors as well as the trends with respect to base fixity are similar between the acceleration and displacement time histories. This is not surprising, since the displacement time histories are derived from the acceleration time histories, but is informative nonetheless, since design and performance assessment require estimation of both the displacement as well as acceleration.

The observations from Figures 5-6 and associated discussion may be interpreted to provide guidance for the modeling of column base connections in steel moment frames. The key takeaways are:
- Simulating column bases as pinned, even when they are constructed as exposed base plates results in gross mischaracterization of frame response
- For exposed base plate connections, simulating the bases using model-based estimates is advisable, since it results in the best agreement (minimum errors) between the recorded and simulated time histories for both acceleration and displacement.
- For embedded base connections, simulating the bases as fixed or with the model based estimates result in the lowest error. This suggests that from a standpoint of elastic building response estimation, it is reasonable to simulate the bases as fixed, given the higher effort and expertise required for model-based estimation.
- Since the response appears to be relatively insensitive to the flexibility in a ±50% neighborhood of the model based estimates, explicit consideration of soil or footing flexibility may not be critical, since previous studies (Zareian and Kanvinde [4]) indicate that these effects do not alter the stiffness by more than 50%.

Summary and Conclusions

This paper uses earthquake recordings from the instrumented buildings to examine the efficacy of various assumptions and practices for modeling column base connections in steel moment frame buildings. Two moment frame buildings instrumented as part of the California Strong Motion Instrumentation Program (CSMIP) were selected for this study. The first building featured exposed base plate type connections, whereas the second one featured embedded column base connections. The methodology of the research involved constructing accurate simulation models for the superstructure, and then trialing a range of base flexibilities with this superstructure to examine the effect on agreement between the simulated and recorded time histories. To this end, simulation models were constructed for each of these buildings using the software ETABS; these models included numerous aspects of response, including geometric nonlinearity, finite joint size, and the simulation of all gravity frames. A sophisticated process was devised to estimate the stiffness associated with the nonstructural components. Each of these models was fitted with base rotational springs reflecting five alternate estimates of base fixity, ranging from pinned to fixed with intermediate values corresponding to model-based estimates. For each of these, the acceleration time histories resulting from the simulations were compared to their recorded counterparts. The agreement between these time history pairs (an indicator of the efficacy of the selected base flexibility) was quantified through an integrated error measure. This dependence of this error measure on numerous factors, pertaining to building/base configuration is studied with the objective of providing guidance regarding appropriate practices for simulating base connections.

The main findings include the following: (1) modeling the bases as pinned results in high error and is not recommended, even when the connection is of an exposed base plate type, (2) simulating bases with the appropriate model-based stiffness estimate (depending on whether they are embedded or exposed) generally results in low error (3) notwithstanding the previous point, in the case of embedded bases, modeling the bases as fixed provides a reasonably good agreement with recorded data and (4) the response is not highly sensitive to the estimated base flexibility, in the neighborhood of the model-based estimate.

Although this study provides the first field-recording based examination of column base fixity, it has limitations, which must be considered while interpreting or applying its recommendations. First, it is important to note that even the best overall agreement between simulated and recorded time histories is not ideal (errors on the order of 30% for the integrated measure), indicating that the representation of the base connections is only one source of error. Nonetheless, the lowest errors noted in this study are comparable to or better than those noted in other comparisons between recorded and high-fidelity simulations. The implications are the following: (1) although the remaining error may be reduced further by making some adjustments to the structural models, e.g., providing irregular strength, stiffness or damping values over various parts of the building, such adjustments are arbitrary with respect to the nominal or best-estimates of these properties, (2) as a result, the remaining error is challenging to minimize further, since it may be attributed to inherent uncertainty in these properties, and (3) the recommendations for simulating base fixity presented herein are justifiable within this overall context. Second, for the buildings studied in this paper, the ground motions were of relatively low intensity, selected to not induce inelastic actions in the structure. This has two additional

implications. First, the rotational response of base connections is nonlinear even in the pre-yield stage. This may be attributed to the following factors: (1) the nonlinearity of concrete, (2) gapping and contact between the steel and concrete components of the connection, and (3) for exposed base plate connections, the change in axial load during seismic loading, which results in a change in stiffness. This must be considered in extrapolating results of this study to buildings subjected to stronger shaking. Second, the results of this study indicate that the error between recorded and simulated time histories does not vary significantly for base fixities between k_{model} and k_∞. This appears to contradict previous findings by Zareian and Kanvinde [4] that indicate higher sensitivity of building response to base fixity. To explain this, it is noted that the Zareian and Kanvinde [4] examine inelastic collapse response of SMRFs. This response is controlled by soft-story formation, which in turn is greatly sensitive to base fixity. Thus, while the Zareian and Kanvinde [4] study underscores the importance of simulating base fixity, a similar degree of sensitivity is not observed in this study, whose objective is to provide insights regarding base flexibility using elastic simulations, rather than to simulate inelastic building response under stronger motions. Notwithstanding these limitations, the analyses presented in this paper are encouraging because they provide the first field-recording based guidance for simulating column base connections in Steel Moment Frames.

Acknowledgments

References

[1] American Institute of Steel Construction, Inc. (AISC). Seismic Provisions for Structural Steel Buildings (ANSI/AISC 341-16). Chicago, (IL, USA): American Institute of Steel Construction; 2016.

[2] American Institute of Steel Construction, Inc. (AISC). Prequalified Connections for Special and Intermediate Steel Moment Frames for Seismic Applications (ANSI/AISC 358-16). Chicago, (IL, USA): American Institute of Steel Construction; 2016.

[3] Fisher JM, Kloiber LA. Base Plate and Anchor Rod Design. AISC Steel Design Guide One, 2nd ed, American Institute of Steel Construction, Chicago, IL. 2006.

[4] Zareian F, and Kanvinde AM. Effect of Column-Base Flexibility on the Seismic Safety of Steel Moment-Resisting Frames. Earthquake Spectra, 29(4): 1537-1559, November 2013.

[5] Gomez IR, Kanvinde AM, Deierlein GG. Exposed Column Base Connections Subjected to Axial Compression and Flexure. Final Report Presented to the American Institute of Steel Construction, Chicago, IL. 2010.

[6] Barnwell N. Experimental Testing of Shallow Embedded Connections Between Steel

Columns and Concrete Footings. Master Thesis, Brigham Young University, Provo, UT. 2015.

[7] Grilli DA, Jones R, Kanvinde AM. Seismic Performance of Embedded Column Base Connections Subjected to Axial and Lateral Loads" Journal of Structural Engineering, ASCE. 143(5): 04017010, 2017.

[8] Tryon JE. Simple Models for Estimating the Rotational Stiffness of Steel Column to Footing Connections. Master Thesis, Brigham Young University, Provo, UT. 2016.

[9] Torres-Rodas P, Zareian F, Kanvinde AM. Rotational Stiffness of Deeply Embedded Column-Base Connections. Journal of Structural Engineering, ASCE, 143(8), August 2017.

[10] Kanvinde AM, Grilli DA, Zareian F. Rotational Stiffness of Exposed Column Base Connections: Experiments and Analytical Models. Journal of Structural Engineering, ASCE, 138(5): 549-560, May 2012.

[11] Naeim F, Hagie S, Alimoradi A, Miranda E. Automated Post-Earthquake Damage Assessment and Safety Evaluation of Instrumented Buildings. John A Martin and Associates Research Report – JAMA Report Number 2005-10639, Los Angeles, CA. 2005.

[12] Occupational Safety and Health Administration (OSHA), Safety Standards for Steel Erection, (Subpart R of 29 CFR Part 1926), Washington, D.C. 2001.

[13] Trautner CA, Hutchinson T, Grosser PR, Silva JF, Effects of Detailing on the Cyclic Behavior of Steel Baseplate Connections Designed to Promote Anchor Yielding. Journal of Structural Engineering, ASCE, 142(2), February 2016.

[14] Computers and Structures, Inc. (CSI). ETABS Integrated Building Design Software. (http://docs.csiamerica.com/manuals/etabs/Analysis%20Reference.pdf), Computers and Structures Inc., Berkeley, CA, 2016.

[15] ATC, Seismic Analysis, Design, and Installation of Nonstructural Components and Systems – Background and Recommendations for Future Work, Report No. NIST GCR 17-917-44, Applied Technology Council, Redwood City, CA, 2017.

[16] McMullin K, Merrick D. Seismic Performance of Gypsum Walls - Experimental Test Program, Report W-15, CUREE Woodframe Project, 2001.

[17] Kanvinde AM, Deierlein GG. Analytical Models for the Seismic Performance of Gypsum Drywall Partitions. Earthquake Spectra, 22(2): 391-411, May 2006.

[18] Jampole E, Deierlein GG, Miranda E, Fell B, Swensen S, Acevedo C. Full-Scale Dynamic Testing of a Sliding Seismically Isolated Unibody House. Earthquake Spectra, 32(4): 2245-2270, November 2016.

[19] Davies R, Retamales R, Mosqueda G, Filiatrault A, Allen D. Effects of Cold-formed Steel Framed Gypsum Partition Walls on the Seismic Response of a Medical Facility. Twenty-First International Specialty Conference on Cold-Formed Steel Structures, St. Louis, Missouri. 2012.

USING CSMIP DATA TO TEST FEMA P58 METHODOLOGY AND THE POTENTIAL FOR AUTOMATED LOSS ESTIMATION

P. Martuscelli, J. P. Moehle

Department of Civil and Environmental Engineering
University of California, Berkeley

Abstract

The research objective is to study whether results of FEMA P58 loss assessment methodology are consistent with damage observations from real earthquakes and to develop automated software routines for projecting losses using the FEMA P58 methodology and instrumental recordings from building responses. To this purpose, a direct loss analysis approach is developed in which instrumental recordings from the California Strong Motion Instrumentation Program are used to define Engineering Demand Parameters (EDPs) for input to the FEMA P58 methodology, which is then used to estimate damage and losses. A subset of instrumented buildings that suffered earthquake damage are selected for the study. Calculated and observed damage are compared to evaluate the reasonableness of the procedures. The study is part of a larger study that will also compare results of the direct loss analysis approach with results obtained by a full implementation of the FEMA P58 methodology.

Introduction

Rapid developments in performance-based seismic design procedures in the United States occurred in the 1980s and 1990s in response to societal reactions to the nearly annual occurrence of damaging earthquakes in the Western United States during this period. These earthquakes did not cause collapse or life safety endangerment in many cases, but they amply demonstrated that the building code provisions permitted extensive damage and economic loss and could readily impair the functionality of important facilities. Interest by owners and tenants to understand performance of new buildings or of seismic upgrades spurred the development of performance-based standards and guidelines and, ultimately, the development of a new engineering methodology implemented in FEMA P58 [6] to calculate expected performance of buildings. The methodology offers the capability to express earthquake losses in probabilistic terms for individual buildings, considering metrics such as capital repair costs, downtime, and casualties.

The FEMA P58 methodology is based on the PEER (Pacific Earthquake Engineering Research Center) PBEE (Performance-Based Earthquake Engineering) framework [14]. The PEER PBEE methodology seeks to treat the seismic risk assessment problem in a probabilistically consistent manner, from expected hazard and building performance, to expected losses, downtime, and casualties. Figure 1 illustrates the various steps in the process. The uncertainties of these steps (hazard analysis, structural analysis, damage analysis, and loss analysis) are explicitly accounted for to create probability distributions for performance measures of interest. In the usual application, the seismic hazard representation is developed

through a probabilistic seismic hazard analysis, representative earthquake ground motions are developed, these are input into a numerical model of the building, engineering demand parameters are calculated, and then these are used to quantify Decision Variables including expected capital losses, downtime, and casualties.
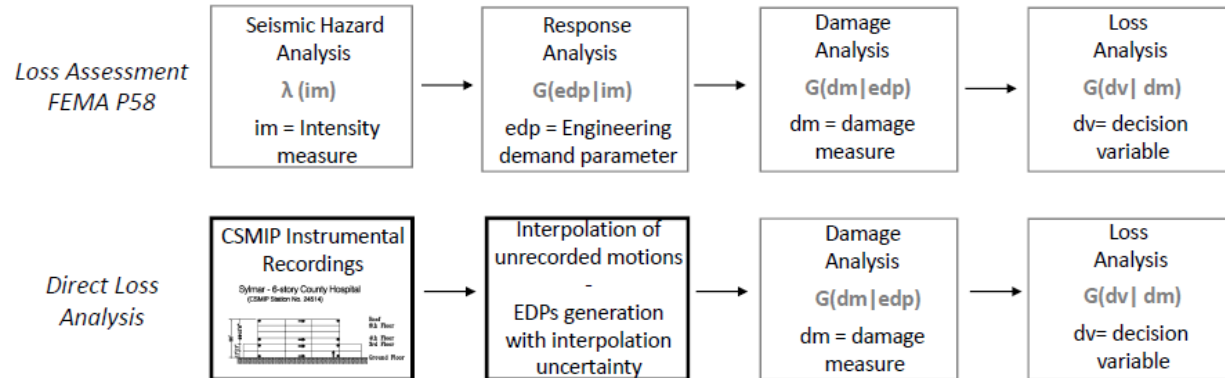
Fig.1: Direct Loss Analysis and FEMA P58 methodology flowcharts

To test the reasonableness of the FEMA P58 calculation of the Decision Variables, we have implemented a direct loss analysis approach that uses CSMIP instrumental recordings for loss estimation of buildings that have been shaken in past earthquakes. Because strong motion instruments are placed sparsely in most instrumented buildings, it is necessary to develop a procedure to reconstruct motions at locations where instruments are absent. For this purpose, an archetype building study is performed to test interpolation techniques and to infer statistical parameters that can be used to characterize approximation uncertainty for the different interpolation methods.

Three CSMIP instrumented buildings that suffered earthquake damage are selected as case-study structures. Results of calculated damage and losses are compared with post-earthquake damage surveys. This initial phase of the study is part of a larger study that will also apply the full FEMA P58 methodology to some of the buildings.

Direct Loss Analysis

Method overview

The direct loss analysis aims to provide an estimation of damage of instrumented buildings by using the instrumental recordings as direct input for loss assessment. As shown in Figure 1, the direct loss analysis process circumvents two steps of the FEMA P58 methodology, namely, the seismic hazard analysis and the structural analysis. Instead, recorded ground and floor motions are used directly to recreate EDPs in terms of peak floor accelerations (PFA) and peak story drift ratios (SDR), which are then used as input for damage and loss analysis using the fragility and consequence functions of FEMA P58.

Common instrumentation layouts for buildings do not include accelerometers at each building floor. The absence of instrumental recording at each level requires a reconstruction

technique for unrecorded floor motions. The direct loss analysis aims to reconstruct missing floor responses through simple interpolation techniques. Then, depending on the chosen interpolation method, an interpolation uncertainty is assigned to the predicted quantity, which then is used through a Monte Carlo simulation to define a probability distribution of the unrecorded EDPs.

In FEMA P58 terms, the direct loss analysis intent is to provide a scenario-based loss estimation, where ground motion uncertainty is negligible due to instrumental data and the only sources of uncertainties are coming from prediction error of the interpolation techniques used to reconstruct unrecorded floor motions and from uncertainties in building contents and their fragilities.

Reconstruction of EDPs

Direct loss analysis aims to reconstruct unrecorded motions and EDPs through simple interpolation techniques, such as: 1) linear interpolation; 2) cubic spline with not-a-knot end conditions; and 3) shape-preserving piecewise cubic interpolation. These interpolation methods represent usual schemes adopted in seismic response reconstruction [4, 10, 12] and their formulations are described in detail by [3, 7]. These techniques can be used to reconstruct missing data either at each time step or exclusively with respect to maximum recorded response. Through the chosen interpolation technique, missing data are reconstructed and EDPs are defined in terms of peak floor acceleration and peak story drift:

$$PFA_j = max|a_j|$$

$$SDR_j = \frac{max|\Delta_j - \Delta_{j-1}|}{h_j}$$

where a_j and Δ_j are the acceleration and displacement at floor j and h_j is the height of story j. A general MATLAB routine, called *CSMIPDataInterpreter*, that elaborates CSMIP instrumental data to define EDPs was developed for the study and will be adopted to explore the feasibility of an automatic loss assessment procedure.

Multiple SDR input vector for torsional response

To account for building torsional response and better represent building damage, multiple story drift ratio (SDR) vectors at different building locations can be calculated from recorded and reconstructed motions and used as input for damage and loss analysis. Calculation of each set of story drift EDPs is performed by identification of displacements at any point of the floors, under the assumption of rigid diaphragm, as described by *Naeim et al.* [12] and shown in Figure 2:

$$\begin{bmatrix} A_x \\ A_y \\ \theta \end{bmatrix} = \begin{bmatrix} \dfrac{y_c - y_3}{x_2 - x_1} & \dfrac{y_3 - y_c}{x_2 - x_1} & 1 \\ \dfrac{x_2 - x_c}{x_2 - x_1} & \dfrac{x_c - x_1}{x_2 - x_1} & 0 \\ -\dfrac{1}{x_2 - x_1} & \dfrac{1}{x_2 - x_1} & 0 \end{bmatrix} \begin{bmatrix} A_1 \\ A_2 \\ A_3 \end{bmatrix}$$

where A1, A2 and A3 are the recorded motions; (x_1, y_1), (x_2, y_2), and (x_3, y_3) are the coordinates of the sensors; and (x_c, y_c) is the coordinate of the point of interest.
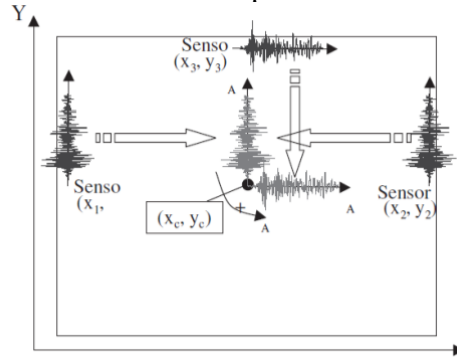
Fig.2: Displacement time-series transformation, after *Naeim et al.* [12]

By being able to calculate story drift ratios at any location of the floor plan and in any direction, it is feasible to assign location-specific story drift EDPs for each structural and non-structural assembly. Inputting more than one SDR vector into the damage and loss analysis framework is allowed by a second Matlab routine developed for this study, called IBLA (Instrumented Building Loss Analyzer).

Uncertainty quantification

The direct loss analysis differs from FEMA P58 in that the analysis does not need to consider the following types of uncertainty: modeling epistemic uncertainty β_m; ground motion uncertainty β_{gm}; and drift and acceleration record-to-record variability ($\beta_{a\Delta}$ and β_{aa}). Other uncertainties, however, need to be considered for direct loss analysis, specifically: instrumentation recording uncertainty β_r; and the uncertainty of unrecorded floor motion prediction through interpolation methods β_i. It is assumed that instrumentation recording uncertainty is negligible and that only the uncertainty introduced by interpolation methods needs to be evaluated here.

For each investigated interpolation method, uncertainty in prediction of EDPs is going to be tested through an archetypes database that is described in a later section. Results from this study will concur to define dispersion for reconstructed peak floor acceleration PFA (β_{PFA}) and peak story drift ratio SDR (β_{SD}), that are:

$$\beta_{SDR} = \sqrt{\left(\beta_{i,SDR}\right)^2 + \beta_{m,D}{}^2}$$

$$\beta_{PFA} = \sqrt{\left(\beta_{i,PFA}\right)^2 + \beta_{m,D}{}^2}$$

where $\beta_{i,SD}$ and $\beta_{i,PFA}$ are the uncertainties in approximation of SDR and PFA through different interpolation techniques and $\beta_{m,D}$ is the epistemic uncertainty related to modeling of the archetype buildings.

Use of FEMA P58 fragility and consequence functions

For the loss analysis, we need to define the structural and non-structural components. The structural components are determined through specific knowledge of the gravity and lateral resisting system of the building as obtained from the structural drawings. In the absence of more detailed knowledge, building content population is defined through the FEMA "Normative Quantitative Estimation Tool" for generic non-structural components. Then, given EDPs and their distribution, likelihood of damage and losses is calculated through uniform random number generation using fragility and consequence functions for each structural and non-structural component. The database of more than 700 fragility and consequence functions, developed for the FEMA P58 project, is adopted for loss calculation here.

Archetypes Study to Test Interpolation Techniques

An archetype buildings database is currently being developed with the intent to test different interpolation techniques for approximating building response at locations within instrumented buildings where there are no instrumental recordings. Of interest are methods for interpolating the peak floor accelerations (PFA) and peak story drift ratios (SDR), including information on bias and uncertainty for each interpolation method. The archetype models are representative of non-ductile reinforced concrete frames designed and constructed in California during 1960s. The archetypes are designed according to the 1961 Uniform Building Code.
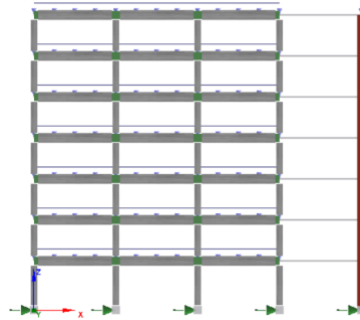
Fig.3: Archetype structural configuration – SeismoStruct by Seismosoft

Preliminary results of this investigation are presented for a set of archetype models that are representative of the first case-study building, a 7-story hotel. The range of design parameters for the archetype models is described in Table 1. The current set of analyses, for five archetype configurations, comprises a total of 200 nonlinear response history analyses that are consistent with the seismic intensity experienced by the 7-story Hotel during 1994 Northridge event.

Model Name	Axial (N/A$_g$f'$_c$)	Size [in]		f'c [ksi] Story		Size [in]		f'c [ksi] Story	Geometry		Design Base Shear Coefficient	First Mode Period [s]	Strong Column Weak Beam	Section Aggregator for Shear
		Columns				Beams					Structure			
Mod.#	Gf	b	h	1,2	3,7	b	h	1,7	N$_{story}$	N$_{bay}$		T$_1$		
A4.3	0.31	26	24	5	4	20	30	4	7	3	0.080	0.81	1.0	No
A4.4	0.31	26	24	5	4	24	32	4	7	3	0.070	0.73	0.9	No
A3.4	0.36	24	22	5	4	24	32	4	7	3	0.060	0.78	0.8	No
A2.4	0.38	24	20	5	4	24	32	4	7	3	0.058	0.84	0.7	No
A1.1	0.43	20	18	5	4	18	24	4	7	3	0.050	1.27	0.7	No

Table.1: Archetypes modeling and design parameters

Structural models for each archetype configuration consist of a two-dimensional representation of the building lateral resisting system; for the first set of architypes presented herein, the two-dimensional representation is characterized by three bays and seven stories (Figure 3). Nonlinear material response is modeled through distributed plasticity elements with force-based formulation; geometric non-linearities are explicitly considered. For several archetype performance groups, shear strength during the analysis is continuously calculated according to ASCE 41-17 equation (10-3) and ACI 318-11 equations (11-5; 11-27; and 11-28) and if demand exceeds capacity, the latter is reduced to a residual value equal to 20%. The two-dimensional structural models include a leaning column that is modeled to represent vertical loads carried by the internal gravity framing system and their effect on system stiffness and stability.

Tested Interpolation methods

The interpolation techniques currently being tested are: 1) linear interpolation; 2) cubic spline with not-a-knot end conditions; and 3) shape-preserving piecewise cubic interpolation. Acceleration response histories are interpolated either at each time step (later referred as **@t_i**) or with respect to maximum recorded response (later referred as **@t_{max}**). Regarding the latter, it is important to underline that for the purpose of the study it is enough to characterize absolute maximum response since loss assessment only requires peak floor acceleration as input. Instead, to characterize absolute maximum story drift, interpolation is preferably performed at each time step.

Instrumentation configurations

The ability of the interpolation techniques to correctly predict response at not instrumented floors is evaluated considering different instrumentation layouts. Four instrumentation configurations are considered (referred as **C1, C2, C3** and **C4**) and are shown in the following figure:
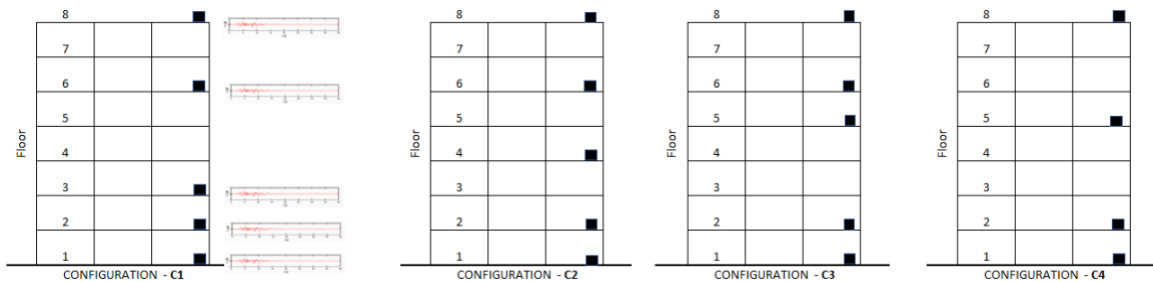
Fig.4: Tested instrumentation configurations

Error measures

The following metric is defined to characterize the interpolation error for the reconstruction of EDPs:

$$E_t = \frac{x_p - \tilde{x}}{\tilde{x}}$$

where x_p represents the interpolation prediction of story drift ratio (SDR) and peak floor acceleration (PFA), and $\tilde{x}$ is the actual value from the nonlinear dynamic structural analysis. It is to be underlined that regardless of how interpolation is done (at each time step or at maximum recorded response), the error is calculated only in terms of absolute maximum SDR and PFA, since these are the only quantities of interest for loss assessment. For each instrumentation configuration, the error is calculated at each "non-instrumented" floor, as shown in the next figure:
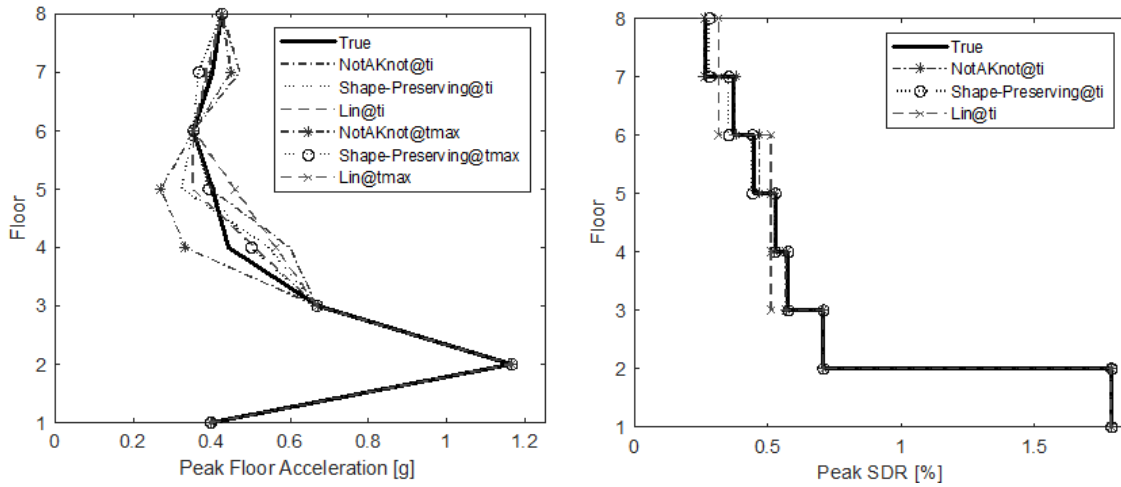
Fig.5: Different interpolation techniques for one NLRHA – Configuration **C1**

An analysis of multiple nonlinear response history analyses shows that there is little variation of interpolation prediction error over the archetype model height, which allows to aggregate the error data for all the floors. The next figures present the interpolation prediction error for different techniques for PFA and peak SDR, considering instrumentation configuration **C1**:
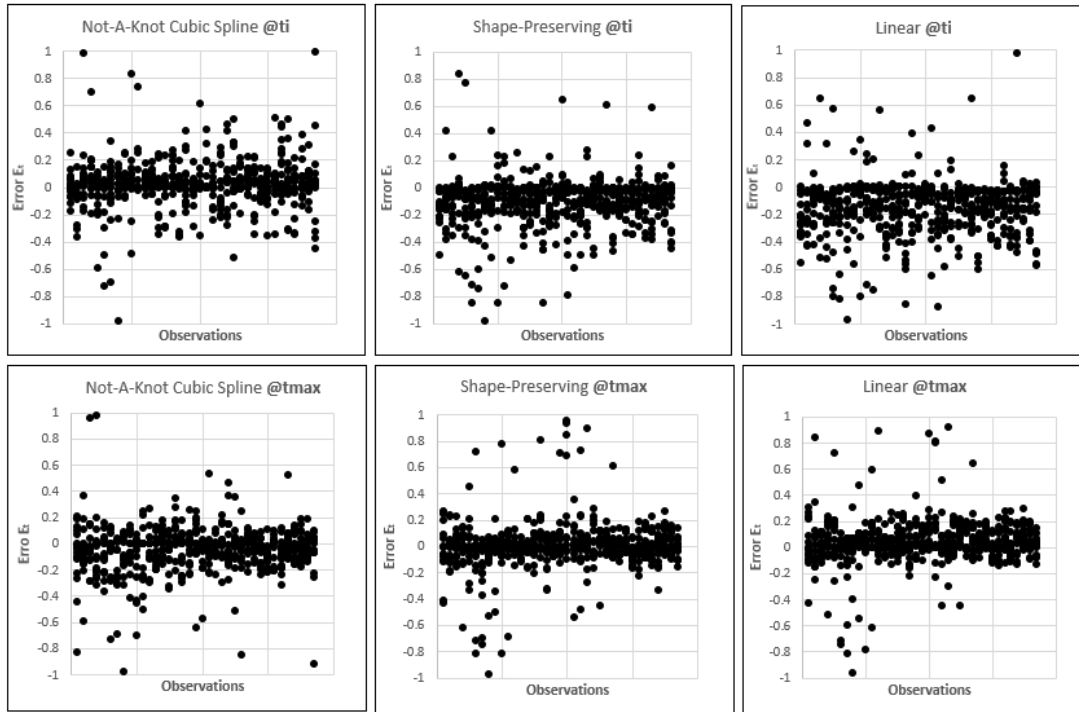
Fig.6: Interpolation error for **PFA** – Configuration **C1**
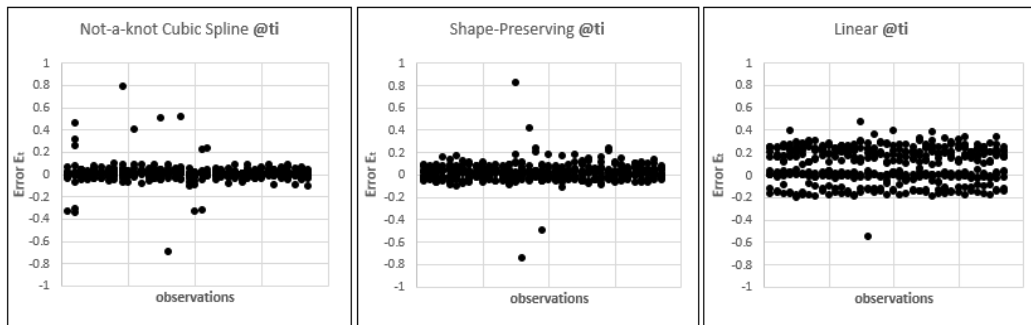
Fig.7: Interpolation error for peak **SDR** – Configuration **C1**

The aggregated data of prediction error for PFA and peak SDR, in their preliminary form, allows to define prediction error statistics for the different interpolation techniques:
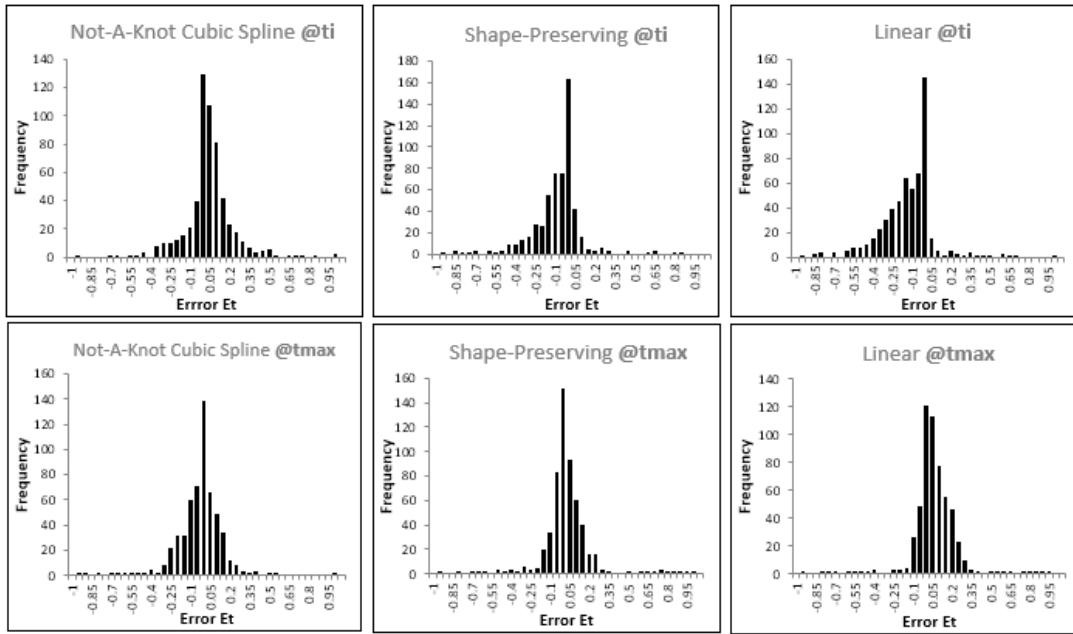
Fig.8: Et frequency distribution for **PFA** – Configuration **C1**
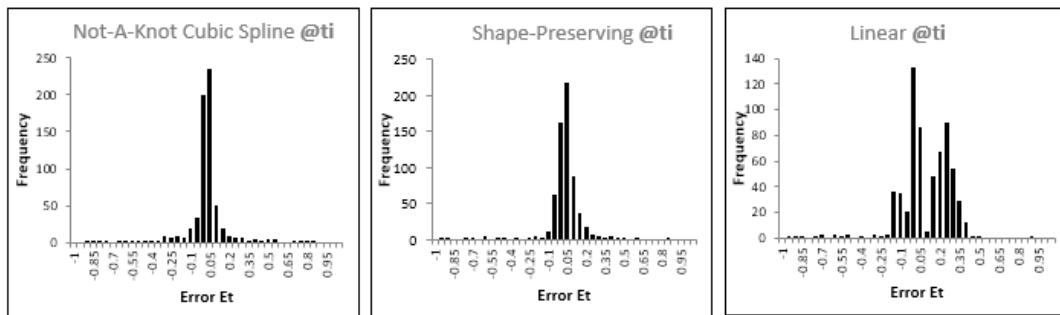
Fig.9: Et frequency distribution for peak **SDR** – Configuration **C1**

The prediction error for the different interpolation methods is calculated also for the other investigated instrumentation configurations, namely **C2**, **C3** and **C4**. The following figure summarizes findings for each interpolation technique and instrumentation layout:
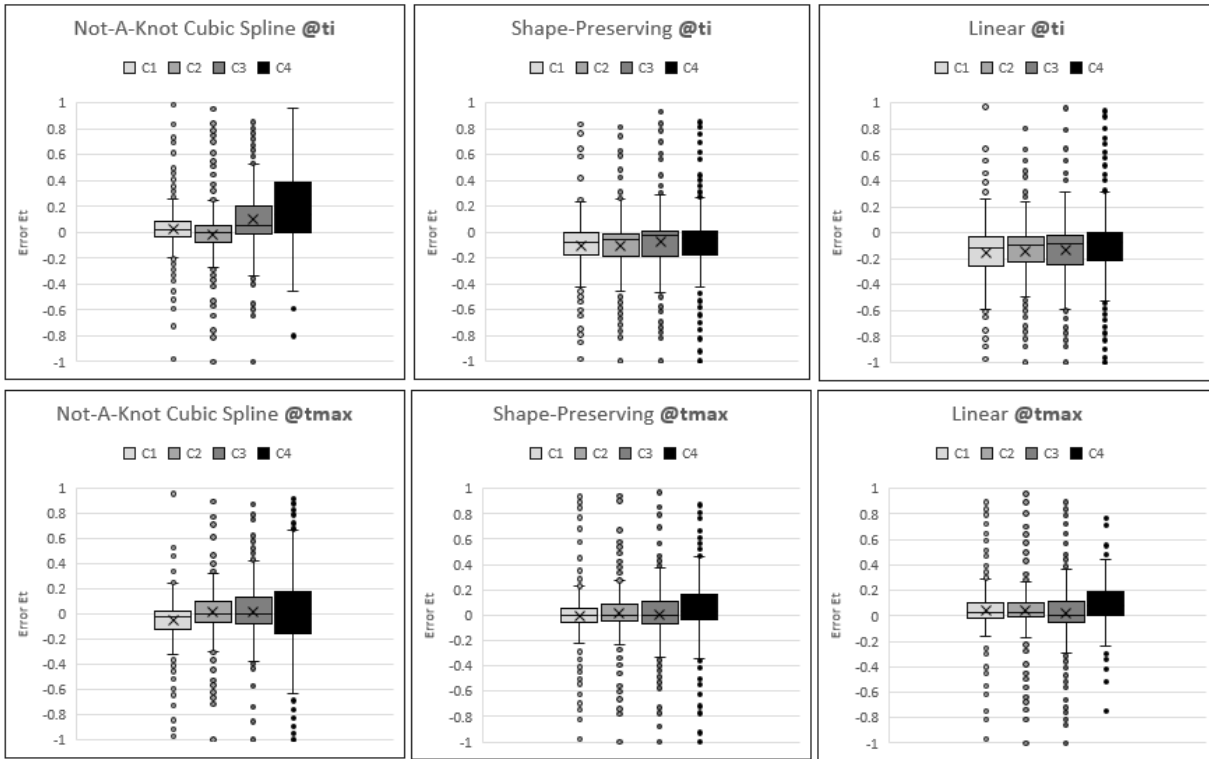
Fig.10: Interpolation error for PFA – Configuration **C1, C2, C3, C4**
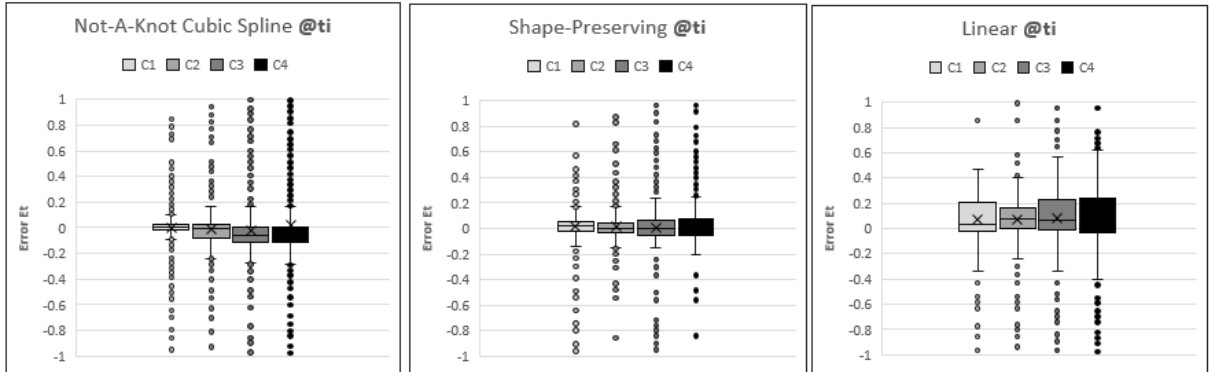
Fig.11: Interpolation error for peak SDR – Configuration **C1, C2, C3, C4**

Once completed in later stages of this study, the archetypes study results will be used to infer dispersion for interpolation prediction error that will then be adopted to determine a probability distribution for unrecorded EDPs.

First Case-Study Building: 7-story Hotel

Building description

The first building selected for the study is a 7-story hotel [CSMIP Station #24386], shown in Figure 12. The building has a seven-story reinforced concrete structure with a floor plan of approximately 150 by 62 feet. The building was designed in 1965 according to the Uniform Building Code (UBC 1961) and constructed in 1966. It is characterized by a lateral-force-resisting system made of non-ductile perimeter moment resisting frames and an internal gravity system comprising a two-way flat slab supported by square columns. The construction cost of the building was $1.3 million in 1966 dollars as reported by John A. Blume & Associates (1973). The 1966 construction cost is equivalent to $6.7 million in 1994 dollars, the year of the 1994 Northridge earthquake, which is assumed as a reference for the following analyses.
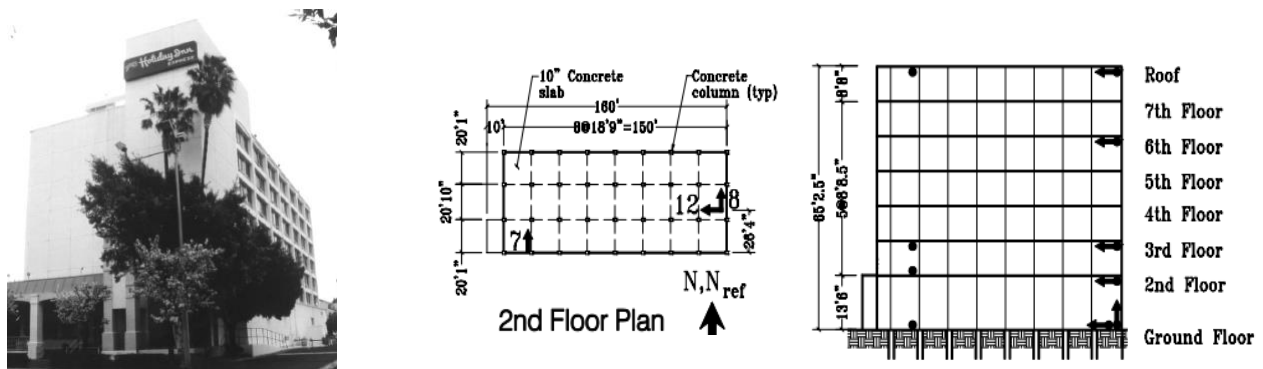
Fig.12: 7-story hotel

The building was instrumented prior to 1971 and its response to major earthquakes was studied extensively [2, 5, 13, 17, 18], including after the 1994 Northridge earthquake that caused severe structural damage, as shown in Figure 13.
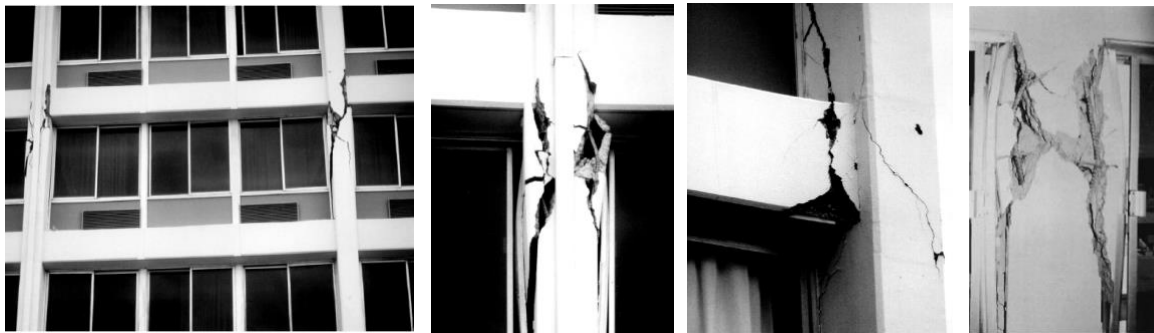
Fig.13: Structural damage during Northridge earthquake

During the Northridge earthquake the building suffered also some light non-structural damage, shown in the next figure:

Fig.14: Non-structural damage during Northridge earthquake

Outline of the analyses

The hotel response is studied through direct loss analysis first for the Northridge earthquake and then for the Landers and Big Bear earthquakes. For the Northridge event, three different types of analyses are performed in terms of input story drift: 1) As Is analysis (**As Is**), where story drift ratio (SDR) is calculated at the instrument locations; 2) geometric center analysis (**GC**), where SDR is calculated at the geometric center of the building floors; and 3) single frame analysis (**SF**), where SDR is calculated at the location and in the direction of each perimeter moment frame, to better account for building torsion. All direct loss analyses are performed in a simplified form in that uncertainties for unrecorded EDPs is not considered.

Reconstruction on of EDPs

The hotel is characterized by an instrumentation layout that is consistent with the investigated configuration **C1** (Figure 4). Floor motions and EDPs are reconstructed for all the analyses adopting a not-a-knot cubic spline interpolation technique at each time step. As shown in previous sections, this method is characterized by minimum prediction errors for story drift ratio (SDR) reconstruction, which is the most important input given the severe structural damage that was observed after the Northridge earthquake. Peak story drift is evaluated, as explained in the outline, at different locations (Figure 15), which are: 1) instruments locations; 2) building geometric center; and 3) center of each perimeter moment frame.
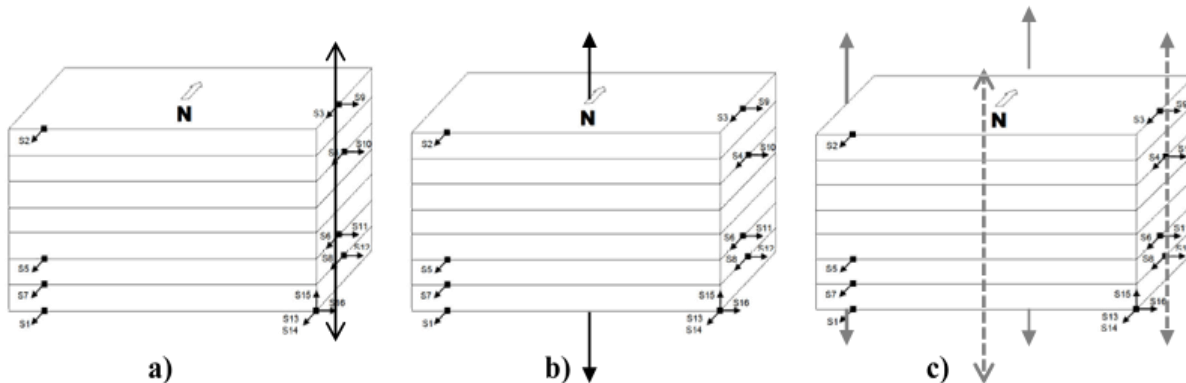
Fig.15: peak SDR location for the different direct loss analysis, a) As Is; b) GC; and c) SF

Figure 16 presents EDPs calculated for the three analyses. It can be appreciated that transposing the displacement to the building geometric center has no effect on East-West direction response. This is because instruments used to infer EDPs are located at mid-span of the North-South building framing, as shown in Figure 12. Also, the EW direction is slightly affected by torsional building response, as it can be seen from north and south frame story drift.
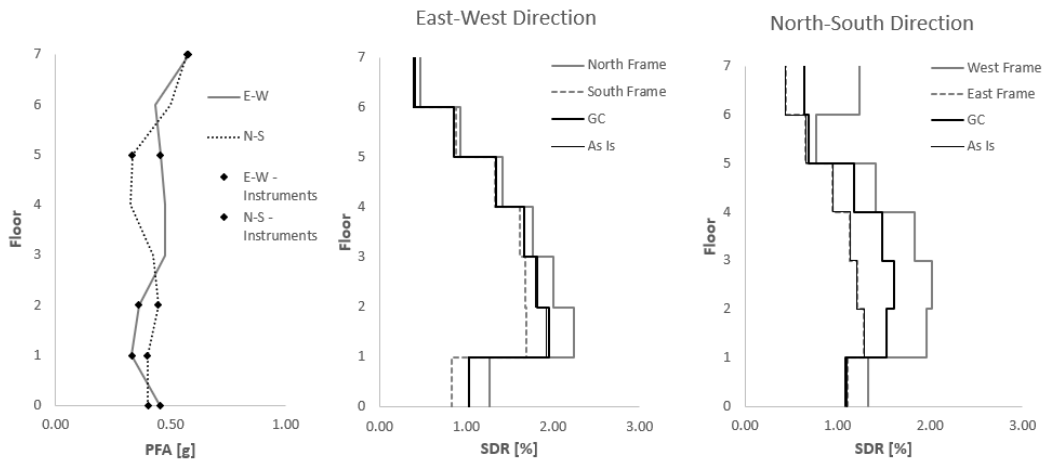

Fig.16: Calculated Engineering Demand Parameters for the building

Direct loss analyses

The loss analyses require the identification of building contents to evaluate likelihood of damage and capital repair costs. Building content population is defined using FEMA P58 "Normative Quantitative Estimation Tool" for generic non-structural components. Structural components and additional non-structural components, such as furniture, were added to the building components population, on the basis of specific knowledge of the building. Detailed information was available for the building, including architectural floors plan and suite floor plan, as shown in Figure 17.

a)   **b)**
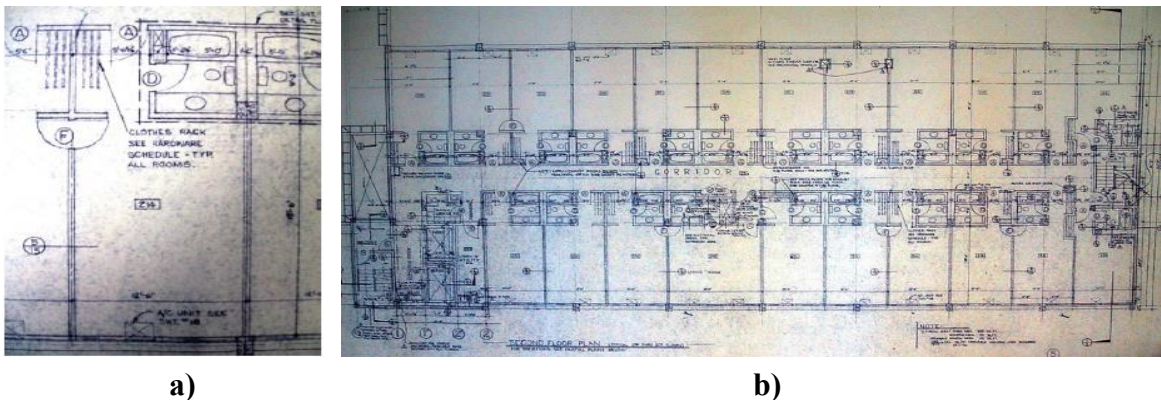
Fig.17: a) typical suite floor plan; b) second floor architectural plan. After *Porter et al.* [2]

The Instrumented Building Loss Analyzer (IBLA) is used to evaluate damage and losses for the structural components, for all types of analyses. The algorithm allows using multiple sets of peak SDR as input for the analysis and it defines the unit repair costs based on the overall number of damaged components in the building. Therefore, in the case of single frame analysis, it aggregates structural damage of each frame before performing the loss analysis. Non-structural components damage and losses are defined through the commercial software SP3 by Haselton Baker Risk Group.

Figure 18 and 19 present the results of the three type of analysis in terms of capital repair costs, normalized with respect to building construction cost, and also an overview of the direct loss analyses results for three earthquakes (Landers, Big Bear, and Northridge) of the 1990s. Figure 18 shows the four largest contributors to loss (structural components; walls, partitions, and external shell; elevators and stairs; and furniture). The next largest loss items were: 1) Ceiling; 2) Piping; 3) Heating, HVAV and VAV; 4) Electrical & fire protection; and 5) Concrete tile roof. Loss for these non-structural components were too small to be identified in Figure 18
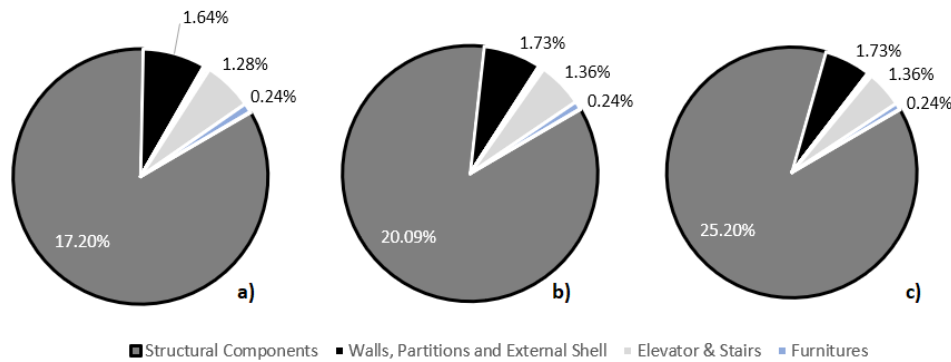
Fig.18: Direct loss analyses results, a) As Is analysis; b) GC analysis; and c) SF analysis
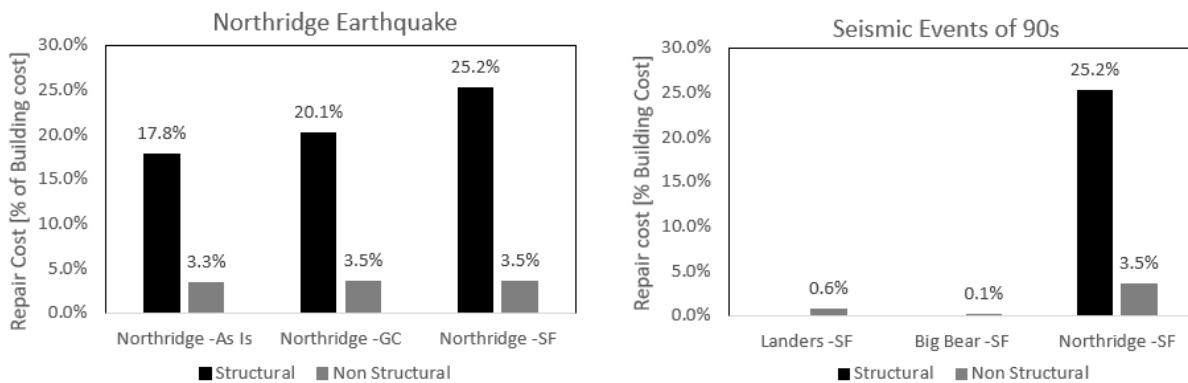

Fig.19: Summary of direct loss analyses results and loss evaluation for the Landers, Big Bear, and Northridge earthquakes

Results comparison with observed damage

Figure 20 shows a site survey of the building during post-Northridge repair works, where significant use of epoxy injection is apparent [11]. Evidence from this photograph is used to update an existing sketch of observed damage for the north frame [17], which does not sufficiently identify the spread of damage in the reinforced concrete beams, columns and joints.

Estimated structural damage for the north frame with the single frame (**SF)** analysis is compared with the above-mentioned damage sketch. The direct loss assessment for structural components seems to be reasonably representing the extent of damage for the north frame, as shown in Figure 21, where the different calculated damage states are identified. For instance, the number of components in damage state DS 3, between third to fifth floor, is consistent with observed damage to beam-column joints and to the frame external columns. Similarly, the observed spread of elements cracking seems to be reasonably identified by the number of elements in damage state DS 1.

Regarding non-structural components, several sources including the *Earthquake Engineering Field Investigation Team* [5] have reported limited damage in the aftermath of the Northridge earthquake. Damage was limited to: 1) minor cracking to external and internal partition walls; 2) tilted furniture; 3) minor damage to elevators (loss of hydraulic fluid); and 4) damage to doors. The single frame loss analysis successfully identified these components as the major non-structural contributors to losses (Figure 18c), except for doors, which were not modeled. For all three of the 1990s earthquakes, namely Landers, Big Bear, and Northridge, non-structural damage calculations seem to be slightly overestimated relative to actual damage. For Big Bear and Landers, damage to non-structural components was not reported, while for Northridge the minor observed damage to elevators and partitions does not seem enough to justify the calculated losses.

Regarding downtime, the single frame (**SF**) analysis estimates a maximum repair time of 316 days, under the hypothesis that one floor is repaired at a time (FEMA P58). This result seems to underestimate the actual downtime considering that repair works was still undergoing during July 1995, as reported by *Lynn et al.* [11] and shown in Figure 20. The disagreement might be due to impeding factors, such as contracting and permitting, that are currently not considered in FEMA P58 methodology.

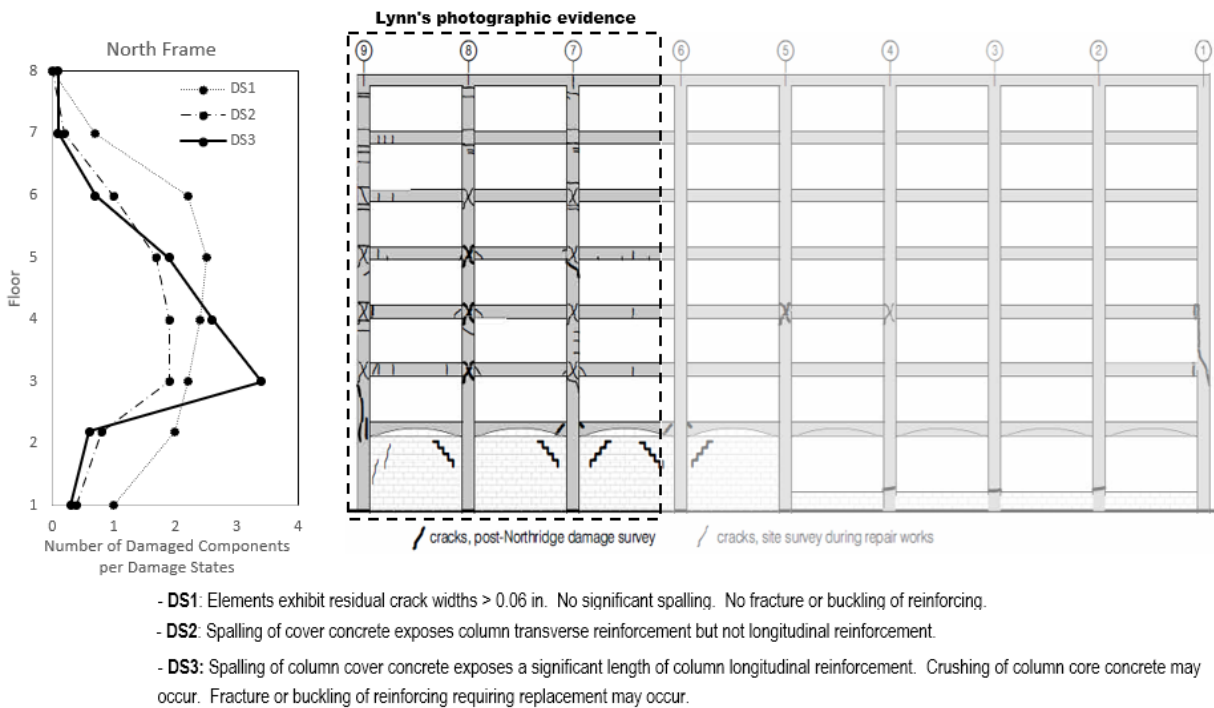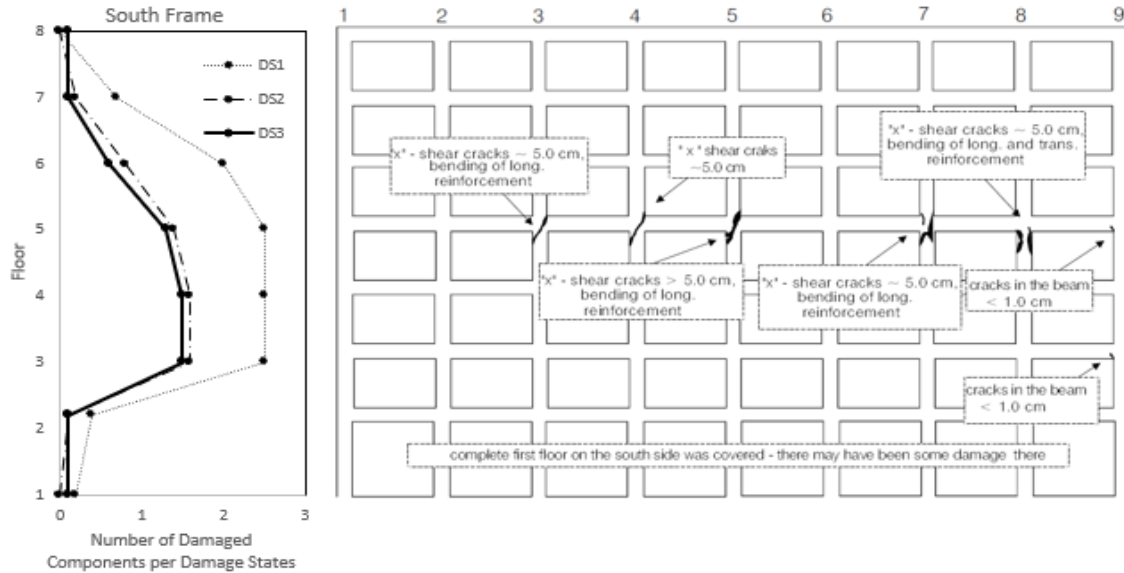*Fig.20*: Building site survey during repair works - July 1995, after *Lynn et al.* [11]

- **DS1**: Elements exhibit residual crack widths > 0.06 in. No significant spalling. No fracture or buckling of reinforcing.
- **DS2**: Spalling of cover concrete exposes column transverse reinforcement but not longitudinal reinforcement.
- **DS3**: Spalling of column cover concrete exposes a significant length of column longitudinal reinforcement. Crushing of column core concrete may occur. Fracture or buckling of reinforcing requiring replacement may occur.

Fig.21: Comparison of calculated damage with updated post-Northridge damage survey (north frame)

- **DS1**: Elements exhibit residual crack widths > 0.06 in. No significant spalling. No fracture or buckling of reinforcing.
- **DS2**: Spalling of cover concrete exposes column transverse reinforcement but not longitudinal reinforcement.
- **DS3**: Spalling of column cover concrete exposes a significant length of column longitudinal reinforcement. Crushing of column core concrete may occur. Fracture or buckling of reinforcing requiring replacement may occur.

Fig.22: Comparison of calculated damage with existing post-Northridge damage survey (south frame)

Second Case-Study Building: The Imperial County Services Building

Building description

The second building selected for study is an administration building [CSMIP Station #01260], shown in Figure 23. The building has a six-story reinforced concrete structure with a floor plan of approximately 136 by 85 feet of office space. The building was designed in 1967, according to the Uniform Building Code (UBC 1967) and constructed in 1969. It was characterized by a lateral-force-resisting system made of four moment-resisting frames in the longitudinal direction and structural walls in the transverse direction, with the west wall being a coupled wall. Gravity loads were sustained by a slab-joist system spanning in the transverse direction and transferred to the ground through the longitudinal frames. The building was instrumented and its response to the Imperial Valley earthquake was extensively studied [8, 9, 15, 16].
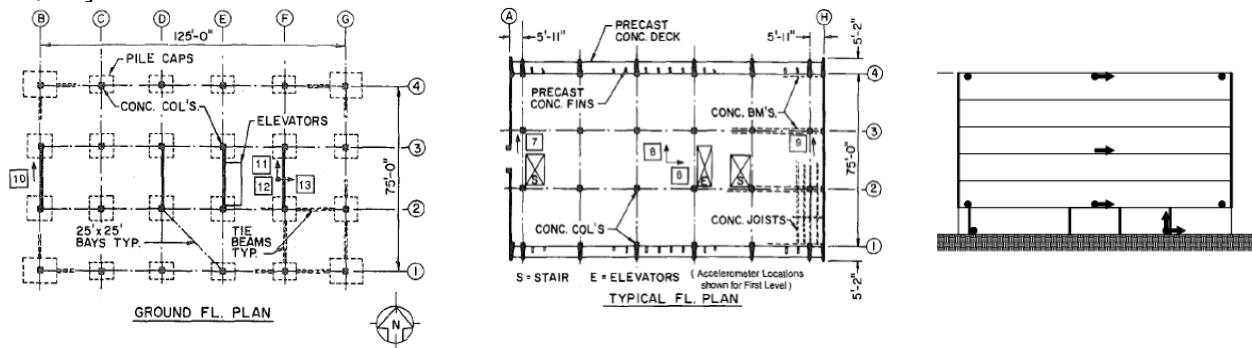

Fig.23: Floor plan and accelerometer locations, after *Sozen et al.* [8]

The building was characterized by significant irregularities in plan and over the building height. At the ground floor, the shear walls were unevenly distributed, likely fostering a building torsional response. Along the building height the shear walls were also discontinuous, as shown in Figure 24. Another irregularity consisted of a column recess provided at the base of all first-story columns, which is also shown in Figure 24. The recess produced a reduced section and required offset column longitudinal reinforcement within a lightly confined length of the column.
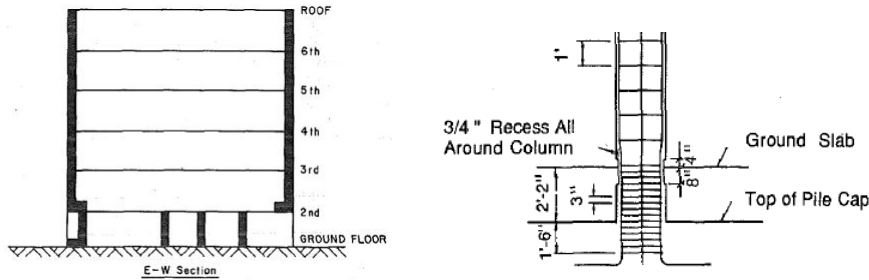
Fig.24: Building irregularities, after *Sozen et al.* [8]

The building suffered extensive structural damage during the 1979 Imperial Valley earthquake, with failure and significant shortening of the east end columns that caused a partial collapse of the same end of the building, as shown in Figure 25. Due to severity of damage the building was later demolished. As reported by *Whitaker et al.* [1], an estimate was made regarding the construction cost of a new building of the same size and design to replace the damaged building, which amounted to $ 6.8 million. This value, in 1980 dollars, is assumed as a reference for the following loss analyses.
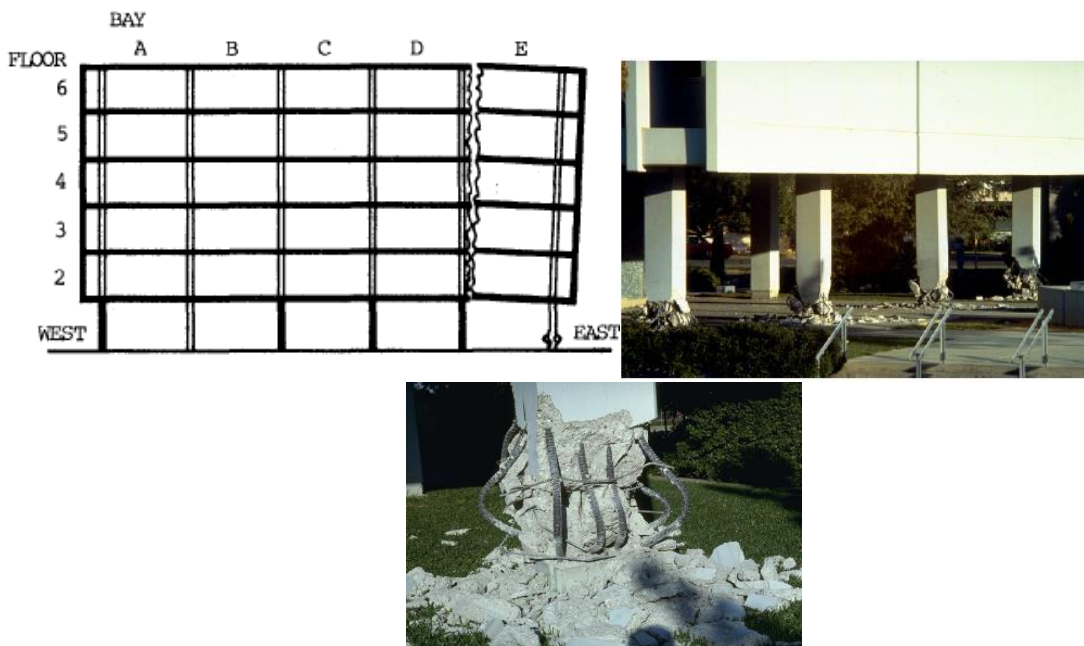

Fig.25: Imperial Valley structural damage to the East end of the structure, *after Whitaker* [1] *and NISEE*

Preliminary direct loss analysis results and comparison with observed damage

The building response to the Imperial Valley earthquake is studied considering as input for the direct loss analysis both the peak floor accelerations and the peak story drift ratios at the geometric center of the building (**GC** analysis) and at the location of each moment frame and shear wall (**SF** analysis). Evaluation of EDPs (Figure 26) at instrumented and non-instrumented floors and loss analysis were performed under the same assumptions adopted for the 7-story hotel.
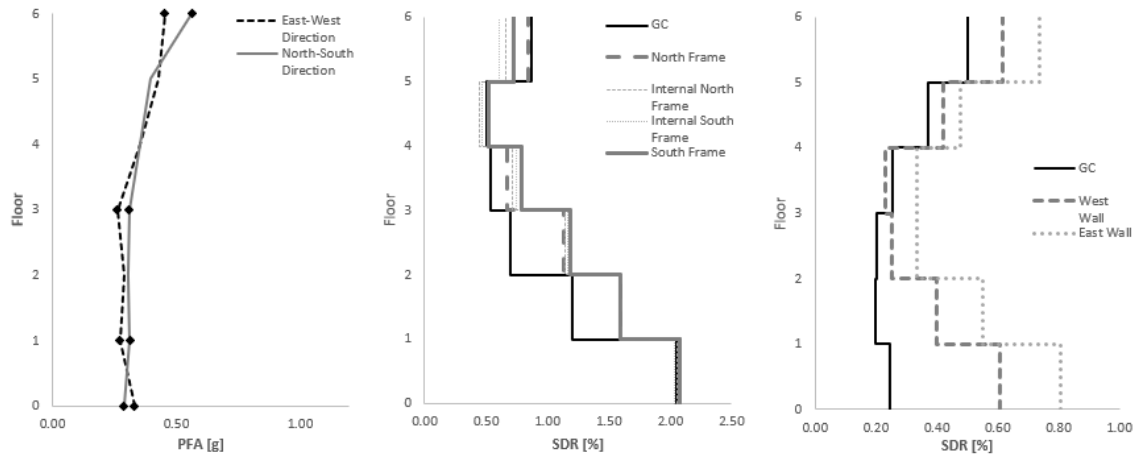
Fig.26: Calculated Engineering Demand Parameters for the building

For damage and loss analysis, the building non-structural content population was defined using FEMA P58 "Normative Quantitative Estimation Tool", while structural components were defined based on specific knowledge of the structural system. Preliminary results, not considering interpolation errors, are presented comparing damage predictions through **SF** analysis to post-earthquake damage observations [19]. The evaluation of damage along the structural height is performed through the Matlab routine IBLA.
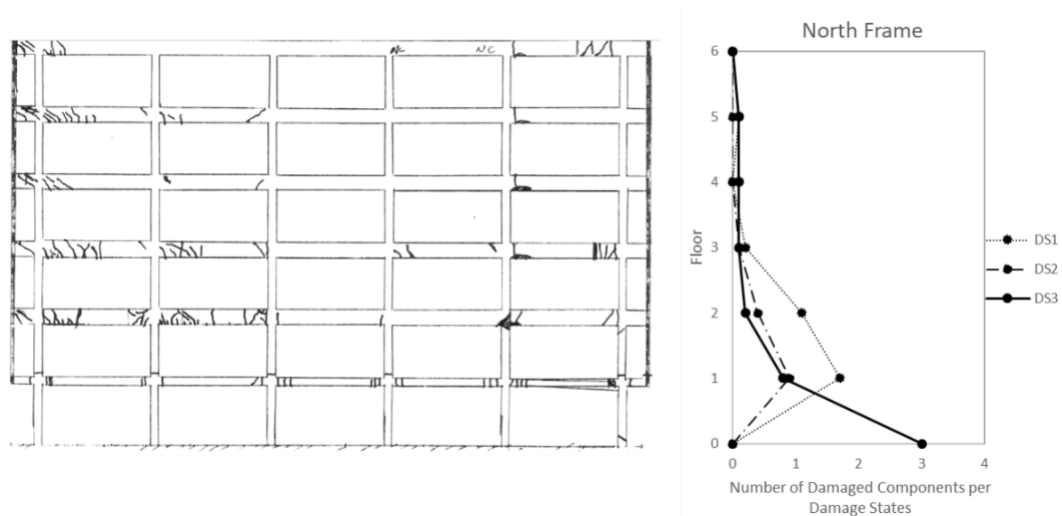

Fig.27: Calculated vs. observed damage to the building north frame

The comparison of calculated and observed damage shows a considerable underestimation of the damage distribution for the north frame. It is to be noted that damage to the east bay beam (right side of the frame in Figure 27), induced by a specific failure mechanism which is the shortening of the columns, is not represented through the FEMA P58 fragility functions, as they only consider peak horizontal story drift ratio, not vertical drift due to column collapse. Notwithstanding this consideration, the direct damage analysis is not identifying any damage above the second floor. Comparison of calculated and observed damage of the other frames and walls shows a similar underestimating trend. We continue to study the discrepancy between calculated and observed damage at the time of this writing.

Figure 28 compares calculated losses with a post-earthquake repair cost estimate prepared by county engineers in the aftermath of Imperial Valley Earthquake, as reported by *Whitaker et al.* [1]. The significant discrepancy is consistent with the discrepancy in results shown in Figure 27.
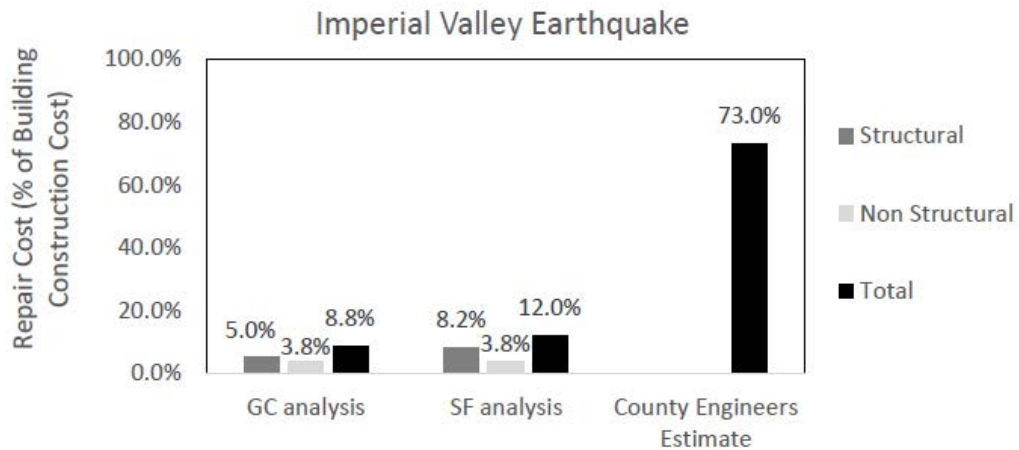

Fig.28: Predicted repair costs vs. repair cost estimate

Current work

The work presented in the previous sections represents preliminary findings to an ongoing study. For this reason, conclusions are not presented herein. Instead a brief description of the current work and anticipated results is presented.

We continue work on the archetype buildings database such that we will be able to draw more general conclusions about the ability of different interpolation methods to reconstruct unrecorded EDPs in an instrumented building. The prediction error for different interpolation techniques is only tested with respect to absolute peak story drift ratio and peak floor acceleration, which are the components of interest for loss analysis. The goal of this archetype study is to characterize interpolation prediction uncertainty that will be then used to define probability distributions of unrecorded EDPs. Once the archetypes study is completed, the direct loss analyses of the buildings presented in this paper will be re-evaluated through a probabilistic approach.

A third case-study building, the Sylmar County Hospital [CSMIP Station #: 24514], that suffered significant non-structural damage during the Northridge event, is currently being analyzed using the direct loss assessment methods described above. The main intent is to evaluate the ability to estimate non-structural components performance and to make an observation of the reasonableness of output from FEMA P58 relative to acceleration-sensitive components.

In parallel to the above-mentioned studies, an industry partner, Interprogetti Engineering Consulting, is currently pursuing the analysis of the first two buildings through the entire FEMA P58 probabilistic loss assessment methodology. Results from the direct loss analysis and the application of the entire FEMA P58 will be compared and their ability to estimate damage will be tested against earthquake damage observations. In particular, the reasonableness of direct loss assessment results is going to be investigated with the intent of evaluating the feasibility of implementing a rapid post-earthquake loss estimation methodology.

Acknowledgment

References

[1] C. Arnold, M. Durkin, R. Eisner and D. Whitaker. "Imperial County Services Building: Occupant Behavior and Operational Consequences as a Result of the 1979 Imperial Valley Earthquake". Information Resources National Science Foundation. 1982;

[2] J.L. Beck, K.A. Porter. "Impact of Seismic Risk on Lifetime Property Values". EERL Report. 2002;

[3] D. Bernal and A. Nasseri. "Schemes for reconstructing the seismic response of instrumented buildings". SMIP Seminar Proceedings. 2009;

[4] G. Cremen and J.W. Baker. "Quantifying the benefits of building instruments to FEMA P-58 rapid post-earthquake damage and loss predictions". Engineering Structures. 2018;

[5] Earthquake Engineering Field Investigation Team. "The Northridge, California Earthquake of 17 January 1994". 1995;

[6] Federal Emergency Management Agency P58-1-2. "Seismic Performance Assessment of Buildings". 2012;

[7] D. Kahaner, C. Moler, and S. Nash. "Numerical Methods and Software", Prentice–Hall, Englewood Cliffs, NJ. 1989;

[8] M. E. Kreger, M. A. Sozen. "Seismic Response of Imperial County Service Building in 1979. Journal of Structural Engineering". 1989;

[9] M. E. Kreger, M. A. Sozen. "A study of the Causes of Column Failures in the Imperial County Services Building during the 15 October 1979 Imperial Valley Earthquake". Dissertation. 1983;

[10] R.R. Lui, S. Mahin, J.P. Moehle. "Seismic Response and Analytical Modeling of the CSULA Administration Building Subjected to the Whitter Narros Earthquake.", SMIP 1990 Seminar on Seismological and Engineering Implications of Recent Strong-Motion Data, pp. 8-1 - 8-10. 1990;

[11] A. Lynn. "Seismic Evaluation of Reinforced Concrete Columns". Doctoral Dissertation. 2001;

[12] F. Naeim, H. Lee, H. Bhatia, A. Alimorandi, E. Miranda. "Three-Dimensional Analysis, Real-Time Visualization, and Automated Post-Earthquake Damage Assessment of Buildings". In: The Structural Design of Tall and Special Buildings. 2006;

[13] Pacific Earthquake Engineering Research Center. "Van Nuys Hotel Building Testbed Report: Exercising Seismic Performance Assessment". PEER report 11. 2005;

[14] K.A. Porter, "An Overview of PEER's Performance-Based Earthquake Engineering Methodology" 9th Int. Conf. Appl. Stat. Probab. Civ. Eng., vol. 273, no. 1995, pp. 973–980, 2003;

[15] R. Shepherd, A.W. Plunkett. "Damage Analyses of Imperial County Service Building". Journal of Structural Engineering. 1983;

[16] M.I. Todorovska, M.D. Trifunac. "Earthquake damage detection in the Imperial County Services Building I: The data and time–frequency analysis". Soil Dynamics and Earthquake Engineering 27, 564–576. 2007;

[17] M.I. Todorovska and M.D.Trifunac. "Impulse response analysis of the Van Nuys 7-storey hotel during 11 earthquakes and earthquake damage detection". Structural Control and Health Monitoring. 2007;

[18] M.D. Trifunac, S.S. Ivanovic, M.I. Todorovska, E.I. Novikova, A.A. Gladkov. "Experimental evidence for flexibility of a building foundation supported by concrete friction piles". Soil Dynamics and Earthquake Engineering. 1999;

[19] C.A. Zeris. "Investigation of the Response of the Imperial County Services Building to the 1979 Imperial Valley Earthquake and Implications to Earthquake-Resistant Design". SEMM Division, University of California Berkeley.